UNIVERSITY OF LEEDS

Kinematics and physical properties of a highly filamentary Infrared Dark Cloud

Jonathan David Henshaw

School of Physics and Astronomy

University of Leeds

Submitted in accordance with
the requirements for the degree of

Doctor of Philosophy

May 2014

The candidate confirms that the work submitted is his own, except where work which has formed part of jointly authored publications has been included. The contribution of the candidate and the other authors of this work has been explicitly indicated. The candidate confirms that appropriate credit has been given within this thesis where reference has been made to the work of others.

For my parents

Preface

Within this thesis, chapters 2 and 3 have been based on work presented in the following jointly authored publications:

I. Complex, quiescent kinematics in a filamentary infrared dark cloud, **J. D. Henshaw**, P. Caselli, F. Fontani, I. Jiménez-Serra, J. C. Tan, A. K. Hernandez, MNRAS, 428, p.3425-3442.

II. The dynamical properties of dense filaments in the Infrared Dark Cloud G035.39-00.33, **J. D. Henshaw**, P. Caselli, F. Fontani, I. Jiménez-Serra, J. C. Tan, MNRAS, 440, p.2860-2881.

Paper I forms the basis of chapter 2. The data were obtained with proposals written by P. Caselli. The data were collected by P. Caselli, F. Fontani, and I. Jiménez-Serra. The primary author (J. D. Henshaw) was responsible for the data analysis and interpretation. The analysis involved the development of a technique required to decompose and analyse the spectra. The information extracted from this analysis technique was then used to comprise the primary results of this paper. Further analysis incorporated the use of radiative transfer code, RADEX, written by F. F. S. Van der Tak. The primary author wrote the initial draft of the publication, and then incorporated comments from co-authors in the final draft.

Paper II forms the basis of chapter 3. The data were obtained with proposals written by the primary author (J. D. Henshaw) and P. Caselli. The primary author was responsible for the data reduction, analysis (including the development of the fitting routine used), and interpretation. The primary author wrote the initial draft of the publication, and then incorporated comments from co-authors in the final draft.

Acknowledgements

First and foremost, I would like to express my gratitude to my supervisor Paola Caselli, for being so generous with her time, patience, knowledge, and for regularly encouraging me to step out of my comfort zone throughout this process. It has been (and continues to be) a pleasure to work with Paola, and a fantastic group of researchers whose knowledge and experience has enriched my research. I would particularly like to thank Izaskun Jiménez-Serra, Francesco Fontani, and Jonathan Tan for their help and guidance, and for taking the time to read countless drafts of papers and proposals. I would also like to thank Jaime Pineda and Cormac Purcell for their assistance, particularly in the earliest stages of my PhD.

I am grateful to my examiners, Gary Fuller and Tom Hartquist, for taking the time to read my thesis, and for making my viva an enjoyable experience. Having been a tutee of Tom during my undergraduate degree, I am extremely proud to have completed my PhD with Tom as my examiner. Thanks must also go to the staff at Leeds, Melvin Hoare, Stuart Lumsden, René Oudmaijer, and Julian Pittard for sharing their knowledge over the years I have spent at Leeds.

A warm thank you goes to my fellow PhD students and the postdoctoral researchers at the University of Leeds. I thank in particular Mo Ali, Robbie Alūzas, Tom Douglas, John Fairlamb, Dan Parsons, Hazel Rogers, and Hugh Wheelwright for making Leeds such an enjoyable place to work. A special thank you goes to my good friends Nichol Cunningham, John Ilee and Luke Maud for always being there for a pint when things got tough (and for those other times, when things were not so tough and we went to the pub anyway).

I am extremely fortunate to have to love and support of my wonderful family and friends. Thank you to my grandparents for always being interested in what I do, it is a constant source of encouragement to know that it makes you proud. To my brother Alex and sister-in-law Gemma, thank you for having been through this experience before me, understanding, and for offering advice whenever I needed it. To Grace, thank you for being so selfless, and for so often picking me up, dusting me off, and sending me back off to work in those last few months. Finally, I would like to thank my parents, Chris and Margaret, for always believing in me, even when I don't always believe in myself.

Abstract

This thesis contains a detailed study of the kinematics and physical properties of a potential site of massive star formation; the IRDC G035.39-00.33.

The gas kinematics are first of all investigated using high-spectral resolution and high-sensitivity data from the IRAM 30 m telescope. The primary focus of this work is the $J = 1 \rightarrow 0$ transition of both N_2H^+ and $C^{18}O$, as well as N_2H^+ $(3-2)$. Dense gas is found to be extended over $\sim$3 pc scales within G035.39-00.33. The $C^{18}O$ observations confirm the presence of at least three morphologically distinct filamentary components. It is speculated that the merging of filaments may be responsible for the formation of localised density enhancements at their interface; the potential sites for massive star and star-cluster formation.

The kinematic properties of the dense gas are then probed at high-angular resolution, using observations of N_2H^+ $(1-0)$ from the Plateau de Bure Interferometer. It is revealed that the dense gas of G035.39-00.33 is organised into a complex network of mildly supersonic filaments separated in velocity by < 1 km s^{-1}. Whilst global velocity gradients throughout each filament are small, there is evidence for dynamic processes on local scales. This suggests that the kinematics are influenced by the dense (and in some cases, starless) cores.

The physical properties of the embedded core population are derived in the final study of this thesis. A total of 14 continuum peaks are identified, representative of the pre- and protostellar core population covering two main clumps within G035.39-00.33. The derived core masses are found to be between 2.4-12.3 $M_\odot$, with sizes and densities between 0.03-0.07 pc and 1.6×10^5-7.3×10^5, respectively. Some of the

cores exhibit irregular boundaries, which may imply the presence of unresolved sub-structure. Although the dynamical state of each core is dependent on both its geometry and density profile (which are both sources of uncertainty) it is found that many of the identified cores are unstable to collapse. Cores which are well represented by monolithic, centrally condensed structures, exhibiting low virial parameters and many Jeans masses, are good candidates for the progenitors of intermediate-to-high-mass stars. Within the selected area of G035.39-00.33, two of the identified cores meet this criteria.

Abbreviations

ALMA	Atacama Large Millimeter Array
arcsec	Arc Second
CMZ	Central Molecular Zone
EMIR	Eight MIxer Receiver
FWHM	Full-Width at Half-Maximum
GMC	Giant Molecular Cloud
HFS	Hyperfine Structure
HMSC	High-Mass Starless Core
HWHM	Half-Width at Half-Maximum
IDL	Interactive Data Language
IMF	Initial Mass Function
IRAM	Institut de Radioastronomie Millimétrique
IRAS	Infrared Astronomical Satellite
IRDC	Infrared Dark Cloud
ISM	Interstellar Medium
ISO	Infrared Space Observatory
LTE	Local Thermodynamic Equilibrium
MIR	Mid-Infrared
MSC	Massive Starless Core
MSX	Midcourse Space Experiment
MYSO	Massive Young Stellar Object
NIR	Near-Infrared
NOEMA	Northern Extended Millimetre Array
PACS	Photodetector Array Camera & Spectrometer
pc	Parsec

PdBI	Plateau de Bure Interferometer
PPV	Position-Position-Velocity
PV	Position-Velocity
RMS	Red MSX Source
SMA	Submillimeter Array
SPIRE	Spectral and Photometric Imaging Receiver
VESPA	VErsatile SPectrometer Assembly

Contents

List of Figures

List of Tables

Chapter 1

Introduction

Massive stars ($> 8\,M_{\odot}$) play a fundamental role in the evolution of our Galaxy. Through powerful stellar winds and expanding HII regions, massive stars sculpt their local environment, which can both aid and inhibit new episodes of star formation. In addition, their violent death in the form of explosive supernovae injects heavy elements into the interstellar medium (hereafter, ISM). The enrichment of the ISM impacts multiple physical scales, driving the evolution of galaxies, and providing the constituent ingredients for the formation of planets.

In spite of the profound effect massive stars have on their environment, and the subsequent interest this has evoked in astronomers, a comprehensive understanding of their formation is still lacking. Massive stars evolve quickly, in clusters, and, during the earliest stages of their formation, they are embedded deep within dense molecular clouds. As massive stars are rare, they are typically found at larger distances than their more common, low-mass counterparts. This poses a significant technological challenge, as telescopes must have sufficient angular resolution to disentangle them from their cluster companions.

Understanding and categorising the *initial conditions* for the formation of massive stars presents a serious challenge for observers and theoreticians alike. This thesis aims to address some of the, as yet, unanswered questions regarding the dynamical and physical processes involved in the earliest stages of massive star formation, with particular emphasis on their host clouds. This introductory chapter is devoted to discussing some of the observational and theoretical concepts surrounding the birthplaces of stars, and the formation of stars themselves. In addition, the main focus of this thesis; Infrared Dark Clouds, will be introduced, and the role they play in the current understanding of star formation, discussed.

1.1 An introduction to molecular clouds

Star formation within our Galaxy occurs exclusively within molecular clouds. Cold and dense ($T \sim$ 10-30 K, $n_{\rm H} \sim 10^2$–10^5 cm^{-3}; Stahler & Palla 2005) molecular clouds are opaque at optical wavelengths as the background starlight is absorbed by tiny dust grains (10^{-9}–10^{-3} m; Draine 2006, Mathis *et al.* 1977). In his photographic survey "On the dark markings of the sky" (Barnard 1919) stated:

> "I did not first believe in these dark obscuring masses. The proof was not conclusive. The increase of evidence, however, from my own photographs convinced me later, especially after investigating some of them visually, that many of these markings were not simply due to an actual want of stars, but were really obscuring bodies nearer to us than the distant stars."

Emission from molecular clouds however, can be detected at the millimetre and sub-millimetre wavelengths indicative of low temperatures. Molecular clouds display a rich variety of chemistry, with over 200 species detected to date (Müller *et al.* 2005, Tielens 2005). It is this molecular line emission, as well as thermal emission from dust particles, that enables astronomers to study the chemical, dynamical, and physical structure of star-forming clouds.

As the formation of stars is intimately entwined with the evolution of their parent material, the following section discusses the physical and dynamic properties, and possible formation mechanisms of molecular clouds.

1.1.1 The structure of molecular clouds

Physical characteristics

Molecular clouds span a wide range of scales in terms of mass, density, and physical size. They can however, be loosely categorised into several groups. The smallest of these are the Bok Globules (Bok & Reilly 1947), of typical size ~ 0.2–$1\,\mathrm{pc}$, and densities $\sim 10^3\,\mathrm{cm}^{-3}$ (Launhardt *et al.* 2010). In order of increasing mass, "dark clouds" (named in reference to their ability to absorb background starlight), are observed either in isolation (with sizes of the order $\sim 2\,\mathrm{pc}$), or part of larger complexes (such as the local clouds within $\sim 500\,\mathrm{pc}$ e.g. Taurus, Perseus, Ophiuchus). These complexes can have masses in the region of $\sim 10^4\,\mathrm{M}_\odot$, and sizes of the order $\sim 10\,\mathrm{pc}$ (Cambrésy 1999), and may give rise to the formation of hundreds of low-mass stars (e.g. the Taurus-Auriga complex, distance $\sim 140\,\mathrm{pc}$; Kenyon *et al.* 1994). At the higher end of this scale are the Giant Molecular Clouds (hereafter, GMCs), that contain $\geq 10^5\,\mathrm{M}_\odot$ of material, sizes $\sim 50\,\mathrm{pc}$, and number densities $\sim 100\,\mathrm{cm}^{-3}$ (e.g. Blitz 1993, and references therein). The observed power law distribution of molecular cloud masses $\gtrsim 10^5\,\mathrm{M}_\odot$ ($dN/dM \sim \mathrm{M}^{-\gamma}$, whereby $\gamma \sim 1.5$–2; e.g. Heyer *et al.* 2001, Roman-Duval *et al.* 2010, Solomon *et al.* 1987a), indicates that the majority of the mass is contained within the most massive clouds.

The gas within molecular clouds is not distributed uniformly. Stars form in concentrated regions of high density. Williams *et al.* (2000) introduced an operational categorisation of the structure of molecular gas within the ISM. The original nomenclature describes clouds, clumps, and cores. Clouds are defined as extended regions of molecular gas. The term 'clump' describes coherent regions in position-position-velocity space that will lead to the formation of star-clusters. Finally,

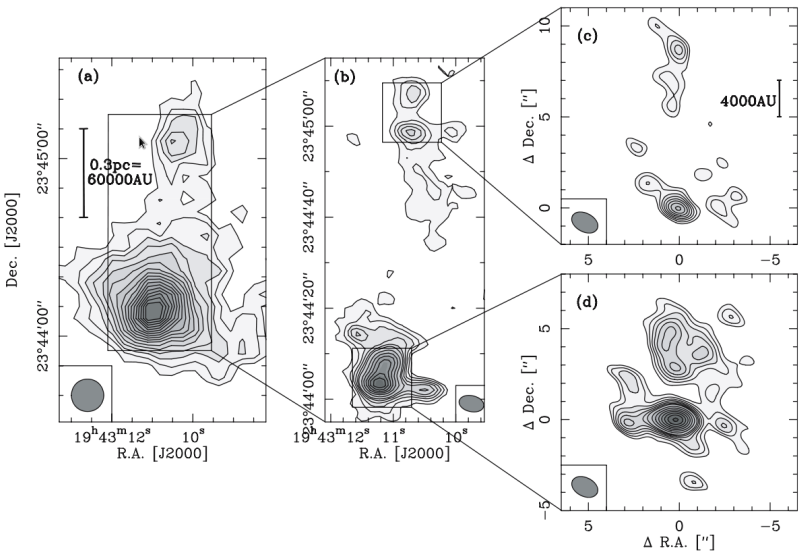

Figure 1.1: Dust continuum images of the massive star forming region IRAS 19410+2336 from Beuther & Schilke (2004). The left image shows 1.2 mm single-dish data obtained with the IRAM 30 m telescope. The middle and right images are 3 mm and 1.3 mm (respectively) data obtained with the IRAM Plateau de Bure Interferometer. The beam sizes for each image can be found in the bottom corners of plots. This image highlights the clumpy, fragmented, internal structure of molecular clouds.

cores are regions out of which single stars (or binaries) form.

In more massive regions, such as GMCs, this characterisation becomes more difficult, as distant massive "cores" have a propensity to exhibit substructure when viewed at high-angular resolution. An example of this can be seen in Figure 1.1 which displays dust continuum emission images from the massive star forming region IRAS 19410+2336 at different spatial scales (Beuther & Schilke 2004). The left-hand image displays single-dish data from the IRAM 30 m telescope at $11''$ resolution. The structure in the left-hand panel covers $\lesssim 1$ pc in spatial extent, two cluster-forming *clumps* are identified by the authors. The middle and right-hand plots are interferometric images at higher-angular resolution ($\sim 5.5'' \times 3.5''$ and

$\sim 1.5'' \times 1.0''$, respectively). The interferometer filters extended emission observed in the left-hand plot, highlighting the individual *cores* that comprise each clump.

The internal structure of molecular clouds has characteristically low temperature, in the region of $\sim$10-20 K. At high column densities ($> N_{\rm H} \sim 10^{21}\,{\rm cm}^{-2}$; Bergin *et al.* 2004), such as those typically observed in dense molecular clouds, gas is shielded from the stellar ultra-violet (UV) component (Mathis *et al.* 1983) of the interstellar radiation field. Heating within molecular clouds is therefore dominated by cosmic ray interactions, whereas the rotational transitions of abundant molecules (such as CO) are important for cooling (Goldsmith 2001).

Morphology

The advent of the *Herschel* Space Observatory (Pilbratt *et al.* 2010) has led to an unprecedented insight into the structure of the cold ISM. One of the most striking results from the *Herschel* Galactic imaging surveys (the Gould Belt Survey; André *et al.* 2010, and the *Herschel* Infrared GALactic plane survey; Molinari *et al.* 2010), is that filamentary structures permeate through *all* of the observed molecular clouds (a filament in this context refers to a structure of high-aspect ratio, i.e. $\sim$5-10, that exhibits a significant density contrast with its surrounding environment; André *et al.* 2013). This filamentary structure is exemplified in Figure 1.2, a composite image of the Orion B molecular cloud taken using both the Photodetector Array Camera and Spectrometer (PACS), and the Spectral and Photometric Imaging Receiver (SPIRE) instruments of *Herschel* (the blue, green, and red colours refer to emission at 70 μm, 160 μm, and 250 μm, respectively). It is evident from this figure that the cold gas ($\sim$12 K; seen in red) is ordered into a complex network of filaments. Moreover, these filaments are spatially coincident

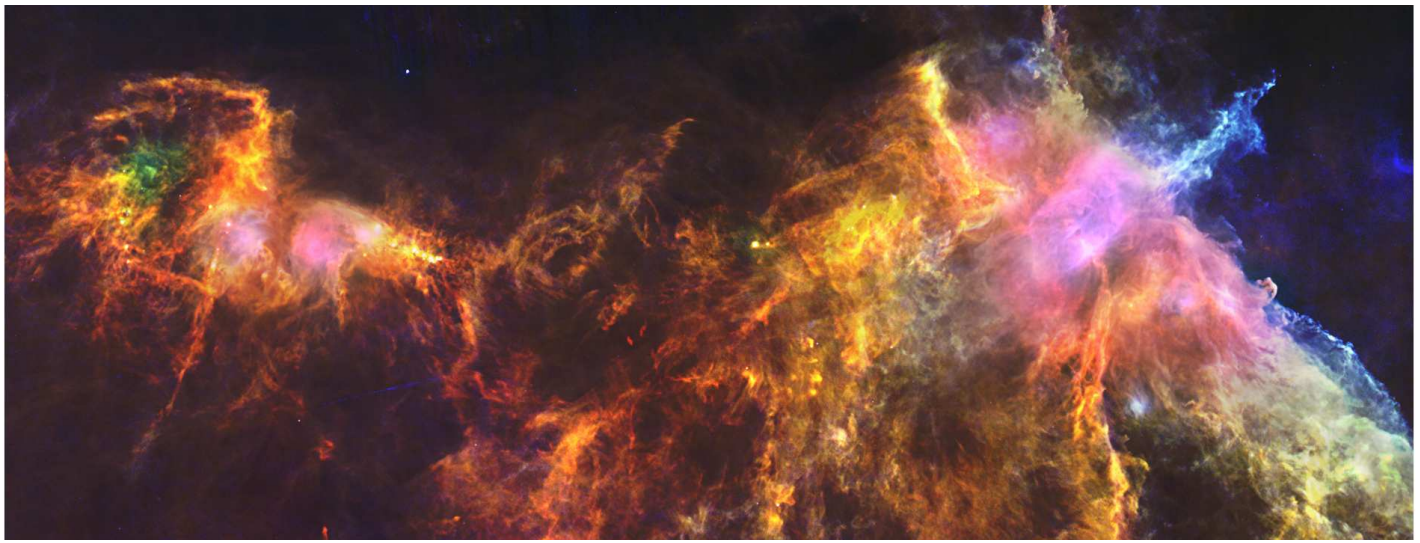

Figure 1.2: A composite image of the Orion B molecular cloud (blue = 70 μm, green = 160 μm, red = 250 μm), by the *Herschel* Space Observatory. In this image, warm gas (blue) can be seen surrounding regions of star formation, whereas cold gas (red) is organised into dense filamentary structures. The Horsehead nebula can be located to the right-hand side of the image (Image credit: N. Schneider, Ph. André, V. Könyves for the 'Gould Belt survey' Key Programme)

with regions of star formation, indicated by the warmer ($\sim 40\,\mathrm{K}$; blue) gas.

It has been known for many years that local star-forming clouds such as the Orion A cloud (e.g. Bally *et al.* 1987) and Taurus (e.g. Schneider & Elmegreen 1979) have filamentary morphology. However, *Herschel* column density maps have revealed that the existence of filamentary structure is unrelated to a cloud's star formation content (André *et al.* 2013). In the Polaris flare, more than 200 gravitationally *unbound* starless cores can be identified (André 2013), and yet filaments are identified throughout (Miville-Deschênes *et al.* 2010). However, the *Herschel* Gould Belt Survey has also revealed that $\sim 70\,\%$ of the identified pre-stellar cores (identified as being gravitationally bound) are spatially coincident with filamentary structures (André 2013).

The left panel of Figure 1.3 shows a three-colour *Herschel* composite image of the Rosette molecular cloud (Schneider *et al.* 2010b). The three colours shown are the 70 μm (blue), 160 μm (green), and 500 μm (red). The background image displays hydrogen Balmer alpha (otherwise known as Hα) emission at a wavelength, $\lambda \sim 656\,\mathrm{nm}$. The right-hand panel shows an enhanced column density map of the same image, with the skeletal features of the dense filamentary structures overlaid (the peak H_2 column density, seen in yellow, is $N(H_2) \sim 2 \times 10^{22}\,\mathrm{cm}^{-2}$). The region is dominated by a single high-column density ridge situated in the centre of the map, and secondary filaments stem from this. Star-forming cores (indicated by the grey triangles) are spatially coincident with both filaments, and junctions between filaments (for reference white and blue stars refer to O-stars and known star-forming clusters, respectively). Understanding the role filaments play therefore, is crucial to developing a complete picture of star formation.

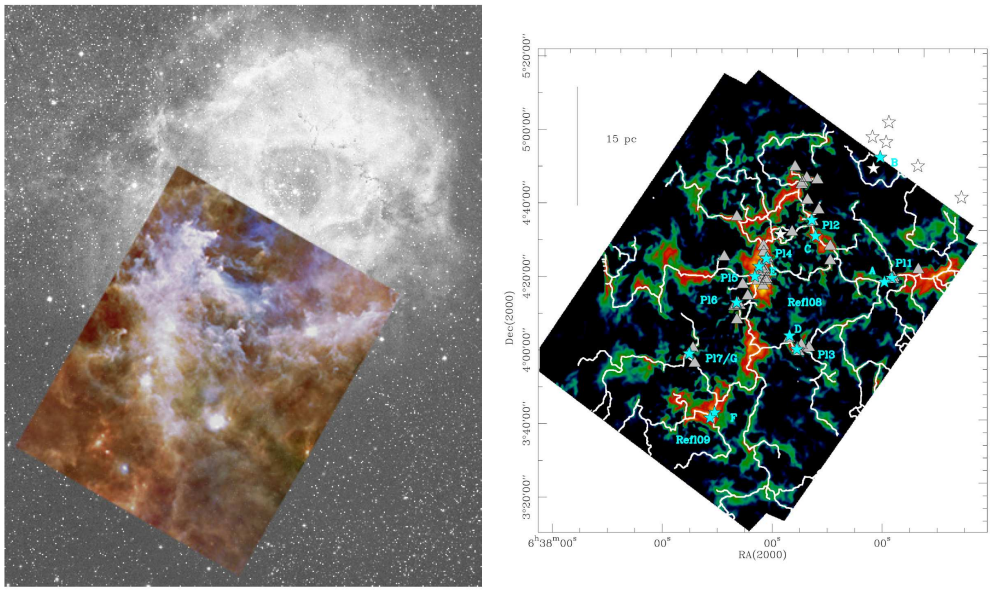

Figure 1.3: Left: *Herschel* three-colour composite image (blue = 70 μm, green = 160 μm, red = 500 μm) of the Rosette nebula, overlaid on a Hα image (taken from Schneider *et al.* 2010b). Right: Column density map of the same region. Filamentary structures are highlighted in white. Grey triangles indicate the massive dense cores identified by Motte *et al.* (2010), the white and blue stars are O-stars and known star-forming clusters, respectively. This figure is taken from Schneider *et al.* 2012.

Dynamic properties

The dynamic properties of molecular clouds are inferred from molecular line observations. These data regularly reveal structure not evident in column density maps. For example, column density maps of the L1495/B213 region of Taurus, imply a single filament of projected length > 5 pc (Palmeirim *et al.* 2013). However, studying the emission from $C^{18}O$, Hacar *et al.* (2013) observe significant substructure, and identify a total of 35 filamentary components within the same region.

Molecular line observations have also revealed large scale systematic motions (velocity gradients) within molecular clouds. Velocity gradients have been inter-

preted as representing global cloud motions, such as rotation (e.g. Imara & Blitz 2011, Imara *et al.* 2011, Rosolowsky *et al.* 2003) or accretion (e.g. Kirk *et al.* 2013, Peretto *et al.* 2014), and therefore may have important implications for star formation. It has also been suggested that observed velocity gradients may be linked to the formation mechanism of the cloud (e.g. Schneider *et al.* 2010a).

As well as indicating the presence of substructure, and revealing bulk gas motions, molecular line observations also provide insight into the internal motions of molecular clouds. Studying such motions may help discern how molecular clouds evolve towards star formation (see also Section 1.2). In molecular clouds, non-thermal gas motions ($\sigma_{\rm NT}$) are often greater than those that can be attributed to temperature alone, i.e. the isothermal sound speed of the gas; $c_{\rm s}$, given by:

$$c_{\rm s} = \sqrt{\frac{k_{\rm B}T}{\mu m_{\rm H}}} = 0.27 \left(\frac{T}{20\,{\rm K}}\right)^{1/2} {\rm km\,s^{-1}}, \tag{1.1}$$

whereby T is the temperature (in this example it has been normalized to 20 K), $k_{\rm B}$ is the Boltzmann constant, μ is the mean molecular weight of a molecule of gas, and $m_{\rm H}$ is the mass of atomic hydrogen. Larson (1979), through observations of the ^{12}CO (1−0) line (^{13}CO was later used in Larson 1981 due to the high opacity of ^{12}CO), showed that the observed line-width of molecular clouds increases with the physical size of the considered region. This, along with two other scaling relations that describe the dynamic properties of molecular clouds were discussed by Larson

(1981), and are often referred to as "Larson's laws":

$$\left(\frac{\sigma}{\mathrm{km\,s^{-1}}}\right) \propto \left(\frac{R}{\mathrm{pc}}\right)^{\alpha} \tag{1.2}$$

$$\left(\frac{\sigma}{\mathrm{km\,s^{-1}}}\right) \propto \left(\frac{M}{\mathrm{M_{\odot}}}\right)^{\beta} \tag{1.3}$$

$$\left[\frac{n(\mathrm{H_2})}{\mathrm{cm^{-2}}}\right] \propto \left(\frac{R}{\mathrm{pc}}\right)^{\gamma}. \tag{1.4}$$

In this case, σ refers to the estimated three-dimensional velocity dispersion, R is the radius of the cloud, and $n(\mathrm{H_2})$ is the number density of molecular hydrogen. Larson (1981) derived the exponents, α, β, and γ empirically to be 0.38, 0.2, and -1.1, respectively ($\alpha = 0.5$ and $\gamma = -1$ are typically adopted; Solomon *et al.* 1987b, Stahler & Palla 2005). The third relation listed implies a near constant column density for molecular clouds. This result has since been questioned as sensitivity limits and choice of molecular tracer may influence the relationship (e.g. Ballesteros-Paredes & Mac Low 2002).

Whilst the dispersion-size relationship is consistently observed (e.g. Caselli *et al.* 1995, Heyer *et al.* 2009, Heyer & Brunt 2004, Larson 1979, Shetty *et al.* 2012, Shirley *et al.* 2003), it is often interpreted in different ways. Heyer *et al.* (2009), extending the study of Larson (1981), found that the velocity dispersion depends on both the radius and the surface density, $\sigma \propto (\Sigma R)^{1/2}$. Both Larson (1981) and Heyer *et al.* (2009) interpret this relationship as an indication that the internal motions of clouds balance gravity, in approximate virial equilibrium. However, recent simulations proposing a highly dynamical mechanism for the formation of molecular clouds (see Section 1.1.2) have called the interpretation of virial equilibrium into question (this will also be discussed in relation to star formation in Section 1.2).

In these simulations, apparent virial balance may be replicated by gravitational contraction of a cloud that is far from equilibrium (Ballesteros-Paredes *et al.* 2011, Vázquez-Semadeni *et al.* 2007).

As the observed properties of molecular clouds (and the route their substructure takes towards star formation) are influenced by their formation, the next section is devoted to discussing some of the theories surrounding the formation of clouds, and the origins of this complex structure.

1.1.2 Formation mechanisms of molecular clouds

Cloud formation theories are typically grouped into two main categories: "top-down" and "bottom-up" (McKee & Ostriker 2007). Top-down mechanisms describe the formation of molecular clouds via instabilities and/or flows within the ISM, whereas the bottom-up notion of cloud formation depends on the agglomeration of smaller clouds.

Top-down formation mechanisms can be further subdivided into two groups: those that present molecular clouds as *transient* entities, never reaching an equilibrium state, resulting in a dynamic picture for cloud (and star) formation; and those that suggest molecular clouds are close to virial *equilibrium*, proceeding towards star formation inefficiently and quasi-statically. One of the reasons for such a dichotomy is because of the uncertainty in the predicted lifetimes of molecular clouds. Transient clouds are expected to exist for $< 10\,\mathrm{Myr}$ before dispersal (Hartmann *et al.* 2001). This is in contrast to those that predict longer lifetimes, typically of the order $\sim 30\,\mathrm{Myr}$ (Blitz & Shu 1980, Kawamura *et al.* 2009), with observations of molecular clouds in interarm regions of external spiral galaxies

predicting even longer lifetimes of $\sim 100\,\mathrm{Myr}$ (Koda *et al.* 2009).

In reality, a combination of physical processes may occur during cloud formation, with different formation mechanisms dominating under different environmental conditions (Dobbs *et al.* 2013, Elmegreen 1993). It has also been suggested that GMCs and smaller molecular clouds represent two distinct populations (Ballesteros-Paredes *et al.* 2007). In this context, GMCs may form through large-scale gravitational instabilities, with smaller molecular clouds forming through more random turbulent compression events (i.e. events that are dependent on environment). The following sections describe these processes in more detail.

Converging/colliding flows

Within the last 15-20 years, several studies have focused on simulating the formation of molecular clouds via the collision of supersonic flows of atomic gas within the ISM (Audit & Hennebelle 2005, Ballesteros-Paredes *et al.* 1999, Heitsch *et al.* 2006, Hennebelle & Pérault 1999, Vazquez-Semadeni *et al.* 1995). Such flows are thought to be a consequence of dynamical processes within the Galactic disc, for example, expanding HII regions or supernovae bubbles (Heitsch *et al.* 2008).

The left-panel of Figure 1.4 depicts a setup of a simulation where two flows are set to collide (Vázquez-Semadeni *et al.* 2007). The compression induced by the flow leads to an increase in the density, and a decrease in the temperature (Audit & Hennebelle 2005, Hennebelle & Pérault 1999, Koyama & Inutsuka 2000). The newly formed dense gas will accrete mass until it becomes Jeans unstable (the Jeans mass will be formally introduced in Section 1.2). The formation of molecular H_2 commences above a column density threshold ($\sim 10^{21}\,\mathrm{cm}^{-2}$; Bergin *et al.* 2004, Lee *et al.* 2012b), after which the clouds "lifetime" will begin (Hartmann *et al.* 2001).

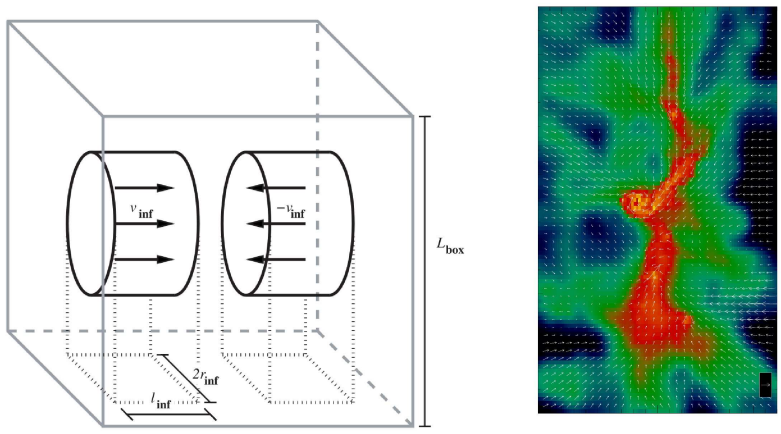

Figure 1.4: Left: The setup of a simulation describing the formation of molecular clouds via converging flows of atomic gas (Vázquez-Semadeni *et al.* 2007). Right: A column density map displaying a filamentary structure formed in an equivalent simulation (at higher resolution; Gomez & Vazquez-Semadeni 2013). The red in this image is high density ($\sim 10^{22}$ cm^{-2}) and the black is low density ($\sim 10^{20}$ cm^{-2}).

The right-panel of Figure 1.4 is a close-up view of a structure formed within such a simulation (Gomez & Vazquez-Semadeni 2013). An encouraging result of the colliding flow formation mechanism is that simulations are able to reproduce the observed filamentary morphology of molecular clouds. The broad line-widths observed within such clouds (see Section 1.1.1) are explained by large-scale gravitational collapse (Ballesteros-Paredes *et al.* 2007), and are not indicative of turbulent support. This mechanism has been used to explain the relatively small age spread of stars observed in local clouds (this is discussed in more detail in Section 1.2.1).

However, although this formation mechanism accounts for the observed large scale supersonic motions of molecular clouds (and their observed substructure), some simulations produce low-mass star-forming cores with a greater degree of non-thermal motions than those observed (Offner *et al.* 2008). In addition, it has

been argued that the molecular clouds formed by such a mechanism may be mass-limited (e.g. Dobbs *et al.* 2013, McKee & Ostriker 2007). The maximum mass is restricted by the mean density and velocity correlation length of the converging flows. While this mechanism may therefore explain the formation of less massive clouds ($\sim 10^4\,\mathrm{M}_\odot$), it may be insufficient in describing the formation of 10^5-$10^6\,\mathrm{M}_\odot$ GMCs.

Gravitational instability

Large-scale instabilities may also lead to the formation of molecular clouds. The stability of an infinitesimally thin, unmagnetised gas disc is approximated using the Toomre parameter, Q. This describes the balance between support due to rotation and susceptibility for collapse due to gravity (Toomre 1964):

$$Q = \frac{\kappa c_\mathrm{s}}{\pi G \Sigma_\mathrm{gal}}, \tag{1.5}$$

whereby κ is the epicyclic frequency, c_s is the sound speed of the gas, G is the gravitational constant, and Σ_gal is the mean gas surface density in the disc. The Toomre criterion imposes a critical value for collapse, i.e. if $Q < 1$, gravity dominates over rotational support (this may vary dependent on the conditions imposed in simulations e.g. $Q \sim 1.2$–1.6; Kim *et al.* 2001, Li *et al.* 2005).

Gravitational instabilities are thought to create the higher end of the mass spectrum of molecular clouds ($\sim 10^6\,\mathrm{M}_\odot$; Kim & Ostriker 2006, Shetty & Ostriker 2006), and has been cited as a possible explanation for observations of regularly spaced HII regions in external galaxies (Elmegreen & Elmegreen 1983). In addition, this mechanism has been used as a measure of a critical surface density for star

formation (Martin & Kennicutt 2001). It is unclear however, whether or not gravitational instabilities would reproduce the full mass spectrum. The production of smaller clouds through this mechanism would require fragmentation of larger structures (McKee & Ostriker 2007).

Cloud agglomeration

A bottom-up method of molecular cloud formation involves the agglomeration of smaller clouds (Field & Saslaw 1965, Oort 1954). A problem faced by early models of cloud agglomeration was that the time-scale required to produce massive clouds was greater than the estimated lifetime of GMCs ($> 10^8$ yrs; e.g. Kwan 1979, Scoville & Hersh 1979). Incorporating a spiral potential (causing clouds to crowd in spiral arms), and cloud self-gravity is able to reduce the cloud formation time (e.g. Casoli & Combes 1982, Kwan & Valdes 1987). However, McKee & Ostriker (2007) argue that, even with the aforementioned considerations, the time-scale needed to build clouds of $10^6\,M_\odot$ from smaller ($\sim 10^4\,M_\odot$) clouds would still exceed expected lifetimes of GMCs (i.e. star formation would occur, and disperse smaller clouds in the time needed to form a $10^6\,M_\odot$ GMC).

The importance of collisions between clouds however, must not be ruled out. More recently, coalescence models of GMC formation have suggested this may be important within the spiral arms due to orbit crowding as a consequence of spiral density waves (Dobbs 2008). However, whilst this mechanism may be able to form clouds in galaxies with spiral arms, high disc surface densities are required in the absence of spiral arms (Tasker & Tan 2009). Whilst some groups envisage cloud collisions to result in molecular clouds that are gravitationally unbound (with star formation proceeding in smaller gravitationally bound clumps; Dobbs *et al.* 2011),

others conclude that cloud collisions are efficient at injecting kinetic energy into GMCs, providing turbulent support against gravity, and maintaining a near virial balance (Tasker & Tan 2009).

1.2 An introduction to star formation

Star formation proceeds in dense molecular cloud cores when gravity overcomes internal support. In the most simplistic sense (considering the collapse of an isothermal sphere supported only by thermal pressure), this will occur when the mass of the considered region (this may be applicable to clouds, or individual star forming cores) reaches the Jeans mass (Jeans 1902):

$$M_{\rm J} = \left(\frac{5c_{\rm s}^2}{G}\right)^{3/2}\left(\frac{3}{4\pi\rho}\right)^{1/2} \sim 160\left(\frac{T}{20\,{\rm K}}\right)^{3/2}\left(\frac{10^2\,{\rm cm}^{-3}}{n}\right)^{1/2}{\rm M}_\odot, \qquad (1.6)$$

whereby ρ and $c_{\rm s}$ are the respective density and sound speed of the region, and G is the gravitational constant. The normalization above is consistent with typical GMC conditions (e.g. Stahler & Palla 2005). Once gravity dominates over support, the time-scale for pressure-free, spherical collapse is given by the free-fall time, $t_{\rm ff}$:

$$t_{\rm ff} = \left(\frac{3\pi}{32G\rho}\right)^{1/2} \sim 3 \times 10^5\left(\frac{10^4\,{\rm cm}^{-3}}{n}\right)^{1/2}{\rm years}, \qquad (1.7)$$

whereby all symbols are equivalent to those described in Equation 1.6. The large masses (relative to the theoretical Jeans mass) of typical GMCs ($\sim 10^5\,{\rm M}_\odot$) implies that such clouds should undergo *global* gravitational collapse.

Within the Milky Way, $<3\,{\rm M}_\odot$ of material is converted into stars every year (e.g. Draine 2011, Evans *et al.* 2009, Lee *et al.* 2012a). In addition, only $\sim 2\,\%$ of the mass of a GMC is converted into stars (Myers *et al.* 1986). This implies that star formation is an inefficient process, which may contradict the above notion of global gravitational collapse (Zuckerman & Palmer 1974). The following sections are therefore devoted to discussing star formation within molecular clouds, and

the differences between low- and high-mass star formation.

1.2.1 Virialized vs. transient clouds

Star formation in globally supported molecular clouds

The classical picture of star formation was reviewed by (Shu *et al.* 1987), and concerns the balance between gravity and the magnetic field. Magnetic fields provide support to molecular clouds, by suppressing the motion of ionic material perpendicular to field lines (Mouschovias & Spitzer 1976). A molecular cloud is sub-critical when the magnetic field provides sufficient support against gravitational collapse. Star formation in sub-critical clouds may proceed via a process known as ambipolar diffusion (Mestel & Spitzer 1956). Here, neutral particles, impervious to the effects of the magnetic field, drift across field lines under the influence of gravity, collating to form a central density enhancement. During this process, magnetic flux is redistributed because of tension in the field. Once enough mass has accumulated, the core becomes *super-critical*, and unstable to gravitational collapse.

In this scenario, star formation proceeds slowly. The time-scale for ambipolar diffusion, $t_{\rm AD}$, is considered to be long (10^7 years; Mac Low & Klessen 2004). Hence, this is often referred to as the quasi-static picture of star formation (where $t_{\rm AD} \gg t_{\rm ff}$). A potential issue is that observations of GMCs indicate that their masses are typically critical or even super-critical (Crutcher 2012). This suggests that magnetic fields (alone) are insufficient in supporting GMCs against gravitational collapse.

A possible solution to such issues may be provided by the presence of super-

sonic, or turbulent, motions within molecular clouds (see Section 1.1.1). Models of ambipolar diffusion that incorporate significant non-thermal motions form stars on shorter time-scales (compared to models only incorporating thermal motions), alleviating some of the problems in the classical argument (Fatuzzo & Adams 2002, Heitsch *et al.* 2004). Moreover, these turbulent motions are often considered to provide (global) support to molecular clouds. Replacing the thermal sound speed in Equation 1.6 with the total velocity dispersion ($\sigma_{\rm obs}$; incorporating both thermal and non-thermal motions) leads to an increase in the Jeans mass of the region. For example, a total velocity dispersion of ~ 1 km s^{-1} would lead to a Jeans mass of 8000 M$_{\odot}$(using $n = 10^2$ cm^{-3}), i.e. a factor of $\sim (\sigma_{\rm obs}/c_{\rm s})^3$ greater than that presented in Equation 1.6.

In this context, GMCs are relatively long-lived ($\sim$20-30 Myr) structures that are supported by magnetic fields and/or random turbulent motions in virial equilibrium (Heyer *et al.* 2009, Larson 1981). Only a small fraction of the mass of the molecular cloud is unstable to gravitational collapse, therefore star formation proceeds slowly and inefficiently.

Star formation in transient molecular clouds

A more recent view of molecular cloud evolution follows their formation from colliding flows (see Section 1.1.2). In this scenario, non-thermal motions observed in molecular clouds are indicative of gravitational collapse (not turbulent support). A significant hurdle for the equilibrium model of molecular clouds is that turbulence decays (Mac Low *et al.* 1998). This implies that without replenishment of the turbulent motions, that are deemed to provide support, molecular clouds will become gravitationally unstable and collapse rapidly. The benefit of the dy-

namic star formation paradigm is that there is no need for the turbulence to be replenished.

The formation of molecular clouds via colliding flows was used initially as an explanation for the small age spreads of stellar populations observed within local clouds (e.g. Ballesteros-Paredes *et al.* 1999, Hartmann *et al.* 2001). Stars within the Taurus molecular cloud complex are typically found to be $\sim$1-3 Myr old (e.g. Palla & Stahler 2000). The crossing time of a molecular cloud is defined as, $t_{\rm cross} \equiv L_{\rm c}/\sigma_{\rm obs}$, where $L_{\rm c}$ is the spatial extent of the cloud. For Taurus, $L_{\rm c}\sim 20\,{\rm pc}$ and $\sigma_{\rm obs} \sim 2$ km s^{-1}, giving $t_{\rm cross} \sim 1 \times 10^7$ yrs. The small age spread of stars compared with the large crossing time, implies that star formation occurring over the large spatial extent of Taurus is not causally related, but that it may have been triggered by a single, large-scale event. The colliding flow scenario may therefore explain how the stellar population has formed with a small age spread, as dense molecular gas is produced within a relatively short time-scale ($3 - 5 \times 10^6$ Myr; Hartmann *et al.* 2001).

The interpretation that the observed broad line-widths are indicative of collapse is not new (Goldreich & Kwan 1974). However, it was quickly thought that rapid free-fall collapse of molecular clouds may lead to a high star formation efficiency, which is not observed (Zuckerman & Palmer 1974). Recent simulations explain low star formation efficiency through the observation that molecular clouds typically exhibit hierarchical structure (see Section 1.1.1). Denser regions in this hierarchy collapse first, since $t_{\rm ff} \propto \rho^{-1/2}$ (see Equation 1.7), leading to star formation in the high-density cores, before the lower density clouds have collapsed completely (Ballesteros-Paredes *et al.* 2011). Feedback from newly formed stars then acts to disperse the remaining cloud, resulting in the inefficient conversion from gas to

stars.

1.2.2 The stellar initial mass function & low-mass star formation

The relative number of newly formed stars (i.e. zero-age main-sequence stars) is often described as a function of their mass, in what is commonly known as the initial mass function (IMF). The importance of the IMF is best explained by considering the observation that its shape is seemingly invariant throughout the Milky Way (Bastian *et al.* 2010, Offner *et al.* 2013). The mechanism(s) by which low- and high-mass star formation proceeds must therefore be able to reproduce this observed invariance.

Several functional forms of the IMF are shown in Figure 1.5. Fitting a power-law slope, $\mathrm{d}N/\mathrm{dlog}(M) \propto M^{-\Gamma}$, to the IMF was introduced by Salpeter (1955), who determined $\Gamma \sim 1.35$. However, a single power-law is not representative of the IMF over all masses. Miller & Scalo (1979) found that the IMF is well represented by a log-normal distribution between $0.1\,\mathrm{M}_{\odot}$ and $\sim 30\,\mathrm{M}_{\odot}$. This however, underestimates the number of high-mass stars. Typically the IMF is represented by a log-normal distribution, with a power-law slope above $\sim 1\,\mathrm{M}_{\odot}$ (e.g. Chabrier 2005), or a series of power-laws (e.g. Kroupa 2001).

Stars of mass $\lesssim 1\,\mathrm{M}_{\odot}$ are most common. The shape of the IMF also exemplifies one of the main difficulties faced when trying to understand the formation of massive stars: their inherent *rarity*. One of the most common ways to describe the formation of massive stars is an extension of the comparatively well constrained model for low-mass star formation. Before introducing the current theories of

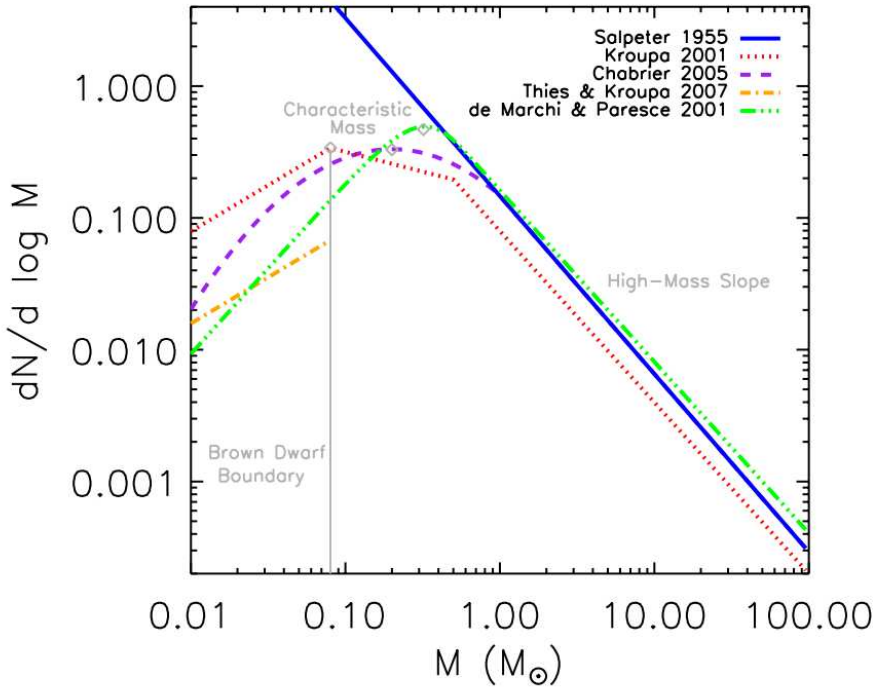

Figure 1.5: Functional forms of the IMF by various authors (Chabrier 2005, de Marchi & Paresce 2001, Kroupa 2001, Salpeter 1955, Thies & Kroupa 2007). With the exception of the Salpeter slope, the curves are normalised such that the integrated mass is unity. This figure is taken from Offner *et al.* (2013).

(and issues with) high-mass star formation, it is therefore prudent to discuss the generally accepted mechanism for low-mass star formation (see e.g. Larson 2003, Shu *et al.* 1987 for more detailed reviews).

The formation of low-mass stars begins following the loss of support against gravity in a pre-stellar core (di Francesco *et al.* 2007, Ward-Thompson *et al.* 1994). In the initial stages of collapse, thermal emission from dust is optically thin. Therefore the temperature changes very little during the initial contraction phase, whereas the density can increase by several orders of magnitude (this stage often assumed to be isothermal).

As the contraction proceeds, the increase in central density leads to an increase in optical depth above $\tau = 1$. At this point the core becomes opaque to its own radiation. The temperature in the central regions rises, supporting the region against further collapse, forming a hydrostatic core (Larson 1969). At this stage the core resides in hydrostatic equilibrium, with thermal pressure preventing further gravitational contraction. Although this phase has not yet been conclusively observed, there are a number of candidates for the hydrostatic core phase of star formation (e.g. Enoch *et al.* 2010, Pineda *et al.* 2011).

A second core is formed at the centre of the first hydrostatic core once the temperature reaches $\sim 2000\,\mathrm{K}$. This temperature is sufficient to dissociate H_2 molecules. At this point the gas pressure can no longer provide support to the first core and a second collapse ensues, forming a protostellar object.

Because of the angular momentum of the initial dense core, an accretion disc forms around the central protostellar object. At this stage, bipolar outflows are driven from the central region. Observations of accretion discs (e.g. Enoch *et al.* 2009, Jørgensen *et al.* 2005, Looney *et al.* 2000) and outflows are helping to categorise the initial phases of low-mass star formation (see e.g. Frank *et al.* 2014, Richer *et al.* 2000, and references therein).

1.2.3 Massive star formation

The understanding of massive star formation faces a number of significant challenges, both observationally and theoretically. Massive stars are rare (see Figure 1.5), statistically therefore, they are found at greater distances from the Sun (in comparison to low-mass stars). In addition, massive stars form in clustered en-

vironments (e.g. Lada & Lada 2003). Both of these factors present observational challenges, as identifying massive cores (as opposed to cores which may harbour sub-fragments) necessitates high angular resolution interferometric observations.

A fundamental difference between high-mass and low-mass stars is that thermonuclear burning begins at the centre of massive cores while they are still deeply embedded within their natal cloud. The Kelvin-Helmholz time is approximately the time a star would have to collapse to its present size for the release of gravitational energy to produce the observed luminosity. It is given by:

$$t_{\rm KH} = \frac{1}{2}\frac{E_{\rm G}}{L_*} \sim 10^7 \left(\frac{M_*}{M_\odot}\right)^2 \left(\frac{R_*}{R_\odot}\right)^{-1} \left(\frac{L_*}{L_\odot}\right)^{-1} \text{yrs}, \tag{1.8}$$

whereby L_*, M_*, and R_* are the luminosity, mass, and radius of a star, respectively (the right-hand side of Equation 1.8 represents the Kelvin-Helmholz timescale for solar quantities). For low-mass stars, $t_{\rm KH} > t_{\rm ff}$. This implies that the core material will be accreted before the protostar reaches its main sequence luminosity. However, for massive stars $t_{\rm KH} < t_{\rm ff}$, the opposite is true. This indicates that massive young stellar objects have no, well defined, observable, pre-main sequence phase.

From a theoretical perspective, understanding massive star formation is mainly approached from two (competing) perspectives; *core accretion* (e.g. McKee & Tan 2002, 2003) and *competitive accretion* (e.g. Bonnell *et al.* 1997). Other mechanisms for the formation of massive stars are also possible, but are largely dependent on environment (e.g. *protostellar collisions*; Bonnell *et al.* 1998). These mechanisms are discussed in more detail in the following sections.

Core accretion

In principle, the core accretion model is an extension of the 'standard model' for low-mass star formation (see Section 1.2.2). Star formation begins in the core accretion model with a gravitationally bound core, scaled-up from the low-mass equivalent, a high-mass starless core (HMSC).

A difference between high-mass and low-mass cores, is that non-thermal motions are observed to dominate in massive cores (e.g. Caselli & Myers 1995). Myers & Fuller (1992) used this observation to modify the standard model for star formation, by incorporating both thermal and non-thermal motions: the "TNT" model. McKee & Tan (2002, 2003) extended this to develop the "Turbulent Core" model. The inclusion of turbulent motions provides support to the core (cf. Equation 1.6). Crucially however, this also leads to an increased accretion rate ($\sim 10^{-3}\,\mathrm{M}_{\odot}\,\mathrm{yr}$; McKee & Tan 2003) enabling cores to attain greater mass through accretion before collapse.

A challenge of this formation scenario regards fragmentation. In the core accretion model, the mass reservoir out of which a massive star will form is attributed solely to a single core. In hydrodynamic simulations of core collapse, Dobbs *et al.* (2005) find that turbulent motions generate substructure, resulting in further fragmentation. To prevent further fragmentation therefore, massive cores must be supported. Such support may be provided by the presence of strong magnetic fields (e.g. Myers *et al.* 2013, Tan *et al.* 2013b), or via radiative feedback from surrounding lower-mass protostars (e.g. Krumholz & McKee 2008).

Another challenge faced by this scenario arises due to the short Kelvin-Helmholz time-scales of massive stars, as the radiation pressure may be sufficient to halt ac-

cretion onto the central object. In the case of spherically symmetric accretion a theoretical upper mass limit of massive stars is implied ($\sim$40-60 $M_\odot$; Kahn 1974, Larson & Starrfield 1971, Wolfire & Cassinelli 1987). This is an issue since massive stars in excess of this limit are observed (e.g. η Carinae; Hillier *et al.* 2001).

A potential solution to this problem may be provided if mass accretion occurs via a disc. In the simulations of Krumholz *et al.* (2009), a 41.5 $M_\odot$ and 29.2 $M_\odot$ companion were formed via disc accretion in $< 10^5$ years. Although this does not greatly exceed the mass limit discussed above, at no point during the simulation did the accretion stop due to radiation pressure. This indicates therefore that massive stars in excess of $\sim 40\,M_\odot$, may form via disc accretion (see also e.g. Kuiper *et al.* 2010).

Competitive accretion

An alternative suggestion is that there may be a paradigm change in the formation mechanisms of low- and high-mass stars. Competitive accretion models are derived as a way to explain the observed characteristic that most massive stars form in clusters (de Wit *et al.* 2005, Lada & Lada 2003, Mason *et al.* 2009).

Figure 1.6 is a schematic of the proposed accretion process within a stellar cluster (from Bonnell *et al.* 2007). The cluster gravitational potential is crucial for the formation of massive stars. In this scenario, a high degree of fragmentation occurs within massive clumps. Many of these fragments will produce low-mass stars, and this model is able to reproduce the shape of the IMF (Bonnell *et al.* 2007). Fragments that form preferentially at the centre of the gravitational potential well accrete more material than those formed elsewhere, attaining more mass. Fragments located at the cluster centre have greater accretion rates, given

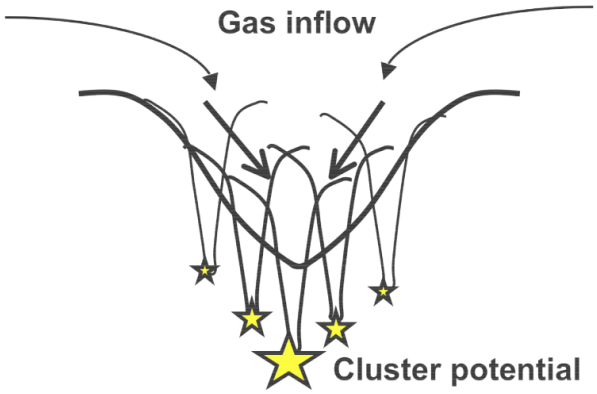

Figure 1.6: A schematic view of the accretion process within a stellar cluster (from Bonnell *et al.* 2007). Gas is funnelled down to the cluster core in order to form massive stars at the centre. The gas reservoir is then replenished via infall into the large-scale cluster potential.

by $\dot{M} \sim \pi \rho v_{\rm rel} R_{\rm acc}^2$ (whereby ρ is the local density, $v_{\rm rel}$ is the relative velocity of the star with respect to the clump gas, and $R_{\rm acc}$ is the accretion radius).

If competitive accretion is the dominant mode of massive star formation, this would imply that these objects would not form in isolation. However, recent observations have identified several candidates for isolated massive star formation (Bressert *et al.* 2012). An important task therefore is to confirm whether or not such candidates have truly formed in isolation.

Protostellar Collisions

In this scenario, protostars coalesce at the centre of dense stellar clusters to form larger stars (Bonnell *et al.* 1998). This formation mechanism would require high-stellar densities of $\gtrsim 10^8\,{\rm stars\,pc^{-3}}$, to be efficient with respect to stellar evolution time-scales. In comparison, Hillenbrand & Hartmann (1998) found that the Orion Nebula Cluster (ONC) has core radius of $\sim 0.2\,{\rm pc}$, and a central stellar density

of $\sim 10^4\,\mathrm{stars\,pc^{-3}}$. This mechanism therefore, cannot be the dominant mode for massive star formation.

Confronting theory with observations

Methods used to observationally constrain the physical processes involved in massive star formation vary. One such method is to investigate the observational characteristics of massive star formation to make comparisons with our current knowledge of the low mass star formation paradigm. For example, the presence of discs around massive stars can be inferred from molecular line observations, in which velocity gradients can be attributed to rotation, and indirectly via the presence of bipolar outflows (see e.g. Cesaroni *et al.* 2007, Tan *et al.* 2014 and references therein). However, identifying characteristics attributed to individual sources may provide a biased view of the massive star formation process.

The Red Midcourse Space Experiment Source survey (the RMS survey; Lumsden *et al.* 2013), has sought to provide a complete and un-biased catalogue of massive young stellar objects (MYSOs). Such surveys can then be used to test the theoretical framework of massive star formation against observational diagnostics. For example, the RMS survey has been used to investigate the Galactic distribution of massive star formation (Urquhart *et al.* 2014), their accretion processes (e.g. the rate of accretion; Davies *et al.* 2011), and to confirm the presence of discs around MYSOs (Ilee *et al.* 2013).

The above described characteristics indicate that star formation has already commenced. An alternative method used to constrain theories of massive star formation is to identify and categorise their earliest phases of evolution, before stellar feedback begins to disrupt the local environment. Studies of this nature necessi-

tate the identification of massive, and relatively quiescent clouds. In recent years, one such group of objects has been subjected to an intense amount of research in the context of massive star formation: Infrared Dark Clouds (hereafter, IRDCs). Studying the initial conditions for star formation within IRDCs provides the focus of this thesis. The next section will introduce the properties of IRDCs, and the role they play in our current understanding of star formation.

1.3 The role of Infrared Dark Clouds

IRDCs were discovered in the mid-1990's by the *Infrared Space Observatory* (*ISO*; Pérault *et al.* 1996), as "unexpected" regions of high-optical depth at mid-infrared (MIR) wavelengths. An additional MIR survey undertaken by the *Midcourse Space eXperiment* (*MSX*; Egan *et al.* 1998), revealed the presence of $\sim$2000 clouds, seen in silhouette between 7 μm and 100 μm. Egan *et al.* (1998) speculated of their origin:

> "A possible explanation for the origin of these relatively common but unusual extincting clouds is that they are naked cores, left behind after the envelopes of giant molecular clouds have been dispersed."

Studying a sub-sample of these clouds further, Carey *et al.* (1998) suggested that the physical properties ($T < 20\,\mathrm{K}$; $n_{\mathrm{H}} > 10^5\,\mathrm{cm}^{-3}$) of IRDCs were conducive to the earliest stages of *massive* star formation. Since then, >10000 IRDCs have been catalogued (Peretto & Fuller 2009, Simon *et al.* 2006a). It is important to note that massive star formation will be restricted to the most extreme (in mass and density) IRDCs, and that the majority of these clouds will be incapable of forming the most massive stars (Kauffmann & Pillai 2010). However, this should not detract from the importance of IRDCs in the field of star formation. The following sections describe the properties of IRDCs that identify them as ideal environments to study the initial phases of star and star-cluster formation.

1.3.1 Physical structure

IRDCs show a range of physical properties. However, generally they are found to have: i) sizes $\sim$1-10 pc (e.g. Rathborne *et al.* 2006, Simon *et al.* 2006b); ii) signif-

icant column densities ($N(H_2) \sim 10^{22}$-$10^{25}\,cm^2$; e.g. Carey *et al.* 1998, Egan *et al.* 1998, Vasyunina *et al.* 2009); iii) large masses of the order 10^2–$10^5\,M_\odot$ (Kainulainen & Tan 2013, Rathborne *et al.* 2006, Simon *et al.* 2006b); iv) high densities $\sim 10^3$–$10^5\,cm^{-3}$ (e.g. Carey *et al.* 1998); v) low temperatures $\lesssim 25\,K$ (e.g. Chira *et al.* 2013, Peretto *et al.* 2010, Pillai *et al.* 2006, Ragan *et al.* 2011). Extreme examples of IRDCs include the "Nessie Nebula" which has a (possibly underestimated) length of $\sim 80\,pc$ (Jackson *et al.* 2010), and G0.253+0.016, otherwise known as the "Brick" (Longmore *et al.* 2012), with a mass of $\sim 10^5\,M_\odot$ and a radius of $\sim 3\,pc$. which has been cited as a possible progenitor cloud for a young massive cluster (although the star forming potential of this cloud is currently debated; Kauffmann *et al.* 2013b).

The potential for IRDCs to harbour *genuine* candidates for the elusive initial stages of massive stars has long been discussed (e.g. Beuther & Steinacker 2007). IRDCs exhibit significant substructure (e.g. Peretto & Fuller 2009, Rathborne *et al.* 2007), and are typically thought of as the precursor clouds to star clusters (Rathborne *et al.* 2006). Several candidates for the HMSC phase exist. For example, the properties of core C1-S in IRDC G028.37+00.07 make it a good HMSC candidate ($R \sim 0.1\,pc$, $M \sim 60\,M_\odot$, $\Sigma \sim 0.5\,g\,cm^{-2}$, and $n_H \sim 6 \times 10^5\,cm^{-3}$; Tan *et al.* 2013a). Follow up observations using tracers of star formation kinematics (see Section 1.3.2) and chemistry (see Section 1.3.3) are needed in order to establish such objects as unambiguously singular, and pre-stellar. A summary of the physical properties of IRDCs and their cores can be found in Table 1.1.

Table 1.1: Physical properties of star-forming structures. Adapted and updated from Rathborne *et al.* (2006) and Bergin & Tafalla (2007)

	Clouds				Cores	
	Bok Globules	Dark Cloud	GMC	IRDC	Pre-Stellar	IRDC
Size (pc)	0.5-2	2-20	~ 50	1-10	0.02–0.1	0.02–0.8
Mass ($M_\odot$)	5-50	10^2–10^4	$>10^5$	10^2–10^5	0.5–10	10–10^3
Density (cm^{-3})	10^3	10^2–10^4	10^2	10^3–10^4	10^4–10^6	10^4–10^8
Temperature (K)	10-20	10-20	20-50	10-20	10	10–20
Example	B68	Taurus	W48	G035.39-00.33	L1544	C1-S
References	1, 2, 3	4, 5	6, 7, 8	9, 10, 11	12, 13,	11, 14

(1) Clemens & Barvainis (1988); (2) Bourke *et al.* (1995); (3) Launhardt *et al.* (2010);(4) Bergin & Tafalla (2007); (5) Cambrésy (1999); (6) Blitz (1993); (7) Solomon *et al.* (1987a); (8) Stahler & Palla (2005); (9) KT13; (10) Peretto *et al.* (2010); (11) Rathborne *et al.* (2006); (12) Myers & Benson (1983); (13) Ward-Thompson *et al.* (1994); (14) Tan *et al.* (2014)

1.3.2 Kinematics

On the large scale, IRDCs typically comprise one or more filaments that are coherent in velocity (Jackson *et al.* 2010, Tanaka *et al.* 2013), similar to the structure identified in local clouds (see Section 1.1.1). In some cases the overall velocity field may display ordered gradients (e.g. Kirk *et al.* 2013, Peretto *et al.* 2014, Tackenberg *et al.* 2014), and inverse P-Cygni profiles indicative of infalling gas motions, and star formation (e.g. Chen *et al.* 2010, Peretto *et al.* 2013, Rygl *et al.* 2013).

High-angular resolution observations reveal that the velocity structure can be complex, and influenced by local regions of star formation (Devine *et al.* 2011, Ragan *et al.* 2012). Line-widths have been observed between 0.5–4 $\mathrm{km\,s^{-1}}$ (dependent on molecular tracer), consistent with varying degrees of supersonic turbulence (e.g. Ragan *et al.* 2012, Sakai *et al.* 2008, Vasyunina *et al.* 2011), and may correlate with the star formation activity of the region (Sanhueza *et al.* 2013). Wang *et al.* (2008) found that line-widths (in this case traced by ammonia) towards G028.37+00.07 increase in cores with accompanying IR emission, i.e. star formation activity. In addition, such cores are often associated with other distinct kinematic traits of star formation, for instance the detection of high-velocity bipolar outflows (Wang *et al.* 2011), measured using the $J = 3 \rightarrow 2$ transition of CO). Conversely, in regions where star formation activity is at a minimum, line-widths are smaller (although still dominated by non-thermal motions; e.g. Tan *et al.* 2013a, measured line-widths of ~ 0.9 $\mathrm{km\,s^{-1}}$ and 1.0 $\mathrm{km\,s^{-1}}$ in 5 intermediate-to-high-mass cores using the deuterated species N_2D^+ and DCO^+, respectively).

1.3.3 Chemistry

IRDCs display a rich variety of chemistry. Globally, fractional abundances (detected in molecules such as N_2H^+, HNC, HCO^+; Vasyunina *et al.* 2011) are similar to low-mass dense *cores*. However, dense gas tracers, such as N_2H^+ and NH_3 are found to be widespread (e.g. Miettinen 2014, Vasyunina *et al.* 2011, Zhang *et al.* 2009). In addition, shocked gas tracers such as SiO can also be widespread, and may be linked to the cloud formation process rather than widespread star formation (e.g. Jiménez-Serra *et al.* 2010, Lis *et al.* 2001, Sanhueza *et al.* 2013). The low temperature and high-density of IRDCs results in prominent CO depletion (e.g. Fontani *et al.* 2012, Hernandez *et al.* 2011, Miettinen & Offner 2013). In addition, high-deuterium fractions have been observed in IRDCs ($D_{\rm frac}[N_2H^+] \sim 0.4$-0.7; Fontani *et al.* 2014). Above $\sim 30\,$K, deuterated species are destroyed through interaction with H_2 molecules (Millar *et al.* 1989). High-deuterium fractions may therefore provide a way of identifying cores in the earliest stages of star formation (i.e. those with temperatures $< 30\,$K; Fontani *et al.* 2011, Tan *et al.* 2013a).

1.4 IRDC summary & thesis motivation

The observed physical properties, and apparent chemical youth of IRDCs indicate that they are excellent environments within which it is possible to study the initial conditions for massive star and star cluster formation. However, given that IRDCs have only been discovered (relatively) recently, our knowledge of their properties is lacking (in comparison to that of local star-forming clouds). This thesis presents an in-depth study of the structure of a single IRDC: G035.39-00.33. The focus of this work is to identify and understand the kinematic signatures of cloud and star formation, and how such traits may be linked to both the fragmentation process, and the physical evolution of dense, star-forming cores.

The thesis is structured as follows:

- Chapter 2 presents high-sensitivity and high-spectral resolution IRAM 30 m observations of G035.39-00.33. The primary molecular tracers used in this study are the $J = 1 \rightarrow 0$ transitions of $C^{18}O$ and N_2H^+. The aim of this study is to compare and contrast the kinematic information obtained from two molecular species that preferentially trace different density regimes. The results from this chapter are discussed in the context of comparable IRDC observations (including previous work on G035.39-00.33), and low-mass star forming regions. It is found that G035.39-00.33 comprises several sub-filaments moving with relative velocity ~ 3 km s^{-1}. These filaments appear to overlap at the densest portion of the mapped region. It is speculated that star formation at this location may have been induced by the merging of the filamentary structures.

- Chapter 3 presents high-sensitivity and high-angular resolution IRAM PdBI observations of N_2H^+ $(1-0)$ towards G035.39-00.33. This is the first, in-depth study of the kinematics of dense IRDC filaments at high-angular resolution. The goal of this study is to understand the kinematics of the dense gas in relation to the star forming cores. It is revealed that velocity gradients observed in Chapter 2 may be explained by the presence of substructure now evident in the high-angular resolution images. Whilst global motions are relatively small (< 0.7 km s^{-1} pc^{-1}), there is evidence for dynamic processes on local scales (1.5-2.5 km s^{-1} pc^{-1}). Moreover there is evidence to suggest that these localised gas motions may be influenced by the presence of star formation.

- Chapter 4 primarily utilises 3.2 mm continuum data from the Plateau de Bure Interferometer (although 1.3 mm submillimeter array observations are also used for comparison). The aim of this study is to establish the physical properties of the core population within G035.39-00.33, and to compare this information with the dynamical behaviour of the cloud established in the previous chapters. A total of 14 cores are identified within the mapped region (at $\sim 4''$ resoltion). It is found that the masses of cores associated with the massive clump discussed in Chapter 2, are greater than those associated with the narrow IRDC filament. Two cores are identified as possible progenitors to intermediate-to-high mass stars.

- The findings from this thesis are summarised in Chapter 5, along with a discussion on how this work may be extended in the future.

Chapter 2

Complex, quiescent kinematics in a highly filamentary infrared dark cloud

2.1 Introduction

2.1.1 G035.39–00.33

This thesis forms part of a larger collaborative effort whose goal is to provide a detailed case study of the chemistry, dynamics, and physical structure of a single IRDC. Figure 2.1 is a *Herschel* image of the W48 star forming region (Nguyen Luong *et al.* 2011). W44, a supernova remnant interacting with its host cloud (Wootten 1977) is highlighted by a black circle. A number of (blue) H II regions dominate the image (e.g. G035.1387–00.7622 and G035.0528-00.5180; Lumsden *et al.* 2013). The focus of this thesis, G035.39-00.33, appears as a tiny filamentary

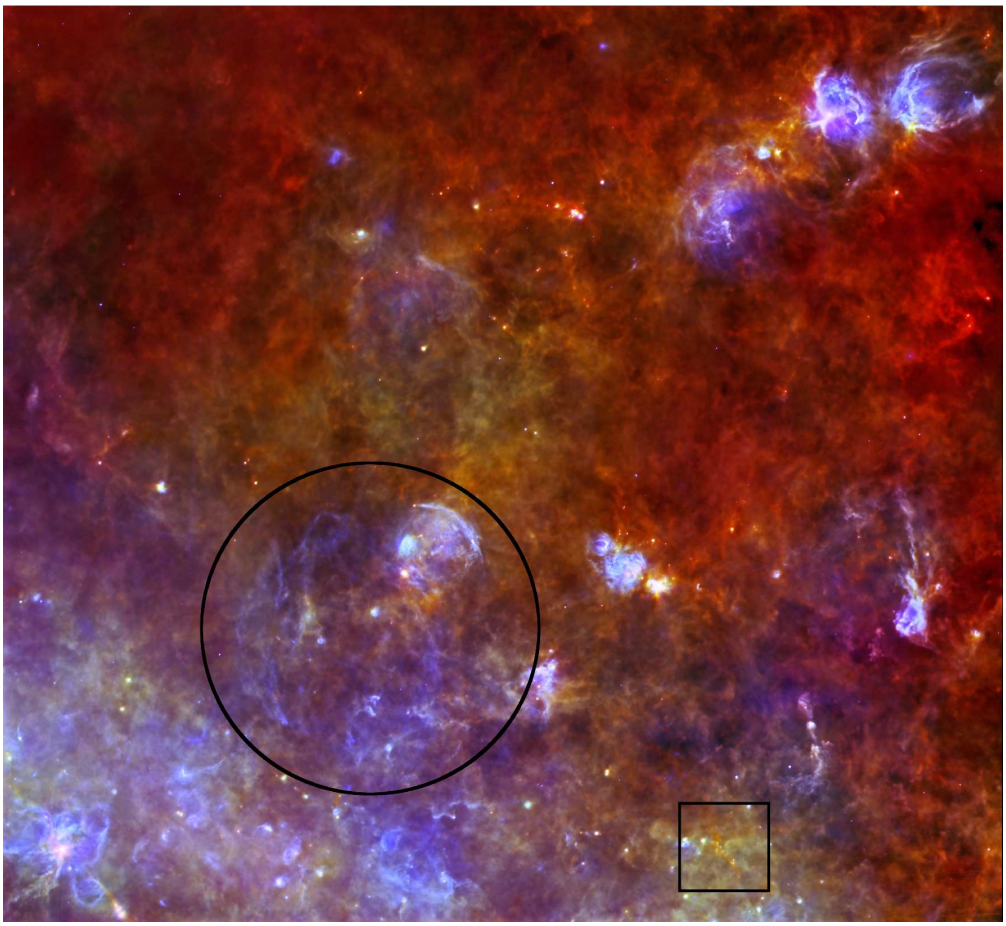

Figure 2.1: Composite *Herschel* image of the W48 star forming complex (image taken from Nguyen Luong *et al.* 2011). The black rectangle highlights G035.39-00.33, whereas the black circle highlights the supernova remnant W44.

structure located at the bottom of this image (highlighted by the black box).

The significance of G035.39-00.33 becomes apparent when observing this cloud at (exclusively) longer wavelengths (i.e. the cold gas observed in the 500 μm *Herschel* image; Nguyen Luong *et al.* 2011). Butler & Tan (2009) (hereafter, BT09) selected 10 IRDCs with the highest contrast against the Galactic MIR background, from the sample of 38 IRDCs studied by Rathborne *et al.* (2006). The BT09 sample covered clouds with a range of morphologies (ranging from extremely filamentary

to elliptical in 2-D projection) and masses (from $0.2 \times 10^3\,\mathrm{M}_\odot$ to $74.3 \times 10^3\,\mathrm{M}_\odot$). G035.39-00.33, cloud H of BT09, was chosen for further study because i) it is extremely filamentary, consistent with the morphology of molecular clouds formed in simulations of colliding flows of atomic gas (see Section 1.1.2); ii) there are extended quiescent regions with little or no signatures of star formation activity (as traced by 4.5, 8, 24 μm emission; Carey *et al.* 2009, Chambers *et al.* 2009); iii) it has a kinematic distance of $\sim 2900\,\mathrm{pc}$ (Simon *et al.* 2006b). Figure 2.2 shows the combined MIR and near infrared (NIR) extinction-derived mass surface density plot of Kainulainen & Tan (2013) (hereafter, KT13). The spatial extent of the IRDC is $> 6\,\mathrm{pc}$ at a kinematic distance of 2900 pc. However, there is more diffuse material to the north and south of the plotted region. The total mass is estimated to be $\sim 10^4\,\mathrm{M}_\odot$(KT13). The locations of the massive cores identified in 1.2 mm continuum emission by Rathborne *et al.* (2006) are indicated by black crosses.

This thesis describes the kinematic and physical properties of the northern portion of G035.39-00.33. Millimetre core 'MM7' (Rathborne *et al.* 2006) or 'H6' (Butler & Tan 2012; hereafter BT12), the northern-most core in Figure 2.2, provides the focus for the follow-up high-angular resolution observations presented in chapters 3 and 4.

2.1.2 Previous work

Jiménez-Serra *et al.* (2010), presented the first results from the molecular line study of G035.39-00.33. One of the key findings was the discovery of faint and narrow ($\Delta v_{\mathrm{obs}} \lesssim 1\ \mathrm{km\,s^{-1}}$) SiO emission, traced over parsec-scales in G035.39-00.33. It was speculated that this emission may be of different origin to the bright and

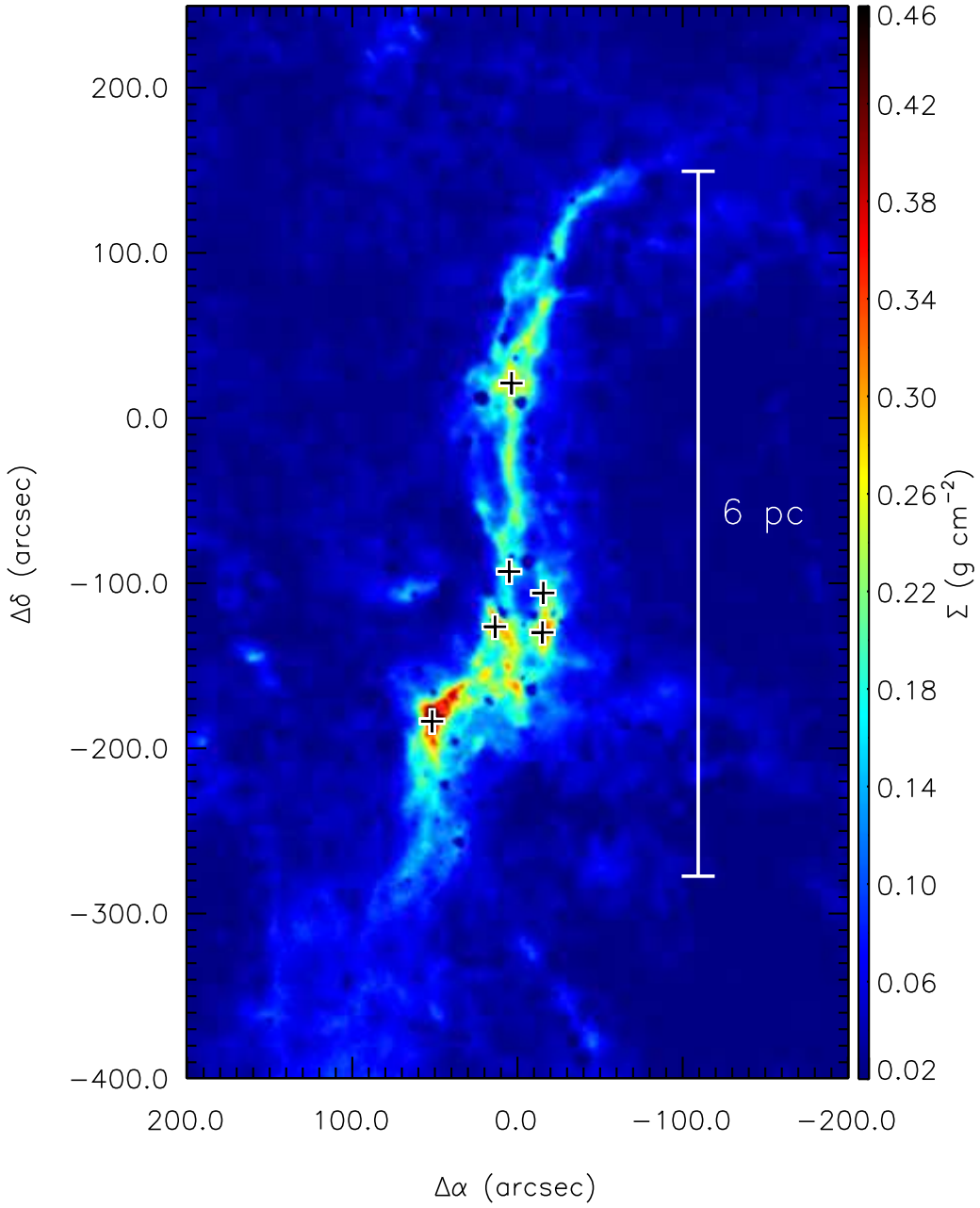

Figure 2.2: The MIR extinction-derived mass surface density plot of G035.39–0.33 (KT13), cloud H of BT09. The scale bar is calculated using a kinematic distance of 2900 pc (Simon *et al.* 2006b). The black crosses indicate the massive cores associated with G035.39-00.33 identified in 1.2 mm continuum emission by Rathborne *et al.* (2006).

broad SiO emission (line-width, $\Delta v_{\rm obs} \sim 4$–$7$ km s^{-1}) that is spatially coincident with regions of star formation in G035.39-00.33 (specifically the three nothern-most crosses in Figure 2.2). Two main suggestions were put forward to explain the narrow SiO emission: i) a population of widespread, and undetected low-mass protostars (the IRAM 30 m beam at ~ 87 GHz is $\sim 28''$, and so beam dilution may be significant); ii) the emission may be the product of a large-scale shock, possibly linked to the formation mechanism of the cloud. Whilst a population of low-mass protostars cannot be ruled out without higher-angular resolution observations of shocked gas tracers, Jiménez-Serra *et al.* (2010) discussed how the morphology of G035.39-00.33 is similar to structures produced in flow-driven models of cloud formation (see Section 1.1.2). If the second scenario were to be confirmed it would indicate that G035.39-00.33 is in an early stage of its evolution. Consequently, the hallmarks of the cloud formation process may still be imprinted in the chemistry and kinematics of the molecular gas.

In the second instalment of this series, Hernandez *et al.* (2011), presented IRAM 30 m observations of the $J = 1 \rightarrow 0$ and $J = 2 \rightarrow 1$ transitions of $C^{18}O$. These were used in comparison with the mass surface density map of BT09. The observed decrease in $\Sigma_{\rm C18O}/\Sigma$ with increasing Σ (whereby $\Sigma_{\rm C18O}$ and Σ are the mass surface densities of the $C^{18}O$ and from BT09, respectively) was interpreted as evidence for CO depletion due to freeze-out onto dust grains. This supports the idea the the molecular gas in G035.39-00.33 has not been greatly affected by stellar feedback (at least on scales equivalent to the resolution of the $C^{18}O$ data presented in Hernandez *et al.* 2011).

Hernandez *et al.* (2012), explored the virial balance of the cloud through the comparison between $C^{18}O$ data obtained with the IRAM 30 m telescope, and the

mass surface density map. Hernandez *et al.* (2012) suggest that the cloud is in approximate virial equilibrium. If this result applies generally to IRDCs, this may suggest that star formation (including massive star and stellar cluster formation) proceeds in structures that have reached virial equilibrium. This would be consistent with the basic assumptions of the core accretion model of massive star formation (McKee & Tan 2002, 2003; see Section 1.2.3).

Outside of this series of papers, Nguyen Luong *et al.* (2011) studied the cloud using the *Herschel* Space Observatory. A total of 15 cores were identified as being associated with G035.39-00.33 (an additional 13 were deemed to be outside the IRDC). By fitting SEDs using multiple wavelength data from the "*Herschel* imaging survey of OB Young Stellar Objects"[1] the authors find average masses of 2–50 $M_\odot$, sizes of 0.1–0.2 pc, and densities of 2–20 $\times 10^5$ cm^{-3}. Of these cores, $\sim$60% are said to be massive ($> 20\,M_\odot$) and IR quiet (24 μm flux < 1 Jy), implying that they are in an early stage of evolution.

2.1.3 Investigating the large-scale structure of G035.39–00.33

The apparent ubiquity of molecular filaments detected at millimetre and sub-millimetre wavelengths throughout the cold interstellar medium has prompted interest in their formation mechanisms and their relation to star formation (André *et al.* 2010, Molinari *et al.* 2010). Current theoretical models describing the origins of filamentary clouds vary from those that propose highly dynamical processes, to those that present a more quasi-static picture (see the discussion on cloud

[1] `http://hobys-herschel.cea.fr`

formation in Section 1.1.2, and the possible consequences for the star formation process in Section 1.2.1). In the dynamical paradigm, colliding flows of atomic or molecular gas, with relative speeds of $\sim$5-20 km s^{-1} (e.g. Ballesteros-Paredes *et al.* 1999), merge, triggering the formation of cold, molecular, filamentary clouds. Consequently, the hallmarks of such a formation mechanism may be imprinted in the kinematic structure of the gas.

This chapter focuses on the structure and kinematics of G035.39-00.33. The primary focus will be observations of the $J = 1 \rightarrow 0$ transition of both N_2H^+ and $C^{18}O$, obtained with the Instituto de Radioastronomía Milimétrica (IRAM) 30 m antenna. N_2H^+ and $C^{18}O$ have been selected for this study since they preferentially trace different density regimes. This allows for the comparison between the dense gas (traced by N_2H^+) and lower density (but comparatively abundant) gas traced by $C^{18}O$. In addition, N_2H^+ $(3-2)$ and SiO $(2-1)$ are used for comparison.

The observations and processing of data are discussed in Section 2.2. The results are discussed in Section 2.3, with specific focus on the physical structure, and kinematics being presented in Sections 2.4 and 2.5, respectively. Selected results have been chosen for a more detailed discussion in Section 2.6. Finally, the conclusions from this chapter are presented in Section 2.7.

2.2 Observations & data processing

The N_2H^+ $(1-0)$, N_2H^+ $(3-2)$, $C^{18}O$ $(1-0)$, and SiO $(2-1)$ observations were mapped with the IRAM 30 m telescope at Pico Veleta, Spain. The N_2H^+ observations were carried out in August 2008 and February 2009, $C^{18}O$ $(1-0)$ in August 2008, and SiO $(2-1)$ observations in December 2008 and February 2009[1].

The large-scale images were obtained in On-The-Fly (OTF) mapping mode. The off-positions used were $(1830'', 658'')$ for the $C^{18}O$ observations, and $(300'', 0'')$ for the N_2H^+ and SiO data, whose emission is concentrated closer to the IRDC. All observations were carried out using the old ABCD receivers. The Half Power Beam Width (HPBW)[2] of the IRAM 30 m antenna is dependent on the frequency of the observations and varies between $9''$ and $28''$ (at 280 GHz and 87 GHz). The central coordinates of the maps are $\alpha(\mathrm{J2000}) = 18^h57^m08^s$, $\delta(\mathrm{J2000}) = 02°10'30''$ ($l = 35°.517$, $b = -0°.274$). Saturn was used for pointing and focus. Further pointing and line calibration was checked using G34.3+0.2. The pointing was repeated every ~ 2 hrs. The VErsatile SPectrometer Assembly (VESPA) provided spectral resolutions between 20 kHz and 80 kHz.

In addition to these data, a single pointing of $C^{17}O$ $(1-0)$ was obtained with the IRAM 30 m antenna towards offset $= (2'', 20'')$, i.e. towards one of the most massive clumps in the mapped area, H6. This observation was carried out in July 2012 using the Eight MIxer Receiver (EMIR). The spectral resolution is 40 kHz, and the rms noise is ~ 0.05 K. Information on the beam sizes, frequencies, spectral resolutions, and typical spectral rms values can all be found in Table 2.1.

[1] Proposal: "The formation of IRDCs: Testing Dynamic versus quiescent theories", PI: Paola Caselli.

[2] HPBW $= 1.166\frac{\lambda}{D}$, where λ is the wavelength of observation and D is the telescope diameter; `http://www.iram.es/IRAMES/mainWiki/Iram30mEfficiencies`.

The data were processed using the GILDAS/CLASS package. Baselines were removed by fitting a first order polynomial to the line-free data. Spectra were extracted for each pixel by convolving the OTF dumps with a Gaussian profile, increasing the signal-to-noise ratio. The convolution was performed with a Gaussian whose full-width at half-maximum (FWHM) was equivalent to the IRAM 30 m beam size at the frequency of the given transition. When making comparison between datasets (for example between $C^{18}O$ and N_2H^+), the data were smoothed to a common map resolution. Pixels were spaced by 0.5 $\times$ the FWHM of the convolving Gaussian.

All intensities were calibrated in units of antenna temperature, T_A^*. Converting these intensities into units of main-beam brightness temperature was carried out using the following equation[1]:

$$T_{MB} = \frac{1}{f_{clump}} \frac{B_{eff}}{F_{eff}} T_A^*, \tag{2.1}$$

whereby f_{clump} is the beam filling factor (assumed $f_{clump} \sim 1$), B_{eff} and F_{eff} are the beam and forward efficiencies, respectively. Values for the beam and forward efficiencies can be found in Table 2.1. These were approximated by performing a linear fit between the frequency and the telescope efficiencies[2].

The 8 μm extinction-derived mass surface density map of BT12, as modified by Kainulainen & Tan (2013) (hereafter, KT13) to include corrections for the presence of the NIR extinction derived IRDC envelope is utilised for comparison. The mass surface density map has $\sim$2" resolution. When comparison is made between the

[1]This equation can be found in the IRAM 30 m manual, at `http://www.iram.es/IRAMES/otherDocuments/manuals/index.html`.

[2]Telescope efficiencies can be found: `http://www.iram.es/IRAMES/mainWiki/Iram30mEfficiencies`.

Table 2.1: Details of the IRAM 30 m observations.

Transition	Frequency (MHz)	Spec. Res. (kHz)	Δv_{res} ($\mathrm{km\,s^{-1}}$)	Beam size (arcsec)	Beam Efficiency	Forward Efficiency	rms† (K)
SiO $J = 2 \rightarrow 1$	86846.9600[a]	80	2.8×10^{-1}	28	0.77	0.98	0.02
N_2H^+ $J = 1 \rightarrow 0$	93173.7637[b]	20	6.4×10^{-2}	26	0.76	0.98	0.06
$C^{18}O$ $J = 1 \rightarrow 0$	109782.1760[c]	20	5.5×10^{-2}	22	0.73	0.96	0.14
$C^{17}O$ $J = 1 \rightarrow 0$	112359.2750[d]	40	1.1×10^{-2}	22	0.79*	0.96*	0.05
N_2H^+ $J = 3 \rightarrow 2$	279511.8320[b]	40	4.3×10^{-2}	9	0.49	0.90	0.16

a: Jiménez-Serra *et al.* (2010), *b*: Pagani *et al.* (2009), *c*: Cazzoli *et al.* (2003), *d*: Ladd *et al.* (1998),
$*$: EMIR, †: Mean spectral rms taken across the mapped region for each transition.

mass surface density and molecular line tracers, the maps are smoothed (using a Gaussian convolution) to an equivalent spatial resolution.

2.3 Observational results

2.3.1 Average spectra and integrated intensity

Line profiles

Figure 2.3 shows the spectra of the isolated N_2H^+ $(1-0)$ hyperfine component (F_1, F = 0,1 $\rightarrow$ 1,2), the N_2H^+ $(3-2)$, the $C^{18}O$ $(1-0)$, and the SiO $(2-1)$, averaged over the N_2H^+ $(1-0)$ mapped region. The spectra are expressed in terms of main beam brightness temperature, $T_{\rm MB}$ (Equation 2.2). The intensity of the N_2H^+ $(1-0)$, N_2H^+ $(3-2)$ and SiO $(2-1)$ lines have been multiplied by factors of 2, 1.5 and 20, respectively, for clarity. The SiO $(2-1)$ shows the broadest width, with emission present up to velocities of $\sim 50\,{\rm km\,s^{-1}}$. The $C^{18}O$ line encloses the emission of the other species, with the exception of the high velocity emission of SiO $(2-1)$, and exhibits a non-Gaussian line profile, indicative of multiple velocity components.

The four molecular gas tracers peak at different velocities. The highest density tracer, N_2H^+ $(3-2)$, peaks at the largest velocity, followed by (in order of decreasing centroid velocity) N_2H^+ $(1-0)$, $C^{18}O$ $(1-0)$ and SiO $(2-1)$. SiO typically traces shocked material (e.g. Jiménez-Serra *et al.* 2009), therefore it is expected that the SiO will exhibit a different centroid velocity to the other species (particularly the dense gas tracers). However, the shift in centroid velocities observed in the more quiescent molecular cloud tracers $C^{18}O$ and N_2H^+, is unexpected. Although $C^{18}O$ and N_2H^+ trace different density regimes (critical densities $\sim 2\times 10^3\,{\rm cm^{-3}}$ and $1.4\times 10^5\,{\rm cm^{-3}}$, respectively[1]), in low-mass star-forming regions their centroid

[1]Estimated for a temperature of 10 K from values provided in the Leiden Atomic and Molecular DAtabase (LAMDA; Schöier *et al.* 2005); `http://home.strw.leidenuniv.nl/~moldata/`

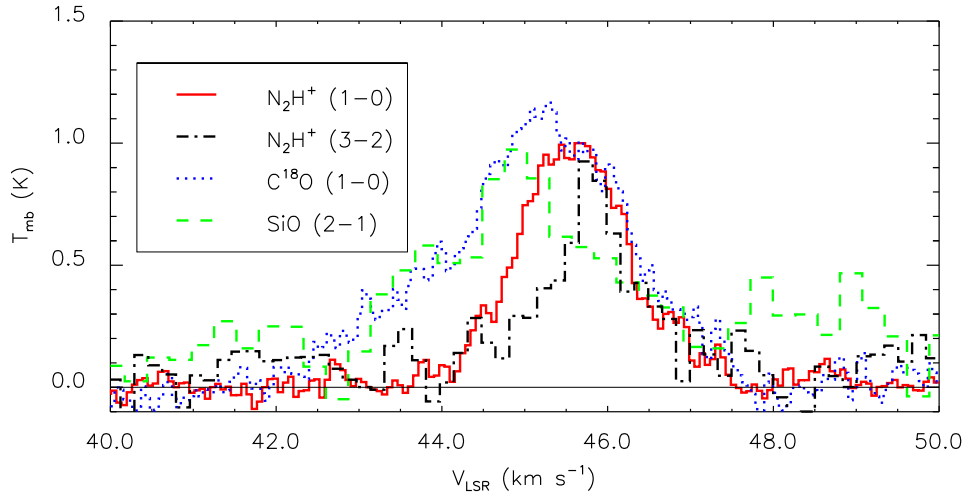

Figure 2.3: Average spectra of (Red) the isolated component of $N_2H^+(1-0)$, (Black) $N_2H^+(3-2)$, (Blue) $C^{18}O$ (1−0), and (Green) SiO (2−1). The $N_2H^+(1-0)$, $(3-2)$ and SiO $(2-1)$ intensities have been multiplied by factors of 2, 1.5 and 20, respectively.

velocities are typically coincident (Hacar & Tafalla 2011, Walsh *et al.* 2004). This feature will be analysed in more detail in Section 2.5.

Intensity distributions

Figure 2.4 presents integrated intensity maps of the $J = 1 \rightarrow 0$ transitions of both N_2H^+ (Red contours; F_1, F = 0,1 → 1,2 hyperfine component), and $C^{18}O$ (Blue contours). Figure 2.5 displays the integrated intensity map of N_2H^+ $(3-2)$. The IRAM 30 m antenna beam size associated with each frequency is shown in the top-left corner of each map (see Table 2.1 for absolute values). The spectra have been integrated between 40–50 km s^{-1}, to include all of the emission (see Figure 2.3). In each case, the contours are overlaid on the mass surface density map of KT13.

The N_2H^+ $(1-0)$ and $(3-2)$ emission is extended over a significant portion

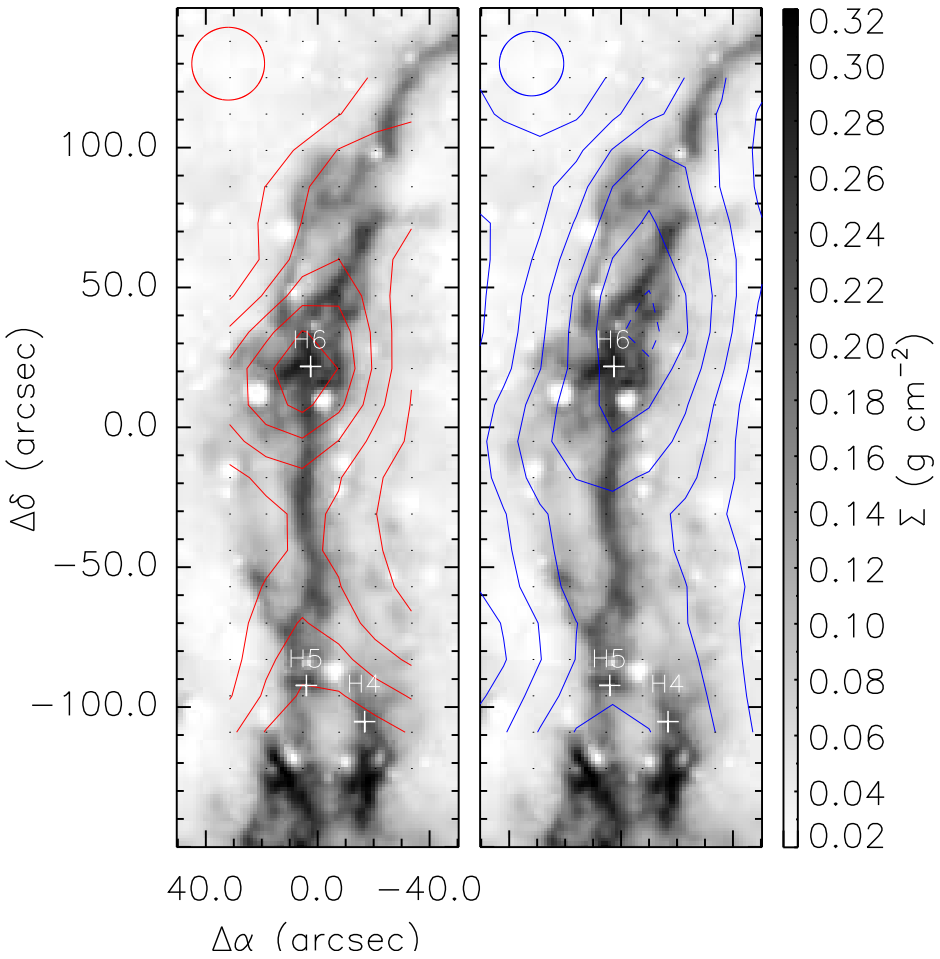

Figure 2.4: Contour maps representing the integrated intensity of (Left) N_2H^+ $(1-0)$ isolated component and (Right) $C^{18}O$ $(1-0)$, overlaid on the mass surface density map of KT13. Contours in both cases start at $10\,\sigma$ and increase in $5\,\sigma$ steps ($\sigma \sim 0.05$ K km s^{-1} and 0.15 K km s^{-1}, respectively). The dashed contour seen in the right hand panel is added to emphasise the location of the peak in $C^{18}O$ $(1-0)$. The red and blue circles in the top left of each panel refer to the beam sizes of the IRAM 30 m telescope ($26''$ and $22''$ at the frequency of N_2H^+ and $C^{18}O$, respectively). White crosses indicate locations of the massive cores identified within G035.39-00.33 (BT12, Rathborne *et al.* 2006).

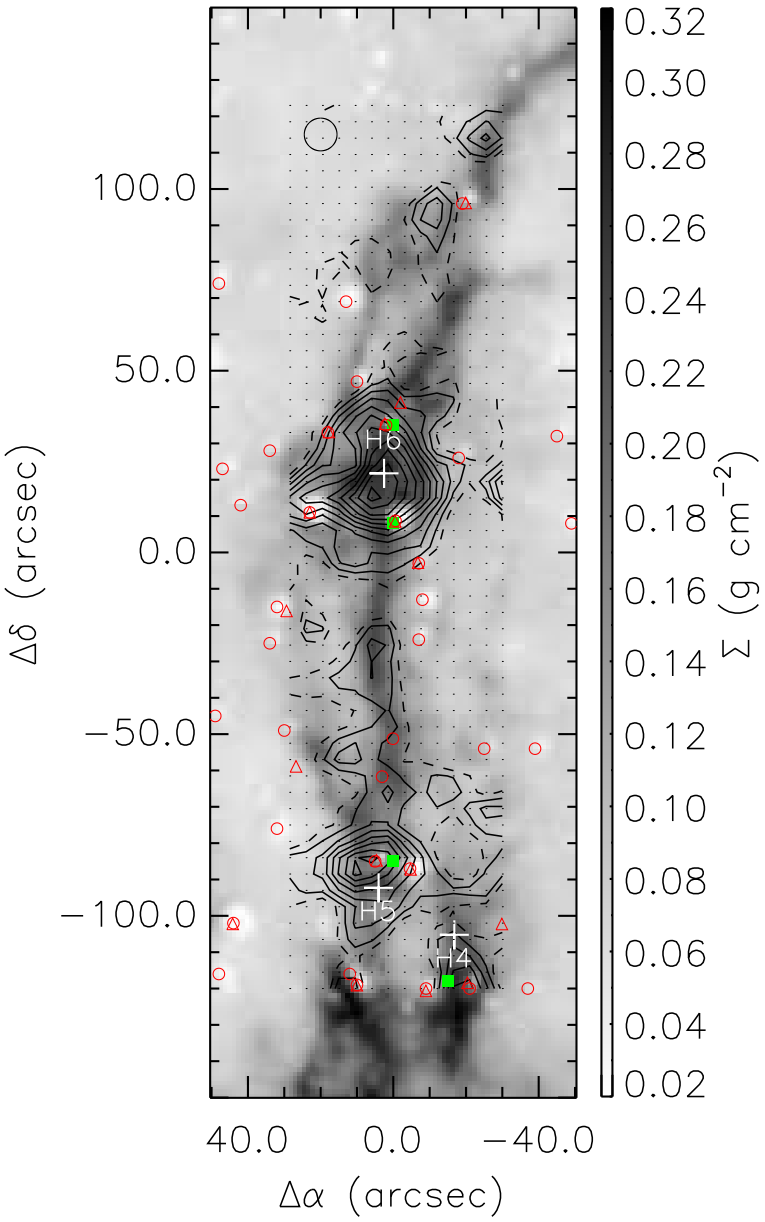

Figure 2.5: Integrated intensity contours of N_2H^+ $(3-2)$, overlaid on the mass surface density map of KT13. Contours start at $3\,\sigma$ and increase in $1\,\sigma$ steps ($\sigma \sim 0.5$ K km s^{-1}). The dashed contour is the $2\,\sigma$ level. White crosses indicate the positions of massive cores identified in BT12. Coloured symbols are $4.5\,\mu$m (green squares; Chambers *et al.* 2009), $8\,\mu$m (red circles) and $24\,\mu$m (red triangles; Carey *et al.* 2009, Jiménez-Serra *et al.* 2010) sources found in the direction of the IRDC.

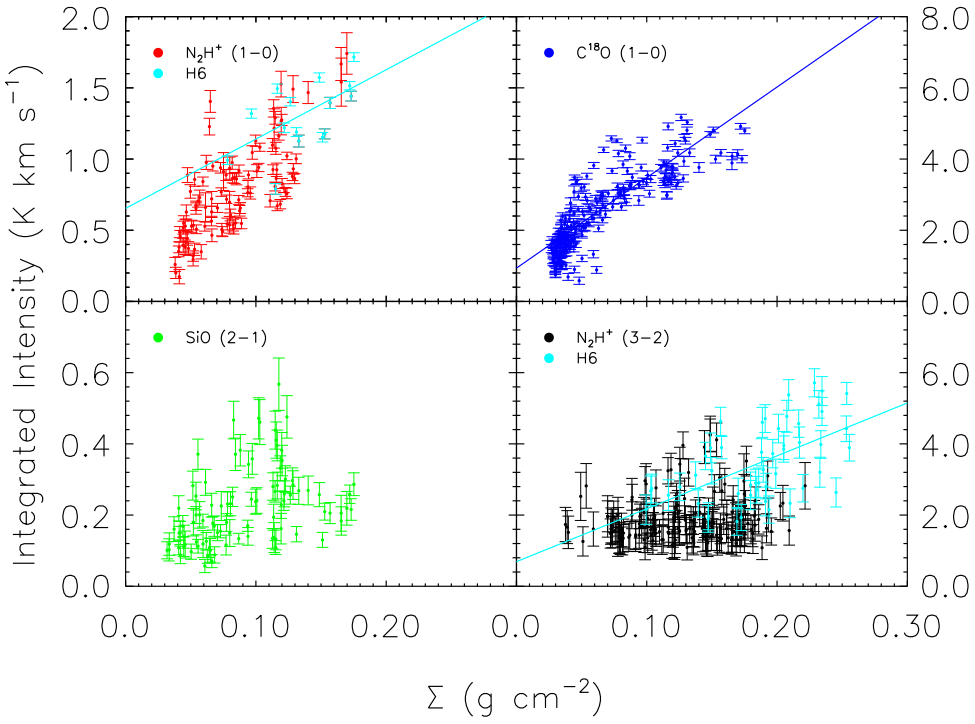

Figure 2.6: Integrated intensity as a function of mass surface density for the (Red) isolated component of N_2H^+ $(1-0)$, (Blue) $C^{18}O$ $(1-0)$, (Green) SiO $(2-1)$, and the (Black) N_2H^+ $(3-2)$. The N_2H^+ integrated intensity spectra within the region of the starless core H6 are displayed in Cyan. Least-squares fits are shown with respect to the $C^{18}O$ data, and to H6 for the $J = 1 \rightarrow 0$ and $J = 3 \rightarrow 2$ transitions of N_2H^+.

of the mapped region. In low-mass star forming regions, N_2H^+ emission is typically correlated with the location of dense cores (e.g. André *et al.* 2007, Caselli *et al.* 2002a, Friesen *et al.* 2010), whereas abundant molecules (such as CO and its isotopologues), are known to trace extended filamentary structures (e.g. Hacar & Tafalla 2011, Mizuno *et al.* 1995). In low-mass star forming regions, it is uncommon to see high-density tracers such as N_2H^+ extending over parsec-scales. Given that the critical density of the N_2H^+ $(1-0)$ transition is $\sim 10^5\,\mathrm{cm}^{-3}$, this may

imply that the overall number density of G035.39-00.33 is similar to the average density of nearby low-mass dense *cores* (i.e. at least one order of magnitude higher than the average density of the clouds within which nearby low-mass cores are embedded, $\leq 10^3\,\mathrm{cm}^{-3}$; e.g. Pineda *et al.* 2008). This will be further investigated in Section 2.4.2.

The N_2H^+ $(3-2)$ emission peaks towards two out of the three massive cores[1] contained within the mapped region (H5, H6: white crosses in Figure 2.5). The peak of the N_2H^+ $(1-0)$ emission is also coincident with the position of core H6. The $C^{18}O$ $(1-0)$ peaks away from core H6 (within ~ 1 beam size). This is consistent with the evidence for freeze-out of CO, most prominent towards core H6 (Hernandez *et al.* 2011). Emission from both N_2H^+ transitions traces the morphology of the extinction fairly well, whereas the emission from the $C^{18}O$ $(1-0)$ covers a larger area (as expected).

Figure 2.6 shows the total integrated intensities of the $J = 1 \rightarrow 0$ (F_1, F = 0,1 $\rightarrow$ 1,2), and $J = 3 \rightarrow 2$ transitions of N_2H^+, $C^{18}O$ $(1-0)$, and SiO $(2-1)$ as a function of mass surface density. To highlight the properties of the H6 region, data from this location have been highlighted in cyan[2]. In each case, the mass surface density of KT13 has been re-gridded onto the map of the molecular species, and smoothed to an equivalent spatial resolution. The lines indicate least-squares fit to the data. In the case of the $J = 1 \rightarrow 0$ and $J = 3 \rightarrow 2$ these lines have been fitted with respect to the core data, whereas all $C^{18}O$ $(1-0)$ data are fitted.

[1] The term "cores" in this context makes reference to the terminolgy used in Rathborne *et al.* (2006), following their identification in 1.2 mm continuum emission. No assumptions are made with regards to the potential star forming content of these objects.

[2] In order to separate this core from the rest of the data the $\sim 5\sigma$ level of the N_2H^+ $(3-2)$ intensity (between $-20.0 \leq \Delta\alpha \leq 20.0$ and $-10.0 \leq \Delta\delta \leq 50.0$) is taken and attributed to the core.

Table 2.2: Correlation strengths between molecular line emission and mass surface density

Transition	Sample size	r_s	P
N_2H^+ $(1-0)$	120	0.77	<0.001
N_2H^+ $(1-0)$: H6	15	0.53	0.04
$C^{18}O$ $(1-0)$	220	0.87	<0.001
$C^{18}O$ $(1-0)$: H6	15	0.04	0.87
SiO $(2-1)$	94	0.51	<0.001
N_2H^+ $(3-2)$	227	0.40	<0.001
N_2H^+ $(3-2)$: H6	50	0.57	<0.001

The Spearman rank correlation coefficient, r_s is calculated in order to investigate the strength of the correlation between emission from each molecular transition and the mass surface density. All but one of the tested correlations are significant to the 0.05 level, indicating that in the majority of cases, there is some correlation between the molecular line emission and the mass surface density. However, some of the correlations are stronger than others. Both the N_2H^+ $(1-0)$ and $C^{18}O$ $(1-0)$ show strong positive correlations with mass surface density. However, the correlation between emission from the H6 region and the mass surface density in $N_2H^+(1-0)$, while still significant, is weaker than that over the whole map. The same test for the $C^{18}O$ $(1-0)$ shows that there is no correlation between its emission and the mass surface density. This makes sense given the spatial separation between the $C^{18}O$ emission peak and the mass surface density peak at the location of H6 (see Figure 2.4). The SiO $(2-1)$ and N_2H^+ $(3-2)$ show moderate correlations with the mass surface density. However, the correlation between the H6 N_2H^+ $(3-2)$ emission is stronger. All information on the correlation tests can be found in Table 2.2.

The $C^{18}O/N_2H^+$ integrated intensity ratio

Tafalla & Santiago (2004) used CO depletion as a "chemical clock", to indicate an evolutionary sequence of individual cores. This is achieved by taking two species that show different amounts of depletion at high densities. $C^{18}O$ freeze-out becomes prominent at densities upwards of a few $10^4\,\mathrm{cm}^{-3}$ (e.g. Caselli & Ceccarelli 2012), whereas N_2H^+ $(1-0)$ remains in the gas phase up to densities $\geq 10^5\,\mathrm{cm}^{-3}$ (e.g., Caselli *et al.* 1999, Tafalla *et al.* 2002). Moreover, N_2H^+ takes longer than $C^{18}O$ to form, due to the slower neutral-neutral reactions involved in the production of N_2, the parent species of N_2H^+ (e.g. Hily-Blant *et al.* 2010). Therefore, an early stage of evolution would be characterised as having undepleted $C^{18}O$ and a low abundance of N_2H^+. As a core increases in density, $C^{18}O$ begins to freeze-out. Thus, with time, the $C^{18}O$ abundance falls while N_2H^+maintains a relatively large abundance up to volume densities of $\geq 10^5\,\mathrm{cm}^{-3}$. Once star formation begins to heat the surrounding environment, $C^{18}O$ returns to the gas phase. Tafalla & Santiago (2004) use the ratio, R:

$$R = \left[\frac{I_{1-0}^{\mathrm{C^{18}O}}}{I_{1-0}^{\mathrm{N_2H^+}}}\right], \tag{2.2}$$

to asses core evolution.

Figure 2.3 indicates that the profiles of the $C^{18}O$ and N_2H^+ differ. This is due to the presence of multiple velocity components throughout the map (the presence of multiple velocity components will be discussed in more detail in Section 2.5). To account for this, emission for both the isolated component of N_2H^+ and the $C^{18}O$ is integrated between 44-46 $\mathrm{km\,s}^{-1}$, focusing solely on the most prominent component. The N_2H^+ integrated emission is then scaled by its relative statistical

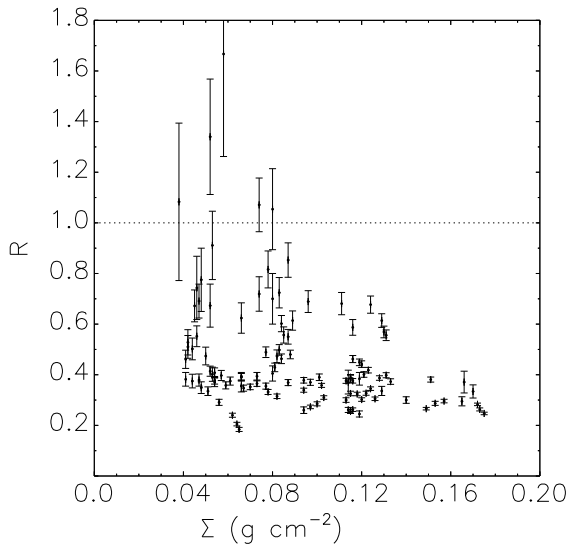

Figure 2.7: Integrated intensity ratio, $R = [I^{C^{18}O}_{1-0}/I^{N_2H^+}_{1-0}]$, as a function of mass surface density. The dotted line indicates where $R = 1$. Uncertainties in R are estimated from the measured integrated intensity values. Uncertainties in Σ are not shown but are of the order $\sim 30\%$ (KT13).

weight (~ 0.11) before comparison.

Regions in which R is large, coupled with relatively low N_2H^+ intensity, *may* be indicative chemical youth, and warrant follow-up observations (cf. L1521E; Tafalla & Santiago 2004). However, this analysis is merely intended as a guide, given that the R value is susceptible to both multiple velocity components and optical depth effects.

Figure 2.7 shows R versus the mass surface density. No R values larger than 1.0 are found at $\Sigma \geq 0.09\,\mathrm{g\,cm^{-2}}$. In addition, R has a value < 1 throughout the whole filament, except in the northern regions (away from the greatest extinction). Therefore no evidence is found for dense regions without $C^{18}O$ depletion. This is consistent with both the widespread dense gas presented here, and the widespread

$C^{18}O$ depletion presented in Hernandez *et al.* (2011).

2.3.2 Optical depth

The non-Gaussian line profiles and velocity shift identified in Figure 2.3 will be analysed in more detail in Section 2.5.4, and discussed in Section 2.6.1. However, at this stage it is important to investigate whether or not such traits are being influenced by optical depth effects.

The optical depth of the N_2H^+ $(1-0)$ line can be estimated directly, by performing a hyperfine structure (HFS) fit in GILDAS/CLASS. Measuring the optical depth of $C^{18}O$ $(1-0)$, however, requires an optically thin isotope, for example $C^{17}O$ $(1-0)$. Both N_2H^+ $(1-0)$ and $C^{17}O$ $(1-0)$ exhibit hyperfine structure. The opacity of individual hyperfine components can be estimated using (Stahler & Palla 2005):

$$\tau(v) \;=\; \tau_{\rm TOT} \sum_{i=1}^{n} r_i \exp\left[-4\ln(2)\left(\frac{(v - v_0 - \Delta v_i)^2}{(\Delta v)^2} \right) \right] \qquad (2.3)$$

whereby, v is the velocity, $\tau_{\rm TOT}$ is the total opacity, r_i is the intensity of the ith hyperfine component (relative to the total intensity of the line), that is displaced in velocity by Δv_i from the $i=0$ component (centred on v_0), and Δv is the FWHM line-width. Since the velocity separation between the $F_1, F=0{,}1 \rightarrow 1{,}2$ component and its neighbouring hyperfines is large (in comparison to the FWHM of the observed line), the opacity at the centre of this *isolated* line can be approximated by $\tau_{\rm i} \sim \tau_{\rm TOT} r_i$. This is true only when the line is sufficiently narrow such that the isolated component does not overlap with adjacent hyperfines. The relative velocities of the hyperfine components for N_2H^+ $(1-0)$ were obtained from Caselli *et al.*

(1995), and the $C^{17}O$ $(1-0)$ from Ladd *et al.* (1998). The HFS fitting technique in GILDAS/CLASS makes comparison between the predicted and observed intensities of the hyperfine components, deriving the total optical depth (along with the $V_{\rm LSR}$ and Δv).

The optical depth of N_2H^+ $(1-0)$ was measured for every pixel in the mapped area. The mean (total) optical depth, $\tau_{\rm TOT}$, throughout the map is <3. The peak optical depth is located at offset $=$ (-33.5″, 138″) and has a value $\tau \sim 11.0 \pm 0.5$. Given that the isolated hyperfine component has a statistical weight of ~ 0.11 (Caselli *et al.* 1995), the maximum optical depth of this component therefore is ~ 1.2, and the mean value is < 0.33. Towards H6, the optical depth is slightly above the mean value.

Unfortunately, the $C^{17}O$ $(1-0)$ has not been observed over the full extent of the $C^{18}O$ $(1-0)$ map. However, a single pointing has been obtained towards H6 $(2'', 20'')$. One can estimate the optical depth of $C^{18}O$ from the $C^{17}O$ by assuming the latter is optically thin. Figure 2.8 shows the spectra of $C^{18}O$ (left panel) and $C^{17}O$ (right panel) at this location. It was not possible to obtain a good fit to the $C^{17}O$ spectrum without fixing τ. The $C^{17}O$ $(1-0)$ spectrum was best reproduced by using a two component HFS fit with $\tau = 0.1$ (see red and green fits to the data). In the case that $C^{18}O$ $(1-0)$ is optically thin, the ratio of the line temperatures should reduce to the typical Galactic abundance ratio, $^{18}O/^{17}O \sim 3.65$ (Penzias 1981). The optical depth can therefore be established using:

$$R = \frac{T_{\rm C^{18}O}^{\rm peak}}{T_{\rm C^{17}O}^{\rm peak}} = \frac{1 - \exp\left[-\tau(v)\right]}{1 - \exp\left[-\tau(v)/a\right]} \tag{2.4}$$

where $a = 3.65$, i.e. the predicted relative abundance. In Figure 2.8, the $C^{17}O$

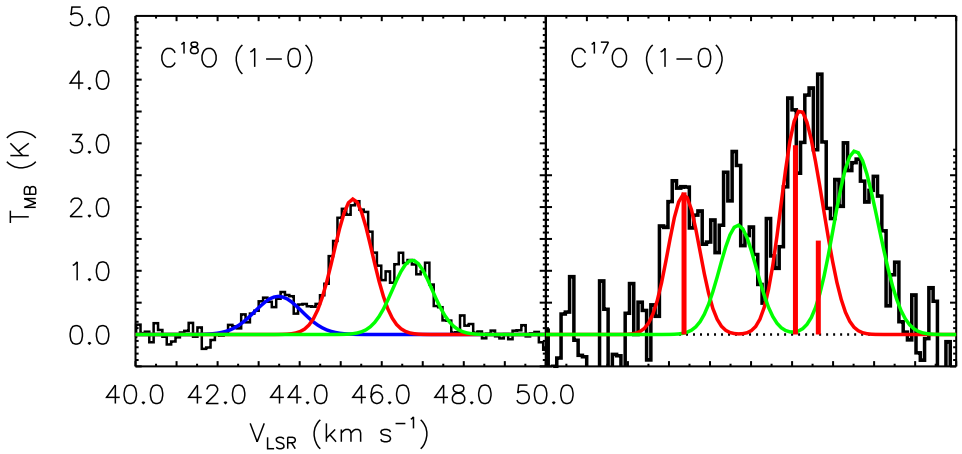

Figure 2.8: A comparison between the (left) $C^{18}O$ $(1-0)$ and (right) $C^{17}O$ $(1-0)$ spectra at the location of H6. The intensity of the $C^{17}O$ $(1-0)$ spectrum has been multiplied by a factor $\sim a/r_i \sim 11$, whereby a is the typical Galactic $^{18}O/^{17}O$ abundance ratio ~ 3.65 (Penzias 1981), and r_i is the statistical weight of the isolated hyperfine component (~ 0.33; see red line at ~ 43.4 km s^{-1}). The coloured Gaussian profiles are the result of a three and two component Gaussian and HFS fit to the $C^{18}O$ $(1-0)$ and $C^{17}O$ $(1-0)$ spectra, respectively. The blue component evident in $C^{18}O$ $(1-0)$ emission (<44 km s^{-1}) is not evident in the $C^{17}O$ $(1-0)$ spectrum.

intensity has been multiplied by a factor $\sim a/r_i \sim 11$, whereby r_i is the statistical weight of the isolated hyperfine component (~ 0.33; see the low-velocity component of Figure 2.8). It is immediately clear that the scaled intensity of the red $C^{17}O$ $(1-0)$ component is comparable to that observed in $C^{18}O$ (indicating that the absolute relative intensity ratio is ~ 3.65). From Equation 2.4 it is found, $\tau \sim 0.12$. Conversely, it is evident the peak temperature of the green $C^{18}O$ component is less than the corresponding scaled $C^{17}O$ component. In this case, $\tau \sim 1.25$. Therefore, this component is moderately optically thick at the location of H6.

Since H6 is one of the densest portions of the mapped region (with the exception of the other identified cores), it is assumed that the optical depth of $C^{18}O$ $(1-0)$ derived here is greater than elsewhere in the mapped region (this statement is also consistent with excitation analysis performed towards G035.39-00.33; Du & Yang 2008, Hernandez *et al.* 2011). Consequently, the influence of opacity on the derived physical and kinematic properties of G035.39-00.33, in both the isolated component of N_2H^+ $(1-0)$ and $C^{18}O$ $(1-0)$, is expected to be small.

2.4 Analysis: The physical properties of G035.39–00.33

2.4.1 Column density

The column density can be estimated for each pixel in the map from the integrated emission of N_2H^+ $(1-0)$ and $C^{18}O$ $(1-0)$. For optically thin emission (see Section 2.3.2) the column density can be calculated using Caselli *et al.* (2002b):

$$N_{\rm tot} = \frac{8\pi I_{\rm tot}}{\lambda^3 A}\frac{g_{\rm l}}{g_{\rm u}}\frac{1}{J_\nu(T_{\rm ex})-J_\nu(T_{\rm bg})}\frac{1}{1-\exp\left(-h\nu/k_{\rm B}T_{\rm ex}\right)}\times \frac{Q_{\rm rot}(T_{\rm ex})}{g_{\rm l}\exp\left(-E_{\rm l}/k_{\rm B}T_{\rm ex}\right)}. \quad (2.5)$$

In this analysis, $I_{\rm tot}$ represents the integrated intensity (in the case of N_2H^+ this is taken across the isolated component and scaled by the relative statistical weight: $I_{\rm tot} = \frac{1}{r_i}\int T_{\rm MB}\,dv$, whereby r_i is the relative statistical weight ~ 0.11), A is the Einstein coefficient for spontaneous emission ($3.63\times10^{-5}\,{\rm s}^{-1}$ and $6.266\times10^{-8}\,{\rm s}^{-1}$ for the $J=1\rightarrow0$ transitions of N_2H^+ and $C^{18}O$, respectively; Schöier *et al.* 2005), g_u and g_l are the statistical weights for the upper and lower states, respectively, $J_\nu(T_{\rm ex})$ and $J_\nu(T_{\rm bg})$ are the equivalent Rayleigh-Jeans excitation and background temperatures ($T_{\rm bg}=2.73\,{\rm K}$), λ and ν are the wavelength and frequency of the $J=1\rightarrow0$ transition, and $k_{\rm B}$ and h are the Boltzmann and Planck constants, respectively. $Q_{\rm rot}(T_{\rm ex})$ is the partition function which is given by:

$$Q_{\rm rot}(T_{\rm ex}) = \sum_{J=0}^{\infty}(2J+1)\exp\left(-E_{\rm J}/k_{\rm B}T_{\rm ex}\right). \quad (2.6)$$

For every line transition there exists a critical density of H_2, $n_{\rm crit}$, at which collisional and radiative downward transitions have equal rates. Above this critical density, collisional de-excitation is most effective. The critical densities of H_2 for $C^{18}O$ $(1-0)$ and N_2H^+ $(1-0)$ are $\sim 10^3\,{\rm cm}^{-3}$, and $\sim 10^5\,{\rm cm}^{-3}$, respectively. Since N_2H^+ $(1-0)$ has a critical density of $\sim 10^5\,{\rm cm}^{-3}$, and it is widespread, it is assumed that the ambient density of the IRDC is greater than the $C^{18}O$ $(1-0)$ critical value. For this analysis it is therefore assumed that $C^{18}O$ is in local thermodynamic equilibrium (LTE). In LTE the energy levels are populated according the Boltzmann distribution, and characterised by a single temperature, $T_{\rm ex} = T_{\rm kin}$.

There are no measurements of the gas temperature across G035.39-00.33. Gas temperatures have been measured towards other IRDCs, using NH_3 observations, and values are typically found to be $< 20\,{\rm K}$ (e.g. Pillai *et al.* 2006, Ragan *et al.* 2011). Towards G035.39-00.33, the *dust* temperature is estimated to be $\sim 15\,{\rm K}$ (Nguyen Luong *et al.* 2011). At high densities ($> 10^{4.5}\,{\rm cm}^{-3}$), gas and dust temperatures are expected to be coupled (Goldsmith 2001). Although a simplistic assumption (given that the dust and $C^{18}O$ may not be tracing equivalent regions), a fiducial value of $T_{\rm ex} = T_{\rm kin} = 15\,{\rm K}$ is used for the $C^{18}O$ $(1-0)$ column density calculation. Given the simplicity of this assumption it is worth noting for excitation temperatures of 10 and 25 K the column density should be multiplied by ~ 0.8 and 1.33, respectively.

For N_2H^+ $(1-0)$ the excitation temperature can be estimated using the following:

$$T_{\rm ex} = \frac{h\nu}{k_{\rm B}} \left[\ln\left(1 + \frac{(h\nu/k_{\rm B})}{T_{\rm MB} + J(T_{\rm bg})} \right) \right]^{-1} \tag{2.7}$$

where $T_{\rm MB}$ is the brightness temperature of the N_2H^+ $(1-0)$ line.

By simply taking the integrated intensity, the influence of multiple velocity components are ignored. This therefore gives an estimate for the total column density (but not columns of individual components). The mean value of the derived excitation temperatures ($T_{\rm ex} = 5.11\,{\rm K}$) is adopted for the calculation (for $T_{\rm ex} = 15\,{\rm K}$ the column density should be multiplied by $\sim$1.1).

Substituting all parameters into Equation 2.5, yields:

$$N(\mathrm{N_2H^+}) = 1.5 \times 10^{12} I_{\rm tot}\,({\rm K\,km\,s^{-1}})\,{\rm cm^{-2}}, \tag{2.8}$$

and for $\mathrm{C^{18}O}$:

$$N(\mathrm{C^{18}O}) = 1.2 \times 10^{15} I_{\rm tot}\,({\rm K\,km\,s^{-1}})\,{\rm cm^{-2}}. \tag{2.9}$$

The mean $\mathrm{N_2H^+}$ column density across G035.39-00.33 is $N(\mathrm{N_2H^+}) = (1.14 \pm 0.11) \times 10^{13}\,{\rm cm^{-2}}$, peaking in the south at offset (5.5″, -122″), with a value of $(2.33 \pm 0.25) \times 10^{13}$ cm^{-2}. The minimum value of $N(\mathrm{N_2H^+})$ is located in the north, at offset (5.5″, 125″), where $N(\mathrm{N_2H^+}) = (2.33 \pm 0.69) \times 10^{12}\,{\rm cm^{-2}}$. The uncertainties on these values are estimated by propagating errors in Δv (measured), $T_{\rm MB}$ (measured), and $T_{\rm ex}$. The true uncertainty is expected to be larger given the simplistic assumptions discussed above.

A significant correlation (Spearman rank correlation coefficient, $r_{\rm s} = 0.77$, $P < 0.001$) between the column density of $\mathrm{N_2H^+}$ $(1-0)$ and the mass surface density is found (as expected given the strong correlation found in Figure 2.6 between the $\mathrm{N_2H^+}$ $(1-0)$ integrated intensity and the mass surface density). A least-squares fit to the data gives $N(\mathrm{N_2H^+}) = (9.8 \pm 0.3) \times 10^{13}\,\Sigma + (1.5 \pm 0.2) \times 10^{12}$. This implies a constant fractional abundance of $\mathrm{N_2H^+}$ (w.r.t. $\mathrm{H_2}$ molecules) of $\simeq 4 \times 10^{-10}$. This fractional abundance is consistent with values quoted towards other IRDCs (10^{-10}–10^{-9}; e.g.

Miettinen *et al.* 2011, Vasyunina *et al.* 2011), and is similar to low-mass *cores* (a few times 10^{-10}; Caselli *et al.* 2002b, Crapsi *et al.* 2005).

The average $C^{18}O$ column density throughout the filament is $N(C^{18}O) = (3.82 \pm 0.04) \times 10^{15}$ cm^{-2}, peaking at position (-10.0, 34.0), north-west of the extinction peak of H6 with a value of $(5.95 \pm 0.72) \times 10^{15}\,\mathrm{cm}^{-2}$. This is consistent with Hernandez *et al.* (2011), who found evidence of CO freeze-out towards the location of H6. In the instances where the optical depth of the $C^{18}O$ $(1-0)$ becomes significant (see discussion in Section 2.3.2), one must correct for the opacity using (Goldsmith & Langer 1999):

$$C_\tau = \frac{\tau}{1 - \mathrm{e}^{-\tau}}. \tag{2.10}$$

Therefore, for an observed opacity of $\tau \sim 1.25$ (Section 2.3.2), the correction factor, $C_\tau \sim 1.75$. This indicates that the column density of $C^{18}O$ $(1-0)$ may be underestimated by a factor of ~ 2 towards H6. This may provide an explanation for the observed plateau in $C^{18}O$ integrated emission towards high mass surface densities in Figure 2.6.

2.4.2 Number density and kinetic temperature

As mentioned in Section 2.3.1, the detection of widespread N_2H^+ emission throughout G035.39-00.33 may indicate that the ambient gas density is greater than that observed in nearby low mass star forming regions ($\sim 10^3\,\mathrm{cm}^{-3}$; Pineda *et al.* 2008). The emission from multiple transitions of the same molecular species can be used, in conjunction with a radiative transfer model, to investigate this theory. For this analysis, the radiative transfer code RADEX (van der Tak *et al.* 2007) is used[1].

[1]The source code for RADEX can be downloaded here: `http://home.strw.leidenuniv.nl/~moldata/radex.html`

The interdependence of the local radiation field and molecular level populations means that solving radiative transfer problems is complex. RADEX circumvents this issue by introducing an escape probability β, the probability that a photon will escape the region from where it was created. This escape probability is dependent on an assumed geometry and the optical depth of the investigated line emission. By assuming a geometry, RADEX effectively decouples the radiative transfer and level population calculations. The model line emission produced as a result of this assumed geometry can then be used to make direct comparison with the observed emission. Three geometries are available in RADEX to create the model line emission: a uniform sphere; an expanding sphere (Large Velocity Gradient, LVG); or a plane-parallel slab. The LVG and plane-parallel approximations are used in this analysis to make comparison with the observed emission from the $J = 1 \rightarrow 0$ and $J = 3 \rightarrow 2$ (smoothed to an equivalent spatial resolution) transitions of N_2H^+.

Input parameters and best fit determination

In order to produce the model emission, RADEX requires a number of input parameters. The spectral range is limited to 90–290 GHz, which incorporates the $J = 1 \rightarrow 0$ and $J = 3 \rightarrow 2$ transitions of N_2H^+. Since this analysis focuses on estimating the volume density and kinetic temperature of G035.39-00.33, RADEX also requires an estimate of the column density. The column density values estimated for each pixel in Section 2.4.1 are therefore used. Finally, RADEX requires an estimate of the line-width for the selected molecular species (the line-width and column density are used to derive an estimate for the optical depth). The average line-width between the N_2H^+ $(1-0)$ and $(3-2)$ is used, as suggested in van der

Tak *et al.* (2007). This final parameter makes the assumption that both the N_2H^+ $(1-0)$ and $(3-2)$ are tracing the same material, and therefore the line-widths are expected to be similar in each pixel. For G035.39-00.33 however, this is not always true. In many instances the widths of the $J = 1 \rightarrow 0$ and $J = 3 \rightarrow 2$ lines vary. To account for this, a limit is imposed on the line-width ratio of the two transitions:

$$0.5 \leq \frac{\Delta\upsilon_{(1-0)}}{\Delta\upsilon_{(3-2)}} \leq 2.0. \tag{2.11}$$

If this condition is satisfied then the pixel is selected and the mean line-width chosen as an input parameter to the calculation. The remaining input parameters are dependent on the method used to estimate either the temperature, density or both.

The model emission from RADEX is then compared to the observed emission of N_2H^+. The best fitting solution is found using the following minimisation:

$$\chi^2 = \frac{1}{3}\left[\left(\frac{I^{\rm OBS}_{1-0}/I^{\rm OBS}_{3-2} - I^{\rm RADEX}_{1-0}/I^{\rm RADEX}_{3-2}}{\sigma(I^{\rm OBS}_{1-0}/I^{\rm OBS}_{3-2})}\right)^2 + \left(\frac{I^{\rm OBS}_{1-0} - I^{\rm RADEX}_{1-0}}{\sigma(I^{\rm OBS}_{1-0})}\right)^2 + \left(\frac{I^{\rm OBS}_{3-2} - I^{\rm RADEX}_{3-2}}{\sigma(I^{\rm OBS}_{3-2})}\right)^2\right], \tag{2.12}$$

where $I^{\rm OBS}$ refers to the observed integrated intensity of the molecular line transition and $I^{\rm RADEX}$ refers to that produced by RADEX. For the N_2H^+ $(1-0)$ emission the total integrated intensity (across all hyperfine components) is compared against the RADEX output. Caselli *et al.* (2002b) set a threshold intensity level above which an accurate measurement of the optical depth could be obtained, $I^{\rm OBS}/\sigma \geq 20$ (since an increased rms can influence the peaks of the individual components). Since the observed N_2H^+ $(3-2)$ emission does not satisfy this criteria

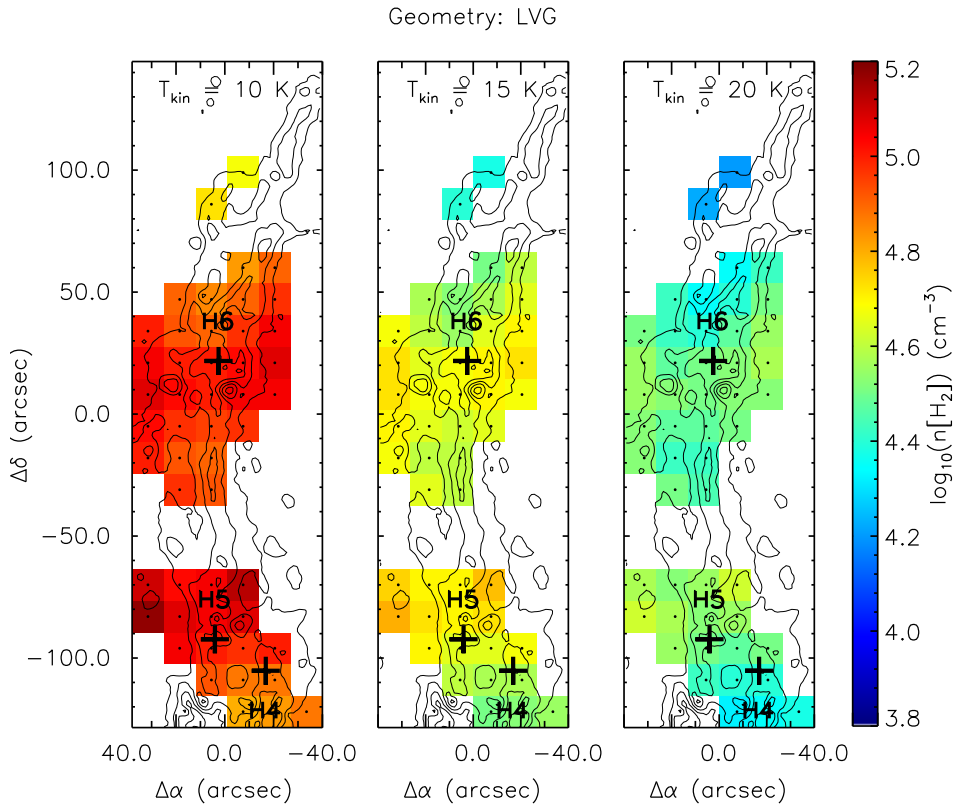

Figure 2.9: Number density maps of G035.39-00.33 obtained from the observed N_2H^+ line intensity ratio, $R = I_{1-0}/I_{3-2}$, and the use of the RADEX code (using the LVG approximation). From left to right, the number density maps are created by assuming constant temperatures of 10 K, 15 K, and 20 K, respectively. The crosses indicate the position of massive cores from BT12. Mass surface density contours of KT13 are used to highlight the morphology of the IRDC.

(at any position in the map), the opacity is fixed at $\tau = 0.1$ during the HFS fitting procedure. Prior to comparison with observations therefore, the model N_2H^+ $(3-2)$ emission is corrected using Equation 2.10.

Given the above assumptions RADEX can be used to constrain both the H_2 number density and the kinetic temperature throughout G035.39-00.33. This analysis has been divided into two sections. In the first, one of either the kinetic temperature or number density is fixed in order to constrain the other (both are quantified

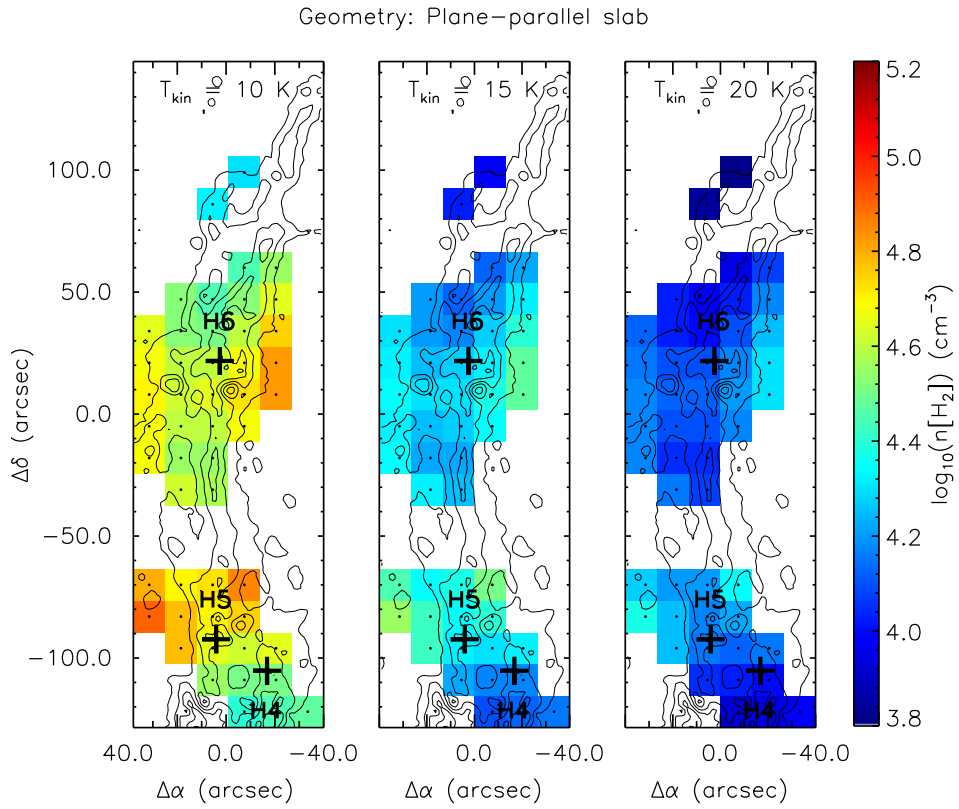

Figure 2.10: The same as Figure 2.9, but for the plane-parallel slab geometry.

separately). In the second section, both the number density and temperature are left as free parameters in the calculation, and solved for simultaneously.

Fixed parameter estimates:

Figures 2.9 and 2.10 show the number density maps of G035.39-00.33 for the LVG and plane-parallel slab approximations, respectively. Each respective map has been produced by fixing the temperature at 10, 15, and 20 K (shown from left to right in both figures, respectively), and varying $n[H_2]$ between 10^3-10^8 cm^{-3}. Each map is shown with an equivalent density scale such that direct comparison can be

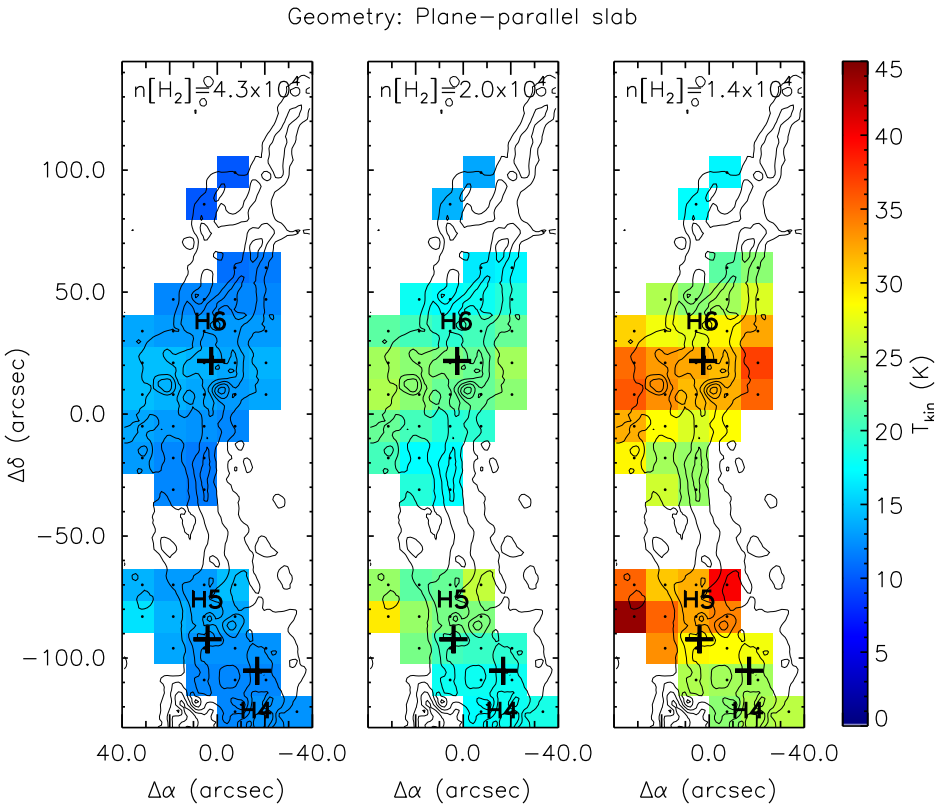

Figure 2.11: Kinetic temperature map of G035.39-00.33 obtained from the observed N_2H^+ line intensity ratio, $R = I_{1-0}/I_{3-2}$, and the use of the RADEX code (using the plane-parallel slab approximation). Constant number densities used in the RADEX calculation are shown at the top of each map. The crosses and contours are equivalent to those in Figures 2.9 and 2.10.

made between the derived $n[H_2]$ values at different temperatures, and between the two geometrical assumptions.

For the LVG model, mean number densities of $9.6 \times 10^4\,\mathrm{cm}^{-3}$, $4.4 \times 10^4\,\mathrm{cm}^{-3}$, and $3.0 \times 10^4\,\mathrm{cm}^{-3}$ are found for temperatures of 10 K, 15 K, and 20 K, respectively. For the plane-parallel slab approximation, mean number densities of $4.3 \times 10^4\,\mathrm{cm}^{-3}$, $2.0 \times 10^4\,\mathrm{cm}^{-3}$, and $1.4 \times 10^4\,\mathrm{cm}^{-3}$ are found for temperatures of 10 K, 15 K, 20 K, respectively.

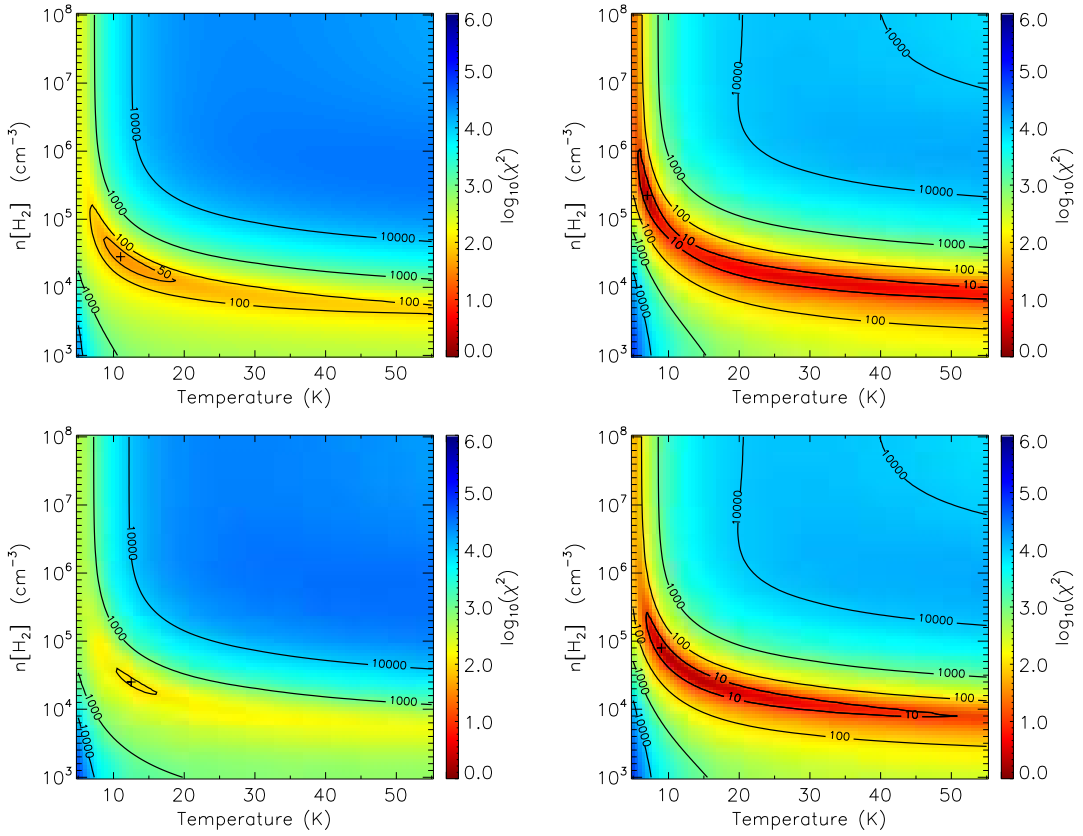

Figure 2.12: χ^2 surface plots derived from Equation 2.12. From left to right and top to bottom the map locations are (-7.5″, -122.0″), (-20.5″, 8.0″), (5.5″, 21.0″), and (18.5″, -70.0″), respectively.

Figure 2.11 is the result of imposing a constant number density across the map to study the variation in temperature. Only the plane-parallel slab approximation is shown (since the LVG approximation produces a qualitatively similar result). The three maps correspond to three different values of number density (the mean number density derived in Figure 2.10). A temperature increase towards cores H5 and H6 is observed. However, it is interesting to note the largest temperatures ($\sim$ 35-45 K for $n[\mathrm{H_2}] \sim 1.4\times10^4\,\mathrm{cm^{-3}}$) are observed either side of both the H5 and H6 core markers, rather than being directly coincident with them. In the next

section the both the number density and temperature are left as free parameters to investigate this further.

Free parameter estimates:

An alternative method of estimating both the number density and kinetic temperature is to leave both parameters free. In this way, a solution that best describes the observed emission can be found without having to impose either a number density or a temperature. For this analysis a 100×100 grid of number density (varied between 10^3-$10^8\,\mathrm{cm}^{-3}$) and temperature (varied between 5-55 K) is created. Best fitting parameters are derived for each map pixel following the minimisation of Equation 2.12.

Figure 2.12 is a sample of four χ^2 surfaces shown in $n[\mathrm{H_2}]$ versus T_{kin} parameter space. These positions have been selected as they provide a representative view of the χ^2 distribution as a result of this analysis. The top-left panel of Figure 2.12 is typical of the mean χ^2 value (~ 40). It has been taken from location = (5.5″,-109.0″), and has $\chi^2 \sim 38$. The bottom-left panel is taken from the H6 region = (5.5″, 21.0″), and is poorly constrained with $\chi^2 \sim 102$. The top-right and bottom right panels are examples of where the parameters are well-constrained according to Equation 2.12, at locations (-20.5″, 8.0″) and (18.5″, -70.0″), respectively ($\chi^2 \sim 0.8$ and 1.0, respectively).

Figure 2.13 shows the result of this analysis over the full mapped region. Overplotted for reference are the locations of 4.5, 8, and 24 μm emission (see also Figure 2.5). Some of the observed 4.5, 8, and 24 μm sources are coincident with a (slight ~ 2 K) increase in temperature. A good example of this is the bright 8 and 24 μm source observed to the south-east of H6.

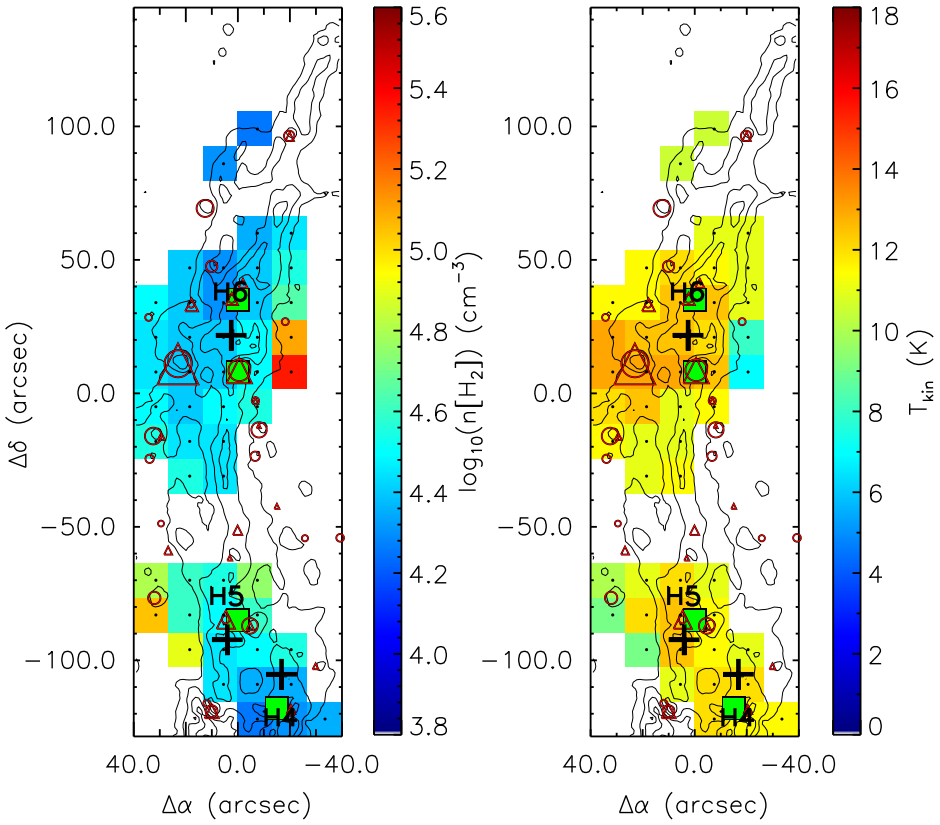

Figure 2.13: H_2 number density (left) and kinetic temperature maps (right) of G035.39-00.33, derived using RADEX under the plane-parallel slab approximation. Overlaid are the mass surface density contours of KT13. Locations of massive dense cores are indicated with black crosses (BT12). The locations of 4.5, 8, and 24 μm, are shown as green squares, open red circles, and open red triangles, respectively (see also Figure 2.5).

An unexpected result of this analysis is the density increase towards the edges of the H6 region. A possible explanation for this is that the analysis is influenced by the presence of multiple velocity components (see Section 2.5). Where multiple velocity components are evident (e.g. towards the H6 region, and towards the south of the map (below $\Delta\delta \sim$-109″), the fits are typically less-well constrained (see the bottom-left hand panel of Figure 2.12). Not all components observed in N_2H^+ $(1-0)$ will be necessarily observed in N_2H^+ $(3-2)$, given its larger critical density (this is analogous to the $C^{18}O$ and $C^{17}O$ spectra observed in Figure 2.8). The relatively simplistic method of taking the total integrated intensity of the N_2H^+ $(1-0)$ employed here, may therefore influence both the number density and temperature in these regions. Comparing trends in different regions as a result of this analysis should therefore be approached with caution. However, assuming the geometry of an expanding sphere, as opposed to a plane-parallel slab, would alter these results by a factor of $\gtrsim 2$ (see Figures 2.9 and 2.10). The global properties (i.e. a mean number density and kinetic temperature values of $\sim 4 \times 10^4\,\mathrm{cm}^{-3}$ and $\sim 12\,\mathrm{K}$, respectively) are therefore expected to be representative of the region traced by N_2H^+ $(1-0)$ and N_2H^+ $(3-2)$.

2.5 Analysis: The kinematics of G035.39–00.33

2.5.1 Evidence for multiple velocity components

Figure 2.14 displays the spectra of the N_2H^+ $(1-0)$ isolated component and $C^{18}O$ $(1-0)$ over the full extent of the N_2H^+ $(1-0)$ map. This is overlaid on top of the mass surface density map of KT13 (smoothed to an equivalent resolution). As noted in the previous sections (and by Jiménez-Serra *et al.* 2010), multiple velocity components appear at various positions within the cloud (e.g. around core H6 and towards the south). This is more apparent in $C^{18}O$ $(1-0)$ as it traces the lower-density, highly-abundant gas. However, in the south and central regions, the N_2H^+ line profiles are very similar to those presented by the $C^{18}O$ spectra. Given that both the $C^{18}O$ $(1-0)$ and the isolated component of N_2H^+ $(1-0)$ are typically optically thin (see Section 2.3.2), the similarity between the spectral profiles is unlikely to be the result of self-absorption. In particular, the profiles of the N_2H^+ $(1-0)$ spectra around the H6 region, with a prominent blue peak and "red shoulder", are simply due to the superposition of different velocity components (see offsets (-7.5″, 8″), (-7.5″, 20″), (5.5″, 8″), and (5.5″, 21″)), and are not due to infall motions (Evans 1999, Myers *et al.* 2000).

A more detailed view of the gas distribution can be found in Figure 2.15. Here the channel maps of the emission seen in N_2H^+ $(1-0)$ (F_1, F = 0,1 → 1,2) and $C^{18}O$ $(1-0)$, between ∼42 and 48 km s^{-1}, integrated in velocity increments of 0.2 km s^{-1} are presented, superimposed on the mass surface density map. It is evident that the emission from different velocity components is morphologically distinct. The first of these components (Filament 1) can be seen between ∼42 and 44 km s^{-1}. In $C^{18}O$ $(1-0)$ the component is seen to run from north-east to

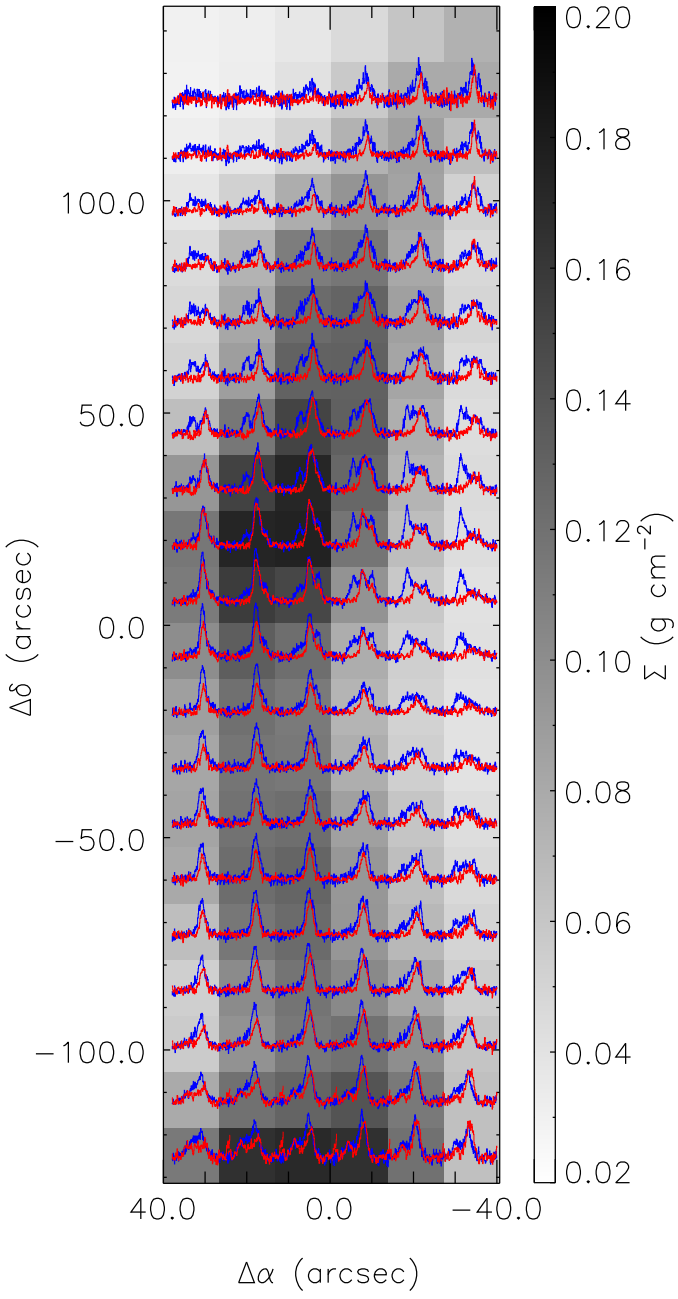

Figure 2.14: Spectra of the (Red) N_2H^+ $(1-0)$ isolated hyperfine component and (Blue) $C^{18}O$ $(1-0)$ at all positions in the cloud, overlaid on the mass surface density map of KT13 (smoothed to an equivalent resolution). Spectra are shown between 41-49 km s^{-1} and -0.1–1.2 K. The intensity of the N_2H^+ $(1-0)$ spectra have been multiplied by a factor of 2 for clarity.

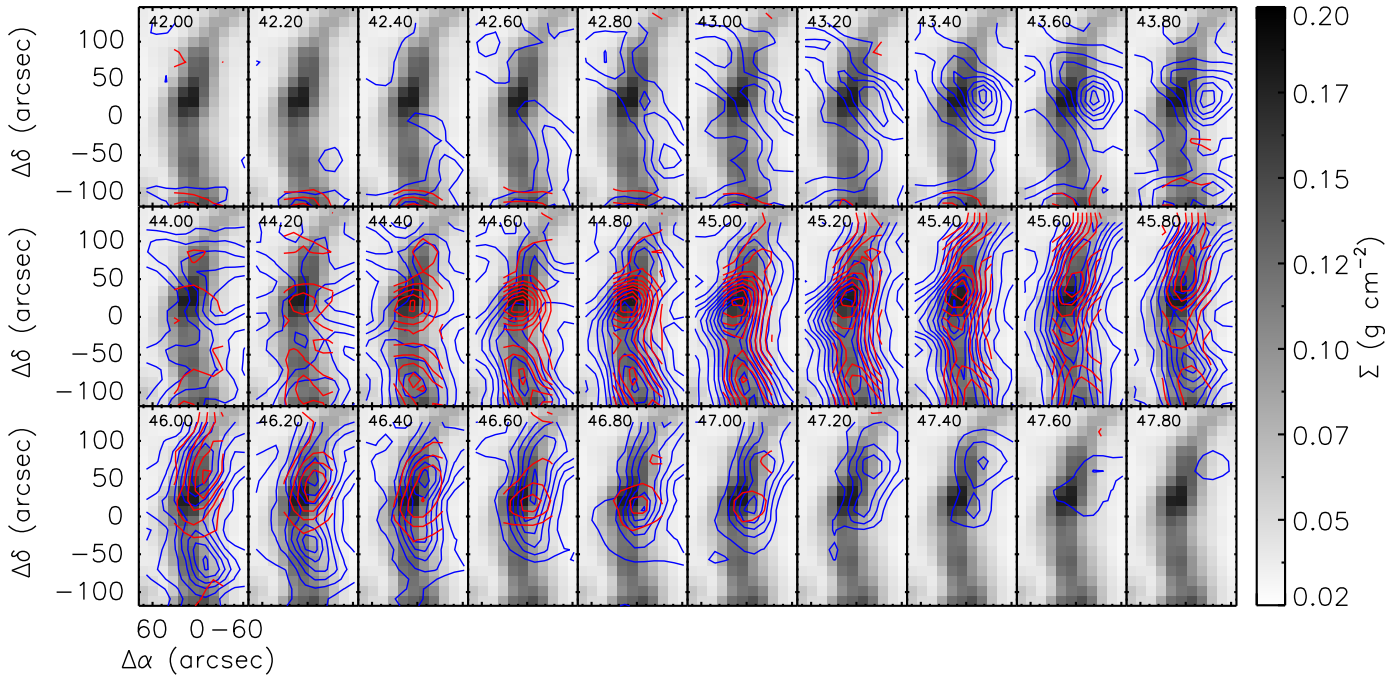

Figure 2.15: Channel maps of (Red) N_2H^+ $(1-0)$ isolated hyperfine component and (Blue) $C^{18}O$ $(1-0)$, overlaid on the mass surface density map. The intensity has been integrated in velocity increments of 0.2 km s^{-1} (velocity in top left corner represents the lower integration limit). In both cases, contours start from 3σ and increase in $3\,\sigma$ steps ($3\,\sigma \sim 0.02$ K km s^{-1} and 0.04 K km s^{-1} for N_2H^+ and $C^{18}O$, respectively).

south-east, curving to the west toward the centre of the map. The N_2H^+ $(1-0)$ emission in this component is restricted to the most southern portion of the cloud. The gas distribution changes shape between $\sim$44 and 46 km s^{-1} (Filament 2), peaking towards the positions of the massive cores (see white crosses in Figure 2.4 for locations). The N_2H^+ $(1-0)$ follows the morphology of Filament 2, and is extended over the whole filament, indicating the presence of widespread dense gas. Both species follow the shape of the extinction map, from north-west to the south, curving slightly to the east. Finally, another component is evident between $\sim$46 and 48 km s^{-1} (Filament 3). This emission overlaps spatially, and is *similar* in morphology to the previous component (although the emission peaks are offset by $\sim$a beam size). This makes the two components difficult to disentangle. However, given that this component appears as a well defined feature in both the spectra (Figure 2.14), and the channel maps (Figure 2.15), it is considered to be a separate velocity component.

2.5.2 Position-velocity analysis

Figure 2.16 shows position-velocity (PV) diagrams of both species (N_2H^+ $(1-0)$ (F_1, F = 0,1 $\rightarrow$ 1,2) in red, and $C^{18}O$ $(1-0)$ in grey-scale), slicing the cloud from north to south, at each offset right ascension in the N_2H^+ $(1-0)$ map. The three velocity components identified in Figure 2.15 are evident in the PV maps. Towards the west of the cloud ($\Delta\alpha$ = -33.5″), the N_2H^+ $(1-0)$ emission follows the $C^{18}O$ $(1-0)$ emission in both the north ($\sim$46.1 km s^{-1}) and south ($\sim$45.0 km s^{-1}). This velocity difference occurs over a distance of $\sim$1.5 pc (angular distance estimated from the 6 σ emission contour; $\sim$110″, between -70″ $< \Delta\delta <$ 40″). As Filament 2

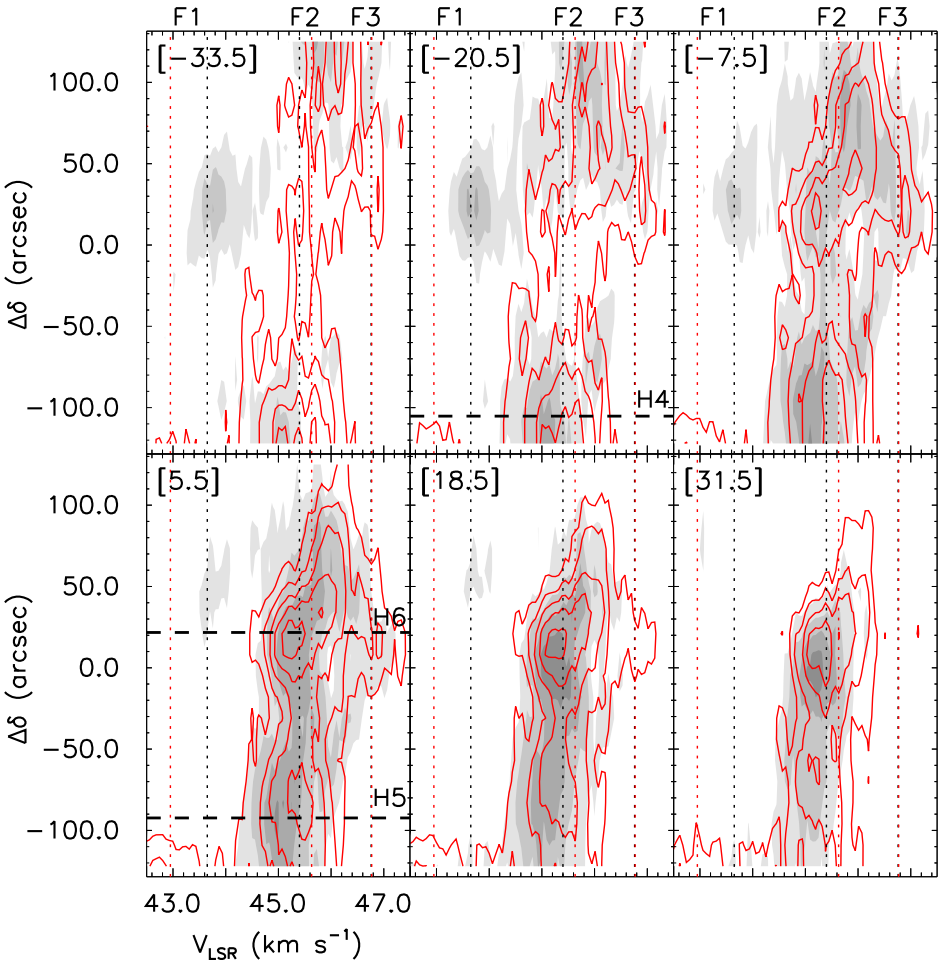

Figure 2.16: Position-Velocity diagrams of both (Red) N_2H^+ $(1-0)$ (F_1, F = 0,1 $\rightarrow$ 1,2) isolated component and (Grey-scale) $C^{18}O$ $(1-0)$. Cuts are taken from north to south through the cloud at each offset right ascension (see top-left of each panel). Emission in N_2H^+ $(1-0)$ and $C^{18}O$ $(1-0)$ is plotted from 3σ ($\sigma \sim 0.06$ K for N_2H^+, and $\sigma \sim 0.14$ K for $C^{18}O$; taken as the mean spectral RMS in both species), and increases in 3σ steps. Vertical dotted lines refer to the centroid velocities derived from the GGF (see Appendix A.1). Horizontal dashed lines at offsets $\Delta\alpha$ = -20.5 and 7.5, at $\Delta\delta$ = -105.3, -92.3, and 21.7, refer to the positions of cores H4, H5, and H6 (the quoted $\Delta\alpha$ values are -16.3, 4.4, 3.0; BT12).

covers the full extent of the map (see Figure 2.15), this velocity difference is interpreted as a gradient rather than the influence of multiple components (Filament 3 appears as a *separate* high-velocity, 46.8 $\mathrm{km\,s^{-1}}$, emission peak at $\Delta\delta \sim 40''$). This gradient therefore has a magnitude of $\sim 0.7\ \mathrm{km\,s^{-1}\,pc^{-1}}$. Such a small gradient is comparable to those found in low-mass cores (e.g. Caselli *et al.* 2002a), but here it is seen over a significantly larger extent. Within the $\Delta\alpha$ = -7.5″ slice, the large-scale gradient observed in N_2H^+ emission appears as a discontinuity in velocity at the location of H6. There is a change in velocity of $\sim 0.6\ \mathrm{km\,s^{-1}}$ over a distance of $\sim 0.5\,\mathrm{pc}$ (estimated from the centres of the two $12\,\sigma$ peaks), implying a velocity gradient of 1.2 $\mathrm{km\,s^{-1}\,pc^{-1}}$. Velocity discontinuities such as this have been explained as accretion signatures in other regions of intermediate-to-high-mass star formation (e.g. Peretto *et al.* 2006). Additional observations of known infall tracers would be needed to confirm this.

Towards the centre of the cloud ($\Delta\alpha$ = -20.5″ and -7.5″), the emission is stronger (max intensity of N_2H^+ $(1-0)$ (F_1, F = 0,1 → 1,2) at -33.5″ = $0.82\,\mathrm{K\,km\,s^{-1}}$ compared to $1.25\,\mathrm{K\,km\,s^{-1}}$ at 5.5″). The emission is also spread over a large velocity range ($\sim 3.5\ \mathrm{km\,s^{-1}}$). Filament 1 is most prominent in the slices -33.5 < $\Delta\alpha$ < -7.5″, whereas Filament 3 is most prominent between -20.5″ < $\Delta\alpha$ < 5.5″. This makes sense given the morphology of the filaments seen in Figure 2.15, in which Filament 1 bends to the west of the cloud. Core H6 lies between -7.5″ < $\Delta\alpha$ < 5.5″ at $\Delta\delta = 20''$. At this offset, all three components are visible, with Filament 2 being the most prominent in N_2H^+ $(1-0)$. The spatial coincidence of all three filaments at the location of H6 can also be seen in Figure 2.15. The spatial coincidence of the velocity components at the locations of the most massive cores in the region (as well as emission features merging in velocity; see Figure 2.15), may be indicative of

interaction/merging between filaments (as first suggested in Jiménez-Serra *et al.* 2010).

2.5.3 Centroid velocity and line-width

The centroid velocity and line-width of the filamentary structures associated with G035.39-00.33 can be extracted by fitting multiple Gaussian profiles simultaneously to the spectral features. To do this, a simple fitting routine was developed: the Guided Gaussian Fit (hereafter, GGF). The details of this fitting routine are outlined in Appendix A.1.

Figure 2.17 shows the centroid velocity map of Filament 2 in N_2H^+ $(1-0)$ (F_1, F = 0,1 $\rightarrow$ 1,2) and $C^{18}O$ $(1-0)$, as derived from the GGF method. The velocity field in both species follows a similar pattern, there is a distinct velocity shift of $\sim 0.5\,\mathrm{km\,s^{-1}}$ from low-velocity ($45.4\,\mathrm{km\,s^{-1}}$) south of H6, to high-velocity ($45.9\,\mathrm{km\,s^{-1}}$) north of H6. This velocity shift occurs within a single beam width, corresponding to a local velocity gradient of $\sim 1.5\,\mathrm{km\,s^{-1}\,pc^{-1}}$. This feature appeared as a velocity discontinuity in the PV diagrams of Figure 2.16. The perceived "jump" in velocity may be a resolution effect, and higher angular resolution observations would be needed to confirm whether the change happens smoothly. The abrupt (but relatively small) velocity change is common to both the dense material and the lower density envelope, which implies it originates from the larger scale structure of the cloud.

South of H6 the velocity structure appears relatively uniform, although there is some evidence for variation on local scales. For example, there is a local increase in velocity in both species at offset (0″,-30″), increasing from ~ 45.25 $\mathrm{km\,s^{-1}}$ in the

surrounding area, to 45.5 $\mathrm{km\,s^{-1}}$ towards the centre. This location coincides with a peak in N_2H^+ $(3-2)$ emission (see Figure 2.5) and is not directly associated with any 4.5, 8, or 24 μm emission, indicating the presence of dense, quiescent gas.

Figure 2.17 also shows the N_2H^+ $(1-0)$ and $C^{18}O$ $(1-0)$ line-width (FWHM) maps of Filament 2, as derived from the GGF method. Adopting an average kinetic temperature of 15 K (Nguyen Luong *et al.* 2011 and Section 2.4.2), the thermal width ($\Delta v_{\mathrm{T}}^2 = 8\ln(2)\,\sigma_{\mathrm{T}}^2$, whereby $\sigma_{\mathrm{T}} = \sqrt{(k_{\mathrm{B}}T/m_{obs})}$, k_{B} is the Boltzmann constant, T is the kinetic temperature of the gas, and m_{obs} is the mass of the observed species = 29 a. m. u. and 30 a. m. u. for N_2H^+ and $C^{18}O$, respectively) for both species is $\sim 0.15\,\mathrm{km\,s^{-1}}$ ($\sigma_{\mathrm{T}} \sim 0.07$ $\mathrm{km\,s^{-1}}$). For $T \sim 15$ K, the isothermal sound speed is $c_{\mathrm{s}} \sim 0.23$ $\mathrm{km\,s^{-1}}$ (given a mean mass per molecule of 2.33 a. m. u.), which corresponds to a Gaussian FWHM of 0.54 $\mathrm{km\,s^{-1}}$. It is evident therefore that the observed line-widths range from approximately transonic (i.e. in the north of G035.39-00.33, where $\sigma_{\mathrm{obs}}/c_{\mathrm{s}} = 1$) to supersonic, $\sigma_{\mathrm{obs}}/c_{\mathrm{s}} \sim 4.5$.

On average, $C^{18}O$ $(1-0)$ and N_2H^+ $(1-0)$ line-widths have similar values. This is in contrast to low-mass star-forming regions. Here, $C^{18}O$ $(1-0)$ is typically found to be broad in comparison to high-density gas tracers (by a factor between 1.5 and 2; e.g. Fuller & Myers 1992, Hacar & Tafalla 2011). However, in G035.39-00.33 this is consistent with the finding that N_2H^+ is widespread across the filament and not preferentially tracing dense *cores* as in low-mass star-forming regions (see Figure 2.4). In both species, the line-widths are narrower towards the northern portion of the cloud and (to a lesser extent) towards H6, indicating the presence of relatively quiescent gas (of lower turbulent content). The mean line-width values for each filament are 1.53 $\mathrm{km\,s^{-1}} \pm 0.46$ $\mathrm{km\,s^{-1}}$, 1.22 $\mathrm{km\,s^{-1}} \pm 0.07$ $\mathrm{km\,s^{-1}}$, and 1.07 $\mathrm{km\,s^{-1}} \pm 0.12$ $\mathrm{km\,s^{-1}}$, for N_2H^+. For $C^{18}O$ the

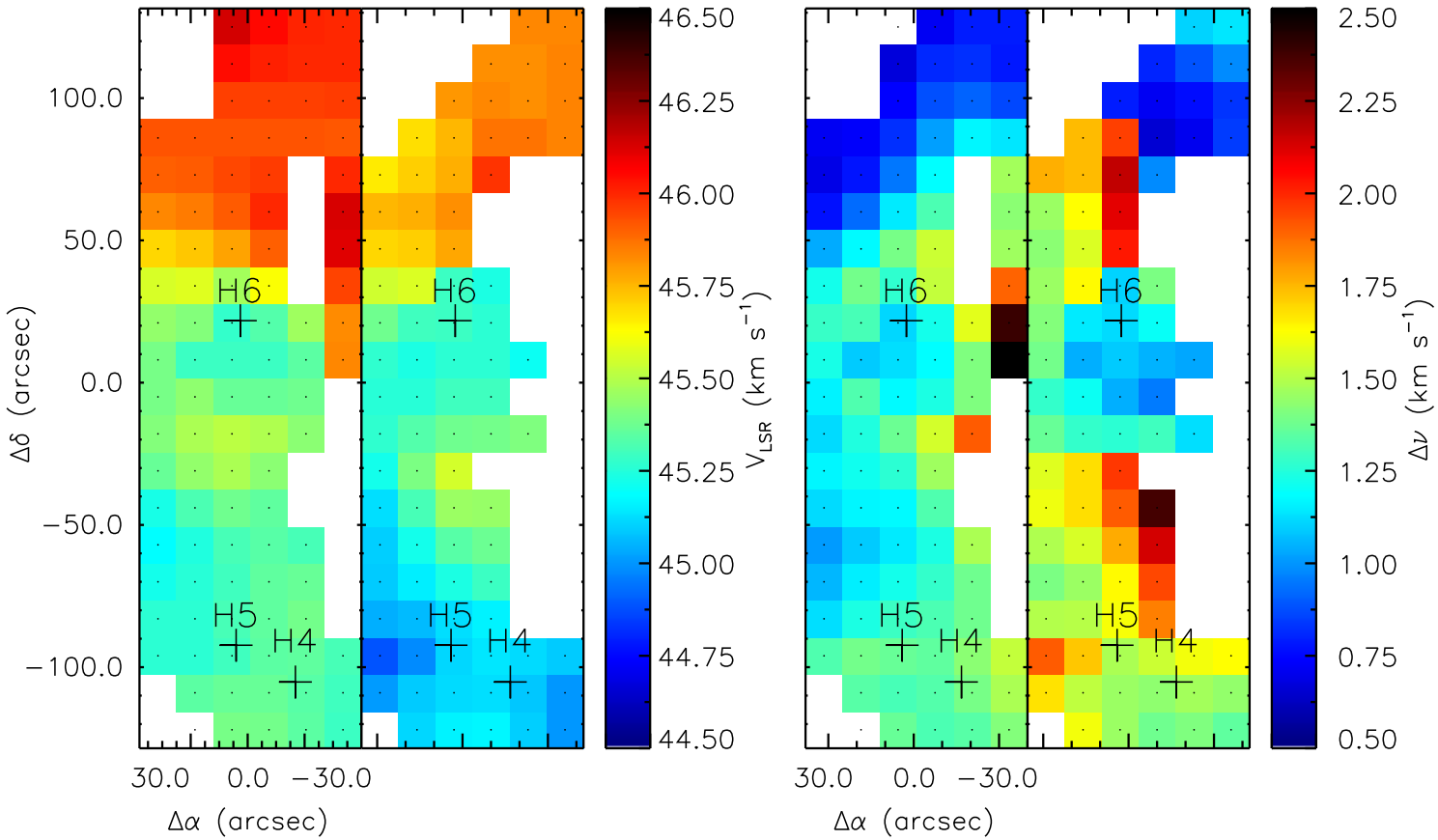

Figure 2.17: V_{LSR} and Δv maps of Filament 2, as derived from the Guided Gaussian Fits (see Appendix,A.1). Maps on the left represent the V_{LSR} of (Left) N_2H^+ $(1-0)$ and (Right) $C^{18}O$ $(1-0)$. Maps on the right represent the line-width, Δv of (Left) N_2H^+ $(1-0)$ and (Right) $C^{18}O$ $(1-0)$. Black crosses indicate the positions of the massive cores from BT12.

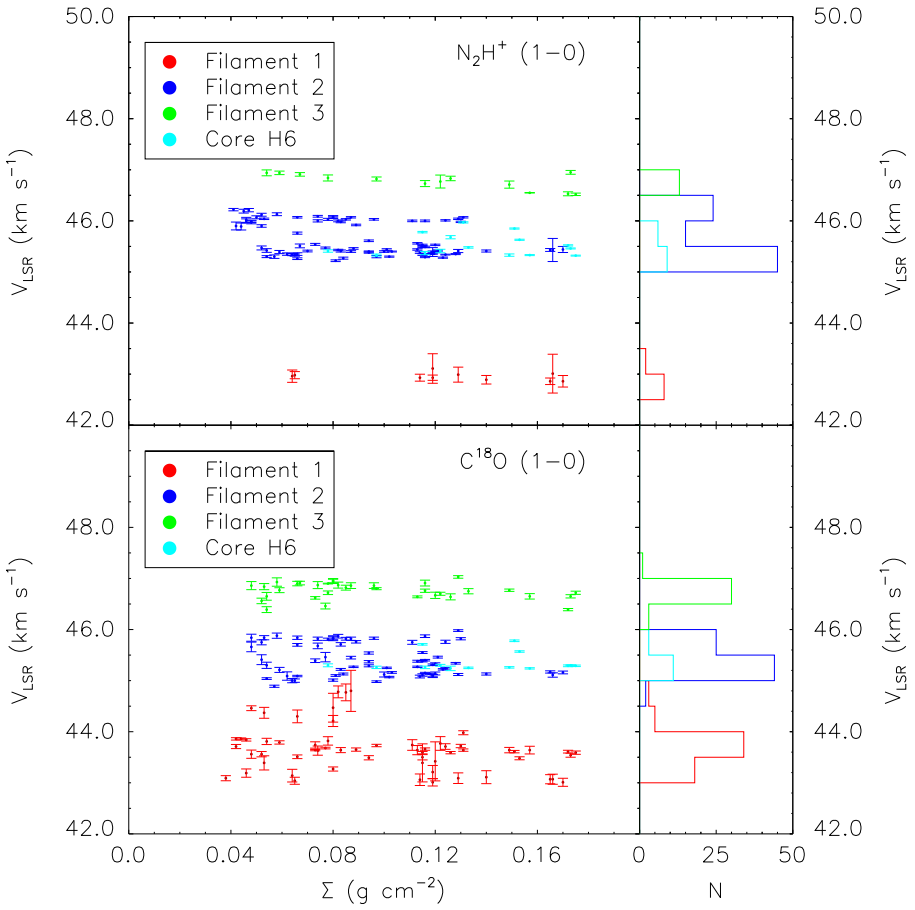

Figure 2.18: $V_{\rm LSR}$ of the individual velocity components as a function of mass surface density for (Top) N_2H^+ $(1-0)$ and (Bottom) $C^{18}O$ $(1-0)$. The right of each plot shows a histogram of the $V_{\rm LSR}$ information. The uncertainty in the $V_{\rm LSR}$ is derived from the Gaussian fits. The uncertainty in Σ is not shown, but is estimated to be $\sim 30\%$ (KT13).

mean line-width values are $1.54\ {\rm km\,s^{-1}} \pm 0.20\ {\rm km\,s^{-1}}$, $1.42\ {\rm km\,s^{-1}} \pm 0.07\ {\rm km\,s^{-1}}$, and $1.09\ {\rm km\,s^{-1}} \pm 0.10\ {\rm km\,s^{-1}}$, for Filaments 1, 2, and 3, respectively.

Figure 2.18 displays the $V_{\rm LSR}$ of the isolated component of N_2H^+ $(1-0)$ and $C^{18}O$ $(1-0)$ as a function of mass surface density. The three filaments are clearly seen as well-separated velocity components. The average velocities of the individ-

ual components differ slightly between the two species. The mean $V_{\rm LSR}$ observed for each filament in N_2H^+ is 42.95 km s^{-1}±0.17 km s^{-1}, 45.63 km s^{-1} ± 0.03 km s^{-1}, and 46.77 km s^{-1} ± 0.06 km s^{-1}, for Filaments 1, 2, and 3, respectively. For $C^{18}O$ the mean $V_{\rm LSR}$ values are, 43.65 km s^{-1} ± 0.12 km s^{-1}, 45.40 km s^{-1} ± 0.03 km s^{-1}, and 46.76 km s^{-1} ± 0.05 km s^{-1}, for Filaments 1, 2, and 3, respectively.

The abrupt change in velocity observed in Filament 2 (Figure 2.16 and 2.17) is seen in Figure 2.18 as the "gap" between the two groups of blue points. Some of the velocities associated with H6 are filling this gap, suggesting that this core may have formed at the interface of material moving at different velocities.

It is noted from Figure 2.18 that the relative velocity between Filament 2 and 1 ($\sim$2.68 km s^{-1}, and 1.75 km s^{-1}, for N_2H^+ and $C^{18}O$, respectively) is larger than that between Filament 2 and 3, in both species ($\sim$1.14 km s^{-1}, and 1.36 km s^{-1}, for N_2H^+ and $C^{18}O$, respectively). In addition, the relative velocity difference between Filaments 2 and 1 is greater for N_2H^+ than it is for $C^{18}O$. This may explain the velocity difference in peak emission observed in Figure 2.3 (see also Figure 2.14). The observed velocity shift is quantified in the next section.

2.5.4 The N_2H^+–$C^{18}O$ velocity shift

Figure 2.19 is a map of the $N_2H^+ - C^{18}O$ velocity shift measured across Filament 2, overlaid with contours of SiO $(2-1)$ from Jiménez-Serra *et al.* (2010). The N_2H^+ $(1-0)$ emission is largely red-shifted with respect to the $C^{18}O$ $(1-0)$ emission (positive values). The largest velocity shifts are seen to the north and south of the cloud. North of offset $\Delta\delta$ = 86.0, the average velocity shift is 0.22 ± 0.04 km s^{-1}, and south of offset $\Delta\delta$ = -70.0″, it is found to be 0.26 ± 0.04 km s^{-1}, between these

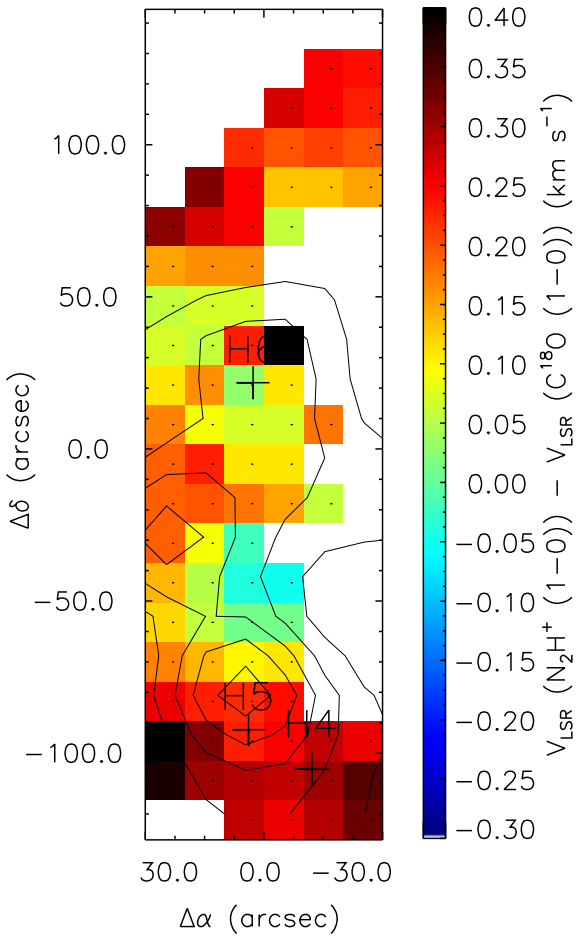

Figure 2.19: Map of the velocity shift between N_2H^+ $(1-0)$ and $C^{18}O$ $(1-0)$ shown for Filament 2 only. Overlaid in black contours is the SiO $(2-1)$ emission. Contours are 3σ to $0.5\,\mathrm{K\,km\,s^{-1}}$ in steps of 3σ ($\sim 0.1\,\mathrm{K\,km\,s^{-1}}$). Black crosses refer to the positions of the massive cores from BT12.

offsets, the velocity shift $0.13 \pm 0.04\,\mathrm{km\,s^{-1}}$. No correlation is found between the velocity shift and the SiO $(2-1)$ integrated intensity. The mean value of this velocity shift is $0.18 \pm 0.04\,\mathrm{km\,s^{-1}}$. Although the velocity shift is small (of the order of the sound speed for a 15 K gas), it is *systematically* skewed to positive values.

Figure 2.20 shows the velocity difference between N_2H^+ and $C^{18}O$ as a function

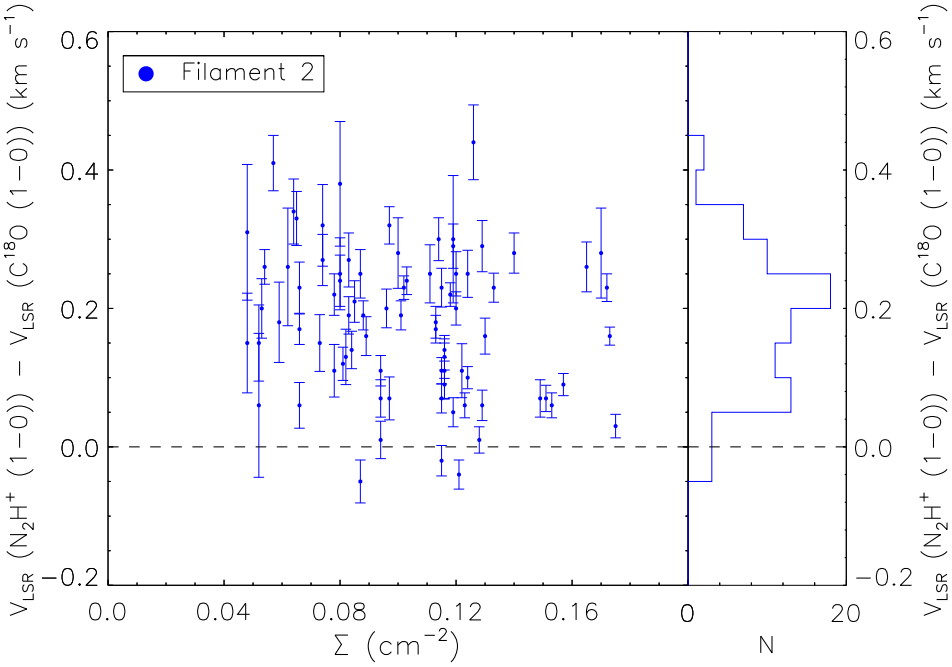

Figure 2.20: Velocity shift between N_2H^+ $(1-0)$ and $C^{18}O$ $(1-0)$ as a function of mass surface density. The right of the plot shows a histogram of this velocity shift information. The uncertainty in Σ is not shown, but is estimated to be $\sim 30\%$ (KT13).

of mass surface density. No correlation is found, but the shift is clearly present across the whole filament. The fact that this velocity shift is seen over the full extent of the cloud, and that the N_2H^+ $(1-0)$ is systematically red-shifted with respect to the $C^{18}O$ $(1-0)$, suggests that this shift is not the result of *random* (turbulent) motions. In addition, given that both the isolated component of N_2H^+ $(1-0)$ and $C^{18}O$ $(1-0)$ are expected to be optically thin (see Section 2.3.2), this feature is unlikely to be due to the influence of opacity on the line profiles.

The velocity shift is not constant along the filament. Figure 2.21 shows the $N_2H^+ - C^{18}O$ velocity difference as a function of declination along the four central

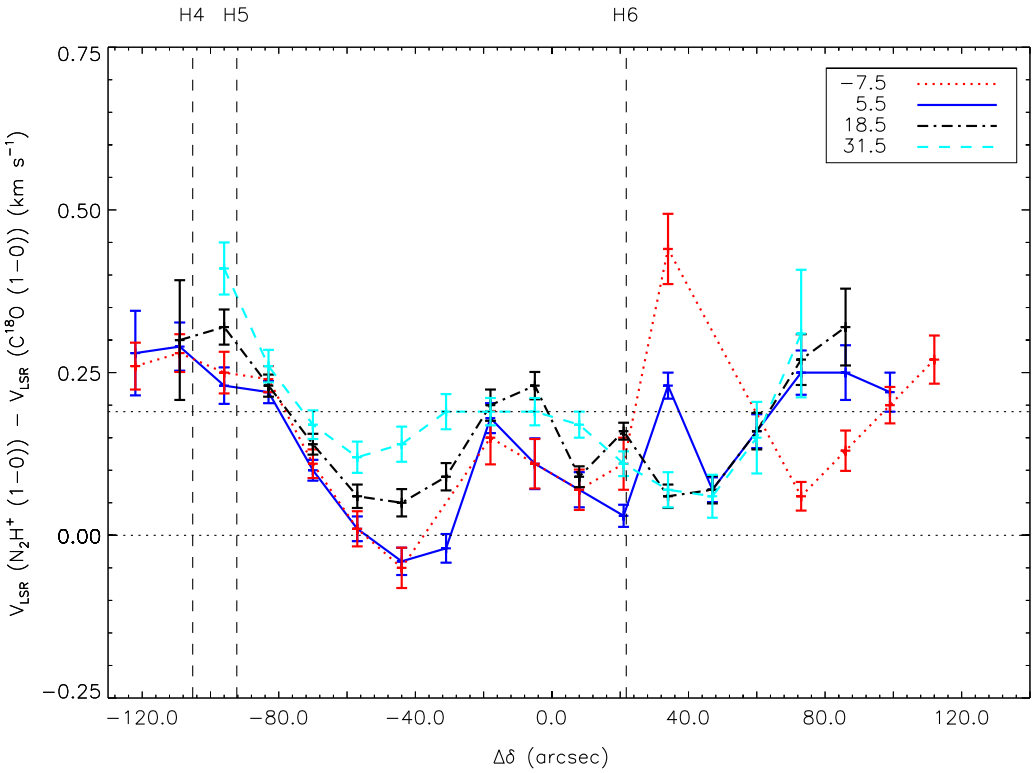

Figure 2.21: Velocity shift between N_2H^+ $(1-0)$ and $C^{18}O$ $(1-0)$ as a function of offset in declination along four strips of constant right ascension (see legend in top right). The blue line refers to the strip passing closer to the center of core H6. Horizontal dotted lines correspond to the mean values of the velocity shift, $0.18\pm0.04\,\mathrm{km\,s^{-1}}$, and the zero line. Vertical dotted lines indicate the positions in offset declination of the three massive cores from BT12.

strips at fixed right ascension offsets -7.5″, 5.5″, 18.5″ and 31.5″. From this figure it is clear that the shifts in the north and south have similar magnitudes, while variations are present in between. The variations along the four strips appear similar from the south, up to $\Delta\delta\sim$-80″, where the magnitude of the velocity shift observed in the central and eastern portions of the map diverges. Towards $\Delta\delta\sim$-40″ the velocity shift remains around ~0.2 km s^{-1} in the east, whereas no velocity shift is seen in the central regions. To the north of H6 ($\Delta\delta\sim35''$) the strip at

$\Delta\alpha$ = -7.5″ (and to a lesser extent the strip passing through the peak of core H6) show different behaviour to the outer strips at $\Delta\alpha$ = 18.5″ and 31.5″, respectively. This is the declination at which the abrupt change in velocity is observed (see Figure 2.17). At $\Delta\delta$ = -40″ (in the $\Delta\alpha$ = -7.5″ and 5.5″ strips), and at the peak of core H6, there appears to be little velocity shift. However, these locations are surrounded by sharp variations. This is especially evident toward core H6. A discussion on a possible origin of this velocity shift can be found in Section 2.6.

2.6 Discussion

2.6.1 Are the filaments of G035.39–00.33 interacting?

A possible explanation for the observed velocity shift between the N_2H^+ $(1-0)$ and $C^{18}O$ $(1-0)$ of Filament 2, is that there is relative motion between the IRDC filament (as traced by N_2H^+ emission), and its lower-density "envelope" (as traced by the highly-abundant $C^{18}O$ emission).

The velocity shift between cores and their respective envelopes has been studied towards low-mass star forming regions. In general, it has been found that cores, and the envelopes they are embedded within, are *velocity coherent* (e.g. Hacar & Tafalla 2011, Kirk *et al.* 2007, Walsh *et al.* 2004). This term is used to describe regions where the motions of cores, with respect to their surrounding envelope, are smaller in magnitude than those described by the thermal sound speed (~ 0.2 km s^{-1}). Hacar & Tafalla (2011) studied the centroid velocities of N_2H^+ $(1-0)$ and $C^{18}O$ $(1-0)$ in L1517, and found a good match between the two tracers. The implication of this is that star-forming cores have little relative motion with respect to their natal filaments.

In the case of G035.39-00.33, it is clear that N_2H^+ $(1-0)$, and to some extent N_2H^+ $(3-2)$, are tracing *extended* structures, and not just cold, dense cores (see Figures 2.4 and 2.5). This implies that any observed velocity shift would be a feature of the large-scale structure of G035.39-00.33.

The channel maps in Figure 2.15 clearly show that significant N_2H^+ $(1-0)$ emission is present over a narrower range of velocities compared to that of the $C^{18}O$ $(1-0)$. In particular, at the lowest velocities identified with Filament 1 (between 42 and 44 km s^{-1}), N_2H^+ is practically undetected along most of the

filament. Whereas Filament 3 (between 46 and 48 $\mathrm{km\,s^{-1}}$) exhibits significant N_2H^+ $(1-0)$ emission up to 47 $\mathrm{km\,s^{-1}}$. In addition, Figure 2.15 shows that at the locations of the most massive cores appear at the interface of multiple velocity components, and that there are no clear boundaries in velocity between filaments (this is clearly evident in the case of $C^{18}O$). It was suggested in Section 2.5.1, that this may support the idea that filaments are merging, as first suggested by Jiménez-Serra *et al.* (2010) as an explanation for the widespread detection of SiO emission across G035.39-00.33.

It is speculated that the observed velocity shift between N_2H^+ and $C^{18}O$ may be result of merging filaments in G035.39-00.33. Filament 3 is of higher density than Filament 1 (supported by the observed widespread detection of $C^{18}O$ emission, in the absence of N_2H^+, across Filament 1), which would imply that Filament 3 is more massive than Filament 1 (over the same spatial extent). Filament 3 would therefore be more effective at "sweeping-up" material during any interaction. This may lead to an asymmetric distribution of material along the line of sight, with a greater amount of low-density material residing at low-velocities. This would imply a blue-shift of the $C^{18}O$ line, as is observed (see Figure 2.20). The variation in the magnitude of this velocity shift across the map may by explained by inhomogeneities along the interacting Filaments 1 and 3. The merger scenario is sketched in Figure 2.22.

2.6.2 The Dynamical evolution of G035.39–00.33

The high-sensitivity and high-spectral resolution maps in both N_2H^+ $(1-0)$ and $C^{18}O$ $(1-0)$ have revealed that the dense gas of the G035.39-00.33 is surrounded

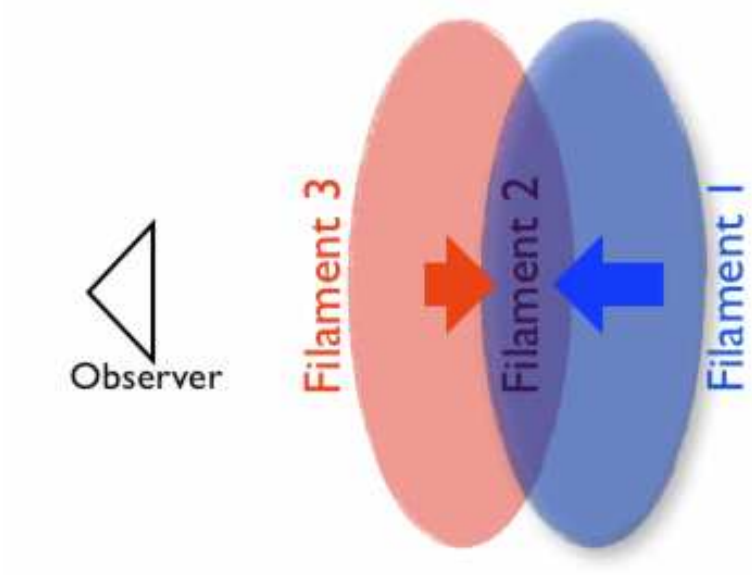

Figure 2.22: Schematic figure illustrating the kinematics of G035.39-00.33.

by complex, lower-density filamentary structures moving at relative velocities of a few $\mathrm{km\,s^{-1}}$.

Hernandez *et al.* (2012) suggested that the filamentary complex was in near virial equilibrium. It should take at least a single crossing time for a structure to reach virial equilibrium. The crossing time is estimated using $t_{\mathrm{cross}} = 2R_{\mathrm{f}}/\sigma_{\mathrm{f}}$, whereby R_{f} is the radius of the filament (Hernandez *et al.* 2012 use their "inner" filament radius, corresponding to the peak in extinction $= 0.465\,\mathrm{pc}$), and $\sigma_{\mathrm{f}} \sim 1.08\ \mathrm{km\,s^{-1}}$ (the velocity dispersion of the inner filament after applying a correction for the envelope; Hernandez *et al.* 2012). The crossing time is therefore $t_{\mathrm{cross}} \sim 0.8\,\mathrm{Myr}$.

Is this time-scale consistent with the build up dense gas at the intersection point of two lower-density structures? If filament merging is responsible for the observed increase in density of the central IRDC (and in particular, towards the

most massive cores), it is possible to estimate the time it would take to create the observed density contrast using (McKee & Ostriker 2007):

$$t_{\rm accum} = \frac{\Sigma_{\rm f}}{v_{\rm flow}\rho_{\rm H,flow}} \tag{2.13}$$

where $\Sigma_{\rm f}$ is the final mass surface density of the filament, $\rho_{\rm H,flow}$ is the mean mass density of the merging Filaments, 1 and 3, and $v_{\rm flow}$ is the relative merger velocity. This equation can be further expressed as:

$$t_{\rm accum} \sim 2\frac{R_{\rm f}}{v_{\rm flow}}\frac{n_{\rm H,f}}{n_{\rm H,flow}} \rightarrow$$
$$2.0\left(\frac{R_{\rm f}}{0.5\,{\rm pc}}\right)\left(\frac{v_{\rm flow}}{5\,{\rm km\,s^{-1}}}\right)^{-1}\left(\frac{n_{\rm H,f}/n_{\rm H,flow}}{10}\right){\rm Myr}, \tag{2.14}$$

where $R_{\rm f}$ is the radius of the filament, here normalized to 0.5 pc, i.e. $36''$ (i.e. close to the 10σ level of N_2H^+ in Figure 2.4, and the inner filament radius reported in Hernandez *et al.* 2012). Assuming that the velocity components in the plane of the sky have similar magnitudes, this implies a collision velocity of $v_{\rm flow} \sim 5\,{\rm km\,s^{-1}}$. Finally, in Section 2.4.2 the volume density of Filament 2 was estimated to be $\sim 4 \times 10^4\,{\rm cm^{-3}}$. Jiménez-Serra *et al.* (2014) estimate a volume density of $\sim 5.1 \times 10^3$ for Filament 1 (the lowest density filament). Assuming that this is representative of the pre-collision density, a density contrast of ~ 10 is used in the above calculation.

It is therefore estimated that the merger of two structures moving with a relative speed of 5 $\rm km\,s^{-1}$ would be sufficient to produce a factor of 10 increase in the number density over a region ~ 1 pc in scale, in ~ 2 Myr. Since $t_{\rm accum} > t_{\rm cross}$ this is consistent with the suggested state of near virial equilibrium Hernandez *et al.*

(2012).

It should be noted that the ratio of the mean densities is difficult to estimate. In this analysis it is assumed that the density of the inner IRDC is similar to that estimated in Section 2.4.2, whereas the pre-collision densities are similar to those estimated for Filament 1 (Jiménez-Serra *et al.* 2014). Hernandez *et al.* (2012) estimated a density contrast of a factor of $\sim$3–4 for the case of the inner filament and its immediate envelope. The volume density measured towards the H6 region in Hernandez *et al.* 2012 is $n_{\rm H_2} \sim 1 \times 10^4\,{\rm cm}^{-3}$. The factor of ~ 4 difference in central density presented here may be a result of using N_2H^+ for the analysis, since the volume density estimated in Section 2.4.2 is restricted to regions of particularly high density, as traced by N_2H^+ $(3-2)$. A density contrast of ~ 4 in Equation 2.14 is therefore likely to be a lower limit to the ratio used in Equation 2.14 and results in $t_{\rm accum} \sim t_{\rm cross} \sim 0.8\,{\rm Myr}$.

The above evidence therefore appears consistent with a scenario in which the density fluctuations observed throughout G035.39-00.33 have been produced due to the merging of several velocity coherent filaments. In particular, this may be responsible for the localised density increase towards H6. Star formation induced as a result of merging filamentary structures has been suggested in other star-forming regions, for instance in the massive star-forming region W33A (Galván-Madrid *et al.* 2010), in the low-mass star-forming region Serpens (Duarte-Cabral *et al.* 2011), and in the L1641-N region (Nakamura *et al.* 2012).

However, it is also noted that the kinematics of G035.39-00.33 are relatively quiescent (at least on these large spatial scales). Toward the northern portion of the IRDC, where star formation activity is at a minimum (see Figure 2.5), the line-widths are similar to the thermal width for a 15 K gas (see Section 2.5.3

and Figure 2.17). Here, $C^{18}O$ $(1-0)$ line widths become close to $0.5\,\mathrm{km\,s^{-1}}$, similar to those measured in low mass star-forming regions (e.g. Fuller & Myers 1992). Where the interaction is expected to be more prominent, the line-widths are notably broader, with $\sigma_{\mathrm{obs}}/c_{\mathrm{s}} \sim 2$–$4$, however this might be explained by embedded (but not yet prominent) star formation activity (see also Devine *et al.* 2011, Ragan *et al.* 2012).

In addition, although velocity gradients are observed, they are small in magnitude ($\sim 1\ \mathrm{km\,s^{-1}\,pc^{-1}}$, see Section 2.5.3). Schneider *et al.* (2010a) identify the presence of variable velocity gradients throughout the DR21 star forming ridge. These velocity gradients are prone to changes in direction. It is suggested that such gradients may be produced during the collision of atomic flows, whereby different regions retain the signature of the external flow that has formed them (Ballesteros-Paredes *et al.* 1999). In this scenario, the complexity in the velocity field arises because of inhomogeneities in the clumpy cloud structure and/or flows.

The quiescent velocity structure of G035.39-00.33 suggests that if filaments are merging, then this interaction must be relatively "gentle" (in comparison to the highly dynamical formation mechanisms of molecular clouds that discuss collisions of relative velocity $\sim 10\ \mathrm{km\,s^{-1}}$, see Chapter 1, Section 1.1.2). Jiménez-Serra *et al.* (2014) discussed the prospect that Filaments 1, 2, and 3 formed from a single turbulent cloud, and the subsequent convergence of the filaments occurs as the parent cloud collapses. The representative velocity of the interaction would then be given by the free-fall velocity of the cloud, $v_{\mathrm{ff}} \sim 2\ \mathrm{km\,s^{-1}}$, i.e. close to the observed value (Jiménez-Serra *et al.* 2014). This *may* indicate that the merging of filamentary components in G035.39-00.33 is the result of gravitational collapse, rather than an event triggered by energetic phenomena such as, for example, expanding H II

regions, or supernovae bubbles (Heitsch *et al.* 2008).

One possible way to corroborate evidence for filament collisions would be to observe other species expected to be abundant in the mantles of CO-rich dust grains. For example CH_3OH may also be expected to be widespread across the cloud in a scenario involving filament mergers. In addition, high-angular resolution observations of shocked gas tracers (such as SiO) are needed in order to rule out a population of lower-mass stars which may also explain the widespread emission of SiO.

2.7 Conclusions

This chapter presents high-sensitivity and high-spectral resolution data of the IRDC G035.39-00.33, selected as it is expected to be in a relatively early stage of formation, and it shows little traces of star formation activity. From this analysis it is concluded that:

1. A total of 3 velocity components are identified in emission from the $J = 1 \rightarrow 0$ transition of both $C^{18}O$ and N_2H^+. The relative velocities between Filaments 1 and 2 in N_2H^+ and $C^{18}O$ are ~ 2.7 km s^{-1}and ~ 1.8 km s^{-1}, respectively. Similarly, the relative velocity between between Filaments 2 and 3 in N_2H^+ and $C^{18}O$ are ~ 1.1 km s^{-1} and ~ 1.4 km s^{-1}, respectively.

2. The mean line-widths observed in N_2H^+ and $C^{18}O$ are similar in all filaments (Filament 2 shows the greatest difference with $\Delta\upsilon_{N_2H^+}/\Delta\upsilon_{C^{18}O} \sim 0.85$). This is in contrast to low-mass star forming regions, and is consistent with the observation that N_2H^+ is widespread within G035.39-00.33 (and is not restricted to star-forming cores). Line-widths indicate the presence of mildly supersonic motions with $\sigma_{obs}/c_s \geq 1$, for a sound speed of 0.23 km s^{-1} at 15 K.

3. Analysis using radiative transfer code, RADEX, gives an average H_2 number density across the IRDC of $\sim 4\times10^4$ cm^{-3} and a mean kinetic temperature of ~ 12 K.

4. There is a local maximum in N_2H^+ emission at the location of the most massive core in the region, H6. This is also spatially coincident with multiple filamentary components. It is speculated that the local density fluctuations

(and, by inference, star formation) observed throughout G035.39-00.33, may be attributed to the merging of filaments.

5. A widespread velocity shift ($\sim 0.2\,\mathrm{km\,s^{-1}}$) is observed between the N_2H^+ $(1-0)$ and $C^{18}O$ $(1-0)$, which may be consistent with the on-going merging of filaments (in which Filament 1 is less massive than Filament 3). The filament merger scenario was first suggested by Jiménez-Serra *et al.* (2010) as a possible explanation for the detection of widespread SiO emission throughout G035.39-00.33. It is estimated that for two filaments merging at a velocity $\sim 5\ \mathrm{km\,s^{-1}}$, it would take $\sim 2\,\mathrm{Myr}$ to induce an order of magnitude increase in the density at their interface.

6. Large-scale velocity coherence (indicated by comparable line widths at most positions, lack of large velocity gradients $< 1\ \mathrm{km\,s^{-1}\,pc^{-1}}$) is evident across G035.39-00.33. If the filament merger scenario is correct therefore, this lack of disturbance would imply that the process is occurring gently.

7. This study has highlighted the importance of high-spectral resolution data of different gas tracers to unveil the kinematics and correctly interpret line asymmetries. Asymmetric blue-peaked profiles found across G035.39-00.33 are due to multiple velocity components along the line of sight. No evidence of large-scale infall motions are found. Higher-angular resolution observations are needed to isolate single centres of accretion (i.e. the star-forming dense cores analogous to the well-studied low-mass cores).

Chapter 3

The dynamical properties of dense filaments in the IRDC G035.39–00.33

3.1 Introduction

One of the many challenges faced by astronomers when attempting to categorise the initial conditions of massive star formation is the inherent *rarity* of these objects (see Section 1.2). Consequently, one must extend the search for *quiescent* massive star forming regions beyond local ($< 500\,\mathrm{pc}$) clouds. This presents a significant technological challenge since greater angular resolution is required in order to study massive star forming environments.

The previous studies in the series of papers dedicated to the investigation of G035.39-00.33, have predominantly focused on data obtained with single-antenna telescopes. As a consequence, this research has been limited to investigating the

large-scale structure of G035.39-00.33. As an example, the beam size of the IRAM 30 m telescope at the frequency of the $J = 1 \rightarrow 0$ transition of N_2H^+ ($\nu_0 = 93173.3637$ MHz; Pagani *et al.* 2009) is $\sim 26''$ (see Table 2.1). Therefore at the distance of G035.39-00.33 (2900 pc; Simon *et al.* 2006b) the spatial resolution is ~ 0.4 pc. Comparing this with the spatial resolution of the 30 m antenna at the distance of Taurus (~ 140 pc; Kenyon *et al.* 1994), ~ 0.02 pc, highlights the fact that equivalent observations are sensitive to very different spatial scales.

Nevertheless, the previous single dish studies have revealed G035.39-00.33 to be an extremely complex structure, consisting of several, morphologically distinct filaments (Chapter 2) exhibiting common velocity gradients (Jiménez-Serra *et al.* 2014). Whilst observations indicate that G035.39-00.33 may be close to virial equilibrium, this remains consistent with the cloud having formed recently (Hernandez *et al.* 2012). The observed widespread CO depletion (Hernandez *et al.* 2011), and N_2H^+ emission (Chapter 2), implies the presence of cold, dense gas that extends over parsec scales. Jiménez-Serra *et al.* (2010) suggested that the presence of widespread SiO emission may be a relic of the cloud formation process, with Chapter 2 and Jiménez-Serra *et al.* (2014) proposing scenarios to explain the observed kinematics and chemistry of the region. The remaining sections of this thesis aim to enhance this project through high-angular resolution interferometric observations.

There are currently few studies dedicated to understanding the internal kinematics of IRDCs at high-angular resolution. Ragan *et al.* (2012) used the Very Large Array (VLA) and Green Bank Telescope (GBT) to study the kinematics of ammonia within a sample of 6 IRDCs down to spatial scales of ~ 0.1 pc. The authors report relatively organised velocity fields, with localised disruptions due to

embedded star formation (observed as changes in the velocity gradients). Such disruptions are also typically combined with an increase in velocity dispersion, which may be indicative of infall or outflow motions. In other high-resolution studies, IRDCs have been found to comprise several velocity components and filaments (Devine *et al.* 2011, Peretto *et al.* 2013).

The focus of this chapter is to study G035.39-00.33 at both high-angular and high-spectral resolution, setting the goal of documenting the kinematic structure of the dense filamentary network that comprises G035.39-00.33. Moreover, this work will be linked to the embedded core population in Chapter 4. The structure of this chapter is as follows: Details of the observations can be found in Section 3.2. Observational results are presented in Section 3.3. The detailed kinematic analysis of these data is presented in Section 3.4. These results are discussed in Section 3.5, and in Section 3.6, the findings are concluded. A detailed step-by-step method of the Gaussian fitting routine, and filament classification algorithm can be found in the Appendix A.2.

3.2 Observations & data reduction

The N_2H^+ observations were carried out using the IRAM Plateau de Bure Interferometer (PdBI), France. A 6-field mosaic has been obtained. The final map area is $\sim 40'' \times 150''$ (corresponding to $\sim 0.6\,\mathrm{pc} \times 2.1\,\mathrm{pc}$, at a distance of 2900 pc). The mosaic covers the inner area of the cloud. The PdBI is suited to observing this long but narrow filament as the width of the filament, traced by N_2H^+ $(1-0)$, is comparable to the primary beam at $\sim 93\,\mathrm{GHz}$ ($\sim 54''$; see Chapter 2, Figure 2.4). Observations were carried out over six days in May, June and October 2011, in the C and D configurations (using 6 and 5 antennas, respectively) offering baselines between 19 m and 176 m to achieve an angular resolution of $\sim 4''$ at $\sim 93\,\mathrm{GHz}$.

The narrow-band correlator was configured to cover the N_2H^+ $(1-0)$ transition (frequency of the isolated, F_1, F = 0,1 $\rightarrow$ 1,2, component = 93176.2522 MHz; Pagani *et al.* 2009), with a bandwidth of 20 MHz. The final spectral resolution is 0.14 $\mathrm{km\,s^{-1}}$. In addition, the WideX correlator was used for the 3.2 mm continuum. The line-free channels gave a total bandwidth of $\sim 3\,\mathrm{GHz}$. System temperatures varied between 125–150 K. In each observation session, phase and amplitude were calibrated using quasars 1749+096 and 1827+062. Bandpass calibration was carried out using 1749+096 on all dates except 03/06/2011 and 06/06/2011, in which 3C454.3 and 3C273 were used, respectively. Flux calibration was carried out using MWC349 (model flux = 1.15 Jy) on all dates. The data reduction was performed using GILDAS[1]/CLIC as part of the GILDAS software.

In addition to the PdBI data, existing IRAM 30 m N_2H^+ $(1-0)$ data has been used to incorporate short-spacing information to the interferometric map. For

[1]GILDAS: Grenoble Image and Line Data Analysis System, see `http://www.iram.fr/IRAMFR/GILDAS`

more details on these data see Chapter 2. The merging of the two data sets was completed within the GILDAS software package, MAPPING, by using 'UVSHORT'. The central coordinates of the PdBI data were re-projected such that both maps have reference coordinates of $\alpha(\mathrm{J2000}) = 18^h57^m08.0^s$, $\delta(\mathrm{J2000}) = 2°10'30.0''$.

The merged mosaic was CLEANed using the Hogbom cleaning algorithm in the GILDAS/MAPPING software (as recommended in cases where sidelobes are prominent). CLEANing was performed using a robust weighting factor of 3.16 (GILDAS task 'UV_STAT WEIGHT' provides information on robust weighting parameters). This weighting factor ensures that the sidelobes are reduced sufficiently to remove artefacts from the data, whilst the rms noise is increased by only $\sim 10\%$. Following the CLEAN procedure, the synthesised beam has angular size $3.9'' \times 3.2''$ (position angle $= 27°$). The data has been converted to units of main beam brightness temperature using the task 'COMBINE' in MAPPING, by multiplying by $11.35\,\mathrm{K}\,(\mathrm{Jy\,beam^{-1}})^{-1}$.

To perform spectral analysis, spectra have been extracted from individual pixels ($0.8''\times0.8''$) within the cube. These data have then been smoothed using a Gaussian weighting (full width at half maximum, FHWM = the major axis of the synthesised beam $\sim 4''$). This reduces the spatial resolution to $\sim 5''$. Pixel spacings are equivalent to $0.5\times$ the major axis of the synthesised beam ($\sim 2''$). The typical spectral RMS noise in each pixel is 0.1 K. The analysis is restricted to the isolated hyperfine component ($\mathrm{F_1}$, F = 0,1 $\rightarrow$ 1,2) of $\mathrm{N_2H^+}$ (1 − 0) unless otherwise stated. This is because the isolated component is expected to be optically thin (this statement will be justified in Section 3.3.3).

The 3.2 mm continuum data has also been CLEANed using the Hogbom algorithm. The synthesised beam is $4.2'' \times 3.1''$, with a position angle of 17.3°. The

typical map RMS noise is 0.07 mJy beam^{-1}, estimated from emission-free regions. In this work the continuum data is used for comparison only. A full discussion and analysis of the continuum data will be provided in Chapter 4.

Utilised throughout this paper is the 8 μm extinction-derived, 2″ resolution, mass surface density map of Butler & Tan (2012), as modified by Kainulainen & Tan 2013 (hereafter, KT13) to include corrections for the presence of the near infrared extinction-derived IRDC envelope. When direct comparison with N_2H^+ data has been made, the mass surface density has been smoothed to an equivalent spatial resolution.

3.3 Observational Results:

3.3.1 Intensity distribution & moment analysis

Figure 3.1 displays the results of moment analysis covering the PdBI map. The zeroth, first, and second order moments are calculated using the following:

$$M_0 = \int T_{\rm MB}(v)\, dv, \tag{3.1}$$

$$M_1 = \frac{\int T_{\rm MB}(v) v\, dv}{\int T_{\rm MB}(v)\, dv}, \tag{3.2}$$

$$M_2 = \frac{\int T_{\rm MB}(v - M_1)^2\, dv}{\int T_{\rm MB}(v)\, dv} \tag{3.3}$$

where $T_{\rm MB}$ is the brightness temperature of the line and v is the velocity. Moment analysis has been performed between 42–48 $\rm km\,s^{-1}$ (to incorporate all emission in the average spectrum), and above 0.3 K (the 3σ level). The left-hand panel of Figure 3.1, compares the spatial distribution of the N_2H^+ $(1-0)$ integrated intensity (black contours; zeroth order moment) with the mass surface density, as derived in KT13 (colour scale). To highlight the densest portion of the cloud, the (solid) contours are plotted from $10\,\sigma$ (the dotted contour refers to the $5\,\sigma$ level). The central panel of Figure 3.1 displays the $V_{\rm LSR}$ map (first order moment), and is shown here between 44.5–47.0 $\rm km\,s^{-1}$ (this narrower velocity range has been chosen to pick out the variation in velocity from the brightest emission). The right-hand panel displays the velocity dispersion of the N_2H^+ $(1-0)$ emission, or second order moment, between 0.0–1.5 $\rm km\,s^{-1}$.

It is evident from the left-hand panel of Figure 3.1, that the N_2H^+ emission is extended over a large portion of the cloud. This confirms the result

from Chapter 2 that the dense gas is extended over parsec scales in G035.39-00.33. The emission traces the morphology of the mass surface density very closely. The white cross indicates the position of H6, as determined in BT12 (position: $\alpha(\mathrm{J2000}) = 18^h57^m08.2^s$, $\delta(\mathrm{J2000}) = 2°10'51.7''$, corresponding to offset: $\Delta\alpha = 2.99''$, $\Delta\delta = 21.7''$). It is clear from Figure 3.1 that the peak in N_2H^+ emission (at offset $1.67'', 22.59''$) and the peak of H6, as determined from extinction mapping (BT12), are spatially coincident (within a single PdBI beam).

The velocity distribution indicates that higher velocities are situated towards the northern and western regions of G035.39-00.33. There are also localised areas of high-velocity (see offset $5''$,-$25''$, this was also noted in the single dish observations of Chapter 2). Since moment analysis is insensitive to multiple spectral features, this may indicate regions where additional velocity components effect the overall trend (see Section 3.4).

A map of the velocity dispersion (i.e. the second order moment) is shown in the right-hand panel of Figure 3.1. The velocity dispersion is fairly constant across G035.39-00.33, with a mean value of 0.45 $\mathrm{km\,s^{-1}}$. A notable exception to this is observed towards the south-west of H6 (peak value > 1 $\mathrm{km\,s^{-1}}$). This location coincides with red-shifted velocity peaks evident in the first order moment map. In Chapter 2, a high-velocity component (filament 3; ~ 47 $\mathrm{km\,s^{-1}}$) was shown to overlap spatially with the "main" IRDC filament (filament 2; 45.63 $\mathrm{km\,s^{-1}}$) at the location of H6. This may indicate that the velocity dispersion is influenced by the presence of an additional component. The presence of multiple velocity components will be further explored in Section 3.4. Considering a mean velocity dispersion of 0.45 $\mathrm{km\,s^{-1}}$, the estimated ratio between the thermal and non-thermal contributions is ~ 7 (for N_2H^+, with a molecular weight of 29 a.m.u., the thermal

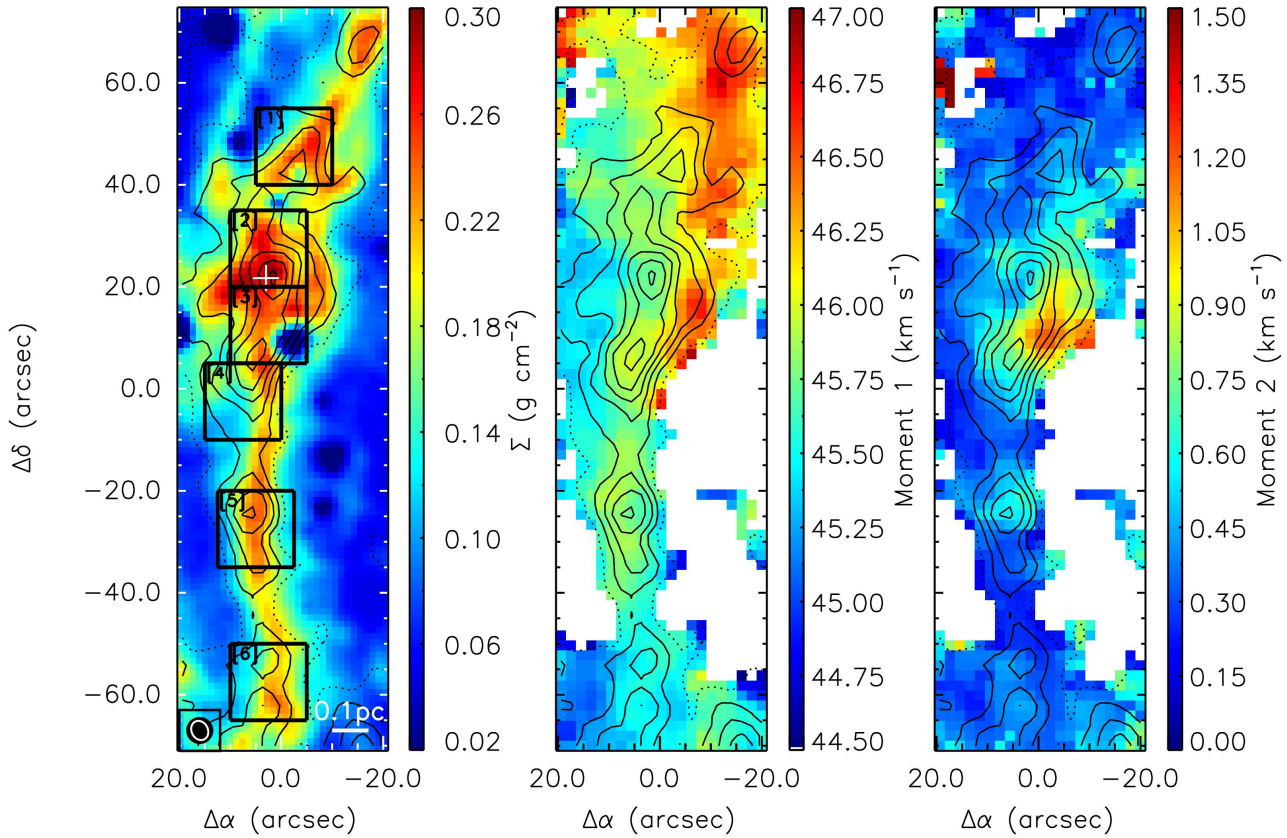

Figure 3.1: Left: Integrated intensity contours (black) of N_2H^+ $(1-0)$, overlaid on top of the mass surface density plot from Kainulainen & Tan (2013). The spectra have been integrated between 42 $\mathrm{km\,s^{-1}}$ and 48 $\mathrm{km\,s^{-1}}$, focusing solely on the isolated (F_1, F = 0,1 → 1,2) hyperfine component. Contours increase from $5\,\sigma$ (dotted contour) in steps of $5\,\sigma$ (solid contours; where $\sigma \sim 0.1\,\mathrm{K\ km\,s^{-1}}$). The synthesised PdBI beam is shown as a white ellipse in the bottom left-corner (the filled black circle is the effective spatial resolution of the map following Gaussian smoothing). The white cross indicates the location of H6, from Butler & Tan (2012). The boxes indicate the regions of interest that have been selected to show in more detail in Figure 3.2. Centre: Map of the velocity field using first order moment analysis. Right: Map of the velocity dispersion using second order moment analysis. The moment analysis has been performed above $3\,\sigma$, between a velocity range of 42–48 $\mathrm{km\,s^{-1}}$. The contours are identical to the left panel.

contribution to the total dispersion is $\sigma_{\rm T} = 0.07$ km s^{-1}, for gas at 15 K; a reasonable estimate based on the dust temperature within G035.39-00.33; Nguyen Luong *et al.* 2011). Comparing this with the sound speed for the mean molecule at an equivalent temperature ($c_{\rm s} = 0.23$ km s^{-1}, using a mean mass per molecule of 2.33 a.m.u.) gives $\sigma_{\rm obs}/c_{\rm s} \sim 2$, similar to Chapter 2 (in N_2H^+), but smaller than that Jiménez-Serra *et al.* (2014).

Figure 3.2 displays the integrated intensity at the six locations highlighted by the black boxes in the left-hand panel of Figure 3.1 (colour scale, between 0.0 – 4.0 K km s^{-1}). Overlaid are the individual $N_2H^+(1-0)$ spectra (isolated component only) associated with these regions (these locations have been selected to show a range of spectral features). A dotted line at 45.8 km s^{-1} (the mean centroid velocity within the map, as calculated from the moment analysis displayed in the central panel of Figure 3.1), is highlighted in each spectrum, for reference. The profiles of the N_2H^+ spectra vary throughout the cloud. In three out of the six regions mapped (regions 2, 3, and 4) there is strong evidence for the presence of multiple velocity components, with further evidence in the remaining regions. Referring back to Figure 3.1, regions 2, 3, and 4 cover the bulk of the emission around H6. Within the vicinity of H6, substructure that is not evident in the single-dish maps of Chapter 2 is detected (see Section 3.4).

How the intensity of the emission changes with respect to the velocity of the gas can be seen in the channel maps of Figure 3.3. This displays the emission (red contours) of N_2H^+ between 44.0 – 48.0 km s^{-1} integrated in increments of 0.5 km s^{-1}. In the single-dish maps presented in the previous chapter, filaments 2 (45.63 ± 0.03 km s^{-1}) and 3 (46.77 ± 0.06 km s^{-1}), whilst clearly spectrally resolved (due to the high-spectral resolution of the IRAM 30 m backends;

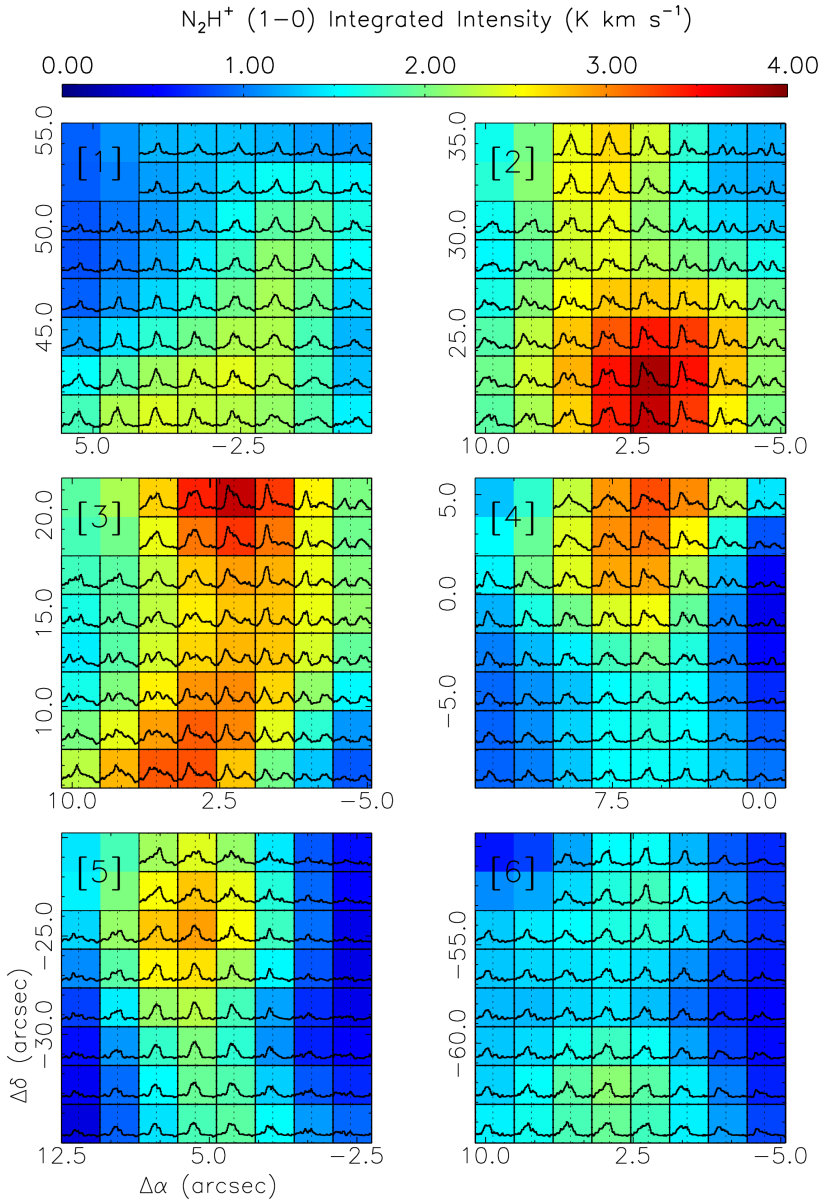

Figure 3.2: Regions of interest as defined in Figure 3.1 (left panel). Here the integrated intensity has been overlaid with individual spectra throughout the maps. The intensity has been integrated over the velocity range 42-48 km s^{-1}, and is displayed between 0.0 K km s^{-1}– 4.0 K km s^{-1}($\sigma \sim 0.1$ K km s^{-1}). Only the isolated (F_1, F = 0,1 $\rightarrow$ 1,2) component is shown, for clarity. The spectra are shown between 44.0–48.0 km s^{-1} (x-axis) and from -0.1–3.5 K (y-axis). The vertical dotted line indicates a velocity of 45.8 km s^{-1}, the mean velocity as calculated from the moment analysis displayed in Figure 3.1.

~ 0.07 km s^{-1}), were not resolved spatially (the IRAM 30 m beam at 93 GHz $\sim 26''$). These velocity components, can now be resolved both spectrally *and* spatially. In the 46.5 km s^{-1} panel, it is evident that filament 3 follows a different portion of the extinction map compared to the main bulk of material observed at lower velocities, between 45.0–46.5 km s^{-1}.

The component identified previously as filament 2 (Chapter 2; $V_{\rm LSR} \sim 45.63$ km s^{-1}), can now be subdivided into two structures. This is most evident in panels 45.0 km s^{-1} and 46.0 km s^{-1}, respectively, with 45.5 km s^{-1} displaying a transition between the two (this is also evident in the spectra of Figure 3.2). These components are hereafter referred to as F2a and F2b (F2a is the more blue-shifted of the two; see Figure 3.3).

Although F2a and F2b are similar in their emission peaks, there are some notable differences. Firstly, F2a is more prominent in the southern portion of the mapped region, up to H6. F2b, is more prominent in the north. Secondly, not all emission peaks are directly coincident. For instance, the peak observed in the north in F2b (offset $\sim$-5$''$, 50$''$; see 46.0 km s^{-1} panel) is not evident in F2a (see 45.0 km s^{-1} panel).

Since F2a is more prominent south of H6, and F2b to the north, treating these two components as a single entity would result in a velocity field that appears to show a discontinuity close to the location of H6. This velocity change at the position of H6 was noted in Chapter 2 (and was also discussed in Jiménez-Serra *et al.* (2014), studying various transitions of CO isotopologues), and is indeed observed in the moment analysis here (central panel, Figure 3.1). If the complex kinematics within G035.39-00.33 are to be understood, then the existence of multiple velocity components poses a significant problem that needs to be addressed. Special

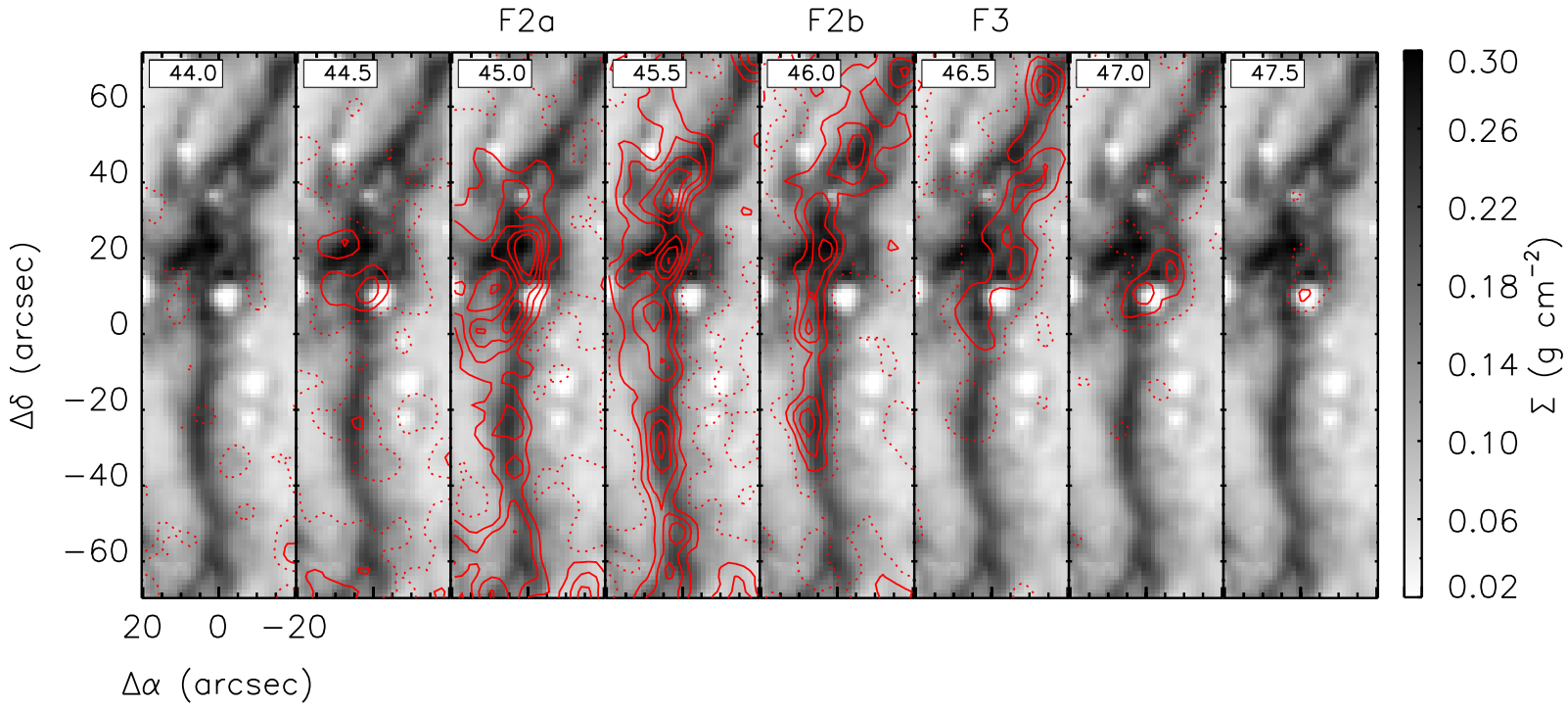

Figure 3.3: Channel maps of the N_2H^+ $(1-0)$ isolated component (F_1, F = 0,1 $\rightarrow$ 1,2). The intensity has been integrated in increments of 0.5 km s^{-1} (velocity in top left corner represents the lower integration limit). Contours are from 0.1 K km s^{-1} (dotted contour; $\sim 5\,\sigma$ over a 0.5 km s^{-1} velocity range), and increase in 0.2 K km s^{-1} steps (solid contours). Contours are overlaid on the mass surface density plot of KT13. Labels F2a, F2b, and F3 refer to the individual filaments discussed in Section 3.3.1, and analysed in Section 3.4.

attention is committed to this topic in Section 3.4.

3.3.2 Position-velocity analysis

Figure 3.4 shows the dissection of G035.39-00.33 into slices that have been selected for PV analysis. Two major longitudinal cuts (A and B, shown in dot-dashed red and solid cyan, respectively, with A being the most northerly) have been selected based on the densest regions of the cloud (as seen in extinction). In this section, the gas motions both along the main axis of the IRDC, and perpendicular to it are explored.

The standard deviation of column density values measured in a region $\sim 10'$ away from the G035.39-00.33 provides a lower limit to which Σ can be probed (KT13). This value is $\sim 0.007\,\mathrm{g\,cm^{-2}}$ (which corresponds to a column density of $\sim 2{\times}10^{21}\,\mathrm{cm^{-2}}$ or an extinction, $A_v = 1.6\,\mathrm{mag}$; KT13). For the gas motions along the main axis, slices are defined by only considering mass surface density values with $\Sigma \geq 9 \times$ this lower limit, i.e. $0.063\,\mathrm{g\,cm^{-2}}$ (corresponding to $A_v = 14.5\,\mathrm{mag}$). This preferentially selects the brightest N_2H^+ emission (Figures 3.1 and 3.10 show the close relationship between mass surface density and N_2H^+ emission). For the slice definition, an intensity-weighted mean offset right ascension was calculated at each increment in offset declination. The mean of these values was then used to make the longitudinal cuts (red dot-dashed and solid cyan lines in Figure 3.4).

Figures 3.5 and 3.6 show PV cuts A and B (identified by dot-dashed red and solid cyan lines in Figure 3.4). Figures 3.7 and 3.8 show the PV data perpendicular to the slices A and B (from east–west), as highlighted in Figure 3.4 (dashed lines). Perpendicular to cut A and cut B, 8 and 25 slices are taken respectively. Each

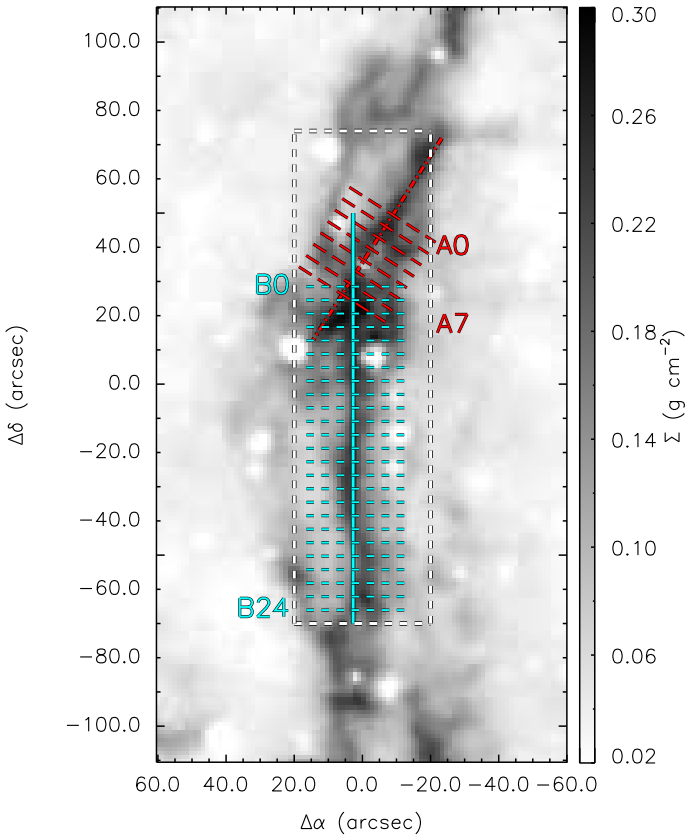

Figure 3.4: The mass surface density plot from KT13, overlaid with locations of the PV slices discussed in Section 3.3.2. Dot-dashed red and solid cyan lines indicate the longitudinal cuts taken from north to south, and dashed lines represent radial slices. Radial slices have been numbered from A0–A7 in the case of cut A, and B0–B24 in the case of cut B. The dashed white box shows the extent of the PdBI map in N_2H^+ $(1-0)$.

radial slice is separated by 2 map pixels (in declination).

Velocity gradients are evident throughout G035.39-00.33. The emission along slices A and B suggest overall negative velocity gradients from north to south. However, the presence of multiple spectral components makes their interpretation difficult. Multiple spectral features were evident in Figure 3.2 and discussed in Section 3.3.1. Comparing with the spectra, and the channel maps of Figure 3.3,

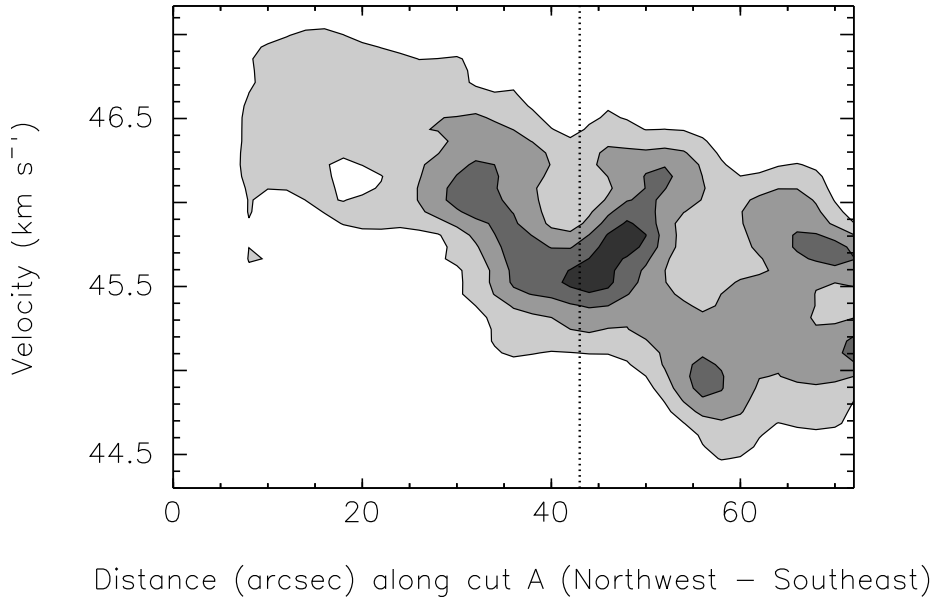

Figure 3.5: Position-velocity diagram of cut A (see red dot-dashed line in Figure 3.4). The filled contours are in units of main beam brightness temperature, and correspond to the 5σ, 10σ, 15σ, and 20σ levels (where $\sigma = 0.1\,\mathrm{K}$). The vertical dotted line refers to the location of continuum peak N (see later discussion, Section 3.5 and Figure 3.19).

F2a and F2b appear at distances $> 40''$ along cut A, whereas F3 is mainly present north of this location. In cut B however, both F2a and F2b are present over the entire length, and so any change in velocity with respect to distance along the PV slice, may be representative of a velocity gradient.

In cut B (Figure 3.6) the broadest velocity span is present between $40''$–$50''$ (with corresponding offsets: $0'' \lesssim \Delta\delta \lesssim 10''$), slightly to the south of the H6 region. Multiple velocity components are also observed in the radial PV slices (Figures 3.7 and 3.8). The frequency at which these components are observed increases towards H6. In Figure 3.7 (slice A6) components F2a, F2b, and F3 are identified in the diagram, exhibiting separations in both position and velocity.

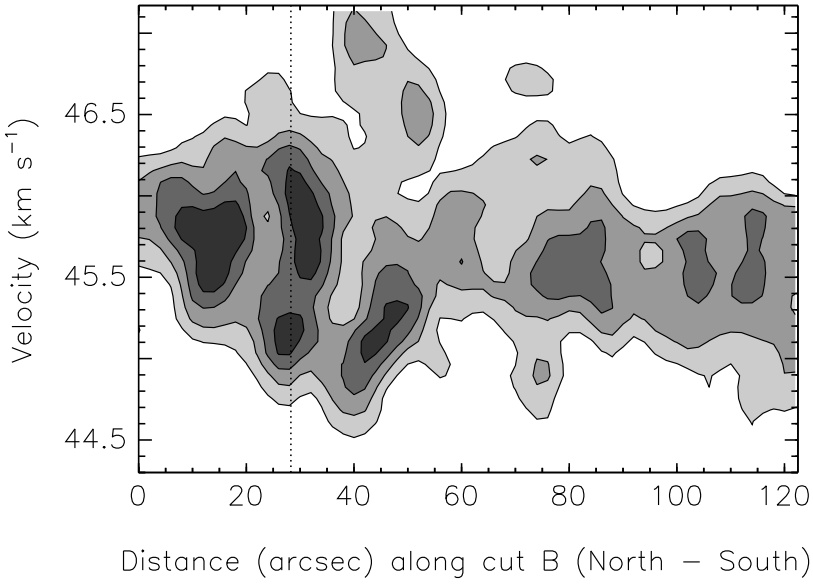

Figure 3.6: Position-velocity diagram of cut B (see cyan solid line in Figure 3.4). The filled contours are in units of main beam brightness temperature and correspond to the 5σ, 10σ, 15σ, and 20σ levels (where $\sigma = 0.1$ K). The vertical dotted line represents the position of H6 along the length of the PV slice.

There is a common elongation in the emission between the peaks identified as components F2a and F2b in a number of PV slices. Whilst this is also evident close to H6 (see for example slices A5, A6, A7, B1, B2, B5), it is preferable to estimate the magnitude of this gradient away from the complexity of this location. Between -40″ $< \Delta\delta <$ -15″, i.e. south of H6, there is a peak in N_2H^+ emission that is IR-quiet (Figure 3.1). This emission is covered in Figure 3.8 by slices B12–B16. The magnitude of this gradient is estimated by firstly selecting the emission $> 9\,\sigma$, in the black dashed boxes shown in Figure 3.8 (criteria (i) Busquet *et al.* 2013: filament emission defined to have SNR > 9), and secondly, selecting PV slices within which the $9\,\sigma$ emission extends over at least 11″ ($\sim 2 \times$ the map resolution). An intensity weighted position for each incremental step in velocity contained

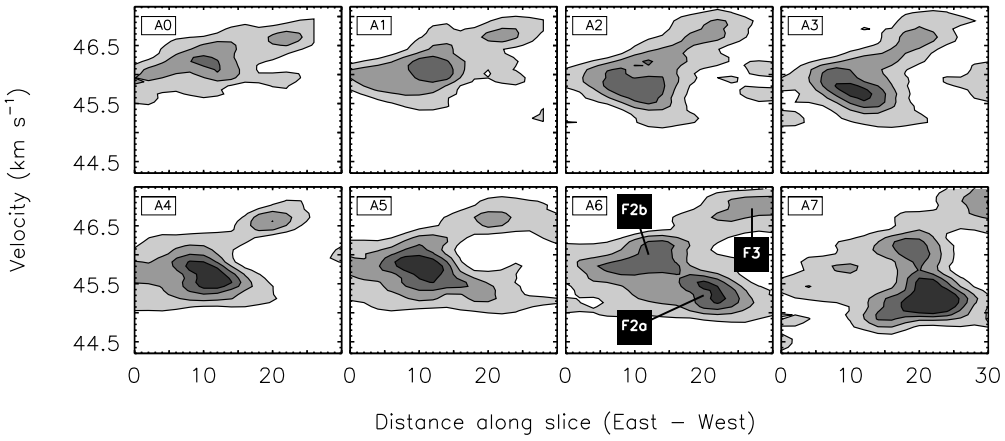

Figure 3.7: Position-velocity diagrams of the 8 slices perpendicular to cut A indicated by dashed red lines in Figure 3.4. The filled contours are in units of main beam brightness temperature, and correspond to the 5σ, 10σ, 15σ, and 20σ levels (where $\sigma = 0.1$ K). The three filaments F2a, F2b, and F3, are clearly seen as emission peaks in slice A6.

within the selected area is then calculated. Following similar analysis to Hily-Blant *et al.* (2005), who investigated rotation in the Horsehead nebula, a linear fit is calculated (under the assumption of solid body rotation) for each box using the intensity weighted position versus velocity. The mean magnitude of this gradient is -13.9 $\pm$ 2.0 km s^{-1} pc^{-1}.

In the analysis of Hily-Blant *et al.* (2005), rotation, rather than shear is favoured as an explanation for velocity gradient patterns in the Horsehead nebula. In the case of G035.39-00.33, the observed gradient may be indicative of shear (relative) motions between filaments. Such shear motions have been discussed in relation to the formation of massive dense cores in DR21 (OH) by Csengeri *et al.* (2011b), who report velocity shears of 2–3 km s^{-1}. However, due to the relatively small angular separation of the two filaments, and considering the uncertainties that arise due to projection effects, this result is approached with caution.

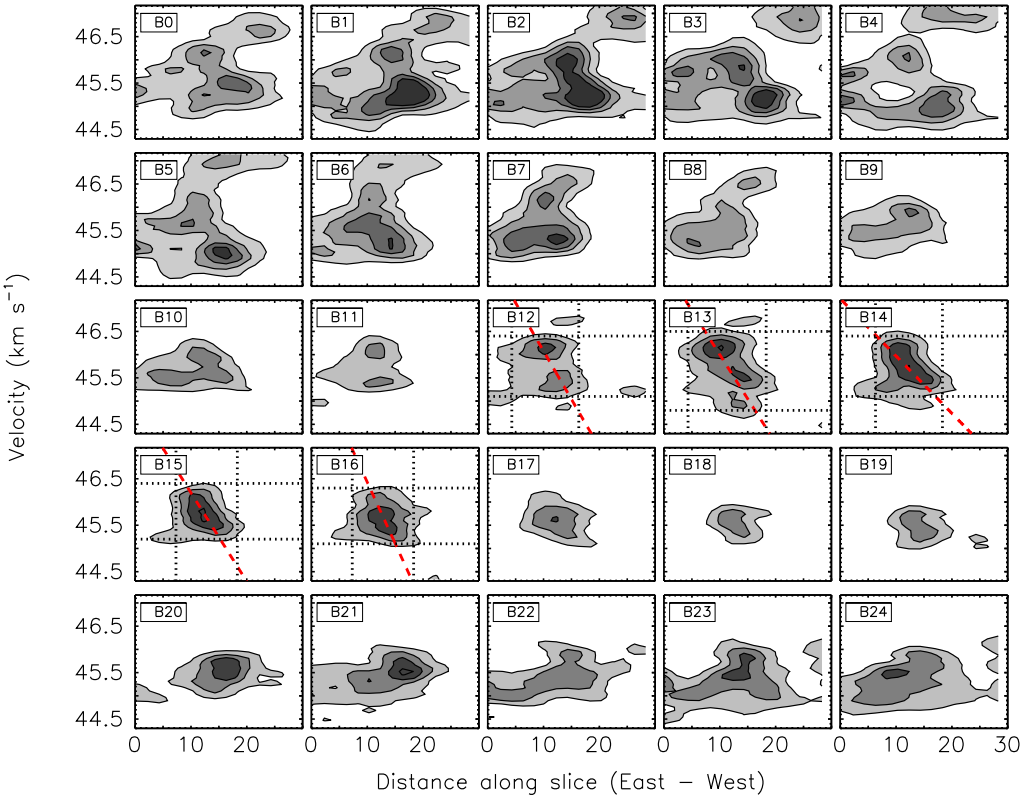

Figure 3.8: Same as Figure 3.7 but for the 25 slices perpendicular to cut B, see dashed cyan lines in Figure 3.4. The black dotted lines in boxes B12–B16 represent the limits over which the velocity gradient (red dashed line) has been calculated. For more information, see Section 3.3.2.

3.3.3 A note on the optical depth of N_2H^+ (1–0)

The identification of multiple velocity components necessitates a discussion on the optical depth of the N_2H^+ $(1-0)$ line emission. In Chapter 2 (Section 2.3.2), the hyperfine structure of N_2H^+ $(1-0)$ was used to show that the isolated component was optically thin (mean *total* optical depth over all 7 hyperfine components < 3, corresponding to an optical depth of the isolated component, ~ 0.33). In addition, the presence of multiple velocity components in N_2H^+ could be verified as the line profiles were similar to the optically thin $C^{18}O$ (the optical depth of $C^{18}O$ was

estimated to be $\lesssim 1$ in the densest portion of the mapped region, see Chapter 2).

In this analysis, no optically thin tracer was available. However, the line is assumed to be optically thin for the following reasons:

1. This study utilises only the isolated hyperfine component of N_2H^+ $(1-0)$, which has a statistical weight of ~ 0.11 (Caselli *et al.* 1995).

2. If the presence of multiple components was simply an effect attributed to the optical depth, then one would assume that multiple velocity components would be restricted to the high-density regions. However, this is not the case; there is also evidence for multiple velocity components away from H6.

3. There is some evidence for multiple velocity components evident in the N_2H^+ $(3-2)$ spectra (from the IRAM 30 m antenna presented in Chapter 2), and these peaks align (within uncertainties) with those observed in the PdBI data, when smoothed to an equivalent resolution. The fact that the N_2H^+ $(3-2)$ line does not peak in between F2a and F2b (as would be expected if the $J = 1 \rightarrow 0$ transition was optically thick, and the $J = 3 \rightarrow 2$ transition, thin) suggests that they trace similar kinematics, and the $J = 1 \rightarrow 0$ isolated hyperfine component is not significantly affected by optical depth effects.

   Figure 3.9 shows the $J = 1 \rightarrow 0$ and $J = 3 \rightarrow 2$ N_2H^+ spectra at offset $(2.5'', 12.5'')$. Both data sets have been smoothed to an equivalent spatial resolution of $15''$. In addition, the N_2H^+ $(3-2)$ has been smoothed to a similar spectral resolution ($\Delta v_{\rm res} \sim 0.16$ km s^{-1}). In spite of the fact that the spectral noise is greater in the N_2H^+ $(3-2)$ data ($\sigma = 0.26$ K), multiple spectral components are evident. Moreover, the observed components are in agreement with those observed in the N_2H^+ $(1-0)$ data.

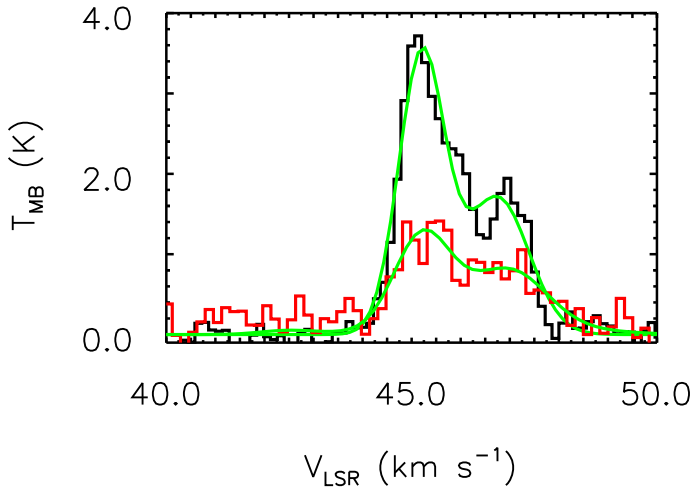

Figure 3.9: N_2H^+ $J = 1 \rightarrow 0$ (black; intensity mutliplied by a factor of 3 for clarity), and $J = 3 \rightarrow 2$ (red) spectra from offset $= (2.5'', 12.5'')$. The data have been smoothed to a comparable $\sim 15''$ spatial resolution. The green lines indicate the fit to each spectrum. A two component Gaussian fit is shown in the case of N_2H^+ $(1-0)$ (component 1: $V_{\rm LSR} = 45.2 \pm 0.1$, $\Delta\upsilon = 1.1 \pm 0.1$; component 2: $V_{\rm LSR} = 46.8 \pm 0.1$, $\Delta\upsilon = 1.5 \pm 0.2$). A two component hyperfine structure fit (using GILDAS/CLASS) has been performed in the case of N_2H^+ $(3-2)$. In each case the optical depth has been fixed at $\tau = 0.1$ (component 1: $V_{\rm LSR} = 45.1 \pm 0.2$, $\Delta\upsilon = 1.3 \pm 0.4$; component 2: $V_{\rm LSR} = 46.8 \pm 0.4$, $\Delta\upsilon = 1.9 \pm 0.9$).

4. Figure 3.10 shows the N_2H^+ $(1-0)$ integrated intensity versus mass surface density over the whole cloud. There is a strong correlation between these two properties (Spearman rank correlation coefficient, $r_{\rm s} = 0.72$, $P < 0.001$), and no plateau is observed towards higher extinction (as would be expected in the case of high optical depth).

5. Multiple component hyperfine structure fits have been performed at several locations and the fit results are consistent with the isolated components being optically thin. Figure 3.11 shows the full spectrum (including all hyperfine components) at offset $= (3.6'', 12.7'')$ as an example (this spectrum is one

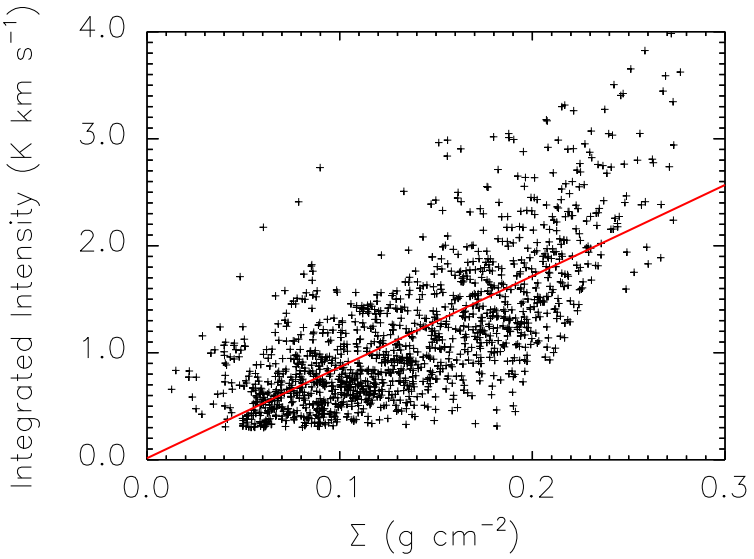

Figure 3.10: Integrated intensity of N_2H^+ $(1-0)$ vs. mass surface density. Intensity has been integrated between 42.0 – 48.0 km s^{-1}. Integrated intensity values are plotted above the typical $3\,\sigma$ uncertainty (~ 0.3 K km s^{-1}). The uncertainty in the mass surface density is estimated at $\sim 30\%$ (see KT13 for more details). The red line indicates the best fit to the data.

of the brightest, and most complex). The hyperfine structure of the N_2H^+ $(1-0)$ line can be used to estimate the optical depth of the individual velocity components (see Chapter 2). Overlaid are markers indicating the velocities of hyperfine components corresponding to F2a (cyan), F2b (red), and F3 (green). The height of each line corresponds to the *expected* intensity of individual hyperfine components assuming optically thin conditions. The solid curve represents a three component hyperfine structure fit performed using the GILDAS/CLASS software. The *total* optical depth of the fitted lines are 5.28 (0.12), 7.92 (0.10), 0.11 (0.05), respectively. For the isolated hyperfine components therefore, the optical depths are ~ 0.7, 0.9, 0.01, respectively.

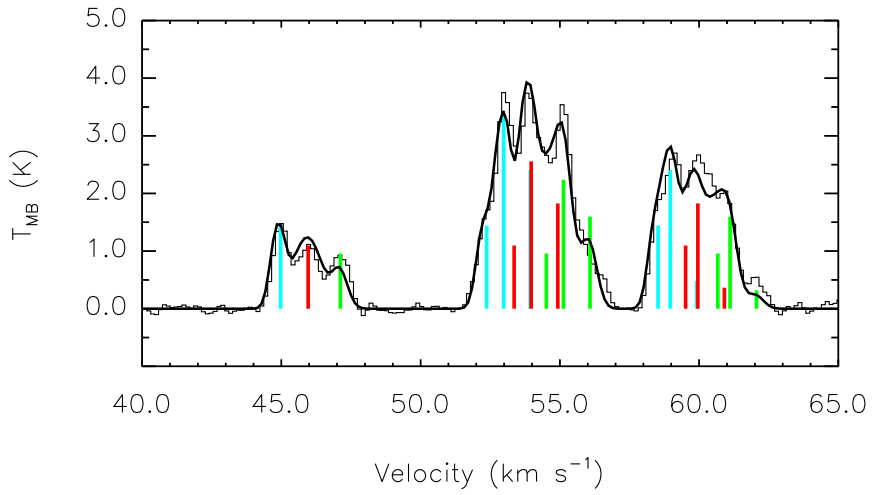

Figure 3.11: N_2H^+ $(1-0)$ spectrum from offset $= (3.6'', 12.7'')$. Coloured lines indicate respective velocities of all hyperfine components of individual velocity components. The solid black line is the result of a hyperfine structure fit, incorporating the three velocity components observed.

This indicates that the isolated components are just *partially* optically thick towards the H6 region. It must be noted however, that whilst the hyperfine structure *can* be fitted in some locations, the complexity of the spectra and the blending of spectral components means that fitting routines can converge to ambiguous results. An accurate optical depth measurement for each pixel in the map is therefore not feasible.

It is concluded from this analysis that the observed spectral components represent independent velocity structures, rather than being a consequence of significant optical depth.

3.3.4 N_2H^+ column density

The column density of the N_2H^+ $(1-0)$ line can be estimated by scaling the integrated intensity of the isolated hyperfine component by its statistical weight (0.11; assuming it is optically thin) following the method outlined in Chapter 2. In this instance, Equation 2.5 reduces to:

$$N(N_2H^+) = 1.3 \times 10^{12} I_{\rm tot}\,({\rm K\,km\,s^{-1}})\,{\rm cm^{-2}}. \tag{3.4}$$

The excitation temperature was estimated from the output parameters of a fit to the hyperfine structure, using GILDAS/CLASS, at the offset of *peak* N_2H^+ emission $(1.67'', 22.59'')$, giving a value of ~ 7.4 K. The column density is estimated for every pixel in the map. The peak column density at offset $(1.67'', 22.59'')$ is $(4.7 \pm 0.5) \times 10^{13}\,{\rm cm^{-2}}$. The mean value over the map is estimated to be $= (1.3 \pm 0.2) \times 10^{13}\,{\rm cm^{-2}}$. In the extreme case whereby the optical depth of each of the isolated hyperfine components approach $\tau \sim 1$, a correction factor of ~ 1.6 would need to be made to the column density. In Section 3.3.3 an example spectrum is shown (offset $= 3.6''$,$12.7''$, i.e. close to the H6 region), with a multiple-component hyperfine structure fit. In this example, corresponding τ values of the isolated hyperfine components are all < 1. Generally speaking therefore, the correction should be < 1.6.

As the integrated intensity is directly proportional to the column density (in the optically thin case), the correlation derived in Figure 3.10 can be used to estimate a fractional abundance of N_2H^+ molecules, with respect to H_2 (as derived from the mass surface density). Assuming a mean mass per molecule of 2.33 a.m.u., the correlation (shown as the red line in Figure 3.10), implies a constant fractional abundance of, $[N_2H^+/H_2] = (3.8 \pm 0.1) \times 10^{-10}$ (consistent with Chapter 2), similar

to the N_2H^+ abundance found in low-mass dense cores (e.g. Caselli *et al.* 2002a), and towards other IRDCs (10^{-10}–10^{-9}; e.g. Miettinen *et al.* 2011, Vasyunina *et al.* 2011). The fractional abundance at peak column density is $[N_2H^+/H_2] = (6.8 \pm 2.2) \times 10^{-10}$ (this uncertainty is estimated from the 30% uncertainty in the mass surface density; KT13).

3.4 Analysis: Kinematics of the dense gas within G035.39-00.33

As shown in Section 3.3, a high-degree of complexity is observed in the N_2H^+ $(1-0)$ emission towards G035.39-00.33. Fitting these data is challenging for a number of different reasons: i) there are multiple velocity components along the line of sight; ii) the velocity separation between components is < 1 km s^{-1} (comparable with the typical FWHM observed; see right-panel of Figure 3.1); iii) each of these components is likely to exhibit its own velocity structure, leading to blending of the spectral features. In Chapter 2 a simple fitting routine (dubbed the Guided Gaussian Fit) was developed that enabled separation of molecular line data into individual components. The Gaussian fitting of the PdBI data, however, presents a more significant challenge due to the additional structure observed in the high-angular resolution map.

Analysis of the PdBI data has been performed using a semi-automated Gaussian fitting procedure. Briefly, the technique works by assuming that the profiles of the spectra remain *relatively* constant over suitably small angular distances ($\lesssim 0.1$ pc). Therefore, one can reduce the number of spectra to fit by only fitting the average spectrum within a user defined area (see Appendix A.2 for details). The output values from the fit to the average spectrum are then used as free-parameter inputs to each spectrum within the area. By overlapping areas, multiple fits are performed to a single spectrum. This ensures a *smooth* transition between adjacent areas. A minimisation technique is then used to compare fits to individual spectra, selecting the "best fit". Individual velocity components are then grouped using an algorithm devoted to seeking out similar components within a user de-

Table 3.1: Fit parameters for the Gaussian profiles to the spectra shown in Figure 3.12.

Filament	$\Delta\alpha$ ($''$)	$\Delta\delta$ ($''$)	T_{peak} (K)	σT_{peak} (K)	V_{LSR} ($km\,s^{-1}$)	σV_{LSR} ($km\,s^{-1}$)	Δv ($km\,s^{-1}$)	$\sigma\Delta v$ ($km\,s^{-1}$)	RMS (K)	Residual (K)
F2b	-16.06	69.87	1.38	0.17	46.12	0.08	0.72	0.04	0.09	0.09
F3	-16.06	69.87	0.86	0.21	46.75	0.11	0.67	0.06	0.09	0.09
F2a	3.64	22.59	1.92	0.04	45.20	0.01	0.63	0.01	0.04	0.03
F2b	3.64	22.59	2.09	0.02	46.06	0.01	0.91	0.01	0.04	0.03
F2a	-4.24	10.77	0.76	0.03	45.05	0.02	0.87	0.02	0.06	0.08
F3	-4.24	10.77	0.77	0.03	47.29	0.02	1.03	0.02	0.06	0.08
F2a	7.58	8.80	0.70	0.07	44.82	0.05	0.69	0.04	0.08	0.10
F2b	7.58	8.80	1.43	0.05	45.93	0.03	1.12	0.05	0.08	0.10
F3	7.58	8.80	0.60	0.07	47.03	0.04	0.62	0.04	0.08	0.10

fined area. This algorithm follows the same underlying principles as the "Friends In VElocity", FIVE, algorithm developed by Hacar *et al.* (2013), in that velocity components are grouped based on how closely they are linked in both position and velocity *simultaneously* (by calculating the velocity gradient; see Appendix A.2), utilising position-position-velocity space.

Figure 3.12 displays individual spectra towards four positions in the N_2H^+ map (only the isolated hyperfine component is shown). The offset right ascension (top) and offset declination (bottom) are highlighted in the top-left corner of each spectrum. For each spectrum, the Gaussian fit to each velocity component (F2a = cyan; F2b = red; F3 = green), and the total fit to the line is overlaid (black). The fit parameters to each Gaussian profile are reported in Table 3.1. For reference, the 3×rms level is highlighted in each panel with a horizontal dotted line. These spectra have been highlighted to show the broad range of profiles, and the fitting procedure's ability to cope with such diversity. The velocity structure is analysed in more detail in the following sections.

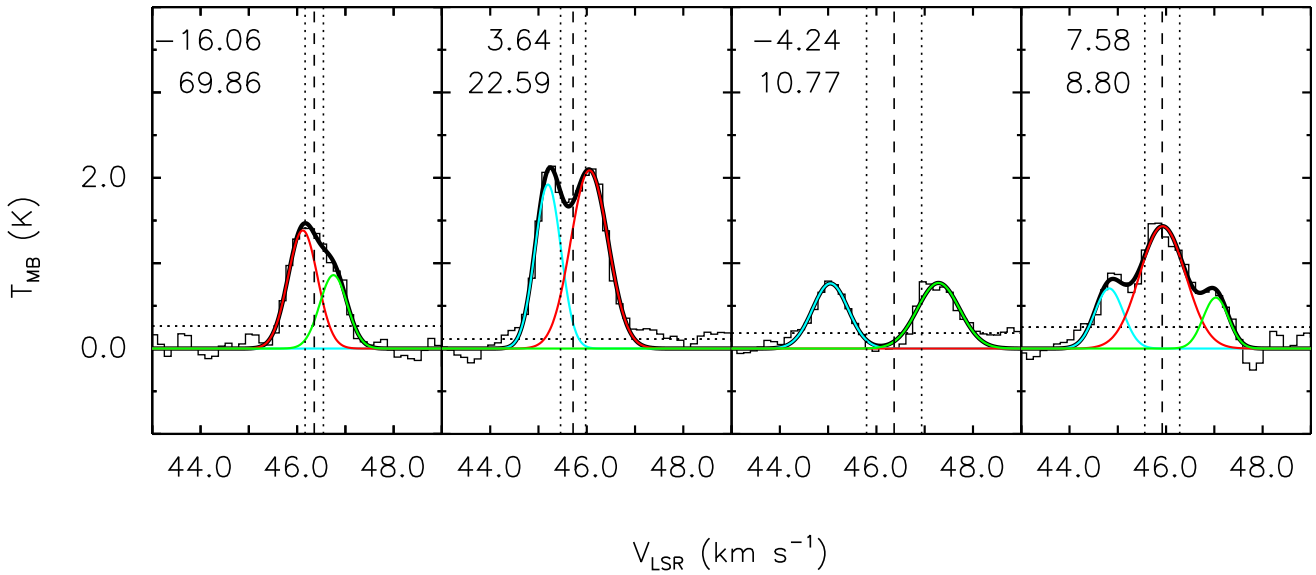

Figure 3.12: Example spectra from four positions (see top left hand corner of each plot for position: top = $\Delta\alpha$, bottom = $\Delta\delta$ in arcsec) in the cloud. The vertical dashed line indicates the velocity as calculated from the first order moment, whereas the vertical dotted lines refer to the velocity dispersion as calculated from the second order moment (moment analysis performed over a velocity range 42–48 km s^{-1}, and where $T_{MB} > 0.3$ K; see Section 3.3.1). The horizontal dotted line corresponds to the 3×rms value for each spectrum. Cyan, red, and green Gaussian profiles are fits to individual velocity components, F2a, F2b, and F3, from the fitting procedure outlined in Appendix A.2. The black profile indicates the total fit to the line. The fit parameters for each Gaussian component can be found in Table 3.1.

3.4.1 Centroid velocity

Figure 3.13 is a position-position-velocity (PPV) representation of the individual velocity components within the cloud. The image shown in position-position space at the base of the figure is the mass surface density map from KT13, overlaid with N_2H^+ contours (identical contours are shown in Figure 3.1). The vertical dotted line indicates the position of H6, and is used for reference.

Six velocity components are identified in total. Cyan and red refer to filaments F2a, and F2b, and filament F3 is displayed in green. Velocity components 4, 5, 6 are displayed in purple, dark blue, and orange, respectively. The combined contribution of components 4, 5, and 6 to the overall number of Gaussian fits is $< 5\%$, and they are therefore not considered to be "filaments" (percentage contributions of each component can be found in Table A.1).

Figure 3.14 displays a histogram of centroid velocities of F2a, F2b, and F3 (red, cyan, and green, respectively), as well as that of the N_2H^+ IRAM 30m data (black). In Chapter 2, the peak at 46.77 ± 0.06 km s^{-1} was interpreted as filament 3. The double peaked component between $\sim$45-46.5 km s^{-1} (mean $V_{\rm LSR} = 45.63$ km s^{-1}), was classified as filament 2, the brightest and therefore "main" filament of the IRDC. The dual-peaked velocity of filament 2 was noted in Chapter 2 and was interpreted as a gradient occurring at the position of H6. Figure 3.14 shows that F2a and F2b peak at similar velocities to the dual peaks of filament 2 in the single-dish data. This suggests that both components were also spectrally evident in the single dish data. However, the sub-components were not categorised as such as they could not be spatially resolved. There is also slight evidence for a double peak evident in the F3 classification. This can be seen as a sharp peak in

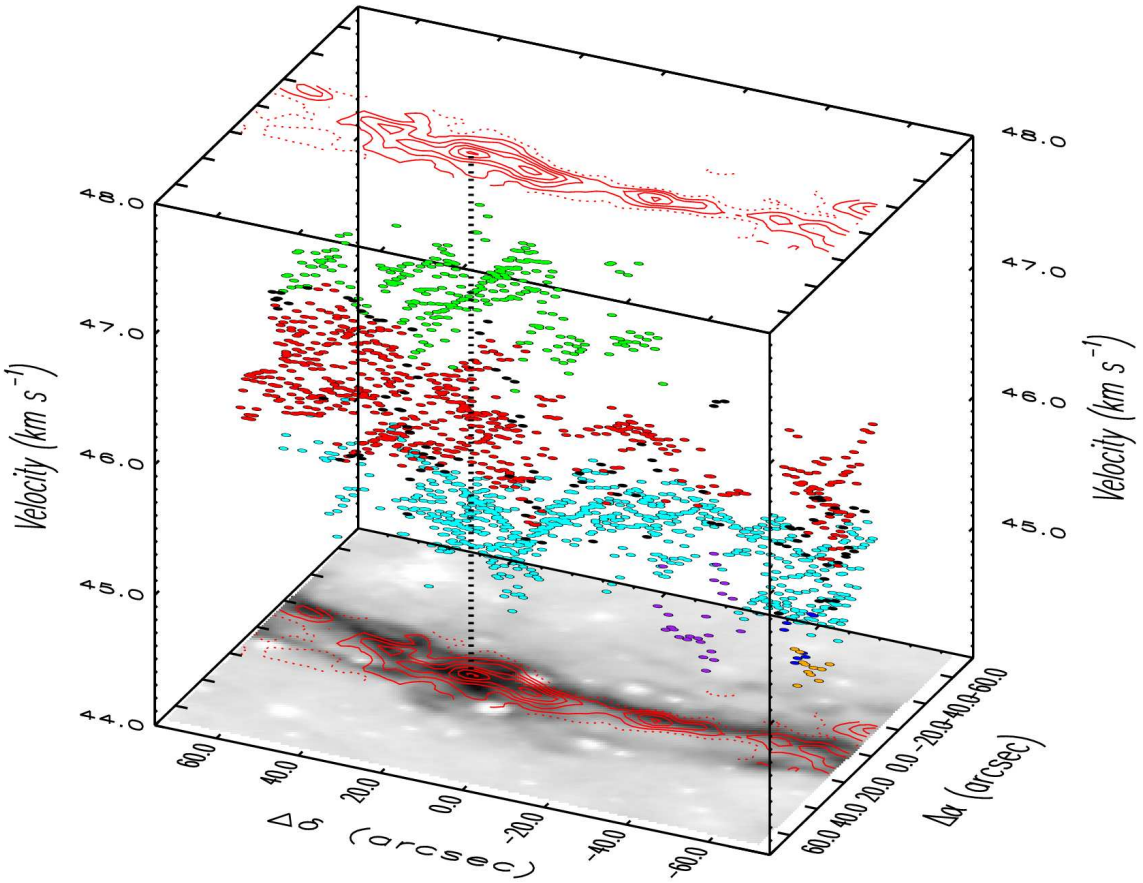

Figure 3.13: Three dimensional position-position-velocity (PPV) cube showing the centroid velocity of the three velocity components: (cyan) F2a, (red) F2b, and (green) F3, observed across G035.39-00.33. Additional velocity components, C4, C5, and C6, are shown in purple, blue, and orange, respectively (see Appendix A.2 for more details). Unassigned data points are shown in black. The mass surface density map can be seen at the base of the cube (grey scale), overlaid with N_2H^+ $(1-0)$ integrated intensity contours. Contour levels increase from $5\,\sigma$ (dotted contour; where $\sigma \sim 0.1$ K km s^{-1}) in steps of $5\,\sigma$ (solid contours), as with Figure 3.1. The vertical dotted line corresponds to the position of H6.

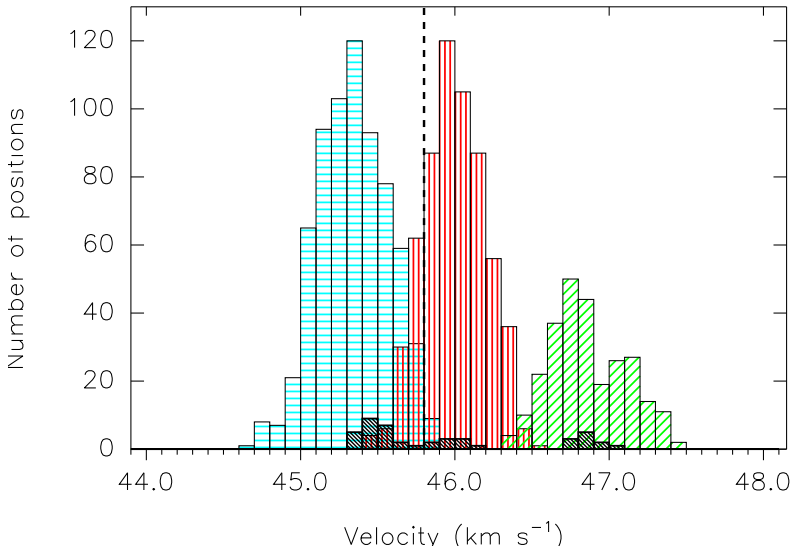

Figure 3.14: Histogram of the centroid velocity at peak intensity of individual velocity components in both the (colour) PdBI data, and (black) IRAM 30 m data of Chapter 2, as determined by the Gaussian fitting technique outlined in Appendix A.2. Filaments 2a, 2b, and 3, are shown in Cyan (horizontal hatch), Red (vertical hatch), and Green (45° hatch), respectively. The vertical dashed line represents the mean velocity derived from the moment analysis in Section 3.3.1.

Figure 3.15 (see $\Delta\delta \sim 10''$), in which the $V_{\rm LSR}$ of each velocity component versus offset declination is plotted (the possible origins of this structure are discussed in more detail in Section 3.5.1).

Filaments F2a, F2b, and F3 have mean $V_{\rm LSR}$ values of 45.34 ± 0.04 km s^{-1}, 46.00 ± 0.05 km s^{-1}, and 46.86 ± 0.04 km s^{-1}, respectively. The mean $V_{\rm LSR}$ of F2a and F2b is (45.67 ± 0.03) km s^{-1}, which is comparable with the quoted value for filament 2 in Chapter 2 (45.63 km s^{-1}). Velocity separations between individual velocity components are (0.66 ± 0.06) km s^{-1}, and (0.86 ± 0.06) km s^{-1}, between F2b–F2a, and F3–F2b, respectively. Although components 4, 5, and 6 have similar mean velocities (all < 45 km s^{-1}), they are separated in position, and there are not

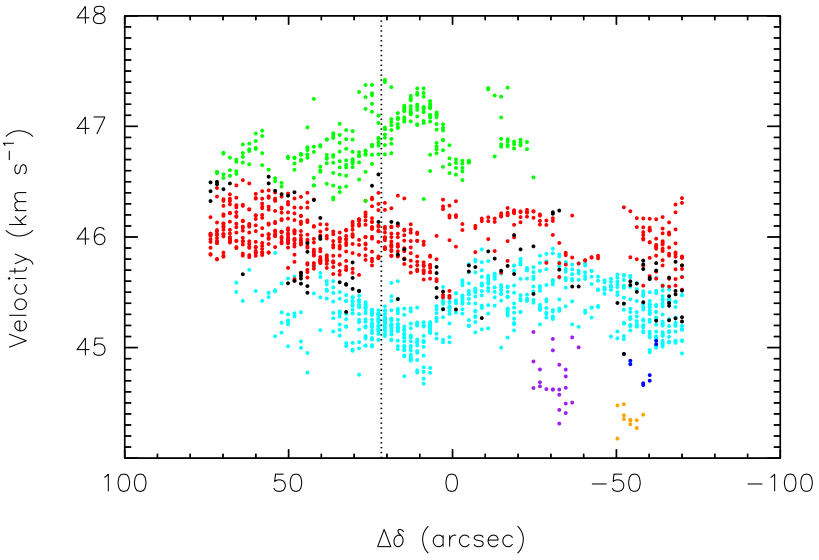

Figure 3.15: Centroid velocity for filaments F2a (cyan), F2b (red), and F3 (green) as a function of offset declination. Additional velocity components, C4, C5, and C6, are shown in purple, blue, and orange, respectively. Unassigned data points are shown in black. The vertical dotted line refers to the offset declination of H6.

enough consecutive data points to conclude that they belong to a single component. In spite of this, it is interesting to note that the velocities of these components are most similar to those derived for filament 1 (Chapter 2 and Jiménez-Serra *et al.* 2014). It is possible that these components may represent high-density portions of filament 1, that are not observed in the low-angular resolution N_2H^+ maps of Chapter 2 (perhaps due to beam dilution), but are observed CO (Jiménez-Serra *et al.* 2014).

The separation between the mean velocities of each individual component are comparable (< 1 km s^{-1}). Each velocity component has a total 3σ dispersion in $V_{\rm LSR}$ that is roughly equivalent to the magnitude of the velocity separation between components. This indicates that there is overlap between velocity components.

This can be seen in Figure 3.13 and even more clearly in Figure 3.15. Additionally, Figure 3.15 shows that it is common for unassigned data points (shown in black) to reside at the boundaries of component definitions. These typically represent positions where there is a transition from multiple to single components, i.e. the limit of the fitting method where individual spectral features can no longer be distinguished.

In general, Figures 3.13 and 3.15 show that the velocity dispersion over all filaments is broadest slightly south of H6. It is also evident that F2a is more prominent towards the south of H6, while F2b mainly traces the region north of H6 (confirming the result found in Figure 3.3). F3 is not evident south of $\Delta\delta \sim$-30″, which is consistent with Chapter 2.

It is noted that there is a gap in the F2b structure at $\Delta\delta \sim$-50″. Whilst the classification scheme identifies the component both above and below $\Delta\delta \sim$-50″ as F2b, it is noted that further mapping of the southern region would be needed to establish whether or not this is a truly independent structure (see Appendix A.2 for velocity component classification parameters).

3.4.2 Velocity gradients

By looking at the $V_{\rm LSR}$ of each individual filament simply as a function of offset declination, as has been plotted in Figure 3.15, it is clear that each individual velocity component has its own complex structure, exhibiting both global, and local, velocity gradients. Overall velocity gradients (calculated using a linear fit between the velocity and offset declination) are small in the north–south direction. F2a and F2b have almost negligible *overall* velocity gradients (0.08 ± 0.02 km s^{-1} pc^{-1},

positive in the north–south direction; and 0.07 ± 0.01 km s^{-1} pc^{-1}, negative in the north–south direction, respectively) between -70″ $\lesssim \Delta\delta \lesssim$ 70″. F3 has a positive gradient in the north–south direction, 0.30 ± 0.04 km s^{-1} pc^{-1} (measured between -25″ $\lesssim \Delta\delta \lesssim$ 70″).

Small velocity gradients over the whole cloud indicate that the gas motions are relatively quiescent (in the north-south direction). However, *local* fluctuations along each filament axis are large compared to the overall gradient. For instance, between $10'' \lesssim \Delta\delta \lesssim 40''$, F2a and F3 show opposing velocity gradients of magnitude ~ 1.5 km s^{-1} pc^{-1}. In addition, velocity gradients may exist in the east–west direction. Therefore, to analyse the gas motions further, a 2-D representation of the velocity gradient is required.

The left-hand panel of Figure 3.16 shows the mass surface density from KT13. Black contours highlight the continuum emission, starting at $3\,\sigma$ (where $\sigma = 7 \times 10^{-2}$ mJy beam^{-1}) and increasing in steps of $2\,\sigma$. Overlaid are the extended 4.5 μm (green squares; Chambers *et al.* 2009), 8 μm (red open circles), and 24 μm emission (red open triangles; Carey *et al.* 2009), as well as the low-mass cores (yellow squares) and high-mass cores (magenta squares) identified using *Herschel* (Nguyen Luong *et al.* 2011). The right hand panels show the $V_{\rm LSR}$ maps and spatial location of all three velocity components, as deduced from the Gaussian fitting routine. Overlaid on top of each map are arrows indicating the magnitude and direction of velocity gradients in 2-D. To achieve this the analysis of Goodman *et al.* (1993) has been followed. By assuming the centroid velocities of observed lines take an approximately linear form:

$$V_{\rm LSR} = V_0 + A\Delta\alpha + B\Delta\delta, \tag{3.5}$$

whereby $\Delta\alpha$ and $\Delta\delta$ are offsets in right ascension and declination, least-squares minimisation can be used to estimate values of A and B, using MPFIT2DFUN (Markwardt 2009). The velocity gradient, ∇v, can then be calculated for a cloud at distance D, using (Goodman *et al.* 1993):

$$\nabla v = \frac{(A^2 + B^2)^{1/2}}{D}, \tag{3.6}$$

and its direction, $\Theta_{\nabla v}$ (direction of increasing velocity, measured east of north), using:

$$\Theta_{\nabla v} = \tan^{-1}\left(\frac{A}{B}\right). \tag{3.7}$$

This method has been adapted following the procedure outlined in Caselli *et al.* (2002a) to calculate multiple gradients within a given region with a good determination of $V_{\rm LSR}$ (seven contiguous positions with significant measurements of $V_{\rm LSR}$). In the case of the PdBI data, the velocity gradient at the location of a given pixel is estimated only if there are a total of 38 pixels within a circular area of 6″ (see the black circle in Figure 3.16). The equivalent pixel area would incorporate at least 7 synthesised beams of the PdBI.

For F2a, the overall velocity gradient (calculated incorporating *all* positions for that filament) has a magnitude of (0.23 ± 0.01) km s^{-1} pc^{-1} in a direction (-168.7$\pm$ 1.7)° east of north. However, the mean magnitude of individual velocity gradients (calculated using the multiple arrow technique) is (1.83 ± 0.05) km s^{-1} pc^{-1}. The overall gradients for F2b, and F3 have magnitudes, (0.56 ± 0.01) km s^{-1} pc^{-1}, and (0.70 ± 0.02) km s^{-1} pc^{-1}, at angles $\Theta_{\nabla v} =$ (-91.1 $\pm$ 0.2)° and (-132.3 $\pm$ 1.2)° east of north, respectively. However, as with F2a, the mean values of individual gradients are comparatively larger, with corresponding values

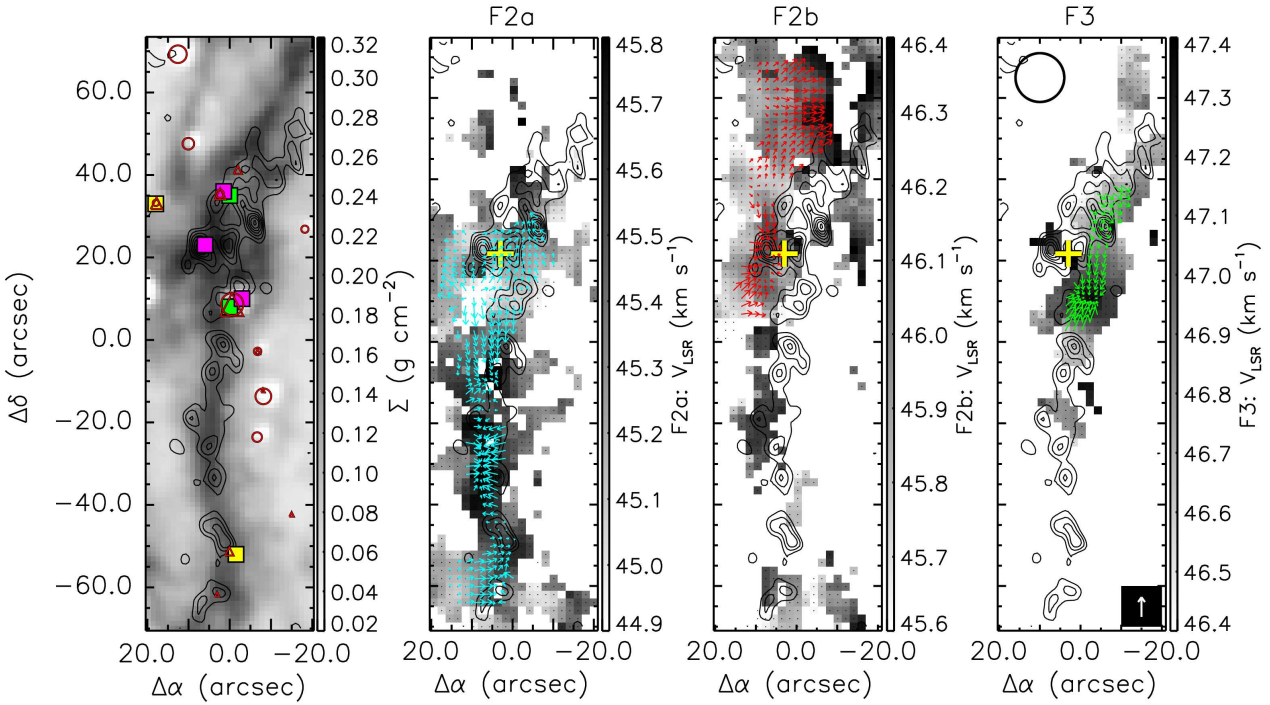

Figure 3.16: (Left) Mass surface density from KT13, overlaid with the PdBI 3.2 mm continuum (black contours). Continuum contours are from $3\,\sigma$ and increase in steps of $2\,\sigma$ ($\sigma = 7{\times}10^{-2}$ mJy beam^{-1}, as calculated from emission free regions in the map). Magenta and yellow squares refer to the high-mass and low-mass dense cores identified in Nguyen Luong *et al.* (2011), respectively. Red circles and red triangles refer to the 8, and 24 μm emission, respectively (Carey *et al.* 2009, Jiménez-Serra *et al.* 2010), and green squares refer to the "green fuzzies" (extended 4.5 μm emission) identified by Chambers *et al.* (2009). (Left-centre, right-centre, and right) V_{LSR} maps of filaments F2a, F2b, and F3, as deduced from the Gaussian fitting routine (see text and Appendix A.2 for more details). The velocity ranges are 44.9–45.8 km s^{-1}, 45.6–46.4 km s^{-1}, 46.4–47.4 km s^{-1}, for F2a, F2b, and F3, respectively. Continuum contours are overlaid in black. The yellow cross indicates the position of H6 from BT12. The arrow size depicts the magnitude of the velocity gradient at each position, and each arrow points in the direction of increasing velocity. The white arrow situated in the right panel displays a velocity gradient of magnitude 5 km s^{-1} pc^{-1}, and the black circle in the top-left of the panel indicates the spatial extent over which the gradients are calculated (see Section 3.4.2).

of (1.65 ± 0.07) km s^{-1} pc^{-1}, and (2.33 ± 0.11) km s^{-1} pc^{-1}, for F2b and F3, respectively. It is concluded therefore, that although overall gradients are observed in each individual filament, the gas motions are dominated by localised flows of material.

In contrast to Jiménez-Serra *et al.* (2014), gas motions are highly non-uniform and unique to individual filaments (rather than each filament exhibiting similar north–south velocity gradients). This complexity is highlighted in F2a (Figure 3.16). Around H6 (yellow cross) the gas motions flow in multiple directions. East of $\Delta\alpha \sim 10''$, gas motion is directed towards the east. West of here, but north of $\Delta\delta \sim 10''$, a positive south–north gradient is found. The arrows here are pointing towards the continuum core to the north–west of H6. South of $\Delta\delta \sim 10''$, the velocity increases towards the south of H6. The arrows here appear to point in the direction of the two continuum peaks between -15$'' < \Delta\delta < 5''$.

South of H6, between -70$'' \lesssim \Delta\delta \lesssim$ -15$''$, the gas motions are not exclusively directed along the main filament axis. Here, it is evident that the large spreads in velocity observed in Figure 3.15 are represented by motions perpendicular to the main filament axis. In this region, gradients are opposing each other (see position -20$'' < \Delta\delta <$ -40$''$), whereas in the very south ($<$ -50$''$), the velocity gradient is directed from east–west. It should be noted however, that in this southern location, the velocity does decrease again further to the west, which would, again, indicate opposing gradients (see Figure 3.16, F2a, between -10$'' < \Delta\alpha < 0''$ and $\Delta\delta <$-60$''$).

In F2b, around H6, the velocity increases towards the position of the continuum core situated slightly east of the yellow cross. To the north of H6, there is a positive velocity gradient from the north–east of H6, to the north–west corner of the map.

Finally, in F3, the velocity gradient analysis shows a uniform transition from

low to high velocity in the north–east to south–west direction just above H6. South of here however, there is evidence for two opposing velocity gradients centred on the continuum peak(s) to the south–west of H6. This peak in continuum is also coincident with 8 μm and 24 μm emission.

In each filament there is evidence that the velocity gradients are directed towards some of the peaks observed in the continuum emission. This implies that the continuum peaks are influencing the dynamics of the surrounding gas. This shall be discussed in more detail in Section 3.5.

3.4.3 Line-width

Figure 3.17 presents the line-width (i.e. the FWHM of the Gaussian components derived in the fitting procedure) at every position in G035.39-00.33, for filaments F2a (left), F2b (centre), and F3 (right). Black contours highlight the continuum emission (contours are identical to Figure 3.16).

Figure 3.17 shows that the distribution of line-widths across each filament is quite varied. Mean line-widths of (0.83 ± 0.04) km s^{-1}, (0.77 ± 0.04) km s^{-1}, and (0.71 ± 0.04) km s^{-1}, are found for filaments F2a, F2b, and F3, respectively.

There is no obvious spatial correlation between the continuum emission peaks and the FWHM of the N_2H^+ velocity components. In F2a, broad line-widths of $\Delta v \sim 1.5$ km s^{-1} are observed between -20″ $< \Delta\delta <$ -30″. Towards H6, the line-width distribution varies towards individual continuum peaks (0.5 km s^{-1} $\lesssim \Delta v \lesssim$ 1.5 km s^{-1}).

The left-hand panel of Figure 3.18 shows a histogram of the ratio between the non-thermal and thermal components of the velocity dispersion, for F2a, F2b,

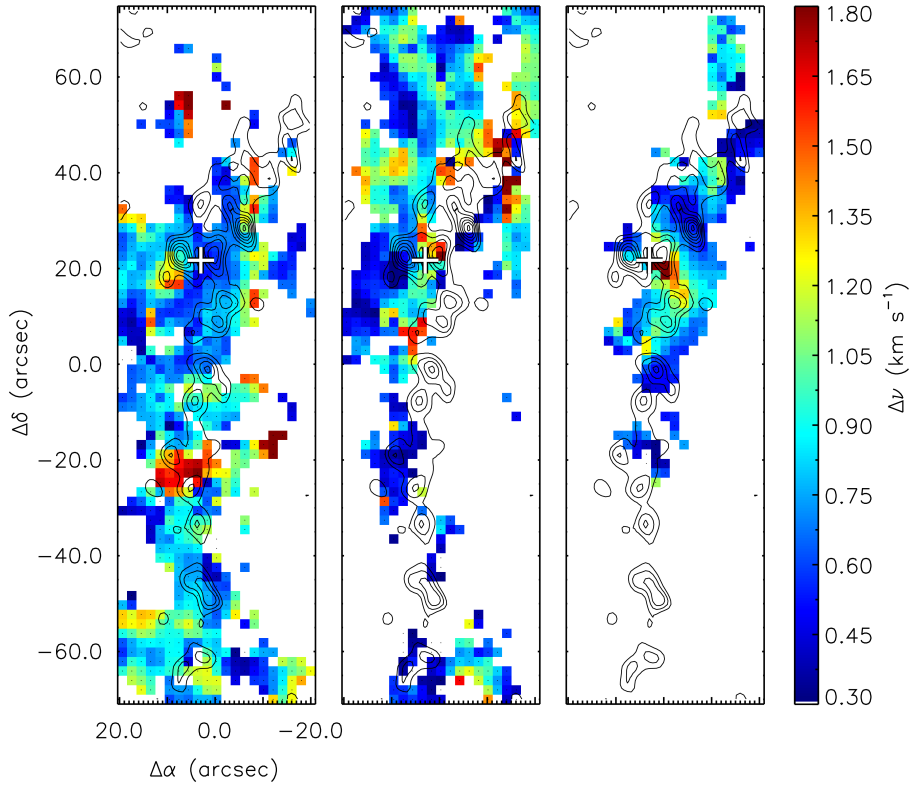

Figure 3.17: Line-width ($\Delta\upsilon$, FWHM) maps (colour scale) of filaments F2a (left), F2b (centre), and F3 (right), calculated using the fitting method outlined in Appendix A.2. Continuum emission is highlighted by the black contours. Contours are the same as in Figure 3.16. The white cross indicates the position of H6 from BT12.

and F3. The non-thermal velocity dispersion is determined from the observed line-width using the following equation (Myers 1983):

$$(\sigma_{\rm NT})^2 = (\sigma_{\rm obs})^2 - (\sigma_{\rm T})^2 \tag{3.8}$$

$$\sigma_{\rm NT} = \sqrt{\frac{\Delta\upsilon^2_{\rm obs}}{8\ln(2)} - \frac{k_{\rm B}T_{\rm kin}}{m_{\rm obs}}} \tag{3.9}$$

where $\sigma_{\rm NT}$, $\sigma_{\rm obs}$, and $\sigma_{\rm T}$, refer to the non-thermal, the observed, and the ther-

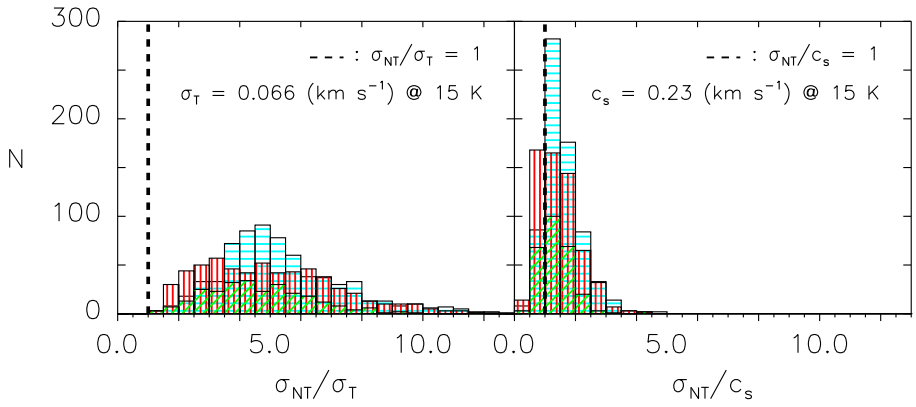

Figure 3.18: Left: Histogram of $\sigma_{\rm NT}/\sigma_{\rm T}$, for filaments F2a, F2b, and F3, shown in cyan (horizontal hatch), red (vertical hatch), and green (45° hatch), respectively. The vertical dashed line refers to $\sigma_{\rm NT}/\sigma_{\rm T} = 1$. $\sigma_{\rm T} = 0.066$ km s^{-1}, for N_2H^+ (29 a.m.u.) at 15 K. Right: Histogram of $\sigma_{\rm NT}/c_{\rm s}$ (markings have the same meaning as the left-hand panel). The sound speed, $c_{\rm s}$ is estimated for a mean molecular mass of 2.33 a.m.u. and has a value $\sim$0.23 km s^{-1}.

mal dispersion, respectively. $\Delta v_{\rm obs}$ refers to the observed line-width (FWHM derived from the fitting procedure), $k_{\rm B}$ is the Boltzmann constant, $T_{\rm kin}$ is the kinetic temperature of the gas, and finally $m_{\rm obs}$ refers to the mass of the observed molecule (29 a.m.u for N_2H^+). Assuming a gas temperature of 15 K (Fontani *et al.* 2012, Pillai *et al.* 2006, Ragan *et al.* 2011), the thermal dispersion of the gas is $\sim$0.07 km s^{-1}. For F2a, F2b, and F3, mean $\sigma_{\rm NT}/\sigma_{\rm T}$ values of 5.4, 5.0, and 4.7 are found, respectively.

The right-hand panel of Figure 3.18 shows a histogram of the ratio between the non-thermal component of the velocity dispersion and the sound speed for a molecule of mean mass 2.33 a.m.u.. The mean $\sigma_{\rm NT}/c_{\rm s}$ values derived for filaments F2a, F2b, and F3, are $\sim$1.6, 1.4, and 1.4, respectively. This indicates that the filaments are *mildly* supersonic. It is worth noting that increasing the mean tem-

perature of the cloud to 25 K would result in the non-thermal motions being comparable to the sound speed. Whilst there are no gas temperature measurements towards G035.39-00.33, the 15 K estimate is based on the dust temperature maps of Nguyen Luong *et al.* (2011). In these maps, very little temperature fluctuation is observed in the central regions (although these maps are of lower angular-resolution than that studied here). The general trend observed in Figure 3.18 therefore, is not expected to change significantly.

3.5 Discussion

3.5.1 Gas dynamics surrounding continuum peaks

Continuum images confirm that the H6 region has fragmented into multiple cores (see left-panel of Figure 3.16). This is in contrast to the single 1.2 mm continuum peak identified by Rathborne *et al.* (2006) (at 11″ resolution). Between $5'' < \Delta\delta < 40''$, there are 6 continuum peaks in total. Two out of the six cores are associated with observable signatures of star formation, as traced by 4.5, 8, and 24 μm emission (Carey *et al.* 2009, Chambers *et al.* 2009, Jiménez-Serra *et al.* 2010). This implies the presence of embedded protostars. In this section the kinematics surrounding both of these continuum cores, plus a further core located to the east of the H6 marker are discussed.

The continuum peaks discussed in this section have been labelled N, E, and SW, in Figure 3.19. Overlaid are the velocity gradients, closest to the E and SW cores, observed in F2b and F3. The light coloured arrows are identical to those in Figure 3.16, whereas the darker arrows represent the velocity gradients calculated from the $V_{\rm LSR}$ of 27 pixels (i.e. the constraint imposed in Section 3.4.2 has been relaxed). This gives a better idea of the spatial extent of the velocity gradients, but they are not included in any analysis due to their lower significance (see Section 3.4.2 for further description of the velocity gradient analysis).

It is stressed that the arrows in the velocity gradient analysis do not indicate the direction of flow of gas, they simply point towards the direction of increasing velocity. Therefore, depending on the orientation, and physical structure of the cloud, there could be several explanations for the observed velocity structure. In this discussion two *opposing* scenarios are considered that may explain the observed

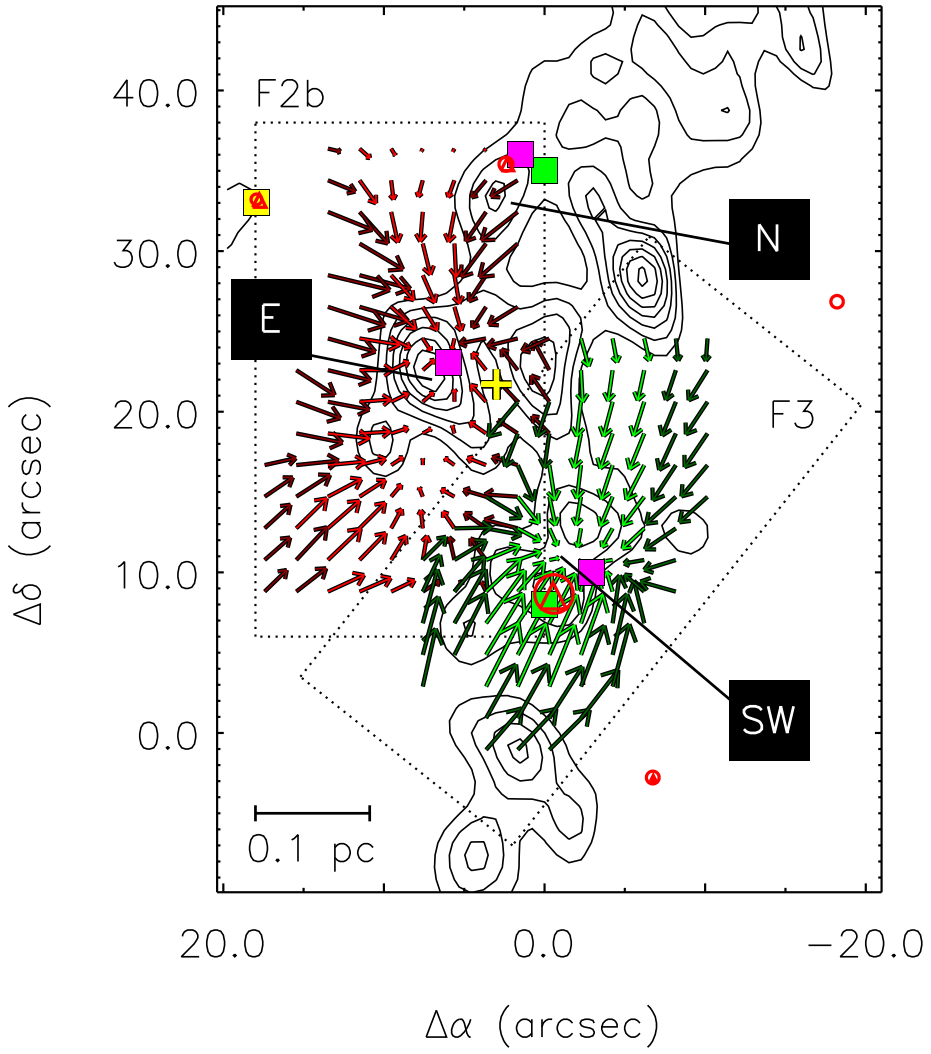

Figure 3.19: A close up image of the region surrounding H6. The size and direction of the arrows correspond to the magnitude and direction of the velocity gradient (pointing in the direction of increasing velocity). Dark green and dark red arrows refer to the velocity gradient calculated at each point, using velocities from the surrounding 27 pixels (note - this is used for a spatial representation only, and not used in the analysis), light green and light red arrows refer to the velocity gradient calculated from the surrounding 38 pixels, for F2b and F3, respectively (see Section 3.4.2 for details). The symbols have the same meaning as in the left panel of Figure 3.16.

pattern of velocity gradients: i) infalling material, and ii) outflowing material.

Scenario 1: Infall

Due to the symmetry in the arrow pattern observed towards the SW core, this continuum peak provides the focus for further discussion. In the infall scenario, the arrows would depict a flow of N_2H^+ converging onto the SW continuum core. The mean magnitude of the velocity gradients towards the SW core is ~ 2.5 km s^{-1} pc^{-1} over a spatial extent of ~ 0.5 pc. This mean velocity gradient is comparable with those observed within the Serpens South cluster-forming region (1.4 km s^{-1} pc^{-1} measured over ~ 0.33 pc; Kirk *et al.* 2013) and the DR21 filament (0.8–2.3 km s^{-1} pc^{-1} measured over $\sim 80''$, equivalent to ~ 0.7 pc using the distance of the DR21 ridge as 1700 pc; Schneider *et al.* 2010a).

Kirk *et al.* (2013) and Friesen *et al.* (2013) interpret the observed velocity gradients in Serpens as flows of material along the filament towards star forming regions. This interpretation arises from making an assumption regarding the geometry of the filament. In the case of the Serpens, assuming the filament is inclined towards the observer, the velocity structure can be interpreted as accretion flows towards the Serpens South Cluster (Kirk *et al.* 2013).

In the case of G035.39-00.33, *if* the velocity gradient is depicting flow of material onto the SW core, the geometry must be different from that observed in Serpens. This is because, rather than a single north–south velocity gradient, there are two opposing velocity gradients. The velocities increase towards a maximum. Geometrically, this *may* be explained by an arced filament.

This geometry is further explored in Figure 3.20. For simplicity, rather than an arc, the filament is assumed to be a "kinked" cylinder, with angles Θ and Φ

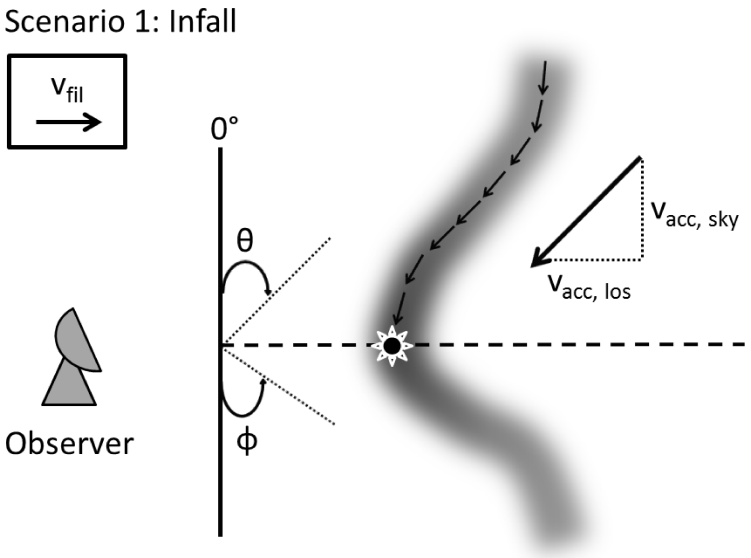

Figure 3.20: A schematic to explain the velocity gradient pattern in Figure 3.19, under the assumption of infalling gas. $v_{\rm fil}$ is the global redshift of F3, Θ is the inclination of the northern part of the filament with respect to the plane of the sky, and Φ is the inclination of the southern part of the filament with respect to the plane of the sky (increasing from the south). In the case shown, $\Theta = 45°$, and $\Phi = 55.6°$ (these have been arbitrarily chosen, although the difference in angles is used to explain the difference in the magnitude in the observed velocity gradient).

representing the inclination of each end of the cylinder with respect to the plane of the sky. Adopting the same reference system as Kirk *et al.* 2013, 0° is parallel to the plane of the sky, whereas 90° lies directly along the line of sight. $v_{\rm acc,sky}$ and $v_{\rm acc,los}$ represent the velocity of the accreting material in both the plane of the sky, and that along the line of sight, respectively.

In the reference frame of the SW continuum peak, the filament gas (to the north and south of the core) is blue-shifted relative to the core (see grey-scale of F3 panel of Figure 3.16). If the filament was structured as shown in Figure 3.20, then this would imply gas accretion *along* filaments towards the core. In the context of the

main IRDC filament ($v_{\rm mean} = 45.8$ km s^{-1}, as calculated from the moment analysis of Section 3.3.1), F3 as a whole is red-shifted. $v_{\rm fil}$ represents the velocity of the F3 system (core + filament), and this is assumed to be equivalent to the velocity at the location of the continuum peak ($\sim 47.4\,{\rm km\,s^{-1}}$). If $v_{\rm acc,los} < (v_{\rm fil} - v_{\rm mean})$, a global red-shift of F3 will be observed with respect to $v_{\rm mean}$.

The mass flow along the filament is estimated by first obtaining an approximate value for the mass contained within the dotted area surrounding the SW core in Figure 3.19. The total mass surface density (taken from KT13) contained within this region is converted to a mass of $\sim 96\,{\rm M_\odot}$. The mass surface density of the filament envelope is estimated by calculating an average value (per pixel) from several polygons, selected to be below a mass surface density of $0.07\,{\rm g\,cm^{-2}}$ (i.e. $10\times$ the lower limit probed by the near infrared extinction map; see KT13 for discussion). Subtracting the estimate for the envelope contribution ($\sim 21\,{\rm M_\odot}$), gives a total mass in this region of the filament of $75\,{\rm M_\odot}$.

This mass estimate incorporates *all* filaments within the dashed area. To estimate the contribution of F3 to the total mass, it is assumed that all filaments have the same (constant) fractional abundance of N_2H^+. By using the intensities and line-widths derived from the Gaussian fitting routine, one can calculate the relative contribution each filament makes to the total mass in the specified area. The percentage contribution F3 makes to the total integrated intensity (and therefore mass) in the area is $\sim 46\%$. The mass contribution of F3 is therefore $(34.5 \pm 17)\,{\rm M_\odot}$ (estimating a $\sim 50\%$ uncertainty in the mass due to 30% and 20% uncertainties in the mass surface density and distance, respectively). This gives a mass per unit length, $M/L_{\rm obs} = m = (69 \pm 37)\,{\rm M_\odot\,pc^{-1}}$, whereby $L_{\rm obs}$ is the observed filament length of $\sim\ (0.5 \pm 0.1)\,{\rm pc}$ (i.e. the length of the dotted box in

Figure 3.19).

The mean line-width ($\Delta\upsilon_{\rm obs}$) of F3 from the Gaussian decomposition in this region is 0.61 $\rm km\,s^{-1}$. The total 1-D velocity dispersion (of the mean molecule) can be calculated using (Fuller & Myers 1992):

$$\sigma_{\rm TOT} = \sqrt{\frac{\Delta\upsilon^2_{\rm obs}}{8{\rm ln}(2)} + k_{\rm B}T_{\rm kin}\left(\frac{1}{\mu m_{\rm H}} - \frac{1}{m_{\rm obs}}\right)} \tag{3.10}$$

whereby μ is the atomic weight of the mean molecule (2.33), and $m_{\rm H}$ is the mass of a Hydrogen atom. The above line-width therefore, corresponds to a 1-D velocity dispersion of $\sigma_{\rm TOT} \sim (0.340 \pm 0.03)$ $\rm km\,s^{-1}$ (this uncertainty incorporates both the error in the measured FWHM (given the Gaussian fitting routine) $\sim 7\%$, and an estimated 33% uncertainty on the temperature, i.e. 15 ± 5 K). The equation for the virial mass per unit length for an isothermal self-gravitating cylinder (Ostriker 1964, Stodólkiewicz 1963) as modified to include the total velocity dispersion of a mean molecule (i.e. including both the thermal and non-thermal contribution to support; Fiege & Pudritz 2000) is:

$$(M/L)_{\rm crit} = m_{\rm crit} = \frac{2\sigma^2_{\rm TOT}}{G}. \tag{3.11}$$

This gives a value of $m_{\rm crit} = (53 \pm 9)\,{\rm M}_\odot\,{\rm pc}^{-1}$, i.e. $m/m_{\rm crit} = 1.3 \pm 0.7$. This value is similar to that derived by Busquet *et al.* (2013) for several filaments in the G14.225–0.506 complex.

The velocity gradients directed towards the continuum peak are not symmetric (north of the central position, and south of this point have mean gradients of ~ 2 $\rm km\,s^{-1}\,pc^{-1}$, and 3 $\rm km\,s^{-1}\,pc^{-1}$, respectively). It is noted however, that this

may simply be a geometric effect caused by the kink in the filament. For simplicity, the velocity gradient at each point is assumed to be constant. Assuming that the northern portion of the filament is inclined at $\Theta = 45°$ (this is an arbitrary choice), would result in the southern portion being inclined by $\Phi = 55.6°$ (or $\Theta = 124.4°$). The flow of mass along the filament, $\dot{M}$, is calculated using (Kirk *et al.* 2013):

$$\dot{M} = v_{\rm acc}\rho A \; = \; v_{\rm acc}m, \tag{3.12}$$

where $v_{\rm acc}$ is the velocity of the accreting material, ρ is the mass density of the filament, A is the area perpendicular to the flow, and m is the mass per unit length. Accounting for projection effects, Equation 3.12 can be rewritten:

$$\dot{M} = \frac{\nabla v M}{tan(\Theta)}, \tag{3.13}$$

using $v_{\rm acc,obs} = \nabla v L_{\rm obs}$, where $v_{\rm acc,obs}$ and $L_{\rm obs}$ are the *observed* line of sight accretion velocity (attributed to the velocity change along the filament), and the observed filament length, respectively (these values are subject to inclination effects). Here, ∇v is the calculated velocity gradient. Assuming an inclination angle of 45.0° north of the core, corresponding to 55.6° to the south (see Figure 3.20), and a velocity gradient, $\nabla v_{\rm acc,los} = (2.0 \pm 0.1)\ {\rm km\,s^{-1}\,pc^{-1}}$ (the mean value calculated north of the core), a total mass accretion rate of $\sim (7 \pm 4) \times 10^{-5}\ {\rm M_\odot\,yr^{-1}}$ is found. Figure 3.21 shows how the mass accretion rate would vary with inclination angle according to Equation 3.13.

A value for the free-fall time of the cylinder, assuming homologous collapse, is

estimated following the analysis of Pon *et al.* (2012):

$$\tau_{1\mathrm{D}} = \tau_{3\mathrm{D}} A \sqrt{\left(\frac{2}{3}\right)}, \tag{3.14}$$

where $\tau_{1\mathrm{D}}$ is the cylinder collapse time-scale, for a cylinder of aspect ratio, A, and where $\tau_{3\mathrm{D}}$ is the classical free-fall time-scale for the collapse of a sphere with an equivalent (constant) volume density ($\tau_{3\mathrm{D}} = \sqrt{[3\pi]/[32G\rho]}$). At a filamentary mass flow rate of $7{\times}10^{-5}\,\mathrm{M_{\odot}\,yr^{-1}}$, $\sim(36 \pm 25)\,\mathrm{M_{\odot}}$ could be accumulated at the central continuum core within an estimated free-fall time of $(5 \pm 3)\times10^{5}$ yrs (for a cylinder of aspect ratio, $\mathrm{A} = \mathrm{L_{obs}}/2\mathrm{r} \sim 2.8 \pm 0.8$, and $\tau_{3\mathrm{D}} \sim (2.3 \pm 0.9)\times10^{5}$ yrs), i.e. similar to the mass of the filament within this region.

A filamentary mass flow of $7{\times}10^{-5}\,\mathrm{M_{\odot}\,yr^{-1}}$ is approximately twice that observed towards the Serpens South cluster ($3{\times}10^{-5}\,\mathrm{M_{\odot}\,yr^{-1}}$; Kirk *et al.* 2013). It is also greater than that traced towards specific continuum peaks in the Serpens South cluster-forming region ($1.4{\times}10^{-5}\,\mathrm{M_{\odot}\,yr^{-1}}$; Friesen *et al.* 2013). In SDC13, Peretto *et al.* (2014) estimate a mass accretion rate of $2.5\times10^{-5}\,\mathrm{M_{\odot}\,yr^{-1}}$ towards the convergence point of three filamentary structures, whose velocity patterns invoke a similar structure to that discussed in Figure 3.20. Towards SDC335.579-0.272 Peretto *et al.* (2013) quote a global mass infall rate of $2.5{\times}10^{-3}\,\mathrm{M_{\odot}\,yr^{-1}}$. However, the quoted *filamentary* mass accretion rate ($7{\times}10^{-4}\,\mathrm{M_{\odot}\,yr^{-1}}$; a factor of 10 larger than that observed in the F3 filament), is the combined accretion rate of 6 filaments. In addition, the mass flow rate within F3 is much smaller than that calculated in Jiménez-Serra *et al.* (2014), i.e. $5{\times}10^{-3}\,\mathrm{M_{\odot}\,yr^{-1}}$, estimated from the velocity gradients observed in CO emission using the IRAM 30 m telescope. This will be discussed further in Section 3.5.2.

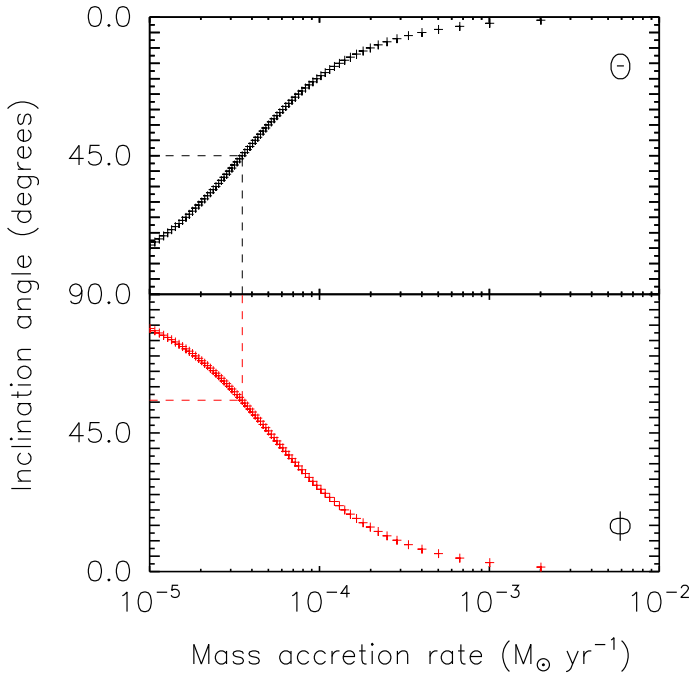

Figure 3.21: Filamentary mass flow rate versus inclination angle for the velocity gradient pattern surrounding the SW core. Highlighted by dashed lines are the mass accretion rates for the northern (black) and southern (red) portions of the filament inclined at angles $\Theta = 45°$ and $\Phi = 55.6°$, respectively (see Figure 3.20). The summation of the two dashed accretion rates gives the total mass accretion rate along filament F3, $\dot{M} \sim 7{\times}10^{-5}\,\mathrm{M_\odot\,yr^{-1}}$.

This velocity pattern is not isolated to this core. Velocity gradients of F2b point towards the 'E' continuum peak (see Figure 3.19). Using the same geometry outlined above for this continuum peak, a similar mass accretion rate of $\sim(8\pm4)\times10^{-5}\,\mathrm{M_\odot\,yr^{-1}}$ is estimated. The mass per unit length of F2b in this region is $(115\pm56)\,\mathrm{M_\odot\,pc^{-1}}$; greater than the critical mass per unit length, $m_{\rm crit} = (59\pm11)\,\mathrm{M_\odot\,pc^{-1}}$, by a factor of $\sim2\pm1$. The free-fall time estimated for this region is $(2\pm1)\times10^5$ yrs (where $L_{\rm obs} = 0.45$ pc, and $r = 0.13$ pc). Therefore, within a single free-fall time, assuming a constant accretion rate, an additional

$\sim (16 \pm 11)\,\mathrm{M}_{\odot}$ of material may accumulate at the continuum peak.

Similar geometry to that illustrated in Figure 3.20 has been previously used to explain filamentary accretion by Balsara *et al.* (2001). Here, material is directed along filamentary structures, decelerating towards a core situated at the apex. In the observation presented here, the magnitude of the velocity gradient decreases towards the central region. However, this alone is not an indication that the mass flow is decelerating towards the centre of the continuum peak.

The reduction in velocity gradient towards the centre is because each gradient is calculated from a relatively large area (see Section 3.4.2). Therefore, towards the centre of the core, the area over which the calculation is performed incorporates velocities that oppose each other (see top-left of F3 panel in Figure 3.16). However, the velocity gradient between the location of peak velocity and the surrounding material can be estimated for a given pixel using:

$$\nabla v_i = \frac{(V_{\mathrm{LSR,peak}} - V_{\mathrm{LSR,i}})}{d}, \tag{3.15}$$

whereby $V_{\mathrm{LSR,peak}}$ is the maximum value of velocity (offset = -2.27″, 10.77″), $V_{\mathrm{LSR,i}}$ is the velocity of a surrounding point, and d is the angular separation between those points. The velocity gradients both to the north, and south of the continuum peak decrease with decreasing angular separation, i.e. $\nabla v_{\mathrm{n}}\,(\,\mathrm{km\,s^{-1}\,pc^{-1}}) = (1.5 \pm 0.1)d + (2.5 \pm 0.1)$, and $\nabla v_{\mathrm{s}}\,(\,\mathrm{km\,s^{-1}\,pc^{-1}}) = (27.2 \pm 0.1)\mathrm{d} + (0.8 \pm 0.1))$, respectively. This implies that the velocity gradient is largest at both ends of the filament, as predicted during free-fall collapse of cylinders (e.g. Myers 2005, Peretto *et al.* 2007, Pon *et al.* 2011). However, it is noted that this decreasing gradient (with respect to the core) may simply be a geometric effect. If the filament has

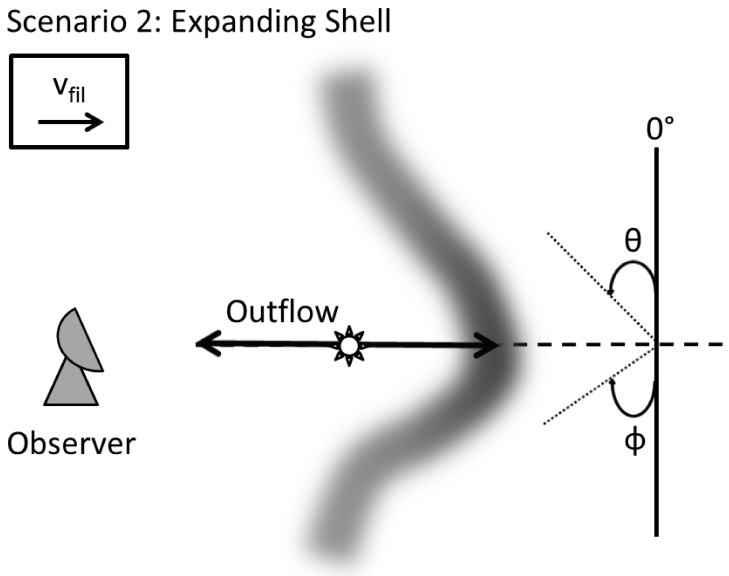

Figure 3.22: A schematic to explain the velocity gradient pattern observed in the top panel, under the assumption that it represents an expanding shell of material. The angles and symbols are identical to Figure 3.20

.

an arc-like structure, a constant accretion velocity may appear as a deceleration towards the core (along the line of sight) as velocity is "lost" to the plane of the sky.

High-angular resolution observations of infall tracers may help to constrain some of the questions this geometry raises (cf. the analysis of Kirk *et al.* 2013 exploiting HNC self-absorption to estimate infall rates).

Scenario 2: Expanding shell

An alternative scenario would involve the opposite geometry to that discussed above. In this case, the N_2H^+ emission and the velocity pattern observed, may be explained by an expanding shell of dense gas (possibly due to the interaction

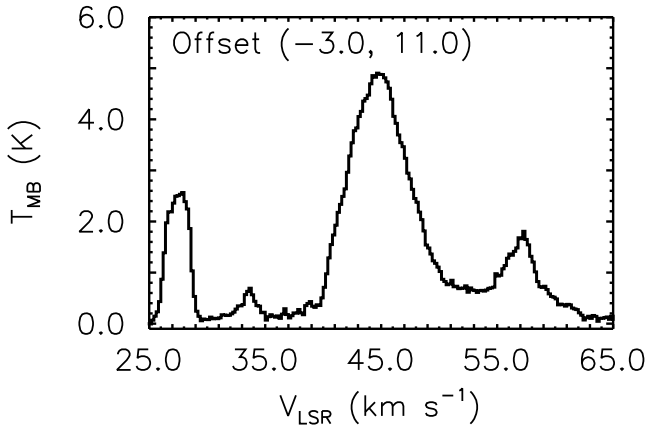

Figure 3.23: CO $(1-0)$ IRAM 30 m data observed towards the SW core (see Section 3.5.1). There is tentative evidence for a high-velocity, red-shifted wing (46.5-49.0 $\mathrm{km\,s^{-1}}$) of emission which may indicate the presence of an outflow towards this location.

of outflows, and/or stellar winds, see Figure 3.22 for a schematic). In symmetry with the infall scenario, only the gas associated with F3 is depicted. The SW peak is coincident with 8 μm, and 24 μm emission. Figure 3.23 is shows a IRAM 30 m ^{12}CO $(1-0)$ spectrum taken towards the location of the SW core. There is tentative evidence for a high-velocity, red-shifted wing. This may indicate the presence of an outflow at this location.

Additional supporting evidence for expanding shells around the protostellar objects in G035.39-00.33, arises from the velocity structure of core labelled 'N' in Figure 3.19. An 'U'-shaped structure (above $10\,\sigma$) is evident in Figure 3.5 between $25'' \lesssim \mathrm{D} \lesssim 50''$ (where 'D' corresponds to the distance along the PV slice), centred on $\sim 40''$ (Figure 3.5). This corresponds to the offset location of core N. Such structures have been discussed by Arce *et al.* (2011), who have modelled expanding

bubbles in a turbulent medium and applied this to shell-like structures in Perseus. If the source is located in the centre of the filament, a ring-like structure will be observed in the PV plane. However, Arce *et al.* (2011) show that if the source is located to the near, or far side of the natal filament/cloud, then emission (of the filament/cloud) in the PV plane would be in a U-shape, either red-shifted or blue-shifted away or towards the observer, respectively. Relating this back to core N, the observed emission pattern in the PV analysis may indicate the interaction between an embedded protostar and the surrounding dense gas (and this may therefore be analogous to the SW core).

Similar structures are also observed towards the SW core (see 'C'-shaped structures in slices B4–B6 in Figure 3.8, which dissect the SW core). However, such patterns may simply be explained due to the emergence of additional components (also note that F3 is detected away from the SW core; see slices A0–A4 in Figure 3.7). This is therefore inconclusive.

It is noted that the velocity gradient arrows of F2a show a similar pattern to those seen in F3, but in the opposite direction, i.e. arrows point away from the SW core (see Figure 3.16). The fact that the apex of both the F2a and F3 structures are not directly coincident (there is a projected separation of the apex of 0.17 pc), could be explained by a non-symmetric interaction between the outflow and the cloud.

The expanding shell scenario would suggest that the SW continuum core is situated at an intermediate velocity between F2a and F3 (i.e. at a velocity most similar to F2b ~ 46 km s^{-1}). One can crudely estimate the momentum of the swept up material using:

$$P_{\rm shell} = M_{\rm shell}(V_{\rm LSR,peak} - V_{\rm LSR,edge}), \tag{3.16}$$

whereby $M_{\rm shell}$ is the mass of the shell (i.e. of filament F3) estimated in the previous section ($34.5 \pm 17\,{\rm M}_{\odot}$), $V_{\rm LSR,peak}$ is the peak velocity in the system, and $V_{\rm LSR,edge}$ is the velocity at the boundary of the velocity gradient analysis. The velocity difference ($V_{\rm LSR,peak} - V_{\rm LSR,edge}$) is ~ 0.7 km s^{-1}, which gives a momentum of $\sim 24 \pm 12\,{\rm M}_{\odot}$ km s^{-1}. This momentum is smaller than those observed towards expanding shells in Perseus (typical values $> 100\,{\rm M}_{\odot}$ km s^{-1}, although it is dependent on the mode of star formation; Arce *et al.* 2011). In addition, the observed spatial extent of the Perseus shells are larger (~ 1 pc, compared with 0.2-0.3 pc in G035.39-00.33). However, Quillen *et al.* (2005) report smaller cavities (of the order 0.1–0.2 pc), with velocity widths $\sim$1-3 km s^{-1} in NGC 1333, comparable to the peak velocity difference between F2a and F3 (see Figure 3.15). In this scenario, "filaments" or, more correctly, shells in G035.39-00.33 may have originally made up a single structure that has subsequently separated as a natural consequence of the dynamic process of star formation.

It must be noted however, that whilst there is *some* evidence for broad red-shifted emission of CO (1-0) at the SW core, no blue-shifted emission is evident at the location of the F2a apex. In addition, in the region of the SW core, filaments F2a and F3 provide contributions of 49% and 46%, to the total integrated intensity (the remaining 5% is attributed to F2b), respectively. This would suggest therefore, that if the continuum peak was situated at an intermediate velocity, this position is almost devoid of N_2H^+ emission, as it has been "swept up" by the expanding shell. However, N_2H^+ emission is typically detected in the regions surrounding forming protostars (at an equivalent scale to the PdBI observations ~ 15000 au; e.g. Fontani *et al.* 2008, Tobin *et al.* 2013). This may indicate that the SW protostar is significantly influencing the surrounding environment, and

the N_2H^+ abundance has reduced as a consequence. Finally, as evidenced in Figure 3.17, no obvious broadening of the lines is observed towards the apex of these structures. If F2a and F3 are treated as a single (expanding shell) entity, as in the moment analysis of Figure 3.1, a broadening of the dispersion is observed. However, as can be clearly seen from offset location (-4.24″, 10.77″) in Figure 3.12, there are two *Gaussian* components, that show no evidence of line-wings. Follow-up high-angular resolution observations of molecular outflow, and shocked gas tracers are needed in order to validate this scenario.

3.5.2 Disentangling the complex kinematics of G035.39-00.33

Interpreting velocity components: Independent structures or projection effects?

The "simple" picture of G035.39-00.33 appearing as a single filamentary structure in the extinction map of KT13, is a deceptive one. Previous single-dish studies (Chapter 2, Jiménez-Serra *et al.* 2010, 2014) have revealed that G035.39-00.33 in fact comprises multiple filamentary structures along the line of sight. Moreover, these filaments overlap towards the position of the most massive core in the region, H6 (Chapter 2, Jiménez-Serra *et al.* 2014). Large-scale kinematic studies revealed the presence of three filaments, filament 1, 42.95 ± 0.17 km s^{-1}; filament 2 (the main IRDC filament), 45.63 ± 0.03 km s^{-1}; and filament 3, 46.77 ± 0.06 km s^{-1} (Chapter 2). Due to the high-angular resolution of this study, it is evident that filament 2 can be resolved into two separate structures, F2a (45.34 ± 0.04 km s^{-1}) and F2b (46.00 ± 0.05 km s^{-1}). In addition, the high-angular resolution PdBI map

reveals that individual filaments can be both spectrally, and spatially resolved (see Section 3.3.1).

Figure 3.24 highlights the "spine", i.e. the peak intensity for each filamentary structure identified in the PdBI data (as derived from the fitting routine outlined in Appendix A.2). This image has been generated by calculating an intensity-weighted offset right-ascension for every offset declination. The decomposition of G035.39-00.33 into multiple velocity components bears striking resemblance to the intricate filamentary structure observed in the L1495/B213 complex in Taurus identified by Hacar *et al.* (2013). In L1495/B213, a total of 35 structures have been identified. In addition, these filaments can be grouped into several "bundles" based on their chemical and kinematic properties. Hacar *et al.* (2013) suggest a possible hierarchical route of fragmentation from cloud $\rightarrow$ bundles $\rightarrow$ filaments $\rightarrow$ cores. In the case of G035.39-00.33, given the discussion posed in Section 3.5.1, it is interesting to ask the question, '*are the observed filaments part of the initial conditions of star formation, or are they a consequence of projection effects, and/or protostellar feedback*?'

Previous single-dish studies, Chapter 2 and Jiménez-Serra *et al.* (2014), noted the presence of a large-scale ($\sim$ 2–3 pc) velocity gradient, with Jiménez-Serra *et al.* (2014) suggesting several plausible reasons for its origin. One scenario involves global accretion of material onto H6, along filament 2. In this scenario, estimating a mass accretion rate gives a value of the order $5{\times}10^{-3}\,\mathrm{M}_{\odot}\,\mathrm{yr}^{-1}$, two orders of magnitude greater than the mass accretion rate estimated towards cluster forming regions in the Serpens molecular cloud (Friesen *et al.* 2013, Kirk *et al.* 2013). This may suggest that F2a and F2b actually represent a change in velocity (i.e. from low-to-high velocity), but are in fact still part of the same parent structure

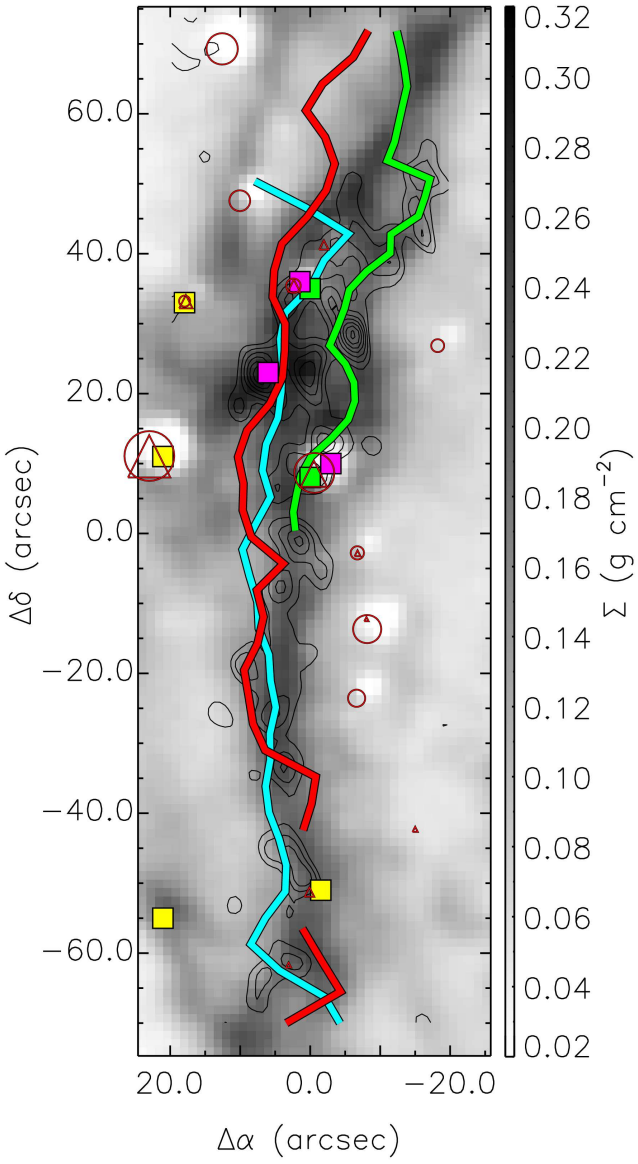

Figure 3.24: The peak intensity "spine" of each filament in G035.39-00.33(see text for details), overlaid on the mass surface density map of KT13, and the 3.2 mm continuum contours. Cyan, red, and green refer to filaments F2a, F2b, and F3, respectively. The additional symbols, and contour values are identical to those in Figure 3.16.

(filament 2). This "jump" in velocity would be similar to the velocity structure of collapsing filaments generated in numerical simulations of colliding flows by Gomez & Vazquez-Semadeni (2013). However, in order to simultaneously observe two spectral velocity components (as opposed to a single component that exhibits an abrupt change in velocity at the location of star formation; Gomez & Vazquez-Semadeni 2013) over a large spatial extent (as is observed in G035.39-00.33; see Figure 3.24), the filament would have to be aligned close to the line of sight. Whilst this cannot be ruled out, G035.39-00.33 is extended over several parsecs in the plane of the sky, and therefore this seems unlikely.

An alternative scenario would be that F2a and F2b may represent the *radial* collapse of the filaments. This would explain why two spectral features are observed over a large spatial extent. In this scenario, F2a and F2b would represent the front and back of an inclined, radially collapsing filament. By inference therefore, this would mean that the N_2H^+ is depleted at intermediate velocities (as the optical depth of the isolated components is typically $\tau < 1$, as seen in Section 3.3.3). Although depletion of N_2H^+ has been observed towards low-mass starless cores (e.g. Bergin *et al.* 2002, Caselli *et al.* 2002b), the observed abundance decrease is typically limited to a factor of ~ 2. In addition, it is clear from Figure 3.10 that the observed integrated N_2H^+ emission rises with increasing mass surface density, suggestive of optically thin conditions and negligible depletion (in fact, there is some indication that the N_2H^+ abundance actually increases towards regions of high extinction).

The PdBI data therefore imply that the global north-south velocity gradient observed in single-dish data may, in fact, be explained by the presence of substructure within "filament 2" (i.e. F2a and F2b). Smith *et al.* (2013), using model

emission profiles from hydrodynamic simulations of a collapsing cloud, show that multiple velocity components are common in optically thin molecular line tracers in massive star forming regions. Moreover, they show that the degree of multiplicity increases with greater angular resolution. This is analogous to the contrast between line-profiles observed in chapter 2 and this chapter. This also confirms that high-angular resolution observations are a necessity when investigating the complex kinematics of massive star forming regions.

The PdBI data indicates that the gas motions are dominated by *local* velocity gradients of the order $\sim$1.5–2.5 km s^{-1} pc^{-1}, whereas global velocity gradients, and those observed in the north–south direction are smaller by comparison ($\sim$0.7 km s^{-1} pc^{-1}, and $<$0.3 km s^{-1} pc^{-1}, respectively; see Section 3.4.2). Given that the filaments are resolved spectrally, have differing velocity patterns, and (in the case of F2a/F2b and F3) are resolved spatially (cf. Figure 3.3), they are identified as independent structures.

Complex velocity patterns

Away from H6, in the very south of F2a ($\Delta\delta <$ -50″) and in the north of F2b ($\Delta\delta >$ 40″), uniform gradients in the east $\rightarrow$ west direction are observed. In addition, the velocity pattern observed in F2a at offset (8″, -30″) indicates that velocity increases towards the centre of the filament (see also Figure 3.1). This feature is spatially coincident with a localised increase in the velocity dispersion (see Figure 3.17). Gradients such as these do not seem to be associated with any specific continuum peak. Thus, it is possible that these gradients may represent global motion of the filaments, rather than those related to the early stages of star formation (as mentioned in Section 3.3.2).

The non-thermal motions of G035.39-00.33's sub-filaments are *mildly* supersonic. The mean velocity dispersion (as calculated from the Gaussian fitting routine) across all three filaments is ~ 0.33 km s^{-1}. Whilst the derived supersonic line-widths are in contrast to low-mass star forming filaments (e.g. Hacar *et al.* 2013, who find $\sigma_{\rm NT}/c_{\rm s} \sim 0.61 \pm 0.17$ km s^{-1}, using N_2H^+ towards the L1495/B213), they are narrower than those observed towards other IRDCs. Sanhueza *et al.* (2012) find that broad N_2H^+ line-widths are correlated with the star formation activity of clumps. They find line-widths in the range 1.6–4.6 km s^{-1} (corresponding to dispersions of $\sim$0.7–2.0 km s^{-1}). Higher-spectral resolution studies are needed to verify results such as these in regions where a broad velocity dispersion may be explained by presence of unresolved spectral features. In regions where multiple spectral features are evident, moment analysis misleadingly indicates a larger dispersion than that of the individual components (by a factor of ~ 2; see Figure 3.1, and the spectrum at offset = -4.24″, 10.77″ in Figure 3.12, for example). Gaussian decomposition of the spectra is therefore necessary to establish the velocity dispersion of *individual* filaments.

The left hand panels of Figure 3.25 show how the non-thermal velocity dispersion of each individual filament changes with respect to the main beam brightness temperature at all positions in the cloud. In Hernandez *et al.* (2012), the total velocity dispersion derived from the $C^{18}O$ $(2-1)$ was identified to decrease towards the central, and dense portion of G035.39-00.33. Similarly, in Jiménez-Serra *et al.* (2014), the relationship between the non-thermal dispersion and $T_{\rm MB}$ was studied for CO isotopologues, ^{13}CO $(2-1)$, ^{13}CO $(3-2)$, and $C^{18}O$ $(2-1)$. In all cases $\sigma_{\rm NT}$ was shown to increase with decreasing $T_{\rm MB}$ with a power law trend. The dependency of $\sigma_{\rm NT}$ on $T_{\rm MB}$ was also shown to decrease with the increasing critical

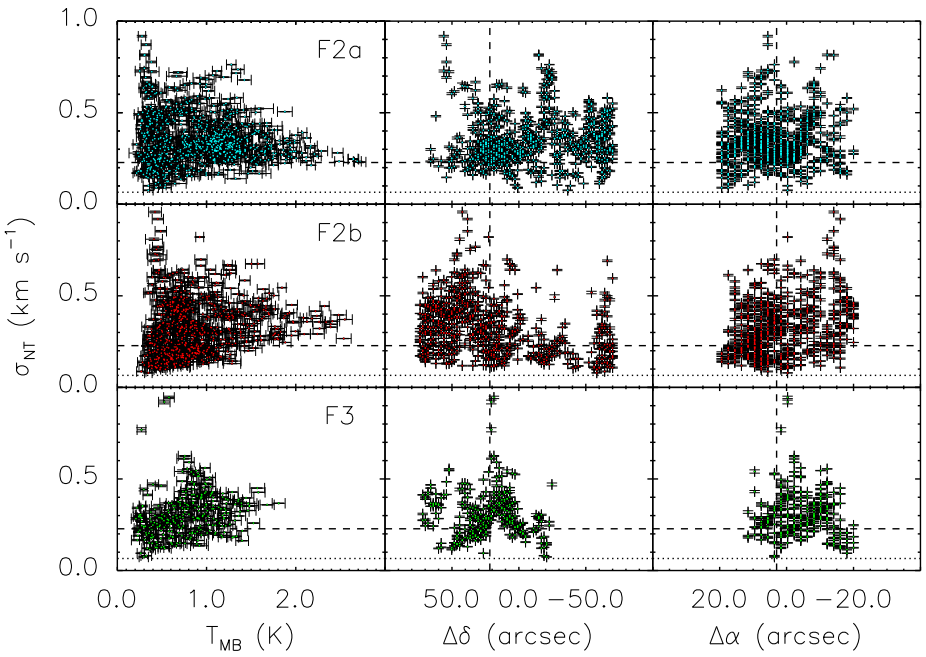

Figure 3.25: Non-thermal velocity dispersion ($\sigma_{\rm NT}$) for F2a, F2b, and F3, derived from N_2H^+ FWHM for every position in the cloud, versus (from left-to-right) main beam brightness temperature ($T_{\rm MB}$), offset declination ($\Delta\delta$), and offset right ascension ($\Delta\alpha$), respectively. In each plot, the horizontal dotted and horizontal dashed lines refer to the approximate thermal velocity dispersion for N_2H^+ at 15 K ($=0.066$ km s^{-1}), and the sound speed for a mean molecular mass of 2.33 a.m.u ($=0.23$ km s^{-1}), respectively. Vertical dashed lines refer to the location of H6 ($\Delta\delta = 21.71''$, $\Delta\alpha = 2.99''$), from BT12.

density of molecular line tracers. In Figure 3.25, a similar trend for filaments F2a and F2b is found, in that there is an overall decrease of the non-thermal component with increasing brightness. In Pineda *et al.* (2010), studying star formation in the B5 region of Perseus, intensity (in this case antenna temperature) is used as a proxy for density. The trend of decreasing turbulent motion with increasing intensity therefore represents a "transition to coherence" within close proximity to the location of star forming cores.

In contrast to filaments F2a and F2b however, turbulent motion actually increases towards H6 in filament F3. This is evident in the central, and right-hand panels of Figure 3.25. Here, the relationship between $\sigma_{\rm NT}$, offset declination (central panels), and offset right ascension (right-hand panels) is plotted for each filamentary structure in G035.39-00.33. In the central and right-hand panels of F3, it is evident that the broadest lines, and therefore the lines with the greatest non-thermal component, are spatially coincident with H6. In low-mass star-forming regions, pre-stellar cores show slight ($\sim$60%) line broadening towards their centres, possibly due to the infall of material (Crapsi *et al.* 2005). In G035.39-00.33, this peak is not directly coincident with the SW continuum core discussed in Section 3.5.1. Instead, the peak in the non-thermal velocity dispersion is coincident with a starless core to the north of here (see Figure 3.17). Higher-angular resolution observations of higher-density tracers are needed in order to understand the behaviour of star forming cores in relation to the surrounding dense filamentary material.

3.6 Conclusions

This chapter has presented a detailed kinematic study using high-sensitivity and high-spectral resolution PdBI observations of N_2H^+ (1-0) towards G035.39-00.33. The results and analysis lead to the following conclusions:

1. Multiple filaments are identified both spectrally and spatially. F2a, F2b, and F3 have mean centroid velocities of 45.34 ± 0.04 km s^{-1}, 46.00 ± 0.05 km s^{-1}, 46.86 ± 0.04 km s^{-1}, respectively.

2. The abrupt change in velocity noted at the location of H6 (Chapter 2, Jiménez-Serra *et al.* 2014), rather than being indicative of large scale flows towards H6, may be explained due to the decomposition of filament 2 into two filaments (F2a and F2b).

3. F2a, F2b, and F3 have mean line-widths (FWHM) of (0.83 ± 0.04) km s^{-1}, (0.77 ± 0.04) km s^{-1}, and (0.71 ± 0.04) km s^{-1}, respectively. The ratio of non-thermal to thermal (for N_2H^+) velocity dispersion for each velocity component is 5.4, 5.0, and 4.7, respectively. The ratio of the non-thermal component of the line-width to the isothermal sound speed for an average molecule (mass = 2.33 a.m.u.) at 15 K are 1.6, 1.4, and 1.4, respectively. This indicates that the gas motions are *mildly* supersonic. In regions where multiple spectral components are evident, moment analysis can overestimate the non-thermal contribution to the line-width by a factor $\gtrsim 2$.

4. Globally, the kinematics of the gas are relatively quiescent, indicated by the small velocity gradients observed over each filament (of the order $<$

0.7 $\mathrm{km\,s^{-1}\,pc^{-1}}$). Locally, however, the mean velocity gradients can reach $\sim$ 1.5–2.5 $\mathrm{km\,s^{-1}\,pc^{-1}}$.

5. There is some indication that the kinematics of the dense gas may be influenced by the self-gravity of dense cores within filaments, or possibly by outflow feedback from already forming stars. Further molecular line observations are required to discern between these two scenarios. For these two opposing scenarios the following has been calculated:

   (a) *Infall*: The mass accretion rate is estimated to be $\sim (7 \pm 4) \times 10^{-5}\ \mathrm{M_\odot\,yr^{-1}}$. The filaments retain their structure within the vicinity of H6, and individual filaments appear to feed individual cores. The SW continuum core could accrete an additional $(36 \pm 25)\,\mathrm{M_\odot}$, in an estimated free-fall time of $(5 \pm 3) \times 10^5$ yrs.

   (b) *Expanding shell*: The momentum for the expanding shell is estimated to be $\sim (24 \pm 12)\,\mathrm{M_\odot\ km\,s^{-1}}$. The dense filamentary structures may have been separated from the main body of IRDC material due to the dynamic processes of star formation.

This analysis highlights the importance of combining high-sensitivity and high-spectral resolution data at high-angular resolution, to put quantitative constraints on the dynamics of high-mass star forming regions.

Chapter 4

Unveiling the core population of the filamentary infrared dark cloud G035.39–00.33

4.1 Introduction

Whether or not massive stars form through a similar mechanism to low-mass stars, or by means of a different paradigm is an open question (see Section 1.2). Intermediate and massive stars may be born from relatively high-mass pre-stellar cores which are more massive than the thermal Jeans mass. Understanding and categorising the initial conditions for star formation would not be complete without studying the *physical* properties of the pre- and protostellar cores out of which stars form.

IRDCs have long been discussed in the context of massive star and stellar cluster formation (e.g. Battersby *et al.* 2010, Rathborne *et al.* 2006). More recently,

IRDC clumps and cores have been subjected to targeted follow-up observations at high-angular resolution attempting to verify their status as the pre-cursors to massive stars (e.g. Rathborne *et al.* 2007, Tan *et al.* 2013b, Wang *et al.* 2014). Such studies have revealed hierarchical fragmentation in dense molecular gas from the clump-scale down to 0.01 pc. Typically, the mass of the fragments is significantly greater than the Jeans mass. This indicates that turbulence and/or magnetic fields may play a significant role in the earliest stages of clustered star formation.

The previous chapters have presented in-depth analysis of both the large- and small-scale kinematics of G035.39-00.33. Chapter 2 revealed that the image of G035.39-00.33 as a single filament (as can be seen in the mass surface density map of Figure 2.2), is deceptive. G035.39-00.33 comprises a complex network of filamentary structures. Chapter 2 also suggested that these filaments appear to overlap towards the densest core in the map, H6. Chapter 3 revealed that at high-angular resolution, the velocity field of each of these filaments is complex, with local gradients dominating over global gradients. Moreover, the kinematics of the gas appears to be influenced by the presence of continuum cores.

To date, no attempt has been made to identify the core population of G035.39-00.33 at high-angular resolution. The aim of this chapter is to reveal the underlying embedded core population and level of fragmentation, as well as establishing masses, densities, and sizes of the star-forming cores within G035.39-00.33. By incorporating the wealth of kinematic information extracted in Chapters 2 and 3 the dynamical state of the cores will also be determined. The ultimate goal of this chapter is to understand the star formation potential of IRDC G035.39-00.33.

This chapter is organised as follows: Details of the observations can be found in Section 4.2. The observational results and the methodology used to identify

structure within the data is described in Section 4.3. In Section 4.4 the physical parameters of identified structures are extracted. The findings are discussed in Section 4.6 before being concluded in Section 4.7.

4.2 Observations

4.2.1 Plateau de Bure Interferometer

The 3.2 mm continuum observations were carried out using the IRAM PdBI, France. A 6-field mosaic was used to cover the inner area of the IRDC as can be seen in Figure 4.1. The final map size is $\sim 40'' \times 150''$ (corresponding to $\sim 0.6\,\mathrm{pc} \times 2.1\,\mathrm{pc}$, at a distance of 2900 pc). Further details of the observations can be located in Chapter 3. The 3.2 mm continuum data was CLEANed using the Hogbom algorithm. Line-free channels give a total bandwidth of ~ 3 GHz. The natural weighting of the data results in a synthesised beam of $4.2'' \times 3.1''$, with a position angle of 17.3°. The typical rms map noise level is $0.07\,\mathrm{mJy\,beam^{-1}}$ as approximated from emission-free regions.

The analysis within this chapter utilises the N_2H^+ $(1-0)$ data discussed further in Chapter 3. Both the merged PdBI and IRAM 30 m data, and the PdBI-only data are shown. The PdBI-only data have been reduced in the same manner as the merged data set (more details on the reduction can be found in Chapter 3). The resulting synthesized beam has angular size $3.9'' \times 3.1''$ (position angle = 33°).

4.2.2 Submillimeter Array

The 1.3 mm continuum data was observed using the Submillimeter Array (hereafter, SMA), in the subcompact configuration[1]. Observations were performed in a single track in March 2011. The phase centre of the observations was set at

[1]Proposal: "The initial conditions of massive star and star cluster formation in IRDCs.", PI: Izaskun Jiménez-Serra

$\alpha(\mathrm{J2000}) = 18^h57^m08^s.00$, $\delta(\mathrm{J2000}) = 02°10'50''.0$ (i.e. towards the H6 region). The receivers were tuned to an LO frquency of 218.112 GHz and the correlator provided a spectral resolution of 3.25 MHz (i.e., $\sim$4.5 km s^{-1}). The continuum emission was extracted using the line-free channels from a maximum available bandwidth of 6.6 GHz. Four higher spectral resolution chunks were used to extract line data (not discussed here).

The data calibration was carried out within the IDL MIR[1] software package. Continuum subtraction, imaging, and deconvolution were performed in MIRIAD. The synthesised beam has dimensions $6.7'' \times 5.1''$, with a position angle of -36.6°. Following CLEANing, the map centre was then re-projected to the centroid coordinates of the PdBI observations.

[1] `https://www.cfa.harvard.edu/cqi/mircook.html`

4.3 Observational results: identifying substructure

The left-hand panel of Figure 4.1 shows the spatial extent of the PdBI 6-field mosaic (dotted circles) with respect to the mass surface density map of G035.39-00.33 (KT13). The 3.2 mm continuum emission is overlaid in black contours. Contour levels begin at $3\,\sigma$, and increase in $2\,\sigma$ steps (where $\sigma \sim 7{\times}10^{-2}\,\mathrm{mJy\,beam^{-1}}$). In addition, the locations of extended 4.5 μm emission (otherwise known as Extended Green Objects; EGOs; Cyganowski *et al.* 2008) are shown as green squares (Chambers *et al.* 2009). The positions of 8 μm and 24 μm sources are overlaid as red circles, and red triangles, respectively (Carey *et al.* 2009, Jiménez-Serra *et al.* 2010). Massive ($> 20\,\mathrm{M_\odot}$) and low-mass cores reported by Nguyen Luong *et al.* (2011) are overlaid as Cyan and Yellow squares, respectively. Finally the locations of the most massive 1.2 mm continuum peaks are plotted as black crosses (Rathborne *et al.* 2006).

Rathborne *et al.* (2006), using observations of 1.2 mm continuum emission from the IRAM 30 m telescope ($11''$ resolution), identified only a single 'core' in the region mapped using the PdBI, MM7 (hereafter H6; BT09). Figure 4.1 reveals G035.39-00.33 harbours multiple cores that are spatially coincident with the regions of greatest extinction. Close-up images of H6 are displayed in the right-hand panels of Figure 4.1. The top panel is the PdBI 3.2 mm data, whereas the bottom panel displays the 1.3 mm SMA data. The peaks identified in the SMA data can be located in the PdBI image, however, the PdBI data reveals substructure not detected by the SMA. This is due to the factor of ~ 2 increase in angular resolution.

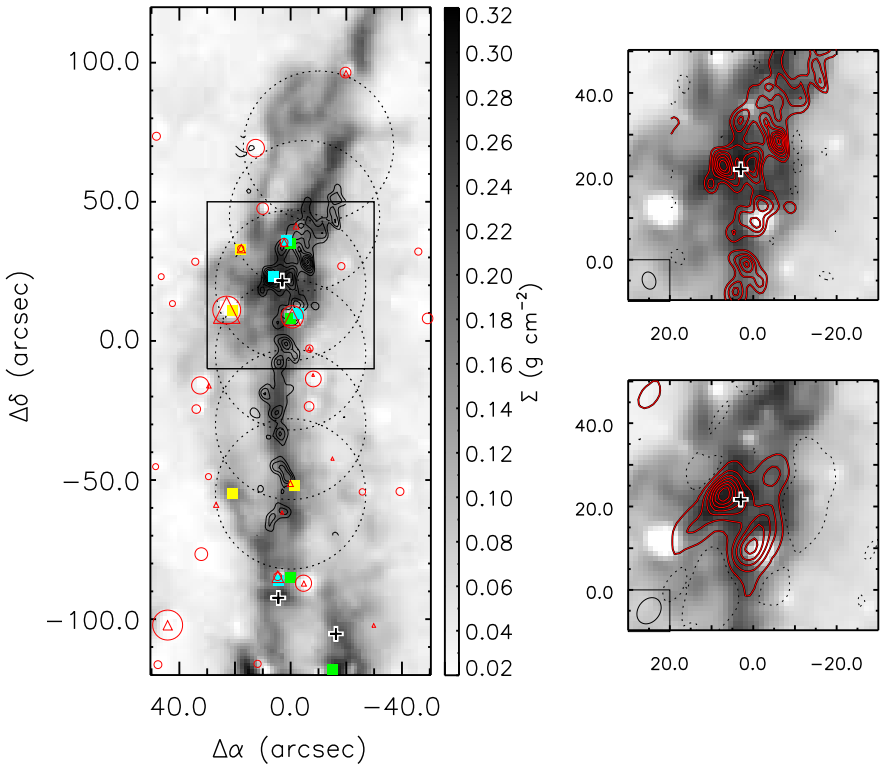

Figure 4.1: Left: The mass surface density plot of KT13 (grey-scale) overlaid with 3.2 mm continuum contours. Contour levels start at $3\,\sigma$ and increase in steps of $2\,\sigma$ (where $\sigma \sim 7 \times 10^{-2}$ mJy beam^{-1}). Dotted circles indicate the 6-field mosaic performed with the PdBI. Cyan and yellow squares refer to the high-mass and low-mass dense cores identified in Nguyen Luong *et al.* (2011). Red circles and red triangles refer to the 8, and 24 μm emission, respectively (Carey *et al.* 2009, Jiménez-Serra *et al.* 2010), and green squares refer to the "green fuzzies" (extended 4.5 μm emission) identified by Chambers *et al.* (2009). Right-top: Close-up image of the square in the left-hand panel enclosing the H6 region (contour levels are the same as the left-hand panel). The PdBI beam ($4.2'' \times 3.1''$; P. A. =17.3°) is indicated in the bottom left-hand corner. Right-bottom: 1.3 mm Submillimeter Array continuum contours. Contours start at $3\,\sigma$, and increase in $9\,\sigma$ steps (where $\sigma \sim 0.3$ mJy beam^{-1}). The SMA beam ($6.7'' \times 5.1''$; P. A. = -36.6°) is indicated in the bottom left-hand corner. In both cases the dotted contour refers to the negative $2\,\sigma$ level.

4.3.1 Methodolgy: dendrograms

In order to extract information on the observed continuum peaks, a form of structure tree analysis is used. Dendrograms have become a popular technique to understand structure in astronomical data (Goodman *et al.* 2009, Houlahan & Scalo 1992, Kirk *et al.* 2013, Rosolowsky *et al.* 2008). This technique is desirable as the primary function is to detect *hierarchical* structures within data, thus allowing one to compare the properties of cores to those of their natal clumps. This analysis uses ASTRODENDRO[1], a Python package used to compute dendrograms from astronomical data.

Dendrograms are split into three main components: trunks, branches, and leaves. To compute the dendrogram, it is stipulated that significant emission lies above the $3\,\sigma$ threshold ($\sim 0.2\,\mathrm{mJy\,beam^{-1}}$ and $0.9\,\mathrm{mJy\,beam^{-1}}$, for the 3.2 mm PdBI and 1.3 mm SMA data, respectively). This defines the *trunk* of the dendrogram (although it is possible for structures to not have any parent material). Secondly, each subsequent structure must be $> 2\,\sigma$ above the value of its parent material. This identifies *branches* (or leaves), embedded within parent material (i.e. the trunk or branch). Thirdly, a *leaf* must include (at least) the equivalent number of pixels as there would be in the synthesised beams of either the PdBI or SMA data (24 and 32, respectively). A leaf is the final piece in the dendrogram hierarchy, and represents the limit imposed by angular resolution.

The ASTRODENDRO package calculates the location, area, peak, and total fluxes of the identified structures. The sizes of the dendrogram leaves are estimated using

[1] `http://www.dendrograms.org/`

the effective radius, $R_{\rm eff}$:

$$R_{\rm eff} = \sqrt{\frac{N_{\rm pix} A_{\rm pix}}{\pi}}, \tag{4.1}$$

where $N_{\rm pix}$ is the total number of pixels that have an area $A_{\rm pix}$. This value corresponds to the radius of a circle that would have the equivalent area of the dendrogram structure (i.e. spherical geometry is assumed). The final radius is expressed following deconvolution with the synthesized beam of the data, using the following equation:

$$R_{\rm decon} = \frac{[(2R_{\rm eff})^2 - (\theta_{\rm mean})^2]^{1/2}}{2}, \tag{4.2}$$

where $\theta_{\rm mean}$ is the geometric mean of the major and minor axes of the synthesized beam. If however, $R_{\rm decon} < \theta_{\rm mean}/2$, i.e. where a source is only marginally resolved, then $R_{\rm eff}$ is used for the radius. In the following sections, when reference is made to the 'radius' of a given structure, the above considerations are implicit.

4.3.2 The hierarchical structure of G035.39–00.33

The upper left-hand image of Figure 4.2 is a surface plot of the 3.2 mm continuum emission. The intensity of the emission increases from blue to red, highlighting the substructure within G035.39-00.33. The result of the dendrogram analysis can be found in the lower left-hand plot of Figure 4.2. The y-axis corresponds to the peak flux of each structure. Leaves are denoted by coloured vertical lines. The local merge levels that stem from branches (i.e. the average flux level of the parent structure to which multiple leaves are embedded), are indicated by horizontal lines. In total, 14 leaves are identified. The mean radius of the leaves is ~ 0.04 pc, comparable to the observed sizes of IRDC cores (e.g. Tan *et al.* 2013b). Each leaf is denoted by the prefix PdBI and an ID number in Table 4.1 (designated in order

of increasing offset declination). There are two main parent structures, the first of which contains the leaves in the region of H6 (from PdBI 8–14), and the second is just south of here (leaves PdBI 3–7). PdBI 1 & PdBI 2 merge with the other leaves at a flux of $\sim 2\,\sigma$, indicating that all continuum leaves have the same parent structure[1]. Information regarding identified leaves is presented in Table 4.1.

The right-hand plot of Figure 4.2 shows the location of the dendrogram leaves overlaid on the 3.2 mm continuum map (grey scale). Each number corresponds to the leaf ID in the dendrogram plot in the left-hand panel. Leaves that have no associated 4.5, 8, or 24 μm emission (i.e. where no IR emission is *spatially coincident*) are colour-filled. Those leaves that overlap spatially with IR emission sources are not filled. These leaves are also represented as dashed lines in the dendrogram plot. Hereafter, leaves are referred to as being either IR dark and IR bright, respectively. The prospect that IR bright and IR dark leaves represent two distinct populations will be discussed further in Section 4.6.2.

The left-hand panel of Figure 4.3 is the dendrogram extracted using the 1.3 mm SMA data (to be compared with PdBI 8-14 in Figure 4.2). Only 2 leaves are identified (these are denoted by the prefix SMA and then an ID number designated in order of increasing offset declination). Once again, any leaf spatially coincident with either 4.5, 8, or 24 μm emission is shown as both a dashed line in the dendrogram, and an non-colour filled contour in the continuum map. The larger radii of the identified SMA leaves (mean radius ~ 0.065 pc compared with 0.04 pc for the PdBI leaves) is consistent with the lower angular-resolution of the SMA data.

In this analysis, and specifically in relation to the PdBI data, the term 'fila-

[1]It is important to note that this may not be the case if one was to include additional velocity information.

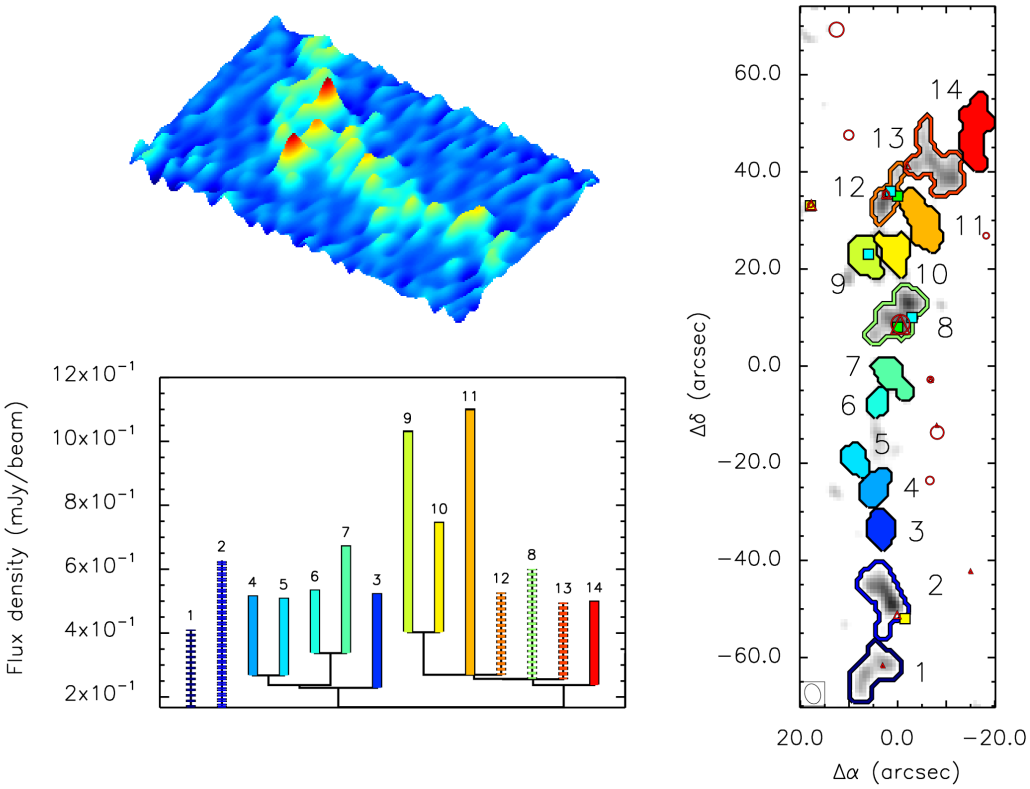

Figure 4.2: Left-top: The 3.2 mm PdBI continuum flux as a 3-D surface plot, highlighting the continuum peaks to be identified in the dendrogram analysis. Left-bottom: The dendrogram tree structure of G035.39-00.33. Leaves are indexed in increasing value of offset declination. Right: The PdBI 3.2 mm continuum map highlighting the spatial extent of the leaves identified in the dendrogram on the right. Each leaf is colour coded and labelled. Non-colour-filled contours correspond to those leaves that are spatially coincident with either 4.5, 8, 24 μm emission (or some combination of these; Carey *et al.* 2009, Chambers *et al.* 2009, Jiménez-Serra *et al.* 2010), which further correspond to the dashed lines in the dendrogram.

ment' is used to describe the largest structure identified in the dendrogram, which encompasses multiple all leaves. As discussed above, two main clumps are identified within G035.39-00.33, one incorporating the H6 leaves, hereafter referred to as the H6 clump, and one to the south of here, hereafter referred to as the narrow clump (due to its association with the darkest, and most narrow, filamentary

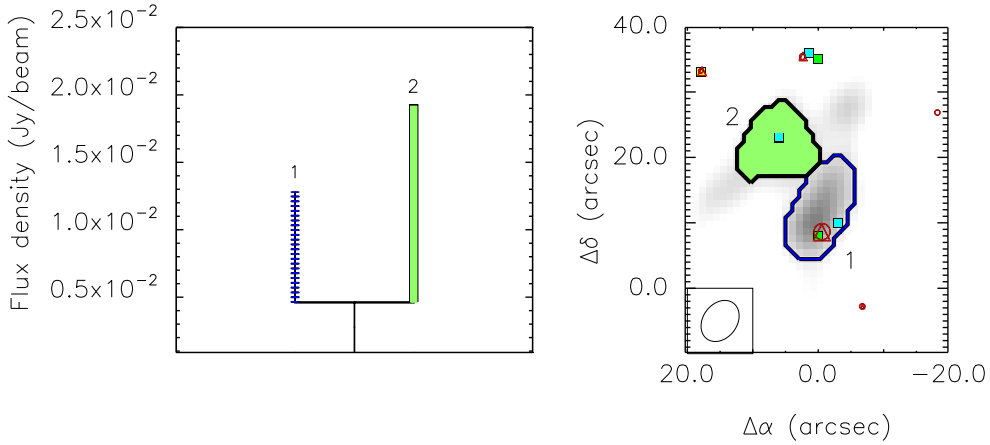

Figure 4.3: Left: The dendrogram tree structure of the H6 region identified with the SMA 1.3 mm continuum. Leaves are indexed in increasing value of offset declination. Right: The SMA 1.3 mm continuum map highlighting the spatial extent of the leaves identified in the dendrogram on the right. Each leaf is colour coded and labelled. Non-colour-filled contours correspond to those leaves that are spatially coincident with either 4.5, 8, 24 μm emission (or some combination of these; Carey *et al.* 2009, Chambers *et al.* 2009, Jiménez-Serra *et al.* 2010), which further correspond to the dashed lines in the dendrogram.

portion in the mapped region).

Given that identification of the smallest components of the dendrogram hierarchy is limited by the angular resolution of the observations, they will retain the identifier 'leaves' (and not cores). It is evident from Figure 4.2, that a number of the leaves exhibit asymmetric boundaries (and in the case of PdBI 13 and PdBI 14, these are very irregular). This is inconsistent with the assumption of spherical symmetry (see Section 4.3.1). It is plausible that a number of these leaves comprise several structures unresolved at the resolution of the PdBI data. By continuing to refer to these structures as leaves, no assumptions are made regarding the possibility of substructure, as has been observed in recent investigations into the

Table 4.1: Output parameters from dendrogram analysis.

ID	$\Delta\alpha^a$ ($''$)	$\Delta\delta$ ($''$)	IR quiet?^{b} (4.5/8/24 μm)	S^c_{peak} (mJy beam^{-1})	S^d_{tot} (mJy)	S^e_{parent} (mJy beam^{-1})	S^f_{corr} (mJy)	Area (pc^2)	$R^g_{\rm decon}$ (pc)
PdBI 1	2.3	-61.6	N	0.41	1.23	0.15	0.55	0.013	0.059
PdBI 2	1.5	-48.6	N	0.63	1.73	0.15	0.94	0.015	0.064
PdBI 3	3.8	-33.4	Y	0.52	0.62	0.23	0.20	0.005	0.031
PdBI 4	5.3	-25.8	Y	0.51	0.69	0.27	0.19	0.005	0.032
PdBI 5	9.1	-19.0	Y	0.51	0.49	0.27	0.13	0.004	0.035
PdBI 6	4.6	-7.6	Y	0.53	0.38	0.34	0.08	0.003	0.028
PdBI 7	1.5	-0.8	Y	0.67	0.90	0.34	0.22	0.006	0.034
PdBI 8	-2.3	12.9	N	0.60	1.94	0.26	0.63	0.015	0.063
PdBI 9	7.6	22.8	Y	1.03	1.50	0.40	0.57	0.007	0.038
PdBI 10	0.8	22.8	Y	0.74	1.09	0.40	0.28	0.006	0.034
PdBI 11	-6.1	28.1	Y	1.10	1.88	0.27	0.90	0.010	0.051
PdBI 12	3.0	33.4	N	0.53	0.81	0.27	0.20	0.007	0.038
PdBI 13	-11.4	38.8	N	0.50	1.88	0.26	0.48	0.016	0.065
PdBI 14	-16.0	42.6	Y	0.50	1.35	0.24	0.43	0.011	0.054
SMA 1	0.8	9.7	N	12.82	19.85	4.61	8.29	0.019	0.066
SMA 2	7.1	22.4	Y	19.19	23.24	4.61	12.21	0.018	0.064

[a] Positions correspond to the offset locations of the peak fluxes within each leaf. [b] "N" indicates that there is either 4.5/8/24 μm (or a combination of these) spatially coincident with the leaf. [c] Peak flux density of dendrogram leaf. [d] Integrated flux within the leaf area. [e] Flux height of first leaf merger. This is used to estimate the flux correction for "core" material (see text for details). [f] Corrected leaf flux, see Section 4.3.3. [g] Deconvolved radius of leaf, see Equation 4.2.

hierarchical fragmentation of IRDCs (e.g. Rathborne *et al.* 2007 and Wang *et al.* 2014 who reserve the term 'condensation' for substructure evident within IRDC cores).

4.3.3 Flux correction

The dendrogram analysis technique's primary function is to identify hierarchical structure within data. In calculating the physical properties of dendrogram leaves, Rosolowsky *et al.* (2008) presented three different "paradigms" in their analysis: i) bijection; ii) clipping; iii) extrapolation. Such considerations were imposed

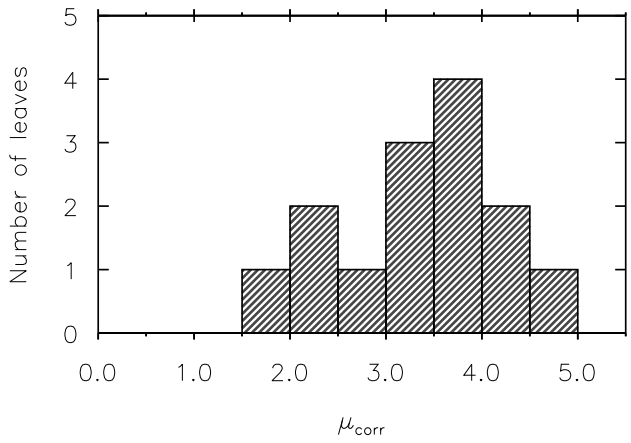

Figure 4.4: A histogram of the flux correction factor, $\mu_{\rm corr}$ (following the nomenclature of Ragan *et al.* 2013). This is defined as the ratio of uncorrected to corrected total leaf flux. The mean value of $\mu_{\rm corr}$ is 3.3.

because of the concern that closed objects, defined using intensity contours, may be inaccurate and influenced by projection. The bijection paradigm attributes all flux within a contour boundary to a given structure (e.g. a dendrogram leaf). The clipping paradigm applies a flux correction to an object by assuming that leaves are embedded within a structure whose brightness is equivalent to the merge level flux (i.e. the peak flux of the parent branch, see Section 4.3.1). In the extrapolation paradigm, the flux is extrapolated to the zero-intensity isosurface.

Ragan *et al.* (2013), using the dendrogram analysis technique to identify substructure within IRDCs adopted the clipping paradigm. To perform this correction, the flux of the parent level is subtracted from each pixel within the leaf boundary. The flux correction factor, $\mu_{\rm corr}$, is defined as the ratio of uncorrected to corrected flux. Figure 4.4 displays a histogram of $\mu_{\rm corr}$, indicating that on average, fluxes are corrected by a factor 3.3. Rosolowsky *et al.* (2008) noted that the clipping method provides an overly conservative estimate of the flux. In this analy-

sis, the bijection paradigm is therefore adopted as the fiducial method for deriving the physical properties of G035.39-00.33 (the extrapolation paradigm has not been selected since it is thought to be most applicable in regions with negligible parent material). However, both the bijection and clipping paradigms are used in parallel, and their relevance is discussed further in Section 4.6.2. Throughout the remaining sections of this chapter the fluxes estimated via the bijection and clipping methods are referred to simply as 'uncorrected' and 'corrected' fluxes, respectively. Information relating to the extracted dendrogram leaves (peak, integrated, branch, and corrected fluxes) can be found in Table 4.1.

4.4 Analysis: Deriving the physical properties of G035.39–00.33

4.4.1 Mass and density estimates

The masses of continuum peaks identified in the dendrogram analysis are determined using the following equation (Hildebrand 1983):

$$M = \frac{S_\nu d^2 R_{\rm gd}}{\kappa_{\nu,{\rm d}} B_\nu(T_{\rm d})}, \tag{4.3}$$

whereby S_ν is the observed integrated source flux density, d is the distance to the object, $R_{\rm gd}$ is the gas-to-dust mass ratio, $\kappa_{\nu,{\rm d}}$ is the dust opactity coefficient at a frequency, ν, and $B_\nu(T_{\rm d})$ is the Planck function at a dust temperature of $T_{\rm d}$. In the interest of making comparison with several other studies, Kauffmann *et al.* (2013a) have taken mass estimates quoted in the literature and normalized these against a set of common parameters. The same parameter selection will be adopted here. The parameters used are as follows: A distance of 2900 pc is assumed for G035.39-00.33 (Simon *et al.* 2006b). A gas-to-dust ratio of $R_{\rm gd} = 100$ is adopted. As a function of frequency, $\kappa_{\nu,{\rm d}} = \kappa_{\nu_{0,{\rm d}}}(\nu/\nu_0)^\beta$, where β is the dust emissivity spectral index. An opacity law for dust grains with thin ice mantles coagulating for 10^5 yr at a density of $10^6\,{\rm cm}^{-3}$ is adopted from (Ossenkopf & Henning 1994), i.e. $\kappa_{\nu_{0,{\rm d}}} = 0.9\,{\rm cm}^2{\rm g}^{-1}$ at a frequency of $\nu_0 = 230$ GHz. A value of $\beta = 1.75$ (Battersby *et al.* 2011) is used to interpolate to $\kappa_{\nu,{\rm d}}$ at 3.2 mm. A value of $\kappa_{\nu,{\rm d}} \sim 0.18\,{\rm cm}^2{\rm g}^{-1}$ is therefore used at $\nu = 93$ GHz. A value of 15 K is assumed for the dust temperature (Nguyen Luong *et al.* 2011).

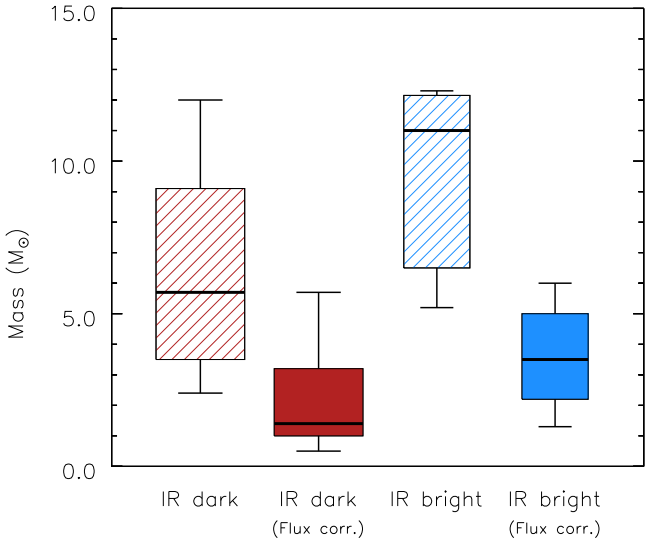

Figure 4.5: A box plot showing the range in masses of the PdBI leaves. Diagonal lined, and filled boxes represent uncorrected and corrected leaves, respectively. Red boxes are IR dark whereas blue boxes are IR bright. The figure highlights the minimum and maximum extent of the data, the length of the box represents the interquartile range, the horizontal line represents the median, and the width of each box is proportional to the square root of the number of data points (9 and 5 for the IR dark and IR bright leaves, respectively).

Using Equation 4.3, the uncorrected leaf masses range from $\sim$2.5 to 12.5 $M_{\odot}$, whereas the corrected masses are smaller, ranging from 0.5 to 6.0 $M_{\odot}$. Figure 4.5 shows the mass distribution before (striped boxes) and after (filled boxes) flux correction. In this diagram, leaves that are IR bright and IR dark are shown separately. Following the flux correction, masses are smaller, and cover a narrower range. The derived physical properties can be found in Table 4.2. The derived masses (and uncertainties) can be found in Columns 5 and 9 (for the uncorrected and corrected leaves, respectively). The uncertainties quoted for the masses incorporate only the error in flux ($\sim$10%) and the uncertainty in distance ($\sim$20%; Simon *et al.* 2006b). The implications of the above parameter selection, in partic-

ular, the influence the dust temperature and opacity coefficient may have on the results will be discussed further in Section 4.6.1.

The particle number density[1] for the individual dendrogram leaves is computed assuming spherical geometry using:

$$n = \frac{M}{\frac{4}{3}\pi R_{\rm decon}^3 \mu m_{\rm H}} \sim 3.4 \times 10^5 \left(\frac{M}{10\,{\rm M}_\odot}\right)\left(\frac{R_{\rm decon}}{0.05\,{\rm pc}}\right)^{-3} {\rm cm}^{-3}. \quad (4.4)$$

Uncorrected leaves have volume densities in the range $n \sim 1.5$–$7.5 \times 10^5\,{\rm cm}^{-3}$ (for the corrected leaves, $n \sim 0.5$–$3 \times 10^5\,{\rm cm}^{-3}$). These values are consistent with those measured towards other IRDCs. For example, Tan *et al.* (2013b) studying 6 IRDC cores with ALMA find hydrogen number densities in the range $n_{\rm H} \sim 0.8$–$6.0 \times 10^5\,{\rm cm}^{-3}$. These values have been recomputed correcting for $R_{\rm gd} = 100$ following Kauffmann *et al.* (2013a) (Tan *et al.* 2013b have used $R_{\rm gd} = 147$, and the quoted range is 1.22–$8.74 \times 10^5\,{\rm cm}^{-3}$). These values correspond to a mean particle number density range of $n \sim 0.5$–$3.6 \times 10^5\,{\rm cm}^{-3}$, for cores of radii ~ 0.03–$0.09\,{\rm pc}$. Number densities of the PdBI leaves can be located in Columns 6 and 10 of Table 4.2.

Figure 4.6 is a mass versus radius plot for the PdBI dendrogram leaves (shown in colour). Crosses with circles refer to IR bright leaves. Overlaid as black squares are the IRDC cores identified in 1.34 mm continuum observations by Tan *et al.* (2013b) using ALMA. In addition, the loci of constant particle number density (n) are shown as diagonal dotted lines. The dashed and dot-dashed lines refer to the theoretical threshold ($1\,{\rm g\,cm}^{-2}$) for massive star formation proposed by Krumholz & McKee (2008), and the empirically derived threshold proposed by Kauffmann

[1]The particle number density, n, and mass density, ρ, are related by $\rho = \mu m_{\rm H} n$, where $\mu \sim 2.33$ is assumed as the mean mass per particle.

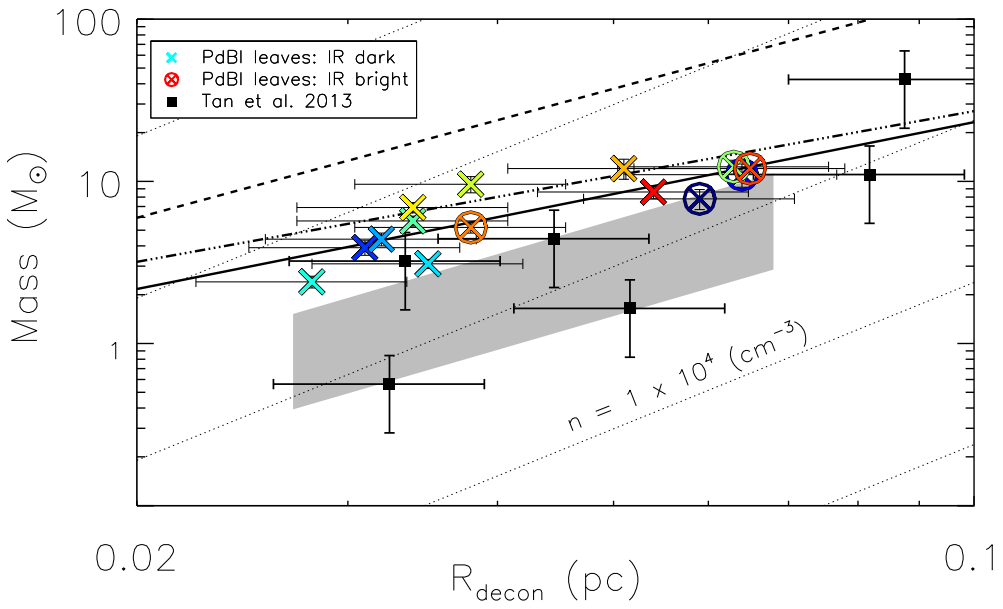

Figure 4.6: A mass versus radius plot for the uncorrected dendrogram leaves identified in G035.39-00.33. Crosses with circles represent IR bright leaves. The black solid line represents a least-squares fit to the PdBI leaves (where $M \propto R_{\rm decon}^{1.5\pm0.2}$). Black squares represent cores identified in the Tan *et al.* (2013b) study (the masses have been corrected according to the parameter selection used in this work, see Section 4.4.1). The dashed and dot-dashed lines refer to the theoretical ($1\,{\rm g\,cm^{-2}}$; Krumholz & McKee 2008) and empirical ($M = 580\,{\rm M_\odot}\,R^{4/3}$; Kauffmann & Pillai 2010) lower limit for massive star formation. Dotted lines represent the loci of constant volume density (from top-left to bottom-right the values are 10^7, 10^6, 10^5, 10^4, $10^3\,{\rm cm^{-3}}$, respectively). The grey box indicates the location of the corrected leaves (see Section 4.3.3).

& Pillai (2010). In the case of the latter, the derived threshold has been reduced from the original relationship of $M \geq 870\,{\rm M_\odot}\,R^{4/3}\,{\rm M_\odot}$ to $M \geq 580\,{\rm M_\odot}\,R^{4/3}\,{\rm M_\odot}$, to make direct comparison with the PdBI masses, which make use of the Ossenkopf & Henning (1994) dust opacity models (see Dunham *et al.* 2011, Kauffmann *et al.* 2013a for a discussion on this correction).

It has previously been suggested that a power-law scaling exists between the

masses and radii of pre-stellar cores (e.g. Kramer *et al.* 1996, Larson 1981, Motte *et al.* 2001). More recently, such studies have been performed towards IRDCs in the interest of identifying the physical properties of potential high-mass pre-stellar cores (e.g. Gómez *et al.* 2014, Kauffmann & Pillai 2010, Ragan *et al.* 2013). The uncorrected leaves follow a power law trend of $M \propto R_{\rm decon}^{1.5 \pm 0.2}$ (Spearman rank correlation coefficient, $r_{\rm s} \sim 0.84$, $P < 0.001$). Studies of other IRDCs have revealed steeper slopes closer to $M \propto R^3$ using similar methods (e.g. Ragan *et al.* 2013).

Ballesteros-Paredes & Mac Low (2002) and Shetty *et al.* (2010), through the use of simulated observations, showed that mass-size relationships may be the influenced by projection effects. Here, structures in synthetic spectral observations (i.e. PPV space) may not correlate with physical structures in the simulations. The same is true for structures extracted from 2-D column density maps.

The definition of R also plays a role in influencing the mass-size relationship. Using the effective radius, rather than the deconvolved radius it is found $\sim 1.7 \pm 0.2$. Corrected leaves would return exponents of 2.0 ± 0.2 and 2.4 ± 0.2 for the deconvolved and effective radii, respectively. The uncertainty in this trend is therefore expected to significant. As discussed in Ragan *et al.* (2013), the exponent is sensitive to the method by which the radii of sources are measured. One must therefore be cautious when drawing conclusions regarding the stability of the leaves.

4.4.2 Fragmentation analysis

Spherical (Jeans) fragmentation

If fragmentation is governed by the Jeans instability, then the maximum mass that thermal pressure can support against gravity is given by the Jeans mass:

$$M_{\rm J} \;=\; \frac{\pi^{5/2}}{6}\left(\frac{k_{\rm B}T}{G\mu m_{\rm H}}\right)^{3/2}\left(\frac{1}{\rho}\right)^{1/2} \;=\; \frac{\pi^{5/2}c_{\rm s}^{3}}{6\sqrt{G^{3}\rho}}, \tag{4.5}$$

whereby $c_{\rm s}$ is the isothermal sound speed of the average particle (if the internal pressure of the gas is dominated by non-thermal motions, the total, i.e. thermal plus non-thermal, velocity dispersion of the mean particle is used instead), G is the gravitational constant, and ρ is the mass density, calculated using $\rho = \mu m_{\rm H} n$, where n is the number density estimated in Section 4.4.1. The isothermal sound speed of the gas is estimated for a temperature of 15 K using $c_{\rm s} = \sqrt{k_{\rm B}T_{\rm kin}/\mu m_{\rm H}}$. Thus $c_{\rm s} \sim 0.23$ km s^{-1}. It is convenient to rewrite Equation 4.5 as:

$$M_{\rm J} \;\approx\; 1.7\left(\frac{T}{15\,{\rm K}}\right)^{3/2}\left(\frac{n}{10^{5}\,{\rm cm}^{-3}}\right)^{-1/2} M_{\odot}, \tag{4.6}$$

where T and n have been normalized to 15 K and 10^5 cm^{-3}, respectively. Columns 7 and 11 of Tables 4.2 display the Jeans masses for the uncorrected and corrected leaves, respectively. In addition, the ratio of the calculated masses to Jeans masses can be found in Columns 8 and 12. In all cases the uncorrected leaves exhibit super-critical masses (super-Jeans). In contrast however, several of the corrected leaves are consistent with having sub-Jeans masses, or masses similar to the Jeans mass ($> 50\%$ of the leaves remain super-Jeans). The instances where $M > M_{\rm J}$ (and the identified leaf is centrally peaked with a low aspect ratio) are unstable against

collapse. If these leaves are not collapsing, this would suggest that non-thermal mechanisms (e.g. turbulence or magnetic pressure) are providing support. This is particularly important in cases where leaves exhibit a super-critical Jeans masses in the corrected data (e.g. PdBI 9). Instances whereby leaves have irregular shapes but are still super-Jeans, could indicate that further fragmentation may have occurred, or is occurring (e.g. PdBI 8). Higher angular resolution observations would be needed to confirm such results.

The Jeans length is defined as the critical size scale above which perturbations grow exponentially. It is given by:

$$\lambda_{\rm J} \, = \, c_{\rm s} \left(\frac{\pi}{G \rho} \right)^{1/2} \, = \, 0.08 \left(\frac{T}{15 \, {\rm K}} \right)^{1/2} \left(\frac{n}{10^5 \, {\rm cm}^{-3}} \right)^{-1/2} {\rm pc}. \tag{4.7}$$

By estimating the (projected) separation between leaves one can make comparison between this, and the expected separation following thermal fragmentation, i.e. $\lambda_{\rm J}$. The average nearest neighbour separation of the leaves is ~ 0.12 pc (with an estimated uncertainty of $\sim 30\%$ given the 20% uncertainty in the distance measurement summed in quadrature). The mean number density of the uncorrected PdBI leaves is $\sim 4 \times 10^5$ cm^{-3}. Substituting this into Equation 4.7 gives $\lambda \sim 0.04$ pc. Given that 0.12 pc is expected to be a lower limit to the separation (considering projection effects, and the fact that individual leaves may be embedded in different filaments; Chapter 3), this suggests that the fragment spacing is inconsistent with thermal Jeans fragmentation (at the resolution of the PdBI observations).

Table 4.2: The physical properties of the dendrogram leaves.

				Uncorrected				Corrected†			
ID	$\Delta\alpha$	$\Delta\delta$	$R_{\rm decon}$	$M^a_{3.2\,\rm mm}$	n^b	$M^c_{\rm J}$	$M/M_{\rm J}$	$M_{3.2\,\rm mm}$	n	$M_{\rm J}$	$M/M_{\rm J}$
	($''$)	($''$)	(pc)	($\rm M_\odot$)	($10^5\,\rm cm^{-3}$)	($\rm M_\odot$)		($\rm M_\odot$)	($10^5\,\rm cm^{-3}$)	($\rm M_\odot$)	
PdBI 1	2.3	-61.6	0.059	7.8 (2.4)	1.6	2.4	3.2	3.5 (1.1)	0.7	3.7	1.4
PdBI 2	1.5	-48.6	0.064	11.0 (3.3)	1.8	2.3	4.7	6.0 (1.8)	1.0	3.2	2.6
PdBI 3	3.8	-33.4	0.031	3.9 (1.2)	5.4	1.3	2.9	1.3 (0.4)	1.8	2.3	1.0
PdBI 4	5.3	-25.8	0.032	4.4 (1.3)	5.4	1.3	3.3	1.2 (0.4)	1.5	2.6	0.9
PdBI 5	9.1	-19.0	0.035	3.1 (0.9)	3.0	1.8	1.8	0.8 (0.2)	0.8	3.5	0.5
PdBI 6	4.6	-7.6	0.028	2.4 (0.7)	4.5	1.5	1.7	0.5 (0.2)	1.0	3.1	0.4
PdBI 7	1.5	-0.8	0.034	5.7 (1.7)	6.1	1.3	4.5	1.4 (0.4)	1.5	2.5	1.1
PdBI 8	-2.3	12.9	0.063	12.3 (3.7)	2.1	2.2	5.7	4.0 (1.2)	0.7	3.8	1.9
PdBI 9	7.6	22.8	0.038	9.6 (2.9)	7.3	1.2	8.3	3.6 (1.1)	2.8	1.9	3.1
PdBI 10	0.8	22.8	0.034	6.9 (2.1)	7.4	1.1	6.0	1.8 (0.5)	1.9	2.3	1.6
PdBI 11	-6.1	28.1	0.051	12.0 (3.6)	3.7	1.6	7.4	5.7 (1.7)	1.8	2.3	3.5
PdBI 12	3.0	33.4	0.038	5.2 (1.6)	4.1	1.5	3.4	1.3 (0.4)	1.0	3.1	0.8
PdBI 13	-11.4	38.8	0.065	12.0 (3.6)	1.8	2.3	5.1	3.1 (0.9)	0.5	4.6	1.3
PdBI 14	-16.0	42.6	0.054	8.6 (2.6)	2.4	2.0	4.3	2.8 (0.8)	0.8	3.6	1.4

[a] Mass estimate derived using the uncorrected flux and the parameters outlined in Section 4.4.1. [b] Number density estimated for a particle of mean mass 2.33 a. m. u.. [c] The Jeans mass assuming $T = 15\,\rm K$. † Masses, densities, and Jeans masses for the flux-corrected leaves.

Cylindrical fragmentation

Given that G035.39-00.33 is highly filamentary, it is prudent to also discuss cylindrical fragmentation. The mass of the filament can be extracted from the dendrogram analysis. Using Equation 4.3, the total mass of the filament (i.e. the trunk containing all branches and leaves) is $\sim 160 \pm 80\,\rm M_\odot$. Considering the filament extends over $\sim 1.8\,\rm pc$ this gives a mass per unit length, $m_{\rm f} \sim 90\,\rm M_\odot\,pc^{-1}$.

For an infinite, isothermal, self-gravitating cylinder, collapse will occur if $m_{\rm f} > m_{\rm crit}$, where the critical mass per unit length is given by (Ostriker 1964, Stodólkiewicz 1963):

$$m_{\rm crit} = \frac{2c_{\rm s}^2}{G} \sim 24.5 \left(\frac{T}{15\,\rm K}\right) M_\odot. \tag{4.8}$$

This indicates that a temperature of 55 K would be needed to support a filament of $m_{\rm f} = 90\,{\rm M}_{\odot}\,{\rm pc}^{-1}$. Alternatively, replacing $c_{\rm s}$ in Equation 4.8 with the mean velocity dispersion of the filament(s) (~ 0.45 km s^{-1}, measured from the $J = 1 \rightarrow 0$ transition of N_2H^+; Chapter 3), $m_{\rm crit} \sim 94\,{\rm M}_{\odot}\,{\rm pc}^{-1}$, giving $m_{\rm crit}/m_{\rm f} \sim 1$.

In the case of cylindrical gravitational collapse, over-densities will tend to grow with a characteristic spacing (i.e. the interval at which the instability grows the fastest). This type of instability has been used to explain the regular spacing of star forming cores in filamentary clouds (e.g. Jackson *et al.* 2010, Miettinen 2012, Wang *et al.* 2011, 2014). The filament scale height is given by $H = c_{\rm s}(4\pi G\rho)^{-1/2}$. For an infinite isothermal cylinder, whose radius $R \gg H$, the spacing between fragments is given by (Nagasawa 1987, Tomisaka 1995):

$$\lambda_{\rm max} \; = \; 22H \; = \; \frac{22 c_s}{(4\pi G \rho)^{1/2}} \; \sim$$
$$0.8 \left(\frac{T}{15\,{\rm K}} \right)^{1/2} \left(\frac{n}{10^4\,{\rm cm}^{-3}} \right)^{-1/2} {\rm pc}. \qquad (4.9)$$

Assuming a filament radius ~ 0.12 pc (taken as the diameter of the largest leaf in order to incorporate all of the emission), the average number density of the filament (assuming cylindrical geometry, a length of 1.8 pc, and a mass of 160 M$_{\odot}$) is n $\sim 3.5 \times 10^4$ cm^{-3}, and so $H \sim 0.02$ pc and $R \gg H$. Under these assumptions $\lambda_{\rm max} \sim 0.4$ pc (which corresponds to $\sim 28''$ at a distance of 2900 pc). Alternatively, using the mean velocity dispersion in Equation 4.9 gives $\lambda_{\rm max} \sim 0.85$ pc (or $\sim 60''$). While the characteristic separation of the leaves is much smaller than either of these values, the separation between the centre of the H6 and narrow clumps (defined as the difference between mean offsets in $\Delta\alpha$ and $\Delta\delta$ covering the emission region of each clump) is comparable, with $\sim 0.7 \pm 0.2$ pc (assuming a 20% uncertainty in

the location of both central locations).

If however, the number density is taken to be that of the mean density of the uncorrected dendrogram leaves, $n \sim 4 \times 10^5\,\mathrm{cm}^{-3}$, then $\lambda_{\mathrm{max}} \sim 0.13\,\mathrm{pc}$ in the case of thermal fragmentation. This is very close to the expected lower limit of leaf separation. Kainulainen *et al.* (2013) found that fragmentation in IRDC G11.11–0.12 is scale-dependent, with core separations reducing to the Jeans length in the highest density regions. In the same way, fragmentation within G035.39-00.33 may therefore be scale dependent. However, it should be noted that this analysis does not account for projection affects. One must therefore proceed with caution when interpreting fragmentation analysis such as this. This is particularly important in the case of G035.39-00.33, where multiple velocity structures are apparent (Chapter 3), and may exhibit their own fragmentation length-scales.

4.5 Analysis: The dynamical state of the dendrogram leaves

4.5.1 The virial parameter

The approximate balance between a (spherical or spheroidal) cloud fragment's kinetic and gravitational energy can be expressed (in terms of observable quantities) in the form of the virial parameter, α, (Bertoldi & McKee 1992):

$$\alpha \equiv \frac{5\sigma_{\rm TOT}^2 R}{GM}, \tag{4.10}$$

whereby $\sigma_{\rm TOT}$, R, and M are the velocity dispersion (calculated for a particle of mean mass 2.33 a. m. u., including both thermal and non-thermal motions), radius, and mass associated with the clump/core being evaluated. It is also possible to write the virial parameter in the form $\alpha = M_{\rm vir}/M$, where $M_{\rm vir} = (5\sigma_{\rm TOT}^2 R)/G$ is known as the virial mass. By using the PdBI 3.2 mm continuum data in conjunction with the N_2H^+ $(1-0)$ presented in Chapter 3, it is possible to examine the dynamical state of the dendrogram leaves. Equation 4.10 ignores any effect magnetic fiels and surface pressures may have on the dynamical state of the leaves. Since the relative contributions of these effects are not known in G035.39-00.33, this analysis is intended to serve only as an approximation.

A value of $\sigma_{\rm TOT}$ is quantified for each dendrogram leaf through the identification of corresponding N_2H^+ $(1-0)$ emission peaks. To calculate $\sigma_{\rm TOT}$ via the observed

velocity dispersion of N_2H^+ the following is used (Fuller & Myers 1992):

$$\sigma_{\rm TOT} = \sqrt{\frac{\Delta\upsilon^2_{\rm corr}}{8\ln(2)} + k_{\rm B}T\left(\frac{1}{\mu m_{\rm H}} - \frac{1}{m_{\rm N_2H^+}}\right)}, \tag{4.11}$$

whereby μ is the atomic weight of the mean molecule (2.33), $m_{\rm H}$ is the mass of a Hydrogen atom, $m_{\rm N_2H^+}$ is the mass of the N_2H^+ molecule (29 a. m. u.), T is the kinetic temperature of the gas (assumed to be 15 K; see Section 4.4.1), and $\Delta\upsilon^2_{\rm corr}$ is the observed line-width of the N_2H^+ corrected for the spectral resolution, $\Delta\upsilon^2_{\rm corr} = \Delta\upsilon^2_{\rm obs} - \Delta\upsilon^2_{\rm channelwidth}$, with $\Delta\upsilon_{\rm channelwidth} \equiv \Delta\upsilon_{\rm res} = 0.14$ km s^{-1} for the N_2H^+ $(1-0)$ PdBI observations.

Chapter 3 revealed that the N_2H^+ (1−0) emission is divided into several velocity components. Each dendrogram leaf is therefore linked to a corresponding filament. The underlying assumption here is that all continuum emission is associated with a single filament (which may, or may not be the case in reality). Values of $V_{\rm LSR}$ and $\Delta\upsilon_{\rm obs}$ were established for each leaf by performing a Gaussian fit to the average spectrum taken over the area covered by the leaf, using the GILDAS/CLASS package. This was performed for both the merged and PdBI-only data. In the cases where the spectra showed multiple components, the emission was checked against the PdBI-only position-position-velocity cube. To be linked to a filament, N_2H^+ peaks must lie within a given radius of the corresponding dendrogram leaf (equivalent to the geometric mean of the major and minor axes of the synthesized PdBI beam $= 3.65''$). The N_2H^+ peak with the smallest projected distance was then selected (typically this was the brightest component). This method was successful for all leaves except for PdBI 9, which displayed an ambiguous result. The classification, $V_{\rm LSR}$, $\Delta\upsilon_{\rm corr}$, and $\Delta\upsilon_{\rm TOT}$ values are presented in Table 4.3, for both the merged

Table 4.3: The kinematic properties of the dendrogram leaves.

					Merged PdBI + 30 m data							PdBI only						
ID	$\Delta\alpha^a$	$\Delta\delta^a$	$R_{\rm decon}$	Fil.	$V_{\rm LSR}$	$\Delta v_{\rm corr}$	$\Delta v_{\rm TOT}$	$M_{\rm vir}$	$M_{\rm vir}^{k_\rho=1.0}$	$M_{\rm vir}^{1.5}$	$M_{\rm vir}^{2.0}$	$V_{\rm LSR}$	$\Delta v_{\rm corr}$	$\Delta v_{\rm TOT}$	$M_{\rm vir}$	$M_{\rm vir}^{k_\rho=1.0}$	$M_{\rm vir}^{1.5}$	$M_{\rm vir}^{2.0}$
	($''$)	($''$)	($''$)		($\rm km\,s^{-1}$)	($\rm km\,s^{-1}$)	($\rm km\,s^{-1}$)	($\rm M_\odot$)	($\rm M_\odot$)	($\rm M_\odot$)	($\rm M_\odot$)	($\rm km\,s^{-1}$)	($\rm km\,s^{-1}$)	($\rm km\,s^{-1}$)	($\rm M_\odot$)	($\rm M_\odot$)	($\rm M_\odot$)	($\rm M_\odot$)
PdBI 1	2.3	-61.6	0.059	F2a	45.4	1.1	1.3	19.2	17.2	15.4	11.5	45.6	0.7	0.9	9.5	8.6	7.7	5.7
PdBI 2	1.5	-48.6	0.064	F2a	45.5	0.8	0.9	7.0	6.3	5.6	4.2	45.6	0.5	0.8	4.7	4.2	3.8	2.8
PdBI 3	3.8	-33.4	0.031	F2a	45.7	1.0	1.1	16.3	14.6	13.1	9.8	45.8	1.0	1.1	17.2	15.4	13.8	10.3
PdBI 4	5.3	-25.8	0.032	F2a	45.7	1.4	1.5	14.5	13.1	11.7	8.7	45.8	1.8	1.8	22.0	19.8	17.7	13.2
PdBI 5	9.1	-19.0	0.035	F2b	46.2	0.4	0.7	3.2	2.9	2.6	1.9	46.2	0.5	0.7	4.1	3.7	3.3	2.5
PdBI 6	4.6	-7.6	0.028	F2a	45.7	0.9	1.1	7.7	6.9	6.2	4.6	45.8	0.8	0.9	5.9	5.3	4.7	3.5
PdBI 7	1.5	-0.8	0.034	F3	46.6	0.5	0.8	4.2	3.8	3.4	2.5	46.5	0.5	0.8	4.2	3.8	3.4	2.5
PdBI 8	-2.3	12.9	0.063	F3	47.1	1.1	1.2	8.7	7.8	7.0	5.2	47.3	1.6	1.7	16.7	15.0	13.4	10.0
PdBI 9	7.6	22.8	0.038	F2a	45.1	0.9	1.1	8.3	7.4	6.6	5.0	44.9	0.6	0.8	4.6	4.1	3.7	2.8
PdBI 9[a]	-	-	-	F2b	46.0	0.6	0.8	4.3	3.9	3.5	2.6	46.1	0.2	0.6	2.4	2.2	1.9	1.4
PdBI 10	0.8	22.8	0.034	F2a	45.2	0.5	0.8	7.7	6.9	6.2	4.6	45.2	0.5	0.7	7.3	6.5	5.8	4.4
PdBI 11	-6.1	28.1	0.051	F3	46.7	0.6	0.8	4.9	4.4	4.0	3.0	46.5	0.8	1.0	7.1	6.4	5.7	4.3
PdBI 12	3.0	33.4	0.038	F2b	45.8	1.0	1.1	8.8	7.9	7.0	5.3	45.7	0.7	0.9	5.7	5.1	4.6	3.4
PdBI 13	-11.4	38.8	0.065	F3	46.7	0.8	1.0	9.8	8.8	7.9	5.9	46.6	0.6	0.8	7.0	6.3	5.6	4.2
PdBI 14	-16.0	42.6	0.054	F3	46.7	0.4	0.7	3.6	3.2	2.9	2.2	46.8	0.4	0.7	3.4	3.0	2.7	2.0

[a] Both fits are shown for PdBI 9 as the identification of the leaf presents an ambiguous result. Given that the line-width of the PdBI only data for the fit to F2b is ~ 0.2 $\rm km\,s^{-1}$ (see Column 13), and the spectral resolution of the PdBI data is 0.14 $\rm km\,s^{-1}$, the F2a association is used throughout the analysis.

and PdBI-only data.

Figure 4.7 displays the results of this virial analysis. The left-hand panels display the mass versus virial mass for the uncorrected leaves. Each dendrogram leaf is highlighted in a different colour according to Figure 4.2. The size of each symbol is proportional to $1/\alpha$, estimated using Equation 4.10. The dot-dashed and dashed lines correspond to the best-fit lines to the uncorrected and corrected masses, respectively (see Section 4.3.3). Loci of $\alpha = 2$, and 1, are indicated by black lines, and incorporate the light-grey and dark-grey shaded areas respectively. The uncertainty in the virial parameter is estimated to be $\sim 55\%$, assuming uncertainties of $\sim 25\%$ in the virial mass (incorporating the uncertainty on the measured FWHM and a 20% uncertainty in the distance), and $\sim 50\%$ in the continuum masses, respectively (see Section 4.6.1 for a discussion on the sources of uncertainty in the mass calculations).

The top-left panel displays virial masses established from line-widths taken from the merged PdBI and IRAM 30 m data, whereas the bottom-left panel is for the PdBI-only data. In both the merged and the PdBI-only data, PdBI 4 shows the largest virial parameter ($\alpha \sim 2.9$ and 4.4, respectively).

However, PdBI 11 exhibits the lowest virial parameter in the merged data ($\alpha \sim 0.5$), whereas PdBI 9 has the lowest virial parameter in the PdBI-only data ($\alpha \sim 0.5$). This reflects the changes in line-width observed when using the PdBI-only data. In the case of PdBI 11, the line-width is greater in the PdBI-only data than in the merged data, whereas for PdBI 9, the opposite is true. For reference, neither of these leaves are IR bright by the classification presented here, although PdBI 9 is bright at 70 μm (Nguyen Luong *et al.* 2011). This serves as an illustration, highlighting how the virial mass calculation is sensitive to fluctuation in

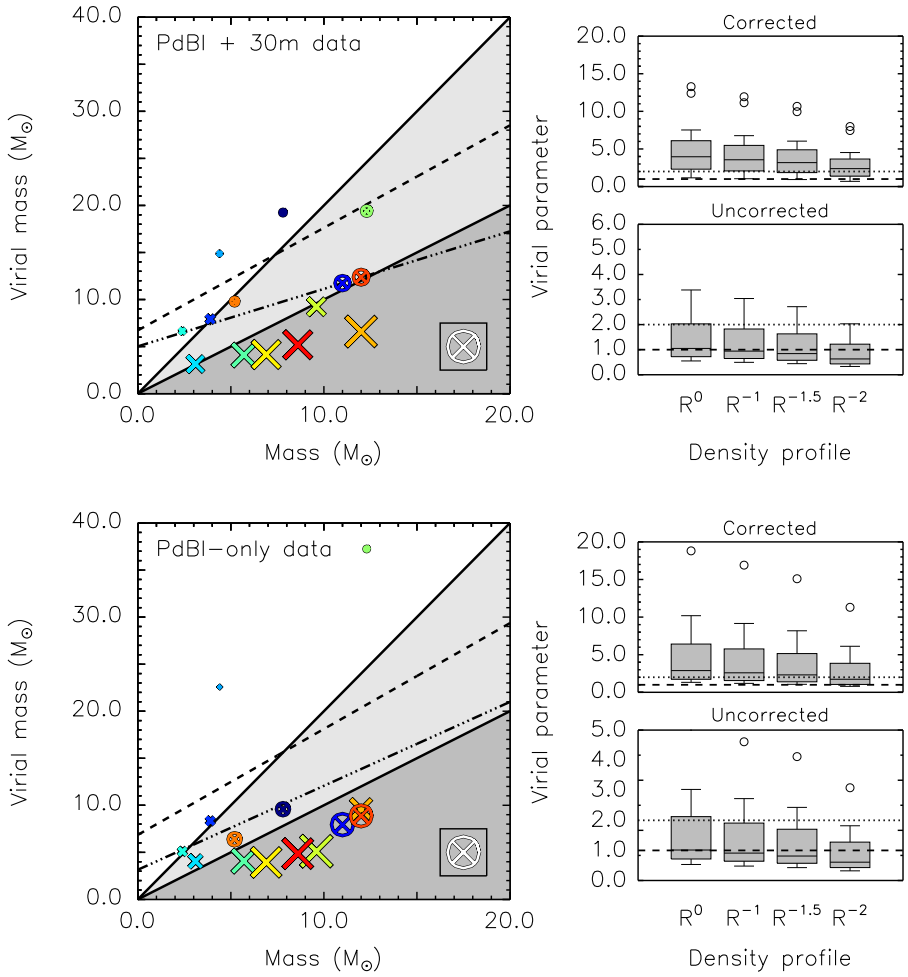

Figure 4.7: Left panels: Uncorrected leaf mass versus virial mass for the PdBI dendrogram leaves. The colour of each leaf is coded according to Figure 4.2. As with Figure 4.6, the crosses with circles refer to those leaves that have spatially coincident 4.5, 8, or 24 μm emission. The size of each symbol is proportional to $1/\alpha$, whereby α is calculated using Equation 4.10 (the size of the white symbol in the box refers a $\alpha = 0.5$). light- and dark-grey shaded areas indicate the loci of where $\alpha = 2$ and 1, respectively, below which structures are super-critical, and therefore unstable to gravitational collapse (with only thermal pressure for support). The dot-dashed and dashed lines refer to least-squares fits to the uncorrected and corrected data, respectively (see Section 4.3.3). The top and bottom panels refer to virial masses calculated for the merged PdBI and IRAM 30 m, and PdBI-only data sets, respectively. Right panels: Boxplots of the virial parameters estimated according to different density profiles, $\rho \propto R^{-k_\rho}$, where $k_\rho = 0$, 1, 1.5, 2. The open circles refer to outlying points (values greater then or less than 1.5$\times$ the interquartile range from the 75$^{\rm th}$ and 25$^{\rm th}$ percentiles, respectively). These are PdBI 4 and PdBI 6 for the merged data, and PdBI 4 for the PdBI-only data, respectively.

spatial scales.

In spite of the fact that the mean virial parameters are approximately equal using the different datasets ($\alpha \sim 1.5$), it is found that virial parameters evaluated for the PdBI-only data, differ from those for the merged data by on average $\sim 30\%$. In the majority of cases (65%) the line-width decreases when considering the PdBI-only data. However, it is important to note that in some cases the line-width *increases* in the PdBI-only data (e.g. PdBI 8 and 11). Virial parameters derived from the comparison between merged (i.e. the PdBI and IRAM 30 m N_2H^+ data) molecular line, and the interferometric-only continuum data are therefore unreliable, as they trace different spatial scales (this was also noted in Beuther *et al.* 2013).

4.5.2 Density profile variation

The virial parameter is sensitive to variations in both the physical geometry of cores, and their density profile (Bertoldi & McKee 1992). For aspect ratios of less than two, i.e. for spherical or spheroidal cores (as is assumed in this analysis), the correction factor is small (~ 1). The correction for a non-uniform density distribution is given by:

$$a = \frac{(1 - k_\rho/3)}{(1 - 2k_\rho/5)}, \tag{4.12}$$

where k_ρ is the power law index of the density profile ($\rho \propto R^{-k_\rho}$). Therefore:

$$M_{\rm vir} = \frac{5\sigma^2_{\rm TOT} R}{aG} = \phi \left(\frac{R_{\rm decon}}{1\,{\rm pc}}\right) \left(\frac{\Delta\upsilon_{\rm TOT}}{1\,{\rm km\,s^{-1}}}\right)^2 {\rm M}_\odot, \tag{4.13}$$

Table 4.4: Virial parameters estimated assuming different density profiles.

				Uncorrected					Corrected				
ID	$\Delta\alpha$	$\Delta\delta$	$R_{\rm decon}$	$M_{3.2\,\rm mm}$	α	α	α	α	$M_{3.2\,\rm mm}$	α	α	α	α
	($''$)	($''$)	($''$)	($\rm M_\odot$)		$k_\rho = 1.0$	$k_\rho = 1.5$	$k_\rho = 2.0$	($\rm M_\odot$)		$k_\rho = 1.0$	$k_\rho = 1.5$	$k_\rho = 2.0$
PdBI 1	2.3	-61.6	0.059	7.8 (2.4)	1.2	1.1	1.0	0.7	3.5 (1.1)	2.7	2.4	2.2	1.6
PdBI 2	1.5	-48.6	0.064	11.0 (3.3)	0.4	0.4	0.3	0.3	6.0 (1.8)	0.8	0.7	0.6	0.5
PdBI 3	3.8	-33.4	0.031	3.9 (1.2)	4.4	3.9	3.5	2.6	1.3 (0.4)	13.2	11.9	10.6	7.9
PdBI 4	5.3	-25.8	0.032	4.4 (1.3)	5.0	4.5	4.0	3.0	1.2 (0.4)	18.3	16.5	14.7	11.0
PdBI 5	9.1	-19.0	0.035	3.1 (0.9)	1.3	1.2	1.1	0.8	0.8 (0.2)	5.0	4.5	4.0	3.0
PdBI 6	4.6	-7.6	0.028	2.4 (0.7)	2.4	2.2	1.9	1.5	0.5 (0.2)	11.0	9.9	8.9	6.6
PdBI 7	1.5	-0.8	0.034	5.7 (1.7)	0.7	0.7	0.6	0.4	1.4 (0.4)	3.0	2.7	2.4	1.8
PdBI 8	-2.3	12.9	0.063	12.3 (3.7)	1.4	1.2	1.1	0.8	4.0 (1.2)	4.2	3.7	3.3	2.5
PdBI 9	7.6	22.8	0.038	9.6 (2.9)	0.5	0.4	0.4	0.3	3.6 (1.1)	1.3	1.1	1.0	0.8
PdBI 10	0.8	22.8	0.034	6.9 (2.1)	1.1	0.9	0.8	0.6	1.8 (0.5)	4.1	3.7	3.3	2.4
PdBI 11	-6.1	28.1	0.051	12.0 (3.6)	0.6	0.5	0.5	0.4	5.7 (1.7)	1.2	1.1	1.0	0.7
PdBI 12	3.0	33.4	0.038	5.2 (1.6)	1.1	1.0	0.9	0.7	1.3 (0.4)	4.6	4.1	3.7	2.7
PdBI 13	-11.4	38.8	0.065	12.0 (3.6)	0.6	0.5	0.5	0.4	3.1 (0.9)	2.3	2.0	1.8	1.4
PdBI 14	-16.0	42.6	0.054	8.6 (2.6)	0.4	0.4	0.3	0.2	2.8 (0.8)	1.2	1.1	1.0	0.7

where $\phi \sim 208$, 187, 167, 125 for $k_\rho = 0$, 1, 1.5, and 2, respectively (following MacLaren *et al.* 1988). The virial masses calculated using Equation 4.13 can be found in Table 4.3. The right-hand panels of Figure 4.7 are box plots of the virial parameters estimated assuming $k_\rho = 0$, 1, 1.5, and 2. Virial parameters for both the uncorrect and corrected leaves are shown, and in both instances virial parameters decrease with increasing k_ρ.

Virial parameters for the corrected leaves are greater than the uncorrected leaves by a factor of ~ 3.5. This is to be expected, given that the fluxes are smaller by $\mu_{\rm corr} \sim 3.3$ on average (see Section 4.3.3). Although the density profiles of star forming cores is uncertain, a value $k_\rho \sim 1.5$ has been estimated for regions of massive star formation, (e.g. Beuther *et al.* 2002, Butler & Tan 2012, van der Tak *et al.* 2000). Using $k_\rho \sim 1.5$ as a fiducial value for the uncorrected leaves, considering the PdBI-only data, returns a mean virial parameter of $\alpha \sim 1$, with $\sim 70\%$ of all leaves found to have $\alpha < 1$. Virial parameters for all density distributions are presented in Tables 4.4 (these are shown exclusively for the velocity dispersions estimated from the PdBI-only data as virial parameters measured from the merged data are inaccurate, see Section 4.5).

For the corrected masses, using $k_\rho \sim 1.5$, and rearranging Equation 4.13, one can estimate the line-width (for a particle of mean mass ~ 2.33 a. m. u.) needed to provide $M_{\rm vir} = M_{\rm corr}$, and therefore $\alpha = 1$ (where $M_{\rm corr}$ represents the mass of flux-corrected dendrogram leaves). On average this line-width is found to be ~ 0.6 km s^{-1}. Using Equation 4.11 it is possible to estimate the observed line-width that one would expect to observe for (for example) N_2H^+ (with $m_{\rm N_2H^+} = 29$ a. m. u., and assuming $T = 15$ K) in the case that the corrected leaves are virialized. This would equate to a line-width of ~ 0.3 km s^{-1} (or dispersion $\sigma = 0.13$ km s^{-1}) for

N_2H^+ (i.e. significantly narrower than those observed). This indicates that a significant reduction in line-width is required in order for the corrected leaves to be virialized.

The large virial parameters of the corrected leaves may be consistent with the flux correction (see Section 4.3.3) underestimating the masses, as suggested by Rosolowsky *et al.* (2008) (i.e. the virial mass is large by comparison). An alternative explanation may be that the velocity dispersions of the leaves are overestimated, and hence so is the virial mass (see Equation 4.10). Pineda & Teixeira (2013) showed that the line-width of cores in NGC 2264-D traced by N_2H^+ $(3-2)$ were $\sim 70\%$ of the N_2H^+ $(1-0)$ values. High-resolution observations of high-density gas tracers, or higher J-transitions of N_2H^+, would be needed to investigate this possibility.

4.6 Discussion

4.6.1 Uncertainties

Deriving the physical properties from dust emission at millimetre wavelengths requires an *a priori* knowledge of the dust temperature, and the dust emissivity spectral index, β. Both of these values are dependant on environment. Consequently, the mass calculations performed in Section 4.4.1 are sensitive to variations in these properties. It is prudent therefore, to discuss the influence these choices may have on the derived masses, and how further observations will help to constrain this information.

Temperature

To estimate the masses of each of the dendrogram leaves in Section 4.4.1, a temperature of 15 K has been used. Nguyen Luong *et al.* (2011) studied G035.39-00.33 using *Herschel* to establish dust temperature maps. By fitting a pixel-by-pixel grey-body SED (using only the four longest wavelength *Herschel* bands, i.e. 160, 250, 350, and 500 μm), the dust temperature was shown to vary between 13-16 K. However, the resolution of the temperature map is $37''$, and is therefore sensitive to larger spatial scales than those traced by the PdBI.

Nguyen Luong *et al.* (2011) also established the temperature of each of the cores identified in the *Herschel* images (see cyan and yellow squares in Figures 4.1 and Figure 4.2), at a resolution of $12''$ (the fluxes detected at longer wavelengths must be scaled to account for the difference in resolution). The emission peaks detected in both the *Herschel* maps and the 3.2 mm continuum map presented here are PdBI 2, 8, 9, 12 (corresponding to cores 12, 18, 6, 28 in the notation of

Nguyen Luong *et al.* 2011). These cores have SED derived temperatures of 14, 14, 16, and 11 K, respectively.

In addition to these *Herschel* temperatures, Rathborne *et al.* (2010) studied the dust properties of several IRDC cores as a follow-up study to Rathborne *et al.* (2006). The H6 region (classified as core MM7 in Rathborne *et al.* 2006) was included in this study. Using 24, 350, 450, and 1200 μm data, the SED derived temperature for H6 was 34 K.

The above discrepancy in the derived temperatures may arise following the inclusion of 24 μm emission in the Rathborne *et al.* (2010) study. The location of MM7 (as deduced in the lower angular resolution study of Rathborne *et al.* 2006) does not directly coincide with any of the 3.2 mm PdBI peaks, nor the 24 μm emission obtained from Carey *et al.* (2009). This is evident in Figure 10 of Nguyen Luong *et al.* (2011). The inclusion of the 24 μm emission in the SED fit leads to an increase in the derived temperature (J. Rathborne, 2014, *private communication*). A uniform temperature of 34 K, incorporating this 24 μm flux, is therefore likely to be an overestimate.

Dust emissivity spectral index

The dust in both diffuse and dark clouds is consistent with an emissivity spectral index $\beta_{\rm ISM} \sim 1.8 \pm 0.2$ in the sub-mm (Draine 2006). Hill *et al.* (2006) find $1.5 \lesssim \beta \lesssim 3$, with values typically close to ~ 2 for a survey of southern massive star forming regions. However, in probing the smaller scale structure of massive star forming regions (< 5000 AU scales), several studies find $\beta \sim$ 1-2 (e.g. Cesaroni *et al.* 1999, Galván-Madrid *et al.* 2010, Zhang *et al.* 2007).

An estimate for β can be extracted from the 3.2 mm PdBI, and 1.3 mm SMA

data. To do this, a taper has been applied during the imaging of the PdBI data, such that the synthesized beam is approximately equal to that of the SMA. The peak flux in the SMA data (18.4 mJy beam^{-1}; see SMA 2 in Table 4.1) is then compared to the flux in the new (degraded resolution) PdBI map at the same location (1.4 mJy beam^{-1}). The spectral index of an SED fitting these two points is $\alpha \sim 3$. Assuming the Rayleigh-Jeans approximation is valid at these long wavelengths ($\alpha = 2+\beta$), $\beta \sim 1$.

An alternative (but crude) estimate for β can be derived using the 3.2 mm data in conjunction with the mass surface density map of KT13. The beam-averaged column density, N, is quantified using:

$$N = \frac{S_{\nu,\mathrm{peak}} R_{\mathrm{gd}}}{\Omega_{\mathrm{beam}} \mu m_{\mathrm{H}} \kappa_{\nu,\mathrm{d}} B_{\nu}(T_{\mathrm{d}})}, \tag{4.14}$$

where $S_{\nu,\mathrm{peak}}$ is the peak flux density (i.e. the peak flux of a dendrogram leaf), and Ω_{beam} is the solid angle of the beam (the remaining variables have the same meaning as those in Equation 4.3). Assuming that the column density derived from Σ (smoothed to the equivalent spatial resolution of the PdBI data) represents an upper limit to the column density (since it traces a high-dynamic range, from $A_{\mathrm{v}} \sim$ 1-100 mag; KT13), one can estimate $\kappa_{\nu,d}$, assuming a temperature. As with the mass calculations, $T_{\mathrm{d}} = 15$ K is assumed. In the estimation of Σ, BT09, use a gas-to-dust ratio, R_{gd}, of 156, and $\kappa_{\nu_{0,d}} = 1.056\,\mathrm{cm^2\,g^{-1}}$ at $\nu_0 = 250$ GHz. These values are therefore adopted in the estimation of β. Any source with associated 8 μm emission has been rejected from this analysis as this would lead to an underestimate of the column density derived from Σ (since Σ is derived from 8 μm extinction).

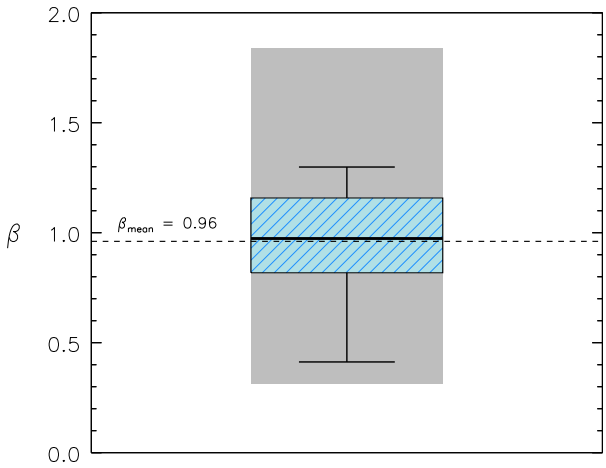

Figure 4.8: A box plot showing the range in β values for the IR dark PdBI leaves, as derived from the mass surface density. The figure highlights the minimum and maximum extent of the data, the length of the box is equivalent to the interquartile range, the horizontal line represents the median, and the width of the box is proportional to the square root of the number of data points. The mean β value of 0.96 is highlighted by the horizontal dashed line. The grey shaded area represents the uncertainty in β following the propagation of 30% errors in the mass surface density.

Figure 4.8 shows range in β values estimated for the IR-dark PdBI cores. Values are found within the range $\beta \sim 0.5$-1.3, with a mean value of $\beta \sim 1$. The uncertainty in β for each dendrogram leaf is represented by the shaded grey area. This is computed by propagating the estimated 30% error in the mass surface density *only* (KT13).

Whilst these derived values are consistent with observations in massive star forming regions that find $\beta \sim$ 1-2, both methods suffer from significant uncertainty. In the case of estimating β from the interferometric observations, the spatial coverage of the SMA and PdBI data in the (u, v) plane is not equivalent (the PdBI data is sensitive to a range $\sim$6-55 kλ, whereas the SMA data is sensitive to $\sim$7-42 kλ). Qualitatively, as the PdBI is sensitive to a greater range of spatial scales,

this estimate for β is likely to represent a lower limit (a decrease in PdBI flux with respect to the SMA flux would increase β). Similarly, estimating β from the mass surface density (with uncertainty $\sim 30\%$) relies on poorly constrained estimates of $T_{\rm d}$ and $\kappa_{\nu_{0,d}}$.

Flux correction

Another potential source of error comes from the uncertain flux distribution of the hierarchical structures identified in G035.39-00.33. The analysis presented in Section 4.4 has used two different flux measurements in order to estimate the physical parameters. Ragan *et al.* (2013) suggested that a correction must be applied to the flux of leaves with identifiable parent structure. Applying this correction makes an attempt to separate a leaf's flux from the parent material within which it is supposedly embedded. This correction however, is relatively simplistic as it is unable to account for projection effects. Ultimately, multiple leaves may *appear* to be embedded within a single parent branch (in the plane of the sky), when they are in fact well-separated (along the line of sight cf. the 'faux-filaments' created in the simulations of Moeckel & Burkert 2014). If this is the case, then the flux of the parent material will be overestimated (and the masses, underestimated). It is (qualitatively) concluded therefore, that the flux-corrected masses are most likely underestimated, as suggested by Rosolowsky *et al.* (2008). This discussion proceeds assuming that the uncorrected fluxes provide the most accurate description of the leaf masses.

Summary of uncertainties

Accounting for the above uncertainties, it is noted that: i) a temperature of 10 K would lead to an increase in the masses of the cores by a factor of ~ 1.6, whereas a temperature of 34 K would lead to a reduction in the masses by a factor of ~ 2.5 (using $\beta = 1.75$); ii) using $\beta = 2$ instead of the fiducial value of 1.75 would lead to a factor of ~ 1.25 increase in the mass, whereas $\beta = 1$ would lead to a factor of ~ 2 decrease in the mass (using $T = 15$ K). In the extreme cases whereby $T = 34$ K and $\beta = 1$, and $T = 10$ K and $\beta = 2$, the mean (uncorrected) masses are 1.5 $M_\odot$ and 15 $M_\odot$.

The above highlights the uncertainty in estimating masses from the dust properties. To constrain both properties, a more thorough analysis is needed. Further work, particularly focusing on the constraint of the (u, v) coverage of the PdBI and SMA data, ensuring that both sets of data cover an equivalent spatial scale (see the recent work of Galván-Madrid *et al.* 2010 and Maud *et al.* 2013 for a methodology), will provide a more accurate estimate of β.

However, the above discussion is intended as a consistency check for the choices of $T = 15$ K and $\beta = 1.75$ in the mass calculations. Propagating errors in the values of the flux (10%), distance (20%), temperature (30%), and opacity coefficient (30%), returns an expected uncertainty on the derived masses of $\gtrsim 50\%$.

4.6.2 The star formation potential of G035.39–0.33

Linking the physical and kinematic properties of G035.39–00.33

The dynamical state of the cores was investigated in Section 4.5. On average, the virial parameter is found to be ~ 1.5, although modifications for the density profile of the cores results in lower values. PdBI 9 and 11 exhibit sub-virial masses irrespective of the density profile assumed (as do PdBI 13, and 14, however, these leaves have irregular shapes and therefore may contain unresolved substructure). Cores would appear sub-virial if their masses were overestimated. Given the estimated uncertainty ($\sim 55\%$) the upper limit of the virial parameter of PdBI 9 would be $\alpha \sim 0.8$ (i.e. the core would still be sub-virial).

The presence of low virial parameters have previously been identified in other massive star forming regions (e.g. Csengeri *et al.* 2011a, Li *et al.* 2013, Pillai *et al.* 2011). Whilst low virial parameters suggest that cores are unstable to gravitational collapse, this is not necessarily an indication that cores are collapsing (Kauffmann *et al.* 2013a). Moreover, as suggested by Tan *et al.* (2013b), low virial parameters derived for cores that are not in free-fall gravitational collapse, may indicate the presence of dynamically important magnetic fields. Such considerations have been excluded in the analysis of Section 4.5.

Virial parameters derived for the leaves in the narrow clump are typically higher than those observed in the H6 clump (mean virial parameters of 2.8 and 0.8, respectively). Since the velocity dispersions of leaves associated with both clumps are comparable, this is most likely because the leaves situated along the narrow filament are less massive than those observed in the H6 region (mean masses $4\,M_\odot$ and $9.5\,M_\odot$, respectively). This is consistent with other regions of massive star

formation in which clusters (and more massive cores) are formed at the junctions of several filaments (Schneider *et al.* 2012). It is speculated that the merging of multiple filaments may be responsible for the increase in mass and density observed in this region (as suggested in Chapter 2).

No significant trends are observed between either the mass or radius and the velocity dispersion of the individual leaves (the null hypothesis, i.e. that there is no correlation, is accepted at the $P = 0.05$ level; this has been tested with all leaves, and considering both IR bright and IR dark leaves individually). All identified leaves exhibit trans- or supersonic non-thermal motions for the estimated temperature of 15 K ($\sigma_{\rm NT}/c_{\rm s} \gtrsim 1$) with the exception of PdBI 14, in which $\sigma_{\rm NT}/c_{\rm s} \sim 0.7$. It has been suggested that line-broadening towards nearby pre-stellar core centres in low-mass star forming regions may be indicative of infall of material (Caselli *et al.* 2002b, Crapsi *et al.* 2005). However, this may also be produced by embedded protostellar activity.

The two leaves with the broadest measured dispersions are PdBI 4 and PdBI 8. Both leaves exhibit complex velocity fields in the N_2H^+ $(1-0)$ emission. Chapter 3 selected PdBI 8 (referring to this peak as the "SW core") for a more detailed study. By making an assumption regarding the geometry of the filament, it was found that such a velocity field may be consistent with either filamentary accretion, or an expanding shell of dense gas. This may indicate that the onset of star formation is influencing the kinematics of the surrounding gas. Identifying signatures of infall (for example the asymmetric profiles traced by optically thick molecular lines, e.g. Evans 1999, Myers *et al.* 2000) with high-angular resolution observations, may aid in establishing whether or not the identified leaves are actively accreting material.

Section 4.4.2 showed that the projected separation between leaves is similar

to that expected from the thermal fragmentation of a cylinder, which may seem counter-intuitive given the prominence of non-thermal motions throughout G035.39-00.33. Teixeira *et al.* (2006, 2007), studying the substructure of NGC 2264-D (otherwise known as the Spokes cluster), identified several protostellar objects with separations comparable to the expected Jeans length, in spite of the non-thermal motions identified using N_2H^+ $(1-0)$ emission (Peretto *et al.* 2006). Pineda & Teixeira (2013) found that when observing N_2H^+ $(3-2)$, a probe of higher density gas, that the velocity dispersions decrease by 30%. Whilst the separation of leaves may be influenced by projection effects in G035.39-00.33 (see Section 4.4.2), this may signify that higher density gas tracers are required in order to accurately measure the dynamical state of the PdBI leaves.

Structure identification

The observations presented here primarily focus on the H6 region of G035.39-00.33, originally identified as MM7 in the survey of Rathborne *et al.* (2006), and the dense, filamentary IRDC ridge. It is found that the H6 region comprises several structures that are only revealed at high-angular resolution. Encompassed within the original angular FWHM diameter of the H6 region derived by Rathborne *et al.* (2006) using 1.2 mm continuum emission ($\sim 40''$), are five substructures, revealed in the $\sim 4''$ resolution PdBI observations. The lower angular resolution observations ($\sim 7''$) performed with the SMA at 1.3 mm identify two out of these five structures.

In total, fourteen leaves are identified in the dendrogram analysis. The mean radius of the leaves is ~ 0.04 pc similar to cores identified in other IRDCs (Tan *et al.* 2013b, Zhang *et al.* 2009), although the irregular boundaries of the leaves (see Figure 4.2) may indicate that unresolved fragments may also be present. Recent

high-angular resolution observations of IRDCs have referred to such structures as 'condensations', the dense nuclei of star-forming IRDC cores (Rathborne *et al.* 2007, Wang *et al.* 2014).

According to the dendrogram, two main branches are identified (the H6 and narrow clump), which contain twelve of the fourteen identified leaves. These branches, and the remaining two leaves, are associated with a larger filament, the darkest structure identified in MIR extinction. This implies that the structure of G035.39-00.33, is organised into a hierarchy of filaments, clumps, and cores, which is consistent with recent observations of other IRDCs (Beuther *et al.* 2013, Pillai *et al.* 2011, Ragan *et al.* 2013, Wang *et al.* 2011, 2014). Of the fourteen identified dendrogram leaves, five have spatially coincident emission at 4.5, 8, or 24 μm (or a combination of these). This indicates that star formation may have commenced within some of the leaves, whereas others remain dark up to 70 μm.

A Kolmogorov-Smirnov two-sample test is used to identify whether or not the IR bright and IR dark leaves are derived from the same population. This has been performed using the mass surface density, estimated from the uncorrected leaf masses and absolute areas (see column 9 of Table 4.1). A significant difference is found between the two populations (K-S probability, $p \sim 0.013$), with the IR dark cores having a greater surface density on average ($0.21\,\mathrm{g\,cm^{-2}}$ compared with the IR bright value of $0.16\,\mathrm{g\,cm^{-2}}$). However, given the small number of leaves in each sample, and the relative uncertainties in both the masses and radii, one should approach this result with caution. However, this does indicate that more in-depth investigation is needed to confirm the star formation content of these leaves.

Figure 4.6 shows that the uncorrected leaves fall very close to the empirical threshold for massive star formation derived by Kauffmann & Pillai (2010).

PdBI 9 and PdBI 11 both lie above this threshold. The masses of the dendrogram leaves can be compared with the empirical limit using $M/M_{\rm HM}$ (where $M_{\rm HM} = 580\,R^{4/3}\,{\rm M}_\odot$). Kauffmann & Pillai (2010) refer to this ratio as the "compactness". The PdBI leaves have compactness values in the range 0.5–1.3 (with a mean of 0.8). In addition, *all* PdBI leaves exhibit super-critical Jeans masses (assuming a temperature of 15 K; see Section 4.4.2).

The mean masses ($\sim 7.5\,{\rm M}_\odot$), radii (~ 0.04 pc), and volume densities ($\sim 4\times10^5$ cm^{-3}) derived for the PdBI leaves are consistent with such parameters derived in other IRDCs (e.g. Tan *et al.* 2013b), and intermediate-to-high mass star forming regions (e.g. Peretto *et al.* 2006). It is noted that many of the dendrogram leaves also show values typical to those observed in low-mass star forming regions (Caselli *et al.* 2002a), particularly those associated with the narrow clump. However, leaves that are well represented by monolithic, centrally concentrated structures (with no traceable substructure), that have compactness parameters > 1, that contain a number of Jeans masses, and have low virial parameters are good candidates for the progenitors to intermediate-to-high mass stars. In this sample, PdBI 9 and 11 satisfy this criteria.

4.7 Conclusions

This chapter presents a high-angular resolution study of the physical properties of the highly filamentary IRDC G035.39-00.33. The results and analysis of the work lead to the following conclusions:

1. Multi-resolution studies using SMA and PdBI images at 1.3 mm ($\sim 7''$ resolution) and 3.2 mm ($\sim 4''$ resolution), respectively, reveal increasing levels of fragmentation in the H6 region. The SMA images identify two substructures, whereas the same region observed with the PdBI reveals five structures. SMA 2 is shown at the PdBI resolution to exhibit two further structures, PdBI 9 and PdBI 10.

2. Dendrogram analysis reveals the presence of fourteen leaves in total, five of which have spatially coincident 4.5, 8, or 24 μm emission (or some combination of these). Whilst some of the leaves appear centrally condensed and monolithic, others have highly irregular boundaries, which may imply the presence of unresolved substructure.

3. Leaves have radii, $R_{\rm decon}$: 0.028-0.065 pc; masses, M: 2.4-12.3 $M_\odot$; number densities, n: 1.6×10^5-7.3×10^5 cm^{-3}. The most massive and dense of the dendrogram leaves are consistent with recent high-angular resolution observations of other IRDC cores (e.g. Tan *et al.* 2013b), and with other intermediate-to-high mass cores (e.g. Peretto *et al.* 2006). However, several of the dendrogram leaves are consistent with the properties of low-mass star forming cores (e.g. Caselli *et al.* 2002a). Further observations at additional wavelengths will help to constrain the physical parameters of the dendrogram

leaves.

4. The masses and radii of leaves associated with the narrow filament are smaller than those identified towards the H6 region. This is consistent with observations of other regions in which clustered, massive star formation is found at the intersection of multiple filaments. It is speculated that the merger of filaments in G035.39-00.33 may be responsible for the increased mass of cores at this location.

5. All leaves are found to exhibit super-critical Jeans masses for their respective densities. Moreover, a number of cores appear to be dynamically unstable following virial analysis.

6. Not all line-widths decrease when considering the PdBI-only data over the merged PdBI plus 30 m data. This may be the result of embedded star-formation, or dynamic effects such as accretion.

7. Although the leaves are typically found to exhibit trans- or supersonic line-widths ($\sigma_{\rm NT}/c_{\rm s} \gtrsim 1$), their projected spacing is consistent with that predicted by the thermal fragmentation of a cylinder ($\sim 0.12\,{\rm pc}$). Further high-angular resolution observations of molecular lines known for tracing high-critical densities are required in order to search for the presence of quiescent gas in this context.

8. There is also some evidence that the fragmentation length may be scale-dependent, with larger structures having separations that are more consistent with turbulent fragmentation. However, this affect may be influenced by projection.

Chapter 5

Conclusions

What are the initial conditions for massive star and cluster formation? Answering such a complex question requires detailed studies of molecular clouds that are in an early stage of their evolution. The large masses ($\sim 10^3$-10^5), high densities ($\sim 10^3$-$10^5\,\mathrm{cm}^{-3}$), and low temperatures ($< 25\,\mathrm{K}$) of IRDCs indicate that these objects could prove to be of great importance in answering such a question. In addition, recently formed molecular clouds may still have signatures of their formation processes imprinted in their chemical, kinematic, and physical structure. IRDCs therefore provide a unique opportunity to study the processes of both cloud and star formation, simultaneously. In spite of this, the study of IRDCs is still in its relative infancy. The following sections summarise the findings of this thesis, before discussing possible avenues for future work.

5.1 Summary

The image of G035.39-00.33 as a simple filamentary structure, as it appears in silhouette against the bright MIR Galactic background, is deceptive. This thesis confirms that G035.39-00.33 is organised into a network of morphologically distinct molecular filaments. By probing multiple physical scales, this thesis presents a detailed investigation into the kinematics and physical structure of a potential site of massive star formation.

Chapter 2 utilises high-spectral resolution and high-sensitivity observations from the IRAM 30 m telescope to study the kinematic structure of G035.39-00.33. N_2H^+ $(1-0)$ and $C^{18}O$ $(1-0)$ were chosen for this study since they allow us to compare and contrast the kinematics of the dense gas (as traced by N_2H^+) and the more abundant material (as traced by $C^{18}O$).

The $C^{18}O$ observations indicate that G035.39-00.33 is divided into at least three sub-filaments, two of which exhibit extended N_2H^+ emission. In low-mass star forming regions N_2H^+ is known to trace regions of high-density (e.g. Caselli *et al.* 2002a, Hacar & Tafalla 2011, Hacar *et al.* 2013, Tafalla *et al.* 2004). The prominence of N_2H^+ emission associated with certain structures, compared with its absence in others, implies that G035.39-00.33's sub-filaments have different density structure (a result that has since been confirmed by Jiménez-Serra *et al.* 2014).

Chapter 2 revealed that one of the sub-filaments of G035.39-00.33 is most prominent (filament 2 in the classification of Chapter 2). The N_2H^+ $(1-0)$ emission associated with the main filament is extended over >3 pc, implying the presence of widespread dense gas. Investigating this further revealed that the mean number

density across G035.39-00.33 is greater than that generally found in low-mass star forming regions (e.g. Pineda *et al.* 2008). This is consistent with the observation of widespread CO depletion throughout G035.39-00.33 (Hernandez *et al.* 2011.

Towards the locations of the most massive cores within G035.39-00.33 (as originally identified in 1.2 mm continuum emission Rathborne *et al.* 2006), multiple velocity components are detected. Jiménez-Serra *et al.* (2010) suggested that filament merging may be responsible for the detection of widespread SiO emission throughout G035.39-00.33. Chapter 2 speculated that such a process may also be responsible for the density enhancements at the locations of the most massive cores. It was estimated that it would take ~ 2 Myr to result in an $\sim$ order of magnitude increase in density at the interface of two merging filaments moving with relative velocity ~ 5 km s^{-1}.

Chapter 3 set out to extend this study by investigating the kinematic properties of the dense sub-filaments at high-angular resolution. It was shown that moment analysis, widely used in the interpretation of molecular line data, may be insufficient in describing the dynamics of massive star forming regions.

Moment analysis was unable to accurately describe the high-angular resolution data, leading to the erroneous interpretation of large-scale velocity gradients and line broadening. Correctly interpreting velocity gradients in molecular clouds is important. Velocity gradients may provide observational clues as to how cluster-forming clumps attain their mass, through the accretion of matter along filaments (e.g. Kirk *et al.* 2013, Peretto *et al.* 2014, Tackenberg *et al.* 2014, this was also presented as one of the possible explanations for the large-scale gradient observed in G035.39-00.33; Jiménez-Serra *et al.* 2014). However, the analysis presented in Chapter 3 should provide an important cautionary note. The high-angular resolu-

tion N_2H^+ $(1-0)$ data reveal sub-structure not evident in the single dish maps presented in Chapter 2. It is apparent that the presence of sub-components may mimic a large-scale velocity gradient when they are observed at lower-angular resolution.

Three sub-filaments separated in velocity by $< 1\ \mathrm{km\,s^{-1}\,pc^{-1}}$ were classified from the high-angular resolution N_2H^+ $(1-0)$ data (this does not include the low-velocity, and low-density filament 1 identified in Chapter 2). The intricate network of filamentary components in G035.39-00.33 bears striking resemblance to that of the L1495/B213 complex in Taurus described by Hacar *et al.* (2013). In contrast with the findings of Hacar *et al.* (2013) however, the dense gas of G035.39-00.33 is widespread, and exhibits mildly supersonic non-thermal motions, consistent with observations of other IRDCs (Battersby *et al.* 2014, Miettinen 2012). The widespread detection of high-density material in IRDCs may represent an important difference between the physical properties of low- and high-mass star forming regions.

The overall velocity gradients observed in the sub-filaments of G035.39-00.33 are small ($< 0.7\ \mathrm{km\,s^{-1}\,pc^{-1}}$). Locally however, observed velocity gradients are larger by comparison (of the order 1.5–2.5 $\mathrm{km\,s^{-1}\,pc^{-1}}$), and the velocity structure of each identified component is independent from the next. Moreover, it is shown that the local velocity gradients may be influenced by the embedded core population that provides the focus for Chapter 4.

Chapter 4 revealed a total of 14 continuum peaks, representative of the pre- and proto-stellar core population covering an area of $\sim 1.3\,\mathrm{pc^2}$ in G035.39-00.33. This is in contrast to previous low-angular resolution studies of G035.39-00.33 (e.g. Nguyen Luong *et al.* 2011, Rathborne *et al.* 2006). Their masses (2.4-12.3 $\mathrm{M_\odot}$),

sizes (0.03-0.07 pc), and volume densities (1.6×10^5-7.3×10^5 cm^{-3}), are consistent with those estimated from other high-angular resolution observations of IRDCs (e.g. Tan *et al.* 2013b). Whilst some of the identified cores appear centrally condensed and monolithic, others exhibit irregular boundaries, which may imply the presence of unresolved substructure.

The N_2H^+ $(1-0)$ presented in Chapter 3 was used in conjunction with the 3.2 mm continuum data to investigate the dynamical state of the identified cores. Although the dynamical state of each core is dependent on both its geometry and density profile it is found that many of the identified cores are unstable to collapse. Cores which are well represented by monolithic, centrally condensed structures, exhibiting low virial parameters and many Jeans masses, are good candidates for the progenitors of intermediate-to-high-mass stars. Within the selected area of G035.39-00.33, two of the identified cores meet this criteria.

5.2 Future work

Although the properties of IRDCs have been intensively researched in recent years, there is still much that we can learn about the cloud and star formation processes through their study. The following section discusses how the research presented in this thesis can be further developed, and highlights possible avenues for future study.

High angular resolution observations of cluster forming clumps:

To understand the role filaments play in the formation of massive cores, we must peer deep into dense molecular clouds; unveiling the population of quiescent pre-

stellar cores. This will be investigated in a future study of the H6 region of G035.39-00.33 using the Atacama Large Millimeter Array (ALMA).

Chapter 4 revealed that the clumps of G035.39-00.33 are highly fragmented. In addition, some of the identified continuum peaks display irregular boundaries. This may imply fragmentation on scales smaller than those probed by the PdBI data presented in Chapter 4. The ALMA study of the H6 clump will identify the core population complete to a resolution of ~ 0.02 pc. This will aid in establishing whether or not the more massive cores within the H6 region show further sub-structure, and help to understand the fragmentation process.

The core accretion model of high-mass star formation invokes turbulence and/or magnetic fields to provide pressure support in massive cores for which thermal support is insufficient (McKee & Tan 2002, 2003). Chapter 3 revealed that N_2H^+ $(1-0)$ traces the dense filamentary structures of G035.39-00.33, and does not exclusively trace the dense cores. One must therefore utilise tracers of even higher density gas to establish the turbulent content of the individual nodes of star formation. ALMA will be used to probe the dense gas of the H6 region using the $J = 3 \rightarrow 2$ transition of N_2H^+. The line-width distribution can then be tested against theories of either thermal or turbulent fragmentation.

This project will also study the kinematics of the star forming cores with respect to their surrounding filaments. Several studies of low-mass star forming regions show that the centroid velocities of dense cores are in good agreement with that of their envelope (e.g. Hacar & Tafalla 2011, Kirk *et al.* 2007, Walsh *et al.* 2004). Because of the greater density of the filaments in G035.39-00.33, this can be tested using the $J = 1 \rightarrow 0$ and $J = 3 \rightarrow 2$ transitions of N_2H^+. Studying the dynamics of the gas in this region with ALMA may also help to resolve the ambiguous

interpretation of the velocity gradient patterns identified in Chapter 3. This may help us to understand the mass assembly of these cores.

A statistical study of the kinematics of IRDCs:

Another important question to address is whether or not G035.39-00.33 is a "typical" IRDC. To answer this, the IRAM 30 m telescope will be used to study the kinematics of the 10 IRDCs presented in Butler & Tan (2009).

The IRDCs in the chosen sample display a range of morphologies (from extremely filamentary, to elliptical in 2-D projection), and have a variety of masses (from cloud I $\sim 2\times 10^2\,M_\odot$ to cloud C $\sim 7.4\times 10^4\,M_\odot$; Kainulainen & Tan 2013). It has been suggested that masses of clouds formed via colliding flows of atomic gas are limited to $\lesssim 10^3$-$10^4\,M_\odot$(e.g. McKee & Ostriker 2007). Studying the kinematic properites of clouds with a variety of physical properties and morphologies is therefore important in establishing their origins.

The early indications from this work are that, within this sample, the IRDCs, as with G035.39-00.33, comprise several velocity coherent structures. Figure 5.1 highlights some of the preliminary results of this study. Figure 5.1 is a position-position-velocity diagram highlighting different velocity components observed in $C^{18}O$ $(1-0)$ emission towards IRDC G028.37+00.07 (cloud C). The velocity structures have been extracted using the tool developed in Chapter 3. It is clear that the molecular gas is distributed across different structures separated in velocity space by a few $km\,s^{-1}$. There is evidence for velocity gradients throughout the map, and $C^{18}O$ overlapping regions coincide with the enhancement of the mass surface density in each IRDC. Moreover, the systemic velocities of the massive cores studied by Tan *et al.* (2013a) appear to be associated with different velocity

components. Similar features are also observed in the PPV structure of the other IRDCs in the sample.

A complimentary study investigating tracers typically associated with shocked gas across these clouds is also under-way (Jiménez-Serra et al., in prep.). The combination of these studies will establish whether or not the kinematics and chemistry of G035.39-00.33 are typical of IRDCs.

Investigating the influence of environment on star formation in IRDCs:

How does star formation vary under different physical conditions? Answering this question requires the study of molecular clouds that are subjected to different environmental conditions. One way to address this question is by comparing and contrasting the kinematic and physical properties of IRDCs contained within the Galactic disc, to those situated within the central molecular zone (CMZ) of the Galaxy.

The CMZ extends to a radius $< 0.5\,\mathrm{kpc}$ from the Galactic centre, and contains $\sim 10\%$ of the Galaxy's total molecular gas. The general properties of GMCs within the disc is known to vary from those of the CMZ. GMCs within the CMZ exhibit greater column and volume densities (by $\sim$ two orders of magnitude), have a greater velocity dispersion over a given physical extent (15–50 $\mathrm{km\,s^{-1}}$ over the area of a GMC), and have a higher kinetic temperature (see Longmore *et al.* 2014, Molinari *et al.* 2014, and references therein).

As well as hosting some of the most prominent sites of star formation within the Galaxy (Sgr B2 and Sgr C), and examples of young massive clusters (the Arches and Quintuplet clusters), the CMZ also contains some of the most extreme IRDCs. G0.253+0.016 otherwise known as the "Brick" is a well studied example of such

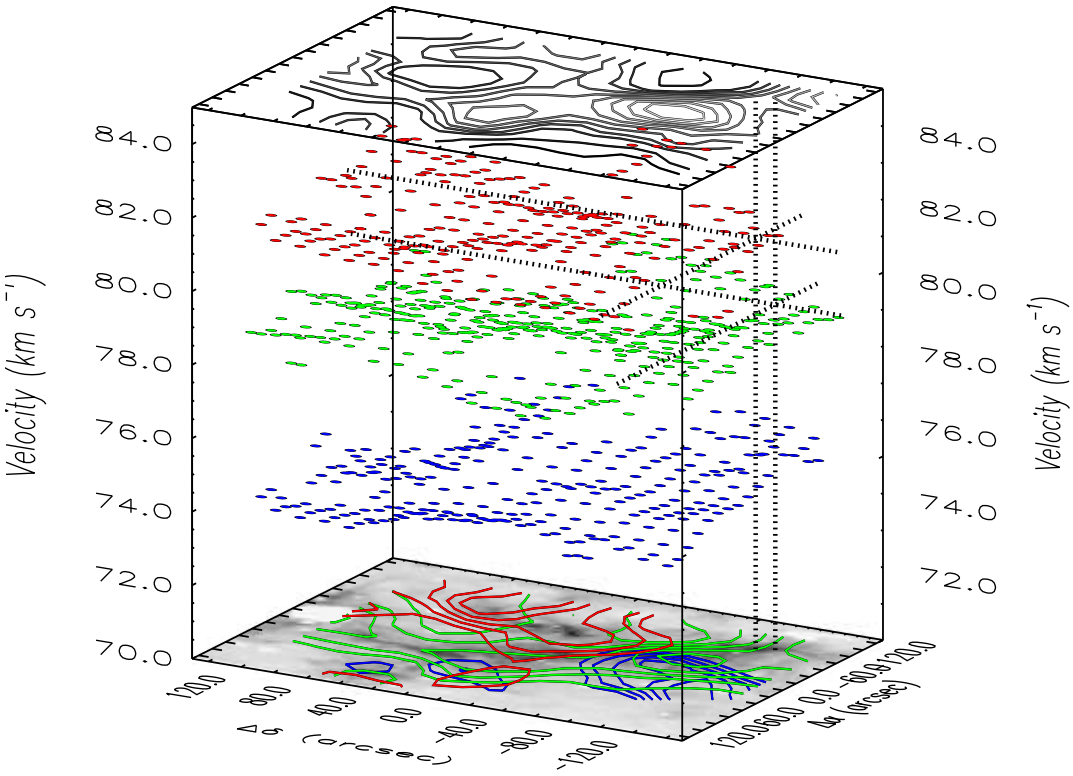

Figure 5.1: Position-position-velocity cube highlighting the velocity structure of cloud C (G028.37+00.07). These structures have been extracted from the $C^{18}O$ $(1-0)$ data using a Gaussian fitting routine presented in Chapter 3. At the base of the figure is the mass surface density map of Kainulainen & Tan 2013. Contour levels at the top of the image refer to the *total* integrated intensity over the full velocity range shown in the z-axis. The contour levels are from 40–60% peak integrated intensity in 10% intervals, and then 65-95% in 5% intervals (peak integrated intensity is $\sim 14\,\mathrm{K\ km\,s^{-1}}$). Contours at the bottom of each figure refer to the intensity of each spectral component integrated over their representative velocity range (contours are 50–90% peak integrated intensity increasing in 10% increments). The location and systemic velocity of the cores identified in N_2D^+ $(3-2)$ emission with ALMA by Tan *et al.* (2013a) are shown ($79.4\ \mathrm{km\,s^{-1}}$ and $81.2\ \mathrm{km\,s^{-1}}$ for C1-S and C1-N, respectively).

a cloud (Bally *et al.* 2010, Higuchi *et al.* 2014, Immer *et al.* 2012, Johnston *et al.* 2014, Kauffmann *et al.* 2013b, Lis & Menten 1998, Lis *et al.* 1994, Longmore *et al.* 2012, Rathborne *et al.* 2014). For a cloud containing $\sim 10^5\,M_\odot$ of gas within a radius of $\sim 3\,pc$, G0.253+0.016 shows very little signs of star formation activity. Consequently, G0.253+0.016 is one of the best examples of IRDCs to study the initial conditions for massive cluster formation.

Molinari *et al.* (2011) suggested that molecular gas within the CMZ was organised into a "twisted ring". Longmore *et al.* (2013) proposed that gas in this ring, and by inference, star formation, may be influenced by passing close to the super-massive black hole, Sgr A*, at the centre of the Milky Way. In this scenario, clouds that have recently (or are yet to) passed Sgr A* should show less star formation activity than those for which a significant amount of time has elapsed since passage. Even though the star formation potential of G0.253+0.016 is currently under debate (e.g. Johnston *et al.* 2014, Kauffmann *et al.* 2013b, Rathborne *et al.* 2014), studying the dynamics of molecular clouds in this region provides an opportunity to investigate the influence of environment on star formation.

5.3 Concluding remarks

Since their discovery as dark extinction features against the bright MIR Galactic background, Infrared Dark Clouds have received significant interest from the star formation community. In particular, Infrared dark clouds provide an exciting opportunity to investigate the initial conditions for massive star and star cluster formation.

The study of G035.39-00.33 presented in this thesis has revealed the kinematics of its dense filamentary network for the first time. Understanding the dynamics of massive star and star cluster formation is important to help test current theoretical models, and to make comparisons with the low-mass star forming environment. This thesis represents a step towards achieving this. However, in order to fully understand the dynamics of massive star forming regions, this study must be extended to different environments. The unprecedented capabilities of facilities such as ALMA and the planned upgraded to PdBI, NOEMA (Northern Extended Millimetre Array), will provide both the resolution and sensitivity needed to deconstruct complex molecular clouds, and help identify the initial conditions for massive star formation.

Appendix A

Gaussian fitting routines

A.1 Fitting routine 1: The Guided Gaussian Fit (GGF)

This fitting routine has been used for the analysis of Chapter 2. Multiple velocity components are evident in both the $C^{18}O$ and N_2H^+ data (see Section 2.5.1). The following steps outline the methodology used to fit these data:

1. Using Figures 2.3 and 2.15, three windows are defined based on the profile of the average spectra, and the differing morphology of the filamentary structures. The same windows are used for both $C^{18}O$ and N_2H^+: 42-44 $\mathrm{km\,s^{-1}}$, 44-46 $\mathrm{km\,s^{-1}}$, and 46-48 $\mathrm{km\,s^{-1}}$.

2. Using these spectral windows as a guide, three Gaussian components are fitted to the average spectra in GILDAS/CLASS. The average spectra that are fitted differ slightly between $C^{18}O$ and N_2H^+:

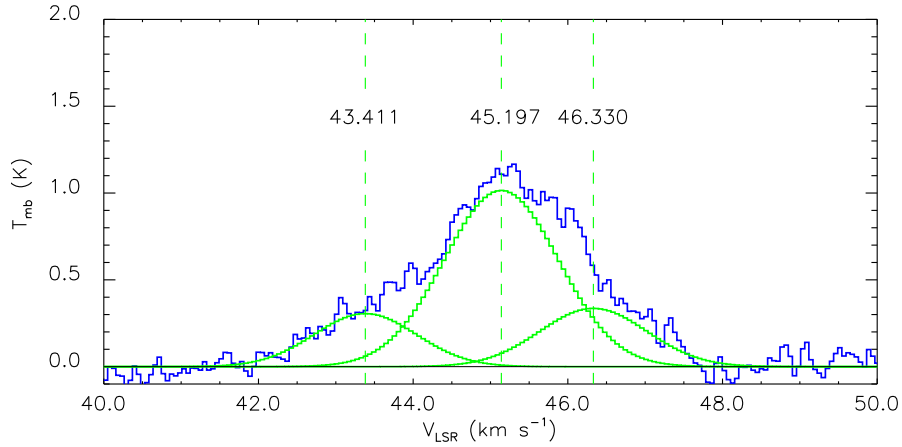

Figure A.1: Average spectrum of the $C^{18}O$ $(1-0)$ shown in blue. Overlaid in green are the three components associated with the average spectrum at velocities, 43.411 $\mathrm{km\,s^{-1}}$, 45.197 $\mathrm{km\,s^{-1}}$, and 46.330 $\mathrm{km\,s^{-1}}$.

(a) For $C^{18}O$: Figure A.1 displays the average $C^{18}O$ spectrum taken over the *entire* mapped region, with the CLASS fit results of three Gaussian profiles overlaid. These peak at velocities of, (Filament 1) 43.411 $\mathrm{km\,s^{-1}}$, (Filament 2) 45.197 $\mathrm{km\,s^{-1}}$, and (Filament 3) 46.330 $\mathrm{km\,s^{-1}}$.

(b) For N_2H^+: The average spectra are taken from the regions of emission (and not over the entire mapped region). This is because Filaments 1 and 3 cover a smaller area in N_2H^+ emission than they do in $C^{18}O$. The centroid velocities for the N_2H^+ components are: 42.985 $\mathrm{km\,s^{-1}}$, 45.582 $\mathrm{km\,s^{-1}}$, and 46.834 $\mathrm{km\,s^{-1}}$, for Filaments 1, 2, and 3, respectively.

3. The observed velocity dispersion from each Gaussian fit is calculated using, $\sigma_{\mathrm{obs}} = \Delta v_{\mathrm{obs}}/2\sqrt{2\ln(2)}$.

4. Using the observed velocity dispersion as a window, the integrated intensity

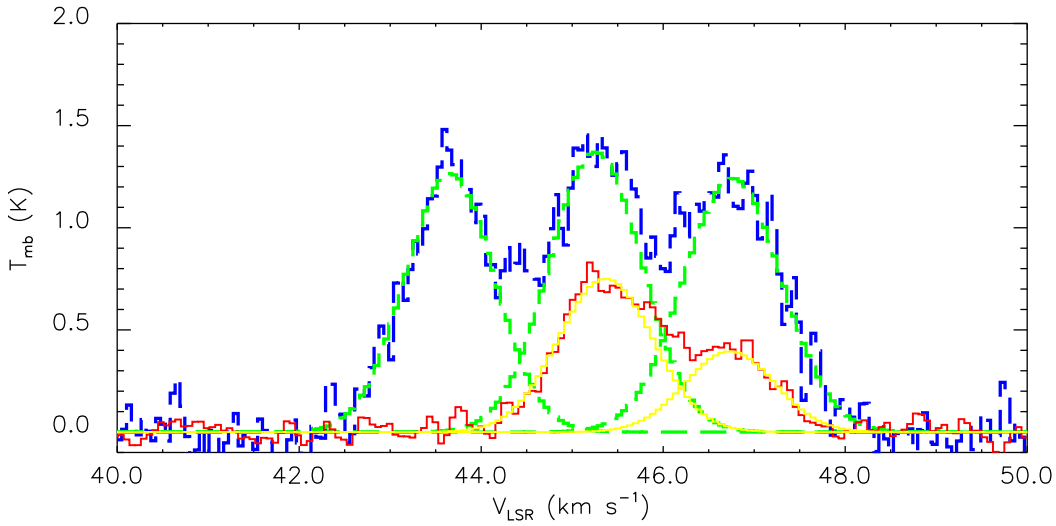

Figure A.2: Spectra at offset (-7.5″, 21″). $C^{18}O$ $(1-0)$ is shown as the dashed profile, in blue with the results of the GGF shown in green. N_2H^+ $(1-0)$ is shown as the solid profile, in red with the results of the GGF in yellow.

is calculated for every spectrum in the mapped region, between the limits $V_{\rm LSR} \pm \sigma_{\rm obs}$, whereby $V_{\rm LSR}$ is the centroid velocity of each component as derived from the average spectra.

5. This integrated intensity is then used as a *guide*. The standard detection threshold for Gaussian profiles is the 3σ level. In the case of G035.39-00.33, three overlapping velocity components are observed. For any individual component to be fitted therefore, a higher signal-to-noise ratio is required. In the case of the IRAM 30 m data, this was set at $S/N \geq 9$. This guide therefore indicates how many, and which velocity components should be fitted for any given spectrum.

6. As a secondary guide, the optically thin, isolated hyperfine component of the N_2H^+ spectrum, is overlaid when fitting the $C^{18}O$. If:

(a) multiple components are observed in the emission profiles of both species: the same features are fitted in both $C^{18}O$ and N_2H^+.

(b) a component is detected in $C^{18}O$, but and not in N_2H^+: The intensity of this profile is checked against the GGF intensity constraint, and also checked spatially using Figure 2.15. If the intensity constraint is satisfied, then the $C^{18}O$ component is fitted.

An example of this fitting procedure can be seen in Figure A.2. This shows the $C^{18}O$ (blue) and N_2H^+ (red) spectra at offset (-7.5″, 21″), $C^{18}O$ $(1-0)$ in blue, and N_2H^+ $(1-0)$. This location is close to H6. The results of the guided Gaussian fit are shown in green and yellow, respectively.

A.2 Fitting routine 2: Gaussian fitting & filament classification

This fitting routine has been used in the analysis of Chapter 3. The routine consists of two main components: A Gaussian fitting procedure, and a classification algorithm that identifies and groups components. In the next two sections the step-by-step methodology from fitting to classification is described.

A.2.1 Fitting routine

1. Firstly, a coverage is defined. The user is asked to provide a radius and spacing. This refers to a radius of a circle, within which the routine will compute an average spectrum from all spectra contained within this limit. The spacing refers to the placement of these preliminary areas. Specifically,

it is an integer number of pixels, starting at the first position in the map. The radius and spacing number should be selected such that a complete coverage of the map is achieved. The radius should be large enough to sufficiently reduce user input, but small enough to avoid diluting the main features within the spectra. For this particular data set, a radius of $6''$, with a spacing of $5.91''$ (i.e. $1.5 \times$ pixels), was used. This provided full coverage with 175 preliminary areas.

2. For each area, all spectra contained within the confining radius are averaged. The user then defines how many Gaussian components to fit to each average spectrum, and to provide initial estimates for the intensity, velocity, and line-width of each component.

3. A minimisation algorithm, MPFITFUN (Markwardt 2009), is used to find best fit results for the single or multiple Gaussian components, displaying the result to the screen.

4. Once satisfied (the residual to the fit is also displayed), the MPFITFUN fit results are then used as initial *free-parameter* estimates for each individual spectrum contained within the preliminary area.

5. The cycle is complete when no more preliminary areas remain.

In order for the routine to identify multiple velocity components, a number of constraints must be satisfied:

1. The spectrum must contain a velocity channel with a measured intensity greater than a user defined intensity threshold (based on the rms). All posi-

tions that do not contain a velocity channel with intensity greater than this threshold are discarded.

2. The FWHM of all Gaussian components must be broader than the velocity resolution ($\Delta v_{\rm res}$). Although simplistic, in very rare occasions the minimisation algorithm can converge on a non-physical solution - typically an extremely narrow (FWHM $<<\Delta v_{\rm res}$), and bright velocity component. These solutions are discarded by the program, and the spectra refit.

3. The separation in centroid velocity between two peaks must be greater than the half-width at half-maximum (HWHM) of the brightest component defined by the average spectrum. This is to prevent the minimisation algorithm converging towards a two component fit, when the spectrum only shows a single peak.

4. The centroid velocity of each Gaussian component in individual spectra must lie within a velocity range defined by $\rm V_{LSR}$–$\rm FWHM_{av} < V_{LSR} < V_{LSR}$+$\rm FWHM_{av}$, where $\rm FWHM_{av}$ refers to the FWHM of the *same component* identified in the average spectrum. This ensures that the same velocity component is fitted in each spectrum, whilst also allowing for velocity gradients on a spectrum-to-spectrum basis.

If the above conditions are not satisfied, the program will aim to fit a lower amount of velocity components, repeating the above checks until they are satisfied. Once satisfied, in order to be verified, the residual value of the resultant fit must be less than 3σ.

Due to the preliminary areas having some level of overlap with neighbouring areas, there are multiple fits to the same position. The benefit of this is that it ensures a smooth transition between areas. In order to select the "best fit" to the spectrum, the solution with the lowest $\chi^2_{\rm red}$ is therefore chosen.

A.2.2 Classification routine

To group velocity components, the map is divided into boxes. Each box has an area of $\sim 12'' \times 12''$ (the equivalent area would contain 9 synthesised PdBI beams). Next, the box with the greatest total integrated intensity is identified. Velocity component classification begins within this box using the following procedure:

1. From the data-set containing the Gaussian fits, the position within the box with the greatest integrated intensity is selected: this is the "seed" position. It is Identified whether or not this position has multiple velocity components associated with it. The first velocity component is selected.

2. The angular distance to every position within the area is calculated using:

$$d_i = \sqrt{(X_{\rm seed/branch} - X_i)^2 + (Y_{\rm seed/branch} - Y_i)^2} \qquad \text{(A.1)}$$

   (see step 4 for "branch" explanation).

3. All positions within a radius equivalent to the maximum distance between two adjacent pixels in the grid are selected. For the PdBI map this is equivalent to $\sqrt{(1.97)^2 + (1.97)^2} \sim 2.8''$ or ~ 0.04 pc at a distance of 2900 pc.

4. Each of these positions is then cycled through, calculating the velocity gradient between each spectral component, and the velocity component of the

seed position ($\nabla v \equiv \frac{|V_i - V_{\rm seed/branch}|}{d_i}$, where V_i is the velocity component of the selected position, $V_{\rm seed/branch}$ is the velocity component of the seed (branch) position, and d_i is the angular distance defined in step 2). If the velocity gradient is $\leq 2\ {\rm km\,s^{-1}\,pc^{-1}}$ (which corresponds to a velocity difference of $\sim 0.1\ {\rm km\,s^{-1}}$ over a distance of 0.04 pc) then accept these components as "linked". If linked, this position is registered as a new "branch" location.

5. Fit components that have then been classified as linked, are then removed from the data set. This ensures no component will be linked twice. For each of the boxes, catalogues are created for the linked components.

6. Each *branch* location is now cycled through, and steps 2–5 are repeated. However, rather than using the seed velocity, the branch velocity is used.

7. Once no more branch locations can be attributed to the original seed, move on to the next seed velocity component and repeat steps 2–5

8. Continue until all velocity components from the seed have been exhausted.

9. Repeat steps 1–8 until all seed locations have then been exhausted.

This method groups Gaussian components that are *closely* linked in velocity (the initial linking gradient over ~ 0.04 pc is $\sim$half of the velocity resolution in the case of the PdBI data). For each box one or more catalogues are returned that contain the linked velocity components. These catalogues contain the kinematic information extracted using the fitting procedure above (see A.2.1).

The above constraints leave a number of points unassigned. In order to group the unassigned data, angular distance from the brightest position in the cloud

versus $V_{\rm LSR}$ is plotted for every Gaussian component within the area. Easily distinguished are the velocity components that have been fitted according to the method outlined above. The remaining unassigned data points are then linked to the group that is closest in velocity. If this presented an ambiguous result, for example in a box where two components converge into a single Gaussian fit, with no obvious asymmetry, then the data point remains unassigned. This analysis is repeated for each box in the mapped area.

At this point, all boxes are *independent* from the surrounding areas. In order to link velocity components between boxes, the brightest box is selected first, and the eight surrounding boxes are arranged in order of descending *total* integrated intensity. By linking boxes that are directly adjacent to one another the risk of linking different velocity components is minimised (maximum distance between two points in adjacent boxes $\sim 34''$; or ~ 0.5 pc at a distance of 2900 pc). Finally, once the procedure is complete, individual positions are checked by eye to see whether or not a different number of velocity components would better represent the data.

The routine returns the following parameters for each individual velocity structure: Ra, Dec, line intensity (with uncertainty), centroid velocity (with uncertainty), FWHM (with uncertainty), base RMS, $\chi^2_{\rm red}$, residual value. The base RMS is calculated within a user defined velocity range. The $\chi^2_{\rm red}$ and residual values are derived from the output parameters of MPFITFUN.

Table A.1 highlights some statistics on the fitting procedure. Out of 1554 positions in the mapped region, a total of 1117 have been fitted with a total of 1700 Gaussian components. This highlights the degree of multiplicity in the cloud and the complexity of the spectra. Following the above procedures, $\sim$9% had to be

Table A.1: Statistics regarding the fitting and classification procedures.

Attribute	value
Total number of pixels	1554
Total number of pixels fitted	1117
Percentage number of fits (%)	71.9
Number of positions refitted (%)	<10.0
Total number of Gaussians fitted	1700
Degree of multiplicity (components per pixel)	1.5
F2a (%)	40.5
F2b (%)	35.3
F3 (%)	15.6
C4 (%)	1.4
C5 (%)	<1.0
C6 (%)	<1.0
Unclassified data (%)	5.9

refitted by hand. The majority of components have been attributed to filaments F2a, F2b, and F3, with contributions from additional components at various positions in the cloud (C4, C5, and C6 are identified as individual components, but cannot be linked to either each other or F2a, F2b, and F3, due to separation in either velocity or position). In total $\sim 6\%$ of the fits remain unclassified.

References

André, P. (2013). The Herschel View of Star Formation. *ArXiv e-prints*, arXiv:1309.7762.

André, P., Belloche, A., Motte, F. & Peretto, N. (2007). The initial conditions of star formation in the Ophiuchus main cloud: Kinematics of the protocluster condensations. A&A, **472**, 519–535.

André, P., Men'shchikov, A., Bontemps, S., Könyves, V., Motte, F., Schneider, N., Didelon, P., Minier, V., Saraceno, P., Ward-Thompson, D., di Francesco, J., White, G., Molinari, S., Testi, L., Abergel, A., Griffin, M., Henning, T., Royer, P., Merín, B., Vavrek, R., Attard, M., Arzoumanian, D., Wilson, C.D., Ade, P., Aussel, H., Baluteau, J.P., Benedettini, M., Bernard, J.P., Blommaert, J.A.D.L., Cambrésy, L., Cox, P., di Giorgio, A., Hargrave, P., Hennemann, M., Huang, M., Kirk, J., Krause, O., Launhardt, R., Leeks, S., Le Pennec, J., Li, J.Z., Martin, P.G., Maury, A., Olofsson, G., Omont, A., Peretto, N., Pezzuto, S., Prusti, T., Roussel, H., Russeil, D., Sauvage, M., Sibthorpe, B., Sicilia-Aguilar, A., Spinoglio, L., Waelkens, C., Woodcraft, A. & Zavagno, A. (2010). From filamentary clouds to prestellar cores to the stellar IMF: Initial highlights from the Herschel Gould Belt Survey. A&A, **518**, L102.

André, P., Di Francesco, J., Ward-Thompson, D., Inutsuka, S.i., Pudritz, R.E. & Pineda, J. (2013). From Filamentary Networks to Dense Cores in Molecular Clouds: Toward a New Paradigm for Star Formation. *ArXiv e-prints*.

Arce, H.G., Borkin, M.A., Goodman, A.A., Pineda, J.E. & Beaumont, C.N. (2011). A Bubbling Nearby Molecular Cloud: COMPLETE Shells in Perseus. ApJ, **742**, 105.

Audit, E. & Hennebelle, P. (2005). Thermal condensation in a turbulent atomic hydrogen flow. A&A, **433**, 1–13.

Ballesteros-Paredes, J. & Mac Low, M.M. (2002). Physical versus Observational Properties of Clouds in Turbulent Molecular Cloud Models. ApJ, **570**, 734–748.

Ballesteros-Paredes, J., Hartmann, L. & Vázquez-Semadeni, E. (1999). Turbulent Flow-driven Molecular Cloud Formation: A Solution to the Post-T Tauri Problem? ApJ, **527**, 285–297.

Ballesteros-Paredes, J., Klessen, R.S., Mac Low, M.M. & Vazquez-Semadeni, E. (2007). Molecular Cloud Turbulence and Star Formation. *Protostars and Planets V*, 63–80.

Ballesteros-Paredes, J., Hartmann, L.W., Vázquez-Semadeni, E., Heitsch, F. & Zamora-Avilés, M.A. (2011). Gravity or turbulence? Velocity dispersion-size relation. MNRAS, **411**, 65–70.

Bally, J., Langer, W.D., Stark, A.A. & Wilson, R.W. (1987). Filamentary structure in the Orion molecular cloud. ApJL, **312**, L45–L49.

Bally, J., Aguirre, J., Battersby, C., Bradley, E.T., Cyganowski, C., Dowell, D., Drosback, M., Dunham, M.K., Evans, N.J., II, Ginsburg, A., Glenn, J., Harvey, P., Mills, E., Merello, M., Rosolowsky, E., Schlingman, W., Shirley, Y.L., Stringfellow, G.S., Walawender, J. & Williams, J. (2010). The Bolocam Galactic Plane Survey: $\lambda = 1.1$ and 0.35 mm Dust Continuum Emission in the Galactic Center Region. ApJ, **721**, 137–163.

Balsara, D., Ward-Thompson, D. & Crutcher, R.M. (2001). A turbulent MHD model for molecular clouds and a new method of accretion on to star-forming cores. MNRAS, **327**, 715–720.

Barnard, E.E. (1919). On the dark markings of the sky, with a catalogue of 182 such objects. ApJ, **49**, 1–24.

Bastian, N., Covey, K.R. & Meyer, M.R. (2010). A Universal Stellar Initial Mass Function? A Critical Look at Variations. ARA&A, **48**, 339–389.

Battersby, C., Bally, J., Jackson, J.M., Ginsburg, A., Shirley, Y.L., Schlingman, W. & Glenn, J. (2010). An Infrared Through Radio Study of the Properties and Evolution of IRDC Clumps. ApJ, **721**, 222–250.

Battersby, C., Bally, J., Ginsburg, A., Bernard, J.P., Brunt, C., Fuller, G.A., Martin, P., Molinari, S., Mottram, J., Peretto, N., Testi, L. & Thompson, M.A. (2011). Characterizing precursors to stellar clusters with Herschel. A&A, **535**, A128.

Battersby, C., Ginsburg, A., Bally, J., Longmore, S., Dunham, M. & Darling, J. (2014). The Onset of Massive Star Formation: The Evolution of Temperature and Density Structure in an Infrared Dark Cloud. *ArXiv e-prints*.

Benson, P.J. & Myers, P.C. (1989). A survey for dense cores in dark clouds. ApJS, **71**, 89–108.

Bergin, E.A. & Tafalla, M. (2007). Cold Dark Clouds: The Initial Conditions for Star Formation. ARA&A, **45**, 339–396.

Bergin, E.A., Alves, J., Huard, T. & Lada, C.J. (2002). N_2H^+ and $C^{18}O$ Depletion in a Cold Dark Cloud. ApJL, **570**, L101–L104.

Bergin, E.A., Hartmann, L.W., Raymond, J.C. & Ballesteros-Paredes, J. (2004). Molecular Cloud Formation behind Shock Waves. ApJ, **612**, 921–939.

Bertoldi, F. & McKee, C.F. (1992). Pressure-confined clumps in magnetized molecular clouds. ApJ, **395**, 140–157.

Beuther, H. & Schilke, P. (2004). Fragmentation in MassiveStar Formation. *Science*, **303**, 1167–1169.

Beuther, H. & Steinacker, J. (2007). The Protostar in the Massive Infrared Dark Cloud IRDC 18223-3. ApJL, **656**, L85–L88.

Beuther, H., Schilke, P., Menten, K.M., Motte, F., Sridharan, T.K. & Wyrowski, F. (2002). High-Mass Protostellar Candidates. II. Density Structure from Dust Continuum and CS Emission. ApJ, **566**, 945–965.

Beuther, H., Linz, H., Tackenberg, J., Henning, T., Krause, O., Ragan, S., Nielbock, M., Launhardt, R., Bihr, S., Schmiedeke, A., Smith, R. & Sakai, T. (2013). Fragmentation and dynamical collapse of the starless high-mass star-forming region IRDC 18310-4. A&A, **553**, A115.

Blitz, L. (1993). Giant molecular clouds. In E.H. Levy & J.I. Lunine, eds., *Protostars and Planets III*, 125–161.

Blitz, L. & Shu, F.H. (1980). The origin and lifetime of giant molecular cloud complexes. ApJ, **238**, 148–157.

Bok, B.J. & Reilly, E.F. (1947). Small Dark Nebulae. ApJ, **105**, 255.

Bonnell, I.A., Bate, M.R., Clarke, C.J. & Pringle, J.E. (1997). Accretion and the stellar mass spectrum in small clusters. MNRAS, **285**, 201–208.

Bonnell, I.A., Bate, M.R. & Zinnecker, H. (1998). On the formation of massive stars. MNRAS, **298**, 93–102.

Bonnell, I.A., Larson, R.B. & Zinnecker, H. (2007). The Origin of the Initial Mass Function. *Protostars and Planets V*, 149–164.

Bourke, T.L., Hyland, A.R., Robinson, G., James, S.D. & Wright, C.M. (1995). Studies of star formation in isolated small dark clouds - II. A southern ammonia survey. MNRAS, **276**, 1067–1084.

Bressert, E., Bastian, N., Evans, C.J., Sana, H., Hénault-Brunet, V., Goodwin, S.P., Parker, R.J., Gieles, M., Bestenlehner, J.M., Vink, J.S., Taylor, W.D., Crowther, P.A., Longmore, S.N., Gräfener, G., Maíz Apellániz, J., de Koter, A., Cantiello, M. & Kruijssen, J.M.D. (2012). The VLT-FLAMES Tarantula Survey. IV. Candidates for isolated high-mass star formation in 30 Doradus. A&A, **542**, A49.

Busquet, G., Zhang, Q., Palau, A., Liu, H.B., Sánchez-Monge, Á., Estalella, R., Ho, P.T.P., de Gregorio-Monsalvo, I., Pillai, T., Wyrowski, F., Girart, J.M., Santos, F.P. & Franco, G.A.P. (2013). Unveiling a Network of Parallel Filaments in the Infrared Dark Cloud G14.225–0.506. ApJL, **764**, L26.

Butler, M.J. & Tan, J.C. (2009). Mid-Infrared Extinction Mapping of Infrared Dark Clouds: Probing the Initial Conditions for Massive Stars and Star Clusters. ApJ, **696**, 484–497.

Butler, M.J. & Tan, J.C. (2012). Mid-infrared Extinction Mapping of Infrared Dark Clouds. II. The Structure of Massive Starless Cores and Clumps. ApJ, **754**, 5.

Cambrésy, L. (1999). Mapping of the extinction in giant molecular clouds using optical star counts. A&A, **345**, 965–976.

Carey, S.J., Clark, F.O., Egan, M.P., Price, S.D., Shipman, R.F. & Kuchar, T.A. (1998). The Physical Properties of the Midcourse Space Experiment Galactic Infrared-dark Clouds. ApJ, **508**, 721–728.

Carey, S.J., Noriega-Crespo, A., Mizuno, D.R., Shenoy, S., Paladini, R., Kraemer, K.E., Price, S.D., Flagey, N., Ryan, E., Ingalls, J.G., Kuchar, T.A., Pinheiro Gonçalves, D., Indebetouw, R., Billot, N., Marleau, F.R., Padgett, D.L., Rebull, L.M., Bressert, E., Ali, B., Molinari, S., Martin, P.G., Berriman, G.B., Boulanger, F., Latter, W.B., Miville-Deschenes, M.A., Shipman, R. & Testi, L. (2009).

MIPSGAL: A Survey of the Inner Galactic Plane at 24 and 70 μm. PASP, **121**, 76–97.

Caselli, P. & Ceccarelli, C. (2012). Our astrochemical heritage. A&AR, **20**, 56.

Caselli, P. & Myers, P.C. (1995). The Line Width–Size Relation in Massive Cloud Cores. ApJ, **446**, 665.

Caselli, P., Myers, P.C. & Thaddeus, P. (1995). Radio-astronomical Spectroscopy of the Hyperfine Structure of N_2H^+. ApJL, **455**, L77+.

Caselli, P., Walmsley, C.M., Tafalla, M., Dore, L. & Myers, P.C. (1999). CO Depletion in the Starless Cloud Core L1544. ApJL, **523**, L165–L169.

Caselli, P., Benson, P.J., Myers, P.C. & Tafalla, M. (2002a). Dense Cores in Dark Clouds. XIV. N_2H^+ (1-0) Maps of Dense Cloud Cores. ApJ, **572**, 238–263.

Caselli, P., Walmsley, C.M., Zucconi, A., Tafalla, M., Dore, L. & Myers, P.C. (2002b). Molecular Ions in L1544. II. The Ionization Degree. ApJ, **565**, 344–358.

Casoli, F. & Combes, F. (1982). Can giant molecular clouds form in spiral arms. A&A, **110**, 287–294.

Cazzoli, G., Puzzarini, C. & Lapinov, A.V. (2003). Precise Laboratory Frequencies for the J = 1-0 and J = 2-1 Rotational Transitions of $C^{18}O$. ApJL, **592**, L95–L98.

Cesaroni, R., Felli, M., Jenness, T., Neri, R., Olmi, L., Robberto, M., Testi, L. & Walmsley, C.M. (1999). Unveiling the disk-jet system in the massive (proto)star IRAS 20126+4104. A&A, **345**, 949–964.

Cesaroni, R., Galli, D., Lodato, G., Walmsley, C.M. & Zhang, Q. (2007). Disks Around Young O-B (Proto)Stars: Observations and Theory. *Protostars and Planets V*, 197–212.

Chabrier, G. (2005). The Initial Mass Function: from Salpeter 1955 to 2005. In E. Corbelli, F. Palla & H. Zinnecker, eds., *The Initial Mass Function 50 Years Later*, vol. 327 of *Astrophysics and Space Science Library*, 41.

Chambers, E.T., Jackson, J.M., Rathborne, J.M. & Simon, R. (2009). Star Formation Activity of Cores within Infrared Dark Clouds. ApJS, **181**, 360–390.

Chen, H.R., Liu, S.Y., Su, Y.N. & Zhang, Q. (2010). Deuterium Fractionation as an Evolutionary Probe in the Infrared Dark Cloud G28.34+0.06. ApJL, **713**, L50–L54.

Chira, R.A., Beuther, H., Linz, H., Schuller, F., Walmsley, C.M., Menten, K.M. & Bronfman, L. (2013). Characterization of infrared dark clouds. NH_3 observations of an absorption-contrast selected IRDC sample. A&A, **552**, A40.

Clemens, D.P. & Barvainis, R. (1988). A catalog of small, optically selected molecular clouds - Optical, infrared, and millimeter properties. ApJS, **68**, 257–286.

Crapsi, A., Devries, C.H., Huard, T.L., Lee, J.E., Myers, P.C., Ridge, N.A., Bourke, T.L., Evans, N.J., II, Jørgensen, J.K., Kauffmann, J., Lee, C.W., Shirley, Y.L. & Young, C.H. (2005). Dynamical and chemical properties of the "starless" core L1014. A&A, **439**, 1023–1032.

Crutcher, R.M. (2012). Magnetic Fields in Molecular Clouds. ARA&A, **50**, 29–63.

Csengeri, T., Bontemps, S., Schneider, N., Motte, F. & Dib, S. (2011a). Gas dynamics in massive dense cores in Cygnus-X. A&A, **527**, A135.

Csengeri, T., Bontemps, S., Schneider, N., Motte, F., Gueth, F. & Hora, J.L. (2011b). Convergent Flows and Low-velocity Shocks in DR21(OH). ApJL, **740**, L5.

Cyganowski, C.J., Whitney, B.A., Holden, E., Braden, E., Brogan, C.L., Churchwell, E., Indebetouw, R., Watson, D.F., Babler, B.L., Benjamin, R., Gomez, M., Meade, M.R., Povich, M.S., Robitaille, T.P. & Watson, C. (2008). A Catalog of Extended Green Objects in the GLIMPSE Survey: A New Sample of Massive Young Stellar Object Outflow Candidates. AJ, **136**, 2391–2412.

Davies, B., Hoare, M.G., Lumsden, S.L., Hosokawa, T., Oudmaijer, R.D., Urquhart, J.S., Mottram, J.C. & Stead, J. (2011). The Red MSX Source survey: critical tests of accretion models for the formation of massive stars. MNRAS, **416**, 972–990.

de Marchi, G. & Paresce, F. (2001). The Mass Function of Galactic Clusters and its Evolution with Time. In E.R. Schielicke, ed., *Astronomische Gesellschaft Meeting Abstracts*, vol. 18 of *Astronomische Gesellschaft Meeting Abstracts*, 551.

de Wit, W.J., Testi, L., Palla, F. & Zinnecker, H. (2005). The origin of massive O-type field stars: II. Field O stars as runaways. A&A, **437**, 247–255.

Devine, K.E., Chandler, C.J., Brogan, C., Churchwell, E., Indebetouw, R., Shirley, Y. & Borg, K.J. (2011). Very Large Array Observations of the Infrared Dark Cloud G19.30+0.07. ApJ, **733**, 44.

di Francesco, J., Evans, N.J., II, Caselli, P., Myers, P.C., Shirley, Y., Aikawa, Y. & Tafalla, M. (2007). An Observational Perspective of Low-Mass Dense Cores I: Internal Physical and Chemical Properties. *Protostars and Planets V*, 17–32.

Dobbs, C.L. (2008). GMC formation by agglomeration and self gravity. MNRAS, **391**, 844–858.

Dobbs, C.L., Bonnell, I.A. & Clark, P.C. (2005). Centrally condensed turbulent cores: massive stars or fragmentation? MNRAS, **360**, 2–8.

Dobbs, C.L., Burkert, A. & Pringle, J.E. (2011). Why are most molecular clouds not gravitationally bound? MNRAS, **413**, 2935–2942.

Dobbs, C.L., Krumholz, M.R., Ballesteros-Paredes, J., Bolatto, A.D., Fukui, Y., Heyer, M., Mac Low, M.M., Ostriker, E.C. & Vázquez-Semadeni, E. (2013). Formation of Molecular Clouds and Global Conditions for Star Formation. *ArXiv e-prints*.

Draine, B.T. (2006). On the Submillimeter Opacity of Protoplanetary Disks. ApJ, **636**, 1114–1120.

Draine, B.T. (2011). *Physics of the Interstellar and Intergalactic Medium*.

Du, F. & Yang, J. (2008). A ^{12}CO, ^{13}CO, and C^{18}O Survey of Infrared Dark Clouds. ApJ, **686**, 384–398.

Duarte-Cabral, A., Dobbs, C.L., Peretto, N. & Fuller, G.A. (2011). Was a cloud-cloud collision the trigger of the recent star formation in Serpens? A&A, **528**, A50.

Dunham, M.K., Rosolowsky, E., Evans, N.J., II, Cyganowski, C. & Urquhart, J.S. (2011). The Bolocam Galactic Plane Survey. VII. Characterizing the Properties of Massive Star-forming Regions. ApJ, **741**, 110.

Egan, M.P., Shipman, R.F., Price, S.D., Carey, S.J., Clark, F.O. & Cohen, M. (1998). A Population of Cold Cores in the Galactic Plane. ApJL, **494**, L199+.

Elmegreen, B.G. (1993). Formation of interstellar clouds and structure. In E.H. Levy & J.I. Lunine, eds., *Protostars and Planets III*, 97–124.

Elmegreen, B.G. & Elmegreen, D.M. (1983). Regular strings of H II regions and superclouds in spiral galaxies - Clues to the origin of cloudy structure. MNRAS, **203**, 31–45.

Enoch, M.L., Corder, S., Dunham, M.M. & Duchêne, G. (2009). Disk and Envelope Structure in Class 0 Protostars. I. The Resolved Massive Disk in Serpens Firs 1. ApJ, **707**, 103–113.

Enoch, M.L., Lee, J.E., Harvey, P., Dunham, M.M. & Schnee, S. (2010). A Candidate Detection of the First Hydrostatic Core. ApJL, **722**, L33–L38.

Evans, N.J., II (1999). Physical Conditions in Regions of Star Formation. ARA&A, **37**, 311–362.

Evans, N.J., II, Dunham, M.M., Jørgensen, J.K., Enoch, M.L., Merín, B., van Dishoeck, E.F., Alcalá, J.M., Myers, P.C., Stapelfeldt, K.R., Huard, T.L., Allen, L.E., Harvey, P.M., van Kempen, T., Blake, G.A., Koerner, D.W., Mundy, L.G., Padgett, D.L. & Sargent, A.I. (2009). The Spitzer c2d Legacy Results: Star-Formation Rates and Efficiencies; Evolution and Lifetimes. ApJS, **181**, 321–350.

Fatuzzo, M. & Adams, F.C. (2002). Enhancement of Ambipolar Diffusion Rates through Field Fluctuations. ApJ, **570**, 210–221.

Fiege, J.D. & Pudritz, R.E. (2000). Helical fields and filamentary molecular clouds - I. MNRAS, **311**, 85–104.

Field, G.B. & Saslaw, W.C. (1965). A Statistical Model of the Formation of Stars and Interstellar Clouds. ApJ, **142**, 568.

Fontani, F., Caselli, P., Bourke, T.L., Cesaroni, R. & Brand, J. (2008). Highly deuterated pre-stellar cores in a high-mass star formation region. A&A, **477**, L45–L48.

Fontani, F., Palau, A., Caselli, P., Sánchez-Monge, Á., Butler, M.J., Tan, J.C., Jiménez-Serra, I., Busquet, G., Leurini, S. & Audard, M. (2011). Deuteration as an evolutionary tracer in massive-star formation. A&A, **529**, L7+.

Fontani, F., Giannetti, A., Beltrán, M.T., Dodson, R., Rioja, M., Brand, J., Caselli, P. & Cesaroni, R. (2012). High CO depletion in southern infrared dark clouds. MNRAS, **423**, 2342–2358.

Fontani, F., Sakai, T., Furuya, K., Sakai, N., Aikawa, Y. & Yamamoto, S. (2014). DNC/HNC and N_2D^+/N_2H^+ ratios in high-mass star-forming cores. MNRAS, **440**, 448–456.

Frank, A., Ray, T.P., Cabrit, S., Hartigan, P., Arce, H.G., Bacciotti, F., Bally, J., Benisty, M., Eislöffel, J., Güdel, M., Lebedev, S., Nisini, B. & Raga, A. (2014). Jets and Outflows From Star to Cloud: Observations Confront Theory. *ArXiv e-prints*.

Friesen, R.K., Di Francesco, J., Shimajiri, Y. & Takakuwa, S. (2010). The Initial Conditions of Clustered Star Formation. II. N_2H^+ Observations of the Ophiuchus B Core. ApJ, **708**, 1002–1024.

Friesen, R.K., Medeiros, L., Schnee, S., Bourke, T.L., Di Francesco, J., Gutermuth, R. & Myers, P.C. (2013). Abundant cyanopolyynes as a probe of infall in the Serpens South cluster-forming region. *ArXiv e-prints*.

Fuller, G.A. & Myers, P.C. (1992). Dense cores in dark clouds. VII - Line width-size relations. ApJ, **384**, 523–527.

Galván-Madrid, R., Zhang, Q., Keto, E., Ho, P.T.P., Zapata, L.A., Rodríguez, L.F., Pineda, J.E. & Vázquez-Semadeni, E. (2010). From the Convergence of Filaments to Disk-outflow Accretion: Massive Star Formation in W33A. ApJ, **725**, 17–28.

Goldreich, P. & Kwan, J. (1974). Molecular Clouds. ApJ, **189**, 441–454.

Goldsmith, P.F. (2001). Molecular Depletion and Thermal Balance in Dark Cloud Cores. ApJ, **557**, 736–746.

Goldsmith, P.F. & Langer, W.D. (1999). Population Diagram Analysis of Molecular Line Emission. ApJ, **517**, 209–225.

Gomez, G.C. & Vazquez-Semadeni, E. (2013). Filaments in Simulations of Molecular Cloud Formation. *ArXiv e-prints*.

Gómez, L., Wyrowski, F., Schuller, F., Menten, K.M. & Ballesteros-Paredes, J. (2014). The mass distribution of clumps within infrared dark clouds. A Large APEX Bolometer Camera study. A&A, **561**, A148, arXiv:1312.4683.

Goodman, A.A., Benson, P.J., Fuller, G.A. & Myers, P.C. (1993). Dense cores in dark clouds. VIII - Velocity gradients. ApJ, **406**, 528–547.

Goodman, A.A., Rosolowsky, E.W., Borkin, M.A., Foster, J.B., Halle, M., Kauffmann, J. & Pineda, J.E. (2009). A role for self-gravity at multiple length scales in the process of star formation. Nature, **457**, 63–66.

Hacar, A. & Tafalla, M. (2011). Dense core formation by fragmentation of velocity-coherent filaments in L1517. A&A, **533**, A34.

Hacar, A., Tafalla, M., Kauffmann, J. & Kovács, A. (2013). Cores, filaments, and bundles: hierarchical core formation in the L1495/B213 Taurus region. A&A, **554**, A55.

Hartmann, L., Ballesteros-Paredes, J. & Bergin, E.A. (2001). Rapid Formation of Molecular Clouds and Stars in the Solar Neighborhood. ApJ, **562**, 852–868.

Heitsch, F., Zweibel, E.G., Slyz, A.D. & Devriendt, J.E.G. (2004). Turbulent Ambipolar Diffusion: Numerical Studies in Two Dimensions. ApJ, **603**, 165–179.

Heitsch, F., Slyz, A.D., Devriendt, J.E.G., Hartmann, L.W. & Burkert, A. (2006). The Birth of Molecular Clouds: Formation of Atomic Precursors in Colliding Flows. ApJ, **648**, 1052–1065.

Heitsch, F., Hartmann, L.W. & Burkert, A. (2008). Fragmentation of Shocked Flows: Gravity, Turbulence, and Cooling. ApJ, **683**, 786–795.

Hennebelle, P. & Pérault, M. (1999). Dynamical condensation in a thermally bistable flow. Application to interstellar cirrus. A&A, **351**, 309–322.

Hernandez, A.K., Tan, J.C., Caselli, P., Butler, M.J., Jiménez-Serra, I., Fontani, F. & Barnes, P. (2011). Mapping Large-scale CO Depletion in a Filamentary Infrared Dark Cloud. ApJ, **738**, 11, (Paper II).

Hernandez, A.K., Tan, J.C., Kainulainen, J., Caselli, P., Butler, M.J., Jiménez-Serra, I. & Fontani, F. (2012). A Virialized Filamentary Infrared Dark Cloud. ApJL, **756**, L13, (Paper III).

Heyer, M., Krawczyk, C., Duval, J. & Jackson, J.M. (2009). Re-Examining Larson's Scaling Relationships in Galactic Molecular Clouds. ApJ, **699**, 1092–1103.

Heyer, M.H. & Brunt, C.M. (2004). The Universality of Turbulence in Galactic Molecular Clouds. ApJL, **615**, L45–L48.

Heyer, M.H., Carpenter, J.M. & Snell, R.L. (2001). The Equilibrium State of Molecular Regions in the Outer Galaxy. ApJ, **551**, 852–866.

Higuchi, A.E., Chibueze, J.O., Habe, A., Takahira, K. & Takano, S. (2014). ALMA View of G0.253+0.016: Can Cloud-Cloud Collision form the Cloud? AJ, **147**, 141.

Hildebrand, R.H. (1983). The Determination of Cloud Masses and Dust Characteristics from Submillimetre Thermal Emission. QJRAS, **24**, 267.

Hill, T., Thompson, M.A., Burton, M.G., Walsh, A.J., Minier, V., Cunningham, M.R. & Pierce-Price, D. (2006). Millimetre continuum observations of southern massive star formation regions - II. SCUBA observations of cold cores and the dust grain emissivity index (β). MNRAS, **368**, 1223–1268.

Hillenbrand, L.A. & Hartmann, L.W. (1998). A Preliminary Study of the Orion Nebula Cluster Structure and Dynamics. ApJ, **492**, 540.

Hillier, D.J., Davidson, K., Ishibashi, K. & Gull, T. (2001). On the Nature of the Central Source in η Carinae. ApJ, **553**, 837–860.

Hily-Blant, P., Teyssier, D., Philipp, S. & Güsten, R. (2005). Velocity field and star formation in the Horsehead nebula. A&A, **440**, 909–919.

Hily-Blant, P., Walmsley, M., Pineau Des Forêts, G. & Flower, D. (2010). Nitrogen chemistry and depletion in starless cores. A&A, **513**, A41+.

Houlahan, P. & Scalo, J. (1992). Recognition and characterization of hierarchical interstellar structure. II - Structure tree statistics. ApJ, **393**, 172–187.

Ilee, J.D., Wheelwright, H.E., Oudmaijer, R.D., de Wit, W.J., Maud, L.T., Hoare, M.G., Lumsden, S.L., Moore, T.J.T., Urquhart, J.S. & Mottram, J.C. (2013). CO bandhead emission of massive young stellar objects: determining disc properties. MNRAS, **429**, 2960–2973.

Imara, N. & Blitz, L. (2011). Angular Momentum in Giant Molecular Clouds. I. The Milky Way. ApJ, **732**, 78.

Imara, N., Bigiel, F. & Blitz, L. (2011). Angular Momentum in Giant Molecular Clouds. II. M33. ApJ, **732**, 79.

Immer, K., Menten, K.M., Schuller, F. & Lis, D.C. (2012). A multi-wavelength view of the Galactic center dust ridge reveals little star formation. A&A, **548**, A120.

Jackson, J.M., Finn, S.C., Chambers, E.T., Rathborne, J.M. & Simon, R. (2010). The "Nessie" Nebula: Cluster Formation in a Filamentary Infrared Dark Cloud. ApJL, **719**, L185–L189.

Jeans, J.H. (1902). The Stability of a Spherical Nebula. *Royal Society of London Philosophical Transactions Series A*, **199**, 1–53.

Jiménez-Serra, I., Martín-Pintado, J., Caselli, P., Viti, S. & Rodríguez-Franco, A. (2009). The Evolution of Molecular Line Profiles Induced by the Propagation of C-Shock Waves. ApJ, **695**, 149–155.

Jiménez-Serra, I., Caselli, P., Tan, J.C., Hernandez, A.K., Fontani, F., Butler, M.J. & van Loo, S. (2010). Parsec-scale SiO emission in an infrared dark cloud. MNRAS, **406**, 187–196, (Paper I).

Jiménez-Serra, I., Caselli, P., Fontani, F., Tan, J.C., Henshaw, J.D., Kainulainen, J. & Hernandez, A.K. (2014). Gas kinematics and excitation in the filamentary IRDC G035.39-00.33. MNRAS, **439**, 1996–2013, 1401.2347 (Paper V).

Johnston, K.G., Beuther, H., Linz, H., Schmiedeke, A., Ragan, S.E. & Henning, T. (2014). The dynamics and star-forming potential of the massive Galactic centre cloud G0.253+0.016. *ArXiv e-prints*.

Jørgensen, J.K., Bourke, T.L., Myers, P.C., Schöier, F.L., van Dishoeck, E.F. & Wilner, D.J. (2005). Probing the Inner 200 AU of Low-Mass Protostars with the Submillimeter Array: Dust and Organic Molecules in NGC 1333 IRAS 2A. ApJ, **632**, 973–981.

Kahn, F.D. (1974). Cocoons around early-type stars. A&A, **37**, 149–162.

Kainulainen, J. & Tan, J.C. (2013). High-dynamic-range extinction mapping of infrared dark clouds. Dependence of density variance with sonic Mach number in molecular clouds. A&A, **549**, A53.

Kainulainen, J., Ragan, S.E., Henning, T. & Stutz, A. (2013). High-fidelity view of the structure and fragmentation of the high-mass, filamentary IRDC G11.11-0.12. A&A, **557**, A120.

Kauffmann, J. & Pillai, T. (2010). How Many Infrared Dark Clouds Can form Massive Stars and Clusters? ApJL, **723**, L7–L12.

Kauffmann, J., Pillai, T. & Goldsmith, P.F. (2013a). Low Virial Parameters in Molecular Clouds: Implications for High-mass Star Formation and Magnetic Fields. ApJ, **779**, 185.

Kauffmann, J., Pillai, T. & Zhang, Q. (2013b). The Galactic Center Cloud G0.253+0.016: A Massive Dense Cloud with low Star Formation Potential. ApJL, **765**, L35.

Kawamura, A., Mizuno, Y., Minamidani, T., Filipović, M.D., Staveley-Smith, L., Kim, S., Mizuno, N., Onishi, T., Mizuno, A. & Fukui, Y. (2009). The Second Survey of the Molecular Clouds in the Large Magellanic Cloud by NANTEN. II. Star Formation. ApJS, **184**, 1–17.

Kenyon, S.J., Dobrzycka, D. & Hartmann, L. (1994). A new optical extinction law and distance estimate for the Taurus-Auriga molecular cloud. AJ, **108**, 1872–1880.

Kim, J., Ryu, D. & Jones, T.W. (2001). Three-dimensional Simulations of the Parker Instability in a Uniformly Rotating Disk. ApJ, **557**, 464–474.

Kim, W.T. & Ostriker, E.C. (2006). Formation of Spiral-Arm Spurs and Bound Clouds in Vertically Stratified Galactic Gas Disks. ApJ, **646**, 213–231.

Kirk, H., Johnstone, D. & Tafalla, M. (2007). Dynamics of Dense Cores in the Perseus Molecular Cloud. ApJ, **668**, 1042–1063.

Kirk, H., Myers, P.C., Bourke, T.L., Gutermuth, R.A., Hedden, A. & Wilson, G.W. (2013). Filamentary Accretion Flows in the Embedded Serpens South Protocluster. ApJ, **766**, 115.

Koda, J., Scoville, N., Sawada, T., La Vigne, M.A., Vogel, S.N., Potts, A.E., Carpenter, J.M., Corder, S.A., Wright, M.C.H., White, S.M., Zauderer, B.A., Patience, J., Sargent, A.I., Bock, D.C.J., Hawkins, D., Hodges, M., Kemball, A., Lamb, J.W., Plambeck, R.L., Pound, M.W., Scott, S.L., Teuben, P. & Woody, D.P. (2009). Dynamically Driven Evolution of the Interstellar Medium in M51. ApJL, **700**, L132–L136.

Koyama, H. & Inutsuka, S.I. (2000). Molecular Cloud Formation in Shock-compressed Layers. ApJ, **532**, 980–993.

Kramer, C., Stutzki, J. & Winnewisser, G. (1996). Structure and excitation conditions of the southern part of the Orion B molecular cloud: a CO multiline study. A&A, **307**, 915–935.

Kroupa, P. (2001). On the variation of the initial mass function. MNRAS, **322**, 231–246.

Krumholz, M.R. & McKee, C.F. (2008). A minimum column density of 1gcm^{-2} for massive star formation. Nature, **451**, 1082–1084.

Krumholz, M.R., Klein, R.I., McKee, C.F., Offner, S.S.R. & Cunningham, A.J. (2009). The Formation of Massive Star Systems by Accretion. *Science*, **323**, 754–.

Kuiper, R., Klahr, H., Beuther, H. & Henning, T. (2010). Circumventing the Radiation Pressure Barrier in the Formation of Massive Stars via Disk Accretion. ApJ, **722**, 1556–1576.

Kwan, J. (1979). The mass spectrum of interstellar clouds. ApJ, **229**, 567–577.

Kwan, J. & Valdes, F. (1987). The spatial and mass distributions of molecular clouds and spiral structure. ApJ, **315**, 92–103.

Lada, C.J. & Lada, E.A. (2003). Embedded Clusters in Molecular Clouds. ARA&A, **41**, 57–115.

Ladd, E.F., Fuller, G.A. & Deane, J.R. (1998). C 18O and C 17O Observations of Embedded Young Stars in the Taurus Molecular Cloud. I. Integrated Intensities and Column Densities. ApJ, **495**, 871.

Larson, R.B. (1969). Numerical calculations of the dynamics of collapsing protostar. MNRAS, **145**, 271.

Larson, R.B. (1979). Stellar kinematics and interstellar turbulence. MNRAS, **186**, 479–490.

Larson, R.B. (1981). Turbulence and star formation in molecular clouds. MNRAS, **194**, 809–826.

Larson, R.B. (2003). The physics of star formation. *Reports on Progress in Physics*, **66**, 1651–1697.

Larson, R.B. & Starrfield, S. (1971). On the formation of massive stars and the upper limit of stellar masses. A&A, **13**, 190–197.

Launhardt, R., Nutter, D., Ward-Thompson, D., Bourke, T.L., Henning, T., Khanzadyan, T., Schmalzl, M., Wolf, S. & Zylka, R. (2010). Looking Into the Hearts of Bok Globules: Millimeter and Submillimeter Continuum Images of Isolated Star-forming Cores. ApJS, **188**, 139–177.

Lee, E.J., Murray, N. & Rahman, M. (2012a). Milky Way Star-forming Complexes and the Turbulent Motion of the Galaxy's Molecular Gas. ApJ, **752**, 146.

Lee, M.Y., Stanimirović, S., Douglas, K.A., Knee, L.B.G., Di Francesco, J., Gibson, S.J., Begum, A., Grcevich, J., Heiles, C., Korpela, E.J., Leroy, A.K., Peek, J.E.G., Pingel, N.M., Putman, M.E. & Saul, D. (2012b). A High-resolution Study of the H I-H_2 Transition across the Perseus Molecular Cloud. ApJ, **748**, 75.

Li, D., Kauffmann, J., Zhang, Q. & Chen, W. (2013). Massive Quiescent Cores in Orion: Dynamical State Revealed by High-resolution Ammonia Maps. ApJL, **768**, L5.

Li, Y., Mac Low, M.M. & Klessen, R.S. (2005). Star Formation in Isolated Disk Galaxies. I. Models and Characteristics of Nonlinear Gravitational Collapse. ApJ, **626**, 823–843.

Lis, D.C. & Menten, K.M. (1998). Infrared Space Observatory Long Wavelength Spectrometer Observations of a Cold Giant Molecular Cloud Core near the Galactic Center. ApJ, **507**, 794–804.

Lis, D.C., Menten, K.M., Serabyn, E. & Zylka, R. (1994). Star formation in the galactic center dust ridge. ApJL, **423**, L39–L42.

Lis, D.C., Serabyn, E., Zylka, R. & Li, Y. (2001). Quiescent Giant Molecular Cloud Cores in the Galactic Center. ApJ, **550**, 761–777.

Longmore, S.N., Rathborne, J., Bastian, N., Alves, J., Ascenso, J., Bally, J., Testi, L., Longmore, A., Battersby, C., Bressert, E., Purcell, C., Walsh, A., Jackson, J., Foster, J., Molinari, S., Meingast, S., Amorim, A., Lima, J., Marques, R., Moitinho, A., Pinhao, J., Rebordao, J. & Santos, F.D. (2012). G0.253 + 0.016: A Molecular Cloud Progenitor of an Arches-like Cluster. ApJ, **746**, 117.

Longmore, S.N., Kruijssen, J.M.D., Bally, J., Ott, J., Testi, L., Rathborne, J., Bastian, N., Bressert, E., Molinari, S., Battersby, C. & Walsh, A.J. (2013). Candidate super star cluster progenitor gas clouds possibly triggered by close passage to Sgr A*. MNRAS, **433**, L15–L19.

Longmore, S.N., Kruijssen, J.M.D., Bastian, N., Bally, J., Rathborne, J., Testi, L., Stolte, A., Dale, J., Bressert, E. & Alves, J. (2014). The Formation and Early Evolution of Young Massive Clusters. *ArXiv e-prints*, arXiv:1401.4175.

Looney, L.W., Mundy, L.G. & Welch, W.J. (2000). Unveiling the Circumstellar Envelope and Disk: A Subarcsecond Survey of Circumstellar Structures. ApJ, **529**, 477–498.

Lumsden, S.L., Hoare, M.G., Urquhart, J.S., Oudmaijer, R.D., Davies, B., Mottram, J.C., Cooper, H.D.B. & Moore, T.J.T. (2013). The Red MSX Source Survey: The Massive Young Stellar Population of Our Galaxy. ApJS, **208**, 11.

Mac Low, M.M. & Klessen, R.S. (2004). Control of star formation by supersonic turbulence. *Reviews of Modern Physics*, **76**, 125–194.

Mac Low, M.M., Klessen, R.S., Burkert, A. & Smith, M.D. (1998). Kinetic Energy Decay Rates of Supersonic and Super-Alfvénic Turbulence in Star-Forming Clouds. *Physical Review Letters*, **80**, 2754–2757.

MacLaren, I., Richardson, K.M. & Wolfendale, A.W. (1988). Corrections to virial estimates of molecular cloud masses. ApJ, **333**, 821–825.

Markwardt, C.B. (2009). Non-linear Least-squares Fitting in IDL with MPFIT. In D.A. Bohlender, D. Durand & P. Dowler, eds., *Astronomical Data Analysis Software and Systems XVIII*, vol. 411 of *Astronomical Society of the Pacific Conference Series*, 251.

Martin, C.L. & Kennicutt, R.C., Jr. (2001). Star Formation Thresholds in Galactic Disks. ApJ, **555**, 301–321.

Mason, B.D., Hartkopf, W.I., Gies, D.R., Henry, T.J. & Helsel, J.W. (2009). The High Angular Resolution Multiplicity of Massive Stars. AJ, **137**, 3358–3377.

Mathis, J.S., Rumpl, W. & Nordsieck, K.H. (1977). The size distribution of interstellar grains. ApJ, **217**, 425–433.

Mathis, J.S., Mezger, P.G. & Panagia, N. (1983). Interstellar radiation field and dust temperatures in the diffuse interstellar matter and in giant molecular clouds. A&A, **128**, 212–229.

Maud, L.T., Hoare, M.G., Gibb, A.G., Shepherd, D. & Indebetouw, R. (2013). High angular resolution millimetre continuum observations and modelling of S140-IRS1. MNRAS, **428**, 609–624.

McKee, C.F. & Ostriker, E.C. (2007). Theory of Star Formation. ARA&A, **45**, 565–687.

McKee, C.F. & Tan, J.C. (2002). Massive star formation in 100,000 years from turbulent and pressurized molecular clouds. Nature, **416**, 59–61.

McKee, C.F. & Tan, J.C. (2003). The Formation of Massive Stars from Turbulent Cores. ApJ, **585**, 850–871.

Mestel, L. & Spitzer, L., Jr. (1956). Star formation in magnetic dust clouds. MNRAS, **116**, 503–+.

Miettinen, O. (2012). A molecular line study of the filamentary infrared dark cloud G304.74+01.32. A&A, **540**, A104.

Miettinen, O. (2014). A MALT90 study of the chemical properties of massive clumps and filaments of infrared dark clouds. A&A, **562**, A3.

Miettinen, O. & Offner, S.S.R. (2013). Dynamics, CO depletion, and deuterium fractionation of the dense condensations within the fragmented prestellar core Orion B9-SMM 6. A&A, **555**, A41.

Miettinen, O., Hennemann, M. & Linz, H. (2011). Deuterium fractionation and the degree of ionisation in massive clumps within infrared dark clouds. A&A, **534**, A134.

Millar, T.J., Bennett, A. & Herbst, E. (1989). Deuterium fractionation in dense interstellar clouds. ApJ, **340**, 906–920.

Miller, G.E. & Scalo, J.M. (1979). The initial mass function and stellar birthrate in the solar neighborhood. ApJS, **41**, 513–547.

Miville-Deschênes, M.A., Martin, P.G., Abergel, A., Bernard, J.P., Boulanger, F., Lagache, G., Anderson, L.D., André, P., Arab, H., Baluteau, J.P., Blagrave, K., Bontemps, S., Cohen, M., Compiegne, M., Cox, P., Dartois, E., Davis, G., Emery, R., Fulton, T., Gry, C., Habart, E., Huang, M., Joblin, C., Jones, S.C., Kirk, J., Lim, T., Madden, S., Makiwa, G., Menshchikov, A., Molinari, S., Moseley, H., Motte, F., Naylor, D.A., Okumura, K., Pinheiro Gonçalves, D., Polehampton, E., Rodón, J.A., Russeil, D., Saraceno, P., Schneider, N., Sidher, S., Spencer, L., Swinyard, B., Ward-Thompson, D., White, G.J. & Zavagno, A. (2010). Herschel-SPIRE observations of the Polaris flare: Structure of the diffuse interstellar medium at the sub-parsec scale. A&A, **518**, L104.

Mizuno, A., Onishi, T., Yonekura, Y., Nagahama, T., Ogawa, H. & Fukui, Y. (1995). Overall distribution of dense molecular gas and star formation in the the Taurus cloud complex. ApJL, **445**, L161–L165.

Moeckel, N. & Burkert, A. (2014). The formation of filamentary bundles in turbulent molecular clouds. *ArXiv e-prints*.

Molinari, S., Swinyard, B., Bally, J., Barlow, M., Bernard, J.P., Martin, P., Moore, T., Noriega-Crespo, A., Plume, R., Testi, L., Zavagno, A., Abergel, A., Ali, B., Anderson, L., André, P., Baluteau, J.P., Battersby, C., Beltrán, M.T., Benedettini, M., Billot, N., Blommaert, J., Bontemps, S., Boulanger, F., Brand, J., Brunt, C., Burton, M., Calzoletti, L., Carey, S., Caselli, P., Cesaroni, R., Cernicharo, J., Chakrabarti, S., Chrysostomou, A., Cohen, M., Compiegne, M., de Bernardis, P., de Gasperis, G., di Giorgio, A.M., Elia, D., Faustini, F., Flagey, N., Fukui, Y., Fuller, G.A., Ganga, K., Garcia-Lario, P., Glenn, J., Goldsmith, P.F., Griffin, M., Hoare, M., Huang, M., Ikhenaode, D., Joblin, C., Joncas, G., Juvela, M., Kirk, J.M., Lagache, G., Li, J.Z., Lim, T.L., Lord, S.D., Marengo, M., Marshall, D.J., Masi, S., Massi, F., Matsuura, M., Minier, V., Miville-Deschênes, M.A., Montier, L.A., Morgan, L., Motte, F., Mottram, J.C., Müller, T.G., Natoli, P., Neves, J., Olmi, L., Paladini, R., Paradis, D., Parsons, H., Peretto, N., Pestalozzi, M., Pezzuto, S., Piacentini, F., Piazzo, L., Polychroni, D., Pomarès, M., Popescu, C.C., Reach, W.T., Ristorcelli, I., Robitaille, J.F., Robitaille, T., Rodón, J.A., Roy, A., Royer, P., Russeil, D., Saraceno, P., Sauvage, M., Schilke, P., Schisano, E., Schneider, N., Schuller, F., Schulz, B., Sibthorpe, B., Smith, H.A., Smith, M.D., Spinoglio, L., Stamatellos, D., Strafella, F., Stringfellow, G.S., Sturm, E., Taylor, R., Thompson, M.A., Traficante, A., Tuffs, R.J., Umana, G., Valenziano, L., Vavrek, R., Veneziani, M., Viti, S., Waelkens, C., Ward-Thompson, D., White, G., Wilcock, L.A., Wyrowski, F., Yorke, H.W. & Zhang, Q. (2010). Clouds, filaments, and protostars: The Herschel Hi-GAL Milky Way. A&A, **518**, L100.

Molinari, S., Bally, J., Noriega-Crespo, A., Compiègne, M., Bernard, J.P., Paradis, D., Martin, P., Testi, L., Barlow, M., Moore, T., Plume, R., Swinyard, B., Zavagno, A., Calzoletti, L., Di Giorgio, A.M., Elia, D., Faustini, F., Natoli, P., Pestalozzi, M., Pezzuto, S., Piacentini, F., Polenta, G., Polychroni, D., Schisano, E., Traficante, A., Veneziani, M., Battersby, C., Burton, M., Carey, S., Fukui, Y., Li, J.Z., Lord, S.D., Morgan, L., Motte, F., Schuller, F., Stringfellow, G.S., Tan, J.C., Thompson, M.A., Ward-Thompson, D., White, G. & Umana, G. (2011). A 100 pc Elliptical

and Twisted Ring of Cold and Dense Molecular Clouds Revealed by Herschel Around the Galactic Center. ApJL, **735**, L33.

Molinari, S., Bally, J., Glover, S., Moore, T., Noriega-Crespo, A., Plume, R., Testi, L., Vázquez-Semadeni, E., Zavagno, A., Bernard, J.P. & Martin, P. (2014). The Milky Way as a Star Formation Engine. *ArXiv e-prints*, arXiv:1402.6196.

Motte, F., André, P., Ward-Thompson, D. & Bontemps, S. (2001). A SCUBA survey of the NGC 2068/2071 protoclusters. A&A, **372**, L41–L44.

Motte, F., Zavagno, A., Bontemps, S., Schneider, N., Hennemann, M., di Francesco, J., André, P., Saraceno, P., Griffin, M., Marston, A., Ward-Thompson, D., White, G., Minier, V., Men'shchikov, A., Hill, T., Abergel, A., Anderson, L.D., Aussel, H., Balog, Z., Baluteau, J.P., Bernard, J.P., Cox, P., Csengeri, T., Deharveng, L., Didelon, P., di Giorgio, A.M., Hargrave, P., Huang, M., Kirk, J., Leeks, S., Li, J.Z., Martin, P., Molinari, S., Nguyen-Luong, Q., Olofsson, G., Persi, P., Peretto, N., Pezzuto, S., Roussel, H., Russeil, D., Sadavoy, S., Sauvage, M., Sibthorpe, B., Spinoglio, L., Testi, L., Teyssier, D., Vavrek, R., Wilson, C.D. & Woodcraft, A. (2010). Initial highlights of the HOBYS key program, the Herschel imaging survey of OB young stellar objects. A&A, **518**, L77.

Mouschovias, T.C. & Spitzer, L., Jr. (1976). Note on the collapse of magnetic interstellar clouds. ApJ, **210**, 326–+.

Müller, H.S.P., Schlöder, F., Stutzki, J. & Winnewisser, G. (2005). The Cologne Database for Molecular Spectroscopy, CDMS: a useful tool for astronomers and spectroscopists. *Journal of Molecular Structure*, **742**, 215–227.

Myers, A.T., McKee, C.F., Cunningham, A.J., Klein, R.I. & Krumholz, M.R. (2013). The Fragmentation of Magnetized, Massive Star-forming Cores with Radiative Feedback. ApJ, **766**, 97.

Myers, P.C. (1983). Dense cores in dark clouds. III - Subsonic turbulence. ApJ, **270**, 105–118.

Myers, P.C. (2005). Centrally Condensed Collapse of Starless Cores. ApJ, **623**, 280–290.

Myers, P.C. & Benson, P.J. (1983). Dense cores in dark clouds. II - NH3 observations and star formation. ApJ, **266**, 309–320.

Myers, P.C. & Fuller, G.A. (1992). Density structure and star formation in dense cores with thermal and nonthermal motions. ApJ, **396**, 631–642.

Myers, P.C., Dame, T.M., Thaddeus, P., Cohen, R.S., Silverberg, R.F., Dwek, E. & Hauser, M.G. (1986). Molecular clouds and star formation in the inner galaxy - A comparison of CO, H II, and far-infrared surveys. ApJ, **301**, 398–422.

Myers, P.C., Evans, N.J., II & Ohashi, N. (2000). Observations of Infall in Star-Forming Regions. *Protostars and Planets IV*, 217.

Nagasawa, M. (1987). Gravitational Instability of the Isothermal Gas Cylinder with an Axial magnetic Field. *Progress of Theoretical Physics*, **77**, 635–652.

Nakamura, F., Miura, T., Kitamura, Y., Shimajiri, Y., Kawabe, R., Akashi, T., Ikeda, N., Tsukagoshi, T., Momose, M., Nishi, R. & Li, Z.Y. (2012). Evidence for Cloud-Cloud Collision and Parsec-scale Stellar Feedback within the L1641-N Region. ApJ, **746**, 25.

Nguyen Luong, Q., Motte, F., Hennemann, M., Hill, T., Rygl, K.L.J., Schneider, N., Bontemps, S., Men'shchikov, A., André, P., Peretto, N., Anderson, L.D., Arzoumanian, D., Deharveng, L., Didelon, P., di Francesco, J., Griffin, M.J., Kirk, J.M., Könyves, V., Martin, P.G., Maury, A., Minier, V., Molinari, S., Pestalozzi, M., Pezzuto, S., Reid, M., Roussel, H., Sauvage, M., Schuller, F., Testi, L., Ward-Thompson, D., White, G.J. & Zavagno, A. (2011). The Herschel view of massive star formation in G035.39-00.33: dense and cold filament of W48 undergoing a mini-starburst. A&A, **535**, A76.

Offner, S.S.R., Krumholz, M.R., Klein, R.I. & McKee, C.F. (2008). The Kinematics of Molecular Cloud Cores in the Presence of Driven and Decaying Turbulence: Comparisons with Observations. AJ, **136**, 404–420.

Offner, S.S.R., Clark, P.C., Hennebelle, P., Bastian, N., Bate, M.R., Hopkins, P.F., Moraux, E. & Whitworth, A.P. (2013). The Origin and Universality of the Stellar Initial Mass Function. *ArXiv e-prints*, ArXiv:1312.5326.

Oort, J.H. (1954). Outline of a theory on the origin and acceleration of interstellar clouds and O associations. Bull. Astron. Inst. Netherlands, **12**, 177.

Ossenkopf, V. & Henning, T. (1994). Dust opacities for protostellar cores. A&A, **291**, 943–959.

Ostriker, J. (1964). The Equilibrium of Polytropic and Isothermal Cylinders. ApJ, **140**, 1056.

Pagani, L., Daniel, F. & Dubernet, M. (2009). On the frequency of N_2H^+ and N_2D^+. A&A, **494**, 719–727.

Palla, F. & Stahler, S.W. (2000). Accelerating Star Formation in Clusters and Associations. ApJ, **540**, 255–270.

Palmeirim, P., André, P., Kirk, J., Ward-Thompson, D., Arzoumanian, D., Könyves, V., Didelon, P., Schneider, N., Benedettini, M., Bontemps, S., Di Francesco, J., Elia, D., Griffin, M., Hennemann, M., Hill, T., Martin, P.G., Men'shchikov, A., Molinari, S., Motte, F., Nguyen Luong, Q., Nutter, D., Peretto, N., Pezzuto, S., Roy, A., Rygl, K.L.J., Spinoglio, L. & White, G.L. (2013). Herschel view of the Taurus B211/3 filament and striations: evidence of filamentary growth? A&A, **550**, A38.

Penzias, A.A. (1981). The isotopic abundances of interstellar oxygen. ApJ, **249**, 518–523.

Pérault, M., Omont, A., Simon, G., Seguin, P., Ojha, D., Blommaert, J., Felli, M., Gilmore, G., Guglielmo, F., Habing, H., Price, S., Robin, A., de Batz, B., Cesarsky, C., Elbaz, D., Epchtein, N., Fouque, P., Guest, S., Levine, D., Pollock, A., Prusti, T., Siebenmorgen, R., Testi, L. & Tiphene, D. (1996). First ISOCAM images of the Milky Way. A&A, **315**, L165–L168.

Peretto, N. & Fuller, G.A. (2009). A catalogue of Spitzer dark clouds (Peretto+, 2009). *VizieR Online Data Catalog*, **350**, 50405–+.

Peretto, N., André, P. & Belloche, A. (2006). Probing the formation of intermediate- to high-mass stars in protoclusters. A detailed millimeter study of the NGC 2264 clumps. A&A, **445**, 979–998.

Peretto, N., Hennebelle, P. & André, P. (2007). Probing the formation of intermediate- to high-mass stars in protoclusters. II. Comparison between millimeter interferometric observations of NGC 2264-C and SPH simulations of a collapsing clump. A&A, **464**, 983–994.

Peretto, N., Fuller, G.A., Plume, R., Anderson, L.D., Bally, J., Battersby, C., Beltran, M.T., Bernard, J.P., Calzoletti, L., Digiorgio, A.M., Faustini, F., Kirk, J.M., Lenfestey, C., Marshall, D., Martin, P., Molinari, S., Montier, L., Motte, F., Ristorcelli,

I., Rodón, J.A., Smith, H.A., Traficante, A., Veneziani, M., Ward-Thompson, D. & Wilcock, L. (2010). Mapping the column density and dust temperature structure of IRDCs with Herschel. A&A, **518**, L98.

Peretto, N., Fuller, G.A., Duarte-Cabral, A., Avison, A., Hennebelle, P., Pineda, J.E., André, P., Bontemps, S., Motte, F., Schneider, N. & Molinari, S. (2013). Global collapse of molecular clouds as a formation mechanism for the most massive stars. A&A, **555**, A112.

Peretto, N., Fuller, G.A., André, P., Arzoumanian, D., Rivilla, V.M., Bardeau, S., Duarte Puertas, S., Guzman Fernandez, J.P., Lenfestey, C., Li, G.X., Olguin, F.A., Röck, B.R., de Villiers, H. & Williams, J. (2014). SDC13 infrared dark clouds: Longitudinally collapsing filaments? A&A, **561**, A83.

Pilbratt, G.L., Riedinger, J.R., Passvogel, T., Crone, G., Doyle, D., Gageur, U., Heras, A.M., Jewell, C., Metcalfe, L., Ott, S. & Schmidt, M. (2010). Herschel Space Observatory. An ESA facility for far-infrared and submillimetre astronomy. A&A, **518**, L1+.

Pillai, T., Wyrowski, F., Carey, S.J. & Menten, K.M. (2006). Ammonia in infrared dark clouds. A&A, **450**, 569–583.

Pillai, T., Kauffmann, J., Wyrowski, F., Hatchell, J., Gibb, A.G. & Thompson, M.A. (2011). Probing the initial conditions of high-mass star formation. II. Fragmentation, stability, and chemistry towards high-mass star-forming regions G29.96-0.02 and G35.20-1.74. A&A, **530**, A118.

Pineda, J.E. & Teixeira, P.S. (2013). Spokes cluster: The search for the quiescent gas. A&A, **555**, A106.

Pineda, J.E., Caselli, P. & Goodman, A.A. (2008). CO Isotopologues in the Perseus Molecular Cloud Complex: the X-factor and Regional Variations. ApJ, **679**, 481–496.

Pineda, J.E., Goodman, A.A., Arce, H.G., Caselli, P., Foster, J.B., Myers, P.C. & Rosolowsky, E.W. (2010). Direct Observation of a Sharp Transition to Coherence in Dense Cores. ApJL, **712**, L116–L121.

Pineda, J.E., Arce, H.G., Schnee, S., Goodman, A.A., Bourke, T., Foster, J.B., Robitaille, T., Tanner, J., Kauffmann, J., Tafalla, M., Caselli, P. & Anglada, G. (2011). The Enigmatic Core L1451-mm: A First Hydrostatic Core? Or a Hidden VeLLO? ApJ, **743**, 201.

Pon, A., Johnstone, D. & Heitsch, F. (2011). Modes of Star Formation in Finite Molecular Clouds. ApJ, **740**, 88.

Pon, A., Toalá, J.A., Johnstone, D., Vázquez-Semadeni, E., Heitsch, F. & Gómez, G.C. (2012). Aspect Ratio Dependence of the Free-fall Time for Non-spherical Symmetries. ApJ, **756**, 145.

Quillen, A.C., Thorndike, S.L., Cunningham, A., Frank, A., Gutermuth, R.A., Blackman, E.G., Pipher, J.L. & Ridge, N. (2005). Turbulence Driven by Outflow-blown Cavities in the Molecular Cloud of NGC 1333. ApJ, **632**, 941–955.

Ragan, S.E., Bergin, E.A. & Wilner, D. (2011). Very Large Array Observations of Ammonia in Infrared-dark Clouds. I. Column Density and Temperature Structure. ApJ, **736**, 163.

Ragan, S.E., Heitsch, F., Bergin, E.A. & Wilner, D. (2012). Very Large Array Observations of Ammonia in Infrared-dark Clouds. II. Internal Kinematics. ApJ, **746**, 174.

Ragan, S.E., Henning, T. & Beuther, H. (2013). APEX/SABOCA observations of small-scale structure of infrared-dark clouds I. Early evolutionary stages of star-forming cores. *ArXiv e-prints*.

Rathborne, J.M., Jackson, J.M. & Simon, R. (2006). Infrared Dark Clouds: Precursors to Star Clusters. ApJ, **641**, 389–405.

Rathborne, J.M., Simon, R. & Jackson, J.M. (2007). The Detection of Protostellar Condensations in Infrared Dark Cloud Cores. ApJ, **662**, 1082–1092.

Rathborne, J.M., Jackson, J.M., Chambers, E.T., Stojimirovic, I., Simon, R., Shipman, R. & Frieswijk, W. (2010). The Early Stages of Star Formation in Infrared Dark Clouds: Characterizing the Core Dust Properties. ApJ, **715**, 310–322.

Rathborne, J.M., Longmore, S.N., Jackson, J.M., Foster, J.B., Contreras, Y., Garay, G., Testi, L., Alves, J.F., Bally, J., Bastian, N., Kruijssen, J.M.D. & Bressert, E. (2014). G0.253+0.016: A Centrally Condensed, High-mass Protocluster. ApJ, **786**, 140.

Richer, J.S., Shepherd, D.S., Cabrit, S., Bachiller, R. & Churchwell, E. (2000). Molecular Outflows from Young Stellar Objects. *Protostars and Planets IV*, 867.

Roman-Duval, J., Jackson, J.M., Heyer, M., Rathborne, J. & Simon, R. (2010). Physical Properties and Galactic Distribution of Molecular Clouds Identified in the Galactic Ring Survey. ApJ, **723**, 492–507.

Rosolowsky, E., Engargiola, G., Plambeck, R. & Blitz, L. (2003). Giant Molecular Clouds in M33. II. High-Resolution Observations. ApJ, **599**, 258–274.

Rosolowsky, E.W., Pineda, J.E., Kauffmann, J. & Goodman, A.A. (2008). Structural Analysis of Molecular Clouds: Dendrograms. ApJ, **679**, 1338–1351.

Rygl, K.L.J., Wyrowski, F., Schuller, F. & Menten, K.M. (2013). Initial phases of massive star formation in high infrared extinction clouds. II. Infall and onset of star formation. A&A, **549**, A5.

Sakai, T., Sakai, N., Kamegai, K., Hirota, T., Yamaguchi, N., Shiba, S. & Yamamoto, S. (2008). A Molecular Line Observation toward Massive Clumps Associated with Infrared Dark Clouds. ApJ, **678**, 1049–1069.

Salpeter, E.E. (1955). The Luminosity Function and Stellar Evolution. ApJ, **121**, 161.

Sanhueza, P., Jackson, J.M., Foster, J.B., Garay, G., Silva, A. & Finn, S.C. (2012). Chemistry in Infrared Dark Cloud Clumps: A Molecular Line Survey at 3 mm. ApJ, **756**, 60.

Sanhueza, P., Jackson, J.M., Foster, J.B., Jimenez-Serra, I., Dirienzo, W.J. & Pillai, T. (2013). Distinct Chemical Regions in the "Prestellar" Infrared Dark Cloud G028.23–00.19. ApJ, **773**, 123.

Schneider, N., Csengeri, T., Bontemps, S., Motte, F., Simon, R., Hennebelle, P., Federrath, C. & Klessen, R. (2010a). Dynamic star formation in the massive DR21 filament. A&A, **520**, A49.

Schneider, N., Motte, F., Bontemps, S., Hennemann, M., di Francesco, J., André, P., Zavagno, A., Csengeri, T., Men'shchikov, A., Abergel, A., Baluteau, J.P., Bernard, J.P., Cox, P., Didelon, P., di Giorgio, A.M., Gastaud, R., Griffin, M., Hargrave, P., Hill, T., Huang, M., Kirk, J., Könyves, V., Leeks, S., Li, J.Z., Marston, A., Martin, P., Minier, V., Molinari, S., Olofsson, G., Panuzzo, P., Persi, P., Pezzuto, S., Roussel, H., Russeil, D., Sadavoy, S., Saraceno, P., Sauvage, M., Sibthorpe, B., Spinoglio, L., Testi, L., Teyssier, D., Vavrek, R., Ward-Thompson, D., White, G., Wilson,

C.D. & Woodcraft, A. (2010b). The Herschel view of star formation in the Rosette molecular cloud under the influence of NGC 2244. A&A, **518**, L83.

Schneider, N., Csengeri, T., Hennemann, M., Motte, F., Didelon, P., Federrath, C., Bontemps, S., Di Francesco, J., Arzoumanian, D., Minier, V., André, P., Hill, T., Zavagno, A., Nguyen-Luong, Q., Attard, M., Bernard, J.P., Elia, D., Fallscheer, C., Griffin, M., Kirk, J., Klessen, R., Könyves, V., Martin, P., Men'shchikov, A., Palmeirim, P., Peretto, N., Pestalozzi, M., Russeil, D., Sadavoy, S., Sousbie, T., Testi, L., Tremblin, P., Ward-Thompson, D. & White, G. (2012). Cluster-formation in the Rosette molecular cloud at the junctions of filaments. A&A, **540**, L11.

Schneider, S. & Elmegreen, B.G. (1979). A catalog of dark globular filaments. ApJS, **41**, 87–95.

Schöier, F.L., van der Tak, F.F.S., van Dishoeck, E.F. & Black, J.H. (2005). An atomic and molecular database for analysis of submillimetre line observations. A&A, **432**, 369–379.

Scoville, N.Z. & Hersh, K. (1979). Collisional growth of giant molecular clouds. ApJ, **229**, 578–582.

Shetty, R. & Ostriker, E.C. (2006). Global Modeling of Spur Formation in Spiral Galaxies. ApJ, **647**, 997–1017.

Shetty, R., Collins, D.C., Kauffmann, J., Goodman, A.A., Rosolowsky, E.W. & Norman, M.L. (2010). The Effect of Projection on Derived Mass-Size and Linewidth-Size Relationships. ApJ, **712**, 1049–1056.

Shetty, R., Beaumont, C.N., Burton, M.G., Kelly, B.C. & Klessen, R.S. (2012). The linewidth-size relationship in the dense interstellar medium of the Central Molecular Zone. MNRAS, **425**, 720–729.

Shirley, Y.L., Evans, N.J., II, Young, K.E., Knez, C. & Jaffe, D.T. (2003). A CS J=5–4 Mapping Survey Toward High-Mass Star-forming Cores Associated with Water Masers. ApJS, **149**, 375–403.

Shu, F.H., Adams, F.C. & Lizano, S. (1987). Star formation in molecular clouds - Observation and theory. ARA&A, **25**, 23–81.

Simon, R., Jackson, J.M., Rathborne, J.M. & Chambers, E.T. (2006a). A Catalog of Midcourse Space Experiment Infrared Dark Cloud Candidates. ApJ, **639**, 227–236.

Simon, R., Rathborne, J.M., Shah, R.Y., Jackson, J.M. & Chambers, E.T. (2006b). The Characterization and Galactic Distribution of Infrared Dark Clouds. ApJ, **653**, 1325–1335.

Smith, R.J., Shetty, R., Beuther, H., Klessen, R.S. & Bonnell, I.A. (2013). Line Profiles of Cores within Clusters. II. Signatures of Dynamical Collapse during High-mass Star Formation. ApJ, **771**, 24.

Solomon, P.M., Rivolo, A.R., Barrett, J. & Yahil, A. (1987a). Mass, luminosity, and line width relations of Galactic molecular clouds. ApJ, **319**, 730–741.

Solomon, P.M., Rivolo, A.R., Barrett, J. & Yahil, A. (1987b). Mass, luminosity, and line width relations of Galactic molecular clouds. ApJ, **319**, 730–741.

Stahler, S.W. & Palla, F. (2005). *The Formation of Stars*.

Stodółkiewicz, J.S. (1963). On the Gravitational Instability of Some Magneto-Hydrodynamical Systems of Astrophysical Interest. Part III. Acta Astronomica, **13**, 30–54.

Tackenberg, J., Beuther, H., Henning, T., Linz, H., Sakai, T., Ragan, S.E., Krause, O., Nielbock, M., Hennemann, M., Pitann, J. & Schmiedeke, A. (2014). Kinematic structure of massive star-forming regions. I. Accretion along filaments. A&A, **565**, A101.

Tafalla, M. & Santiago, J. (2004). L1521E: The first starless core with no molecular depletion. A&A, **414**, L53–L56.

Tafalla, M., Myers, P.C., Caselli, P., Walmsley, C.M. & Comito, C. (2002). Systematic Molecular Differentiation in Starless Cores. ApJ, **569**, 815–835.

Tafalla, M., Myers, P.C., Caselli, P. & Walmsley, C.M. (2004). On the internal structure of starless cores. I. Physical conditions and the distribution of CO, CS, N_2H^+, and NH_3 in L1498 and L1517B. A&A, **416**, 191–212.

Tan, J.C., Kong, S., Butler, M.J., Caselli, P. & Fontani, F. (2013a). The Dynamics of Massive Starless Cores with ALMA. ApJ, **779**, 96.

Tan, J.C., Shaske, S.N. & Van Loo, S. (2013b). Molecular Clouds: Internal Properties, Turbulence, Star Formation and Feedback. In T. Wong & J. Ott, eds., *IAU Symposium*, vol. 292 of *IAU Symposium*, 19–28.

Tan, J.C., Beltran, M.T., Caselli, P., Fontani, F., Fuente, A., Krumholz, M.R., McKee, C.F. & Stolte, A. (2014). Massive Star Formation. *ArXiv e-prints*, arXiv:1402.0919.

Tanaka, T., Nakamura, F., Awazu, Y., Shimajiri, Y., Sugitani, K., Onishi, T., Kawabe, R., Yoshida, H. & Higuchi, A.E. (2013). The Dynamical State of the Serpens South Filamentary Infrared Dark Cloud. ApJ, **778**, 34.

Tasker, E.J. & Tan, J.C. (2009). Star Formation in Disk Galaxies. I. Formation and Evolution of Giant Molecular Clouds via Gravitational Instability and Cloud Collisions. ApJ, **700**, 358–375.

Teixeira, P.S., Lada, C.J., Young, E.T., Marengo, M., Muench, A., Muzerolle, J., Siegler, N., Rieke, G., Hartmann, L., Megeath, S.T. & Fazio, G. (2006). Identifying Primordial Substructure in NGC 2264. ApJL, **636**, L45–L48.

Teixeira, P.S., Zapata, L.A. & Lada, C.J. (2007). A Dense Microcluster of Class 0 Protostars in NGC 2264 D-MM1. ApJL, **667**, L179–L182.

Thies, I. & Kroupa, P. (2007). A Discontinuity in the Low-Mass Initial Mass Function. ApJ, **671**, 767–780.

Tielens, A.G.G.M. (2005). *The Physics and Chemistry of the Interstellar Medium*.

Tobin, J.J., Bergin, E.A., Hartmann, L., Lee, J.E., Maret, S., Myers, P.C., Looney, L.W., Chiang, H.F. & Friesen, R. (2013). Resolved Depletion Zones and Spatial Differentiation of N_2H^+ and N_2D^+. ApJ, **765**, 18.

Tomisaka, K. (1995). Collapse and fragmentation of magnetized cylindrical clouds. ApJ, **438**, 226–243.

Toomre, A. (1964). On the gravitational stability of a disk of stars. ApJ, **139**, 1217–1238.

Urquhart, J.S., Figura, C.C., Moore, T.J.T., Hoare, M.G., Lumsden, S.L., Mottram, J.C., Thompson, M.A. & Oudmaijer, R.D. (2014). The RMS survey: galactic distribution of massive star formation. MNRAS, **437**, 1791–1807.

van der Tak, F.F.S., van Dishoeck, E.F., Evans, N.J., II & Blake, G.A. (2000). Structure and Evolution of the Envelopes of Deeply Embedded Massive Young Stars. ApJ, **537**, 283–303.

van der Tak, F.F.S., Black, J.H., Schöier, F.L., Jansen, D.J. & van Dishoeck, E.F. (2007). A computer program for fast non-LTE analysis of interstellar line spectra. With diagnostic plots to interpret observed line intensity ratios. A&A, **468**, 627–635.

Vasyunina, T., Linz, H., Henning, T., Stecklum, B., Klose, S. & Nyman, L.Å. (2009). Physical properties of Southern infrared dark clouds. A&A, **499**, 149–161.

Vasyunina, T., Linz, H., Henning, T., Zinchenko, I., Beuther, H. & Voronkov, M. (2011). Chemistry in infrared dark clouds. A&A, **527**, A88.

Vazquez-Semadeni, E., Passot, T. & Pouquet, A. (1995). A turbulent model for the interstellar medium. 1: Threshold star formation and self-gravity. ApJ, **441**, 702–725.

Vázquez-Semadeni, E., Gómez, G.C., Jappsen, A.K., Ballesteros-Paredes, J., González, R.F. & Klessen, R.S. (2007). Molecular Cloud Evolution. II. From Cloud Formation to the Early Stages of Star Formation in Decaying Conditions. ApJ, **657**, 870–883.

Walsh, A.J., Myers, P.C. & Burton, M.G. (2004). Star Formation on the Move? ApJ, **614**, 194–202.

Wang, K., Zhang, Q., Wu, Y. & Zhang, H. (2011). Hierarchical Fragmentation and Jet-like Outflows in IRDC G28.34+0.06: A Growing Massive Protostar Cluster. ApJ, **735**, 64.

Wang, K., Zhang, Q., Testi, L., Tak, F.v.d., Wu, Y., Zhang, H., Pillai, T., Wyrowski, F., Carey, S., Ragan, S.E. & Henning, T. (2014). Hierarchical fragmentation and differential star formation in the Galactic 'Snake': infrared dark cloud G11.11-0.12. MNRAS.

Wang, Y., Zhang, Q., Pillai, T., Wyrowski, F. & Wu, Y. (2008). NH_3 Observations of the Infrared Dark Cloud G28.34+0.06. ApJL, **672**, L33–L36.

Ward-Thompson, D., Scott, P.F., Hills, R.E. & Andre, P. (1994). A Submillimetre Continuum Survey of Pre Protostellar Cores. MNRAS, **268**, 276.

Williams, J.P., Blitz, L. & McKee, C.F. (2000). The Structure and Evolution of Molecular Clouds: from Clumps to Cores to the IMF. *Protostars and Planets IV*, 97.

Wolfire, M.G. & Cassinelli, J.P. (1987). Conditions for the formation of massive stars. ApJ, **319**, 850–867.

Wootten, H.A. (1977). The molecular cloud associated with the supernova remnant W44. ApJ, **216**, 440–445.

Zhang, Q., Hunter, T.R., Beuther, H., Sridharan, T.K., Liu, S.Y., Su, Y.N., Chen, H.R. & Chen, Y. (2007). Multiple Jets from the High-Mass (Proto)stellar Cluster AFGL 5142. ApJ, **658**, 1152–1163.

Zhang, Q., Wang, Y., Pillai, T. & Rathborne, J. (2009). Fragmentation at the Earliest Phase of Massive Star Formation. ApJ, **696**, 268–273.

Zuckerman, B. & Palmer, P. (1974). Radio radiation from interstellar molecules. ARA&A, **12**, 279–313.